FINAL TECHNICAL REPORT

CONTRACT N° :FIKW-CT-2000-00031

PROJECT N° : FIS5-00150

ACRONYM : HINDAS

TITLE : High and Intermediate energy Nuclear Data for Accelerator-driven Systems

PROJECT CO-ORDINATOR :

Université catholique de Louvain (B) - Institut de Physique Nucléaire – Louvain-la-Neuve.

PARTNERS :

Université de Nantes (F) – Labor. de Physique subatomique.
CNRS Laboratoire de Physique Corpusculaire de Caen (F).
Rijksuniversiteit Groningen (Nl) – Kernfysisch Versneller Insituut.
Uppsala Universitet (S) – Departement of Neutron Research.
Universität Hannover (D) – Zentrum für Strahlenschutz une une Radiökologie.
Physikalisch-Technische Bundesanstalt (D) – Department of Ionizing Radiation.
Swisss federal institute of Technology (ETH) Zürich (CH) – Institute of Particle Physics.
Paul Scherrer Institute (CH) – Laboratory Radio- and Enviromental Chemistry.
Forschungzentrum Jülich Gmbh (D) – Insitut für Kernphysik.
Commissariat à l'Energie Atomique-Saclay (F) -DSM/DAPNIA- Service de Physique Nucléaire.
Commissariat à l'Energie Atomique-Bruyères-le-Châtel-(F) -Service de physique Nucléaire.
Gesellschaft für Scwherionenforschung mbH (D) – Accelerator department.
Universidade de Santiago de Compostela (E) – Departamento de Fisica de particulas.
Université de Liège (B) – Institut de Physique.
Nuclear Research and consultancy Group - Petten (Nl) – Fuel, Actinides and Isotopes.

REPORTING PERIOD : FROM September 1, 2000 TO November 30, 2003

PROJECT START DATE : September 1, 2000 DURATION : 39 months

Date of issue of this report : January 2005

	Project funded by the European Community under the 'Fifth' Programme (1998-2002)

HINDAS

Detailed Final Report

Editors

J.P. Meulders (Coordinator – UCL)
A.Koning (NRG-Petten)
S.Leray (CEA-Saclay)

List of Contents

Executive summary

HINDAS (**H**igh and **I**ntermediate Energy **N**uclear **D**ata for **A**ccelerator Driven **S**ystems) is an European project in the framework of partitioning and transmutation of radioactive waste. Its objective was to obtain a general understanding and modelling of nuclear reactions in the intermediate energy range between 20 MeV and 200 MeV, and in the high energy range between 200 MeV and 2 GeV, in order to build reliable and validated tools for the detailed design of an Accelerator Driven System. For an ADS, the major benefit of accurate nuclear data specifically relates to avoiding unnecessary conservatism related to important issues such as shielding requirements, power coefficients for a core loaded with minor actinides, and the related power requirements of the proton accelerator. A good control over nuclear data in the entire energy range is then indispensible.

This objective has been pursued by associating 16 European laboratories in the following program :

- Measurement of the most complete set of data from three selected elements, namely Fe as a shielding element, Pb as target element and U as element representative of the actinides.
- Improvement and validation of the relevant nuclear physics models on the basis of the new experimental data.
- Generation of evaluated data libraries (20 – 200 MeV) and implementation of the high-energy models into high-energy transport codes 200 – 2000 MeV).

The **experiments at intermediate energies** were performed at three accelerators : TSL-Uppsala, KVI-Groningen and UCL-Louvain-la-Neuve. A large amount of new double differential cross sections (DDXS), energy differential cross sections, angular distributions and total cross sections have been measured between 20 and 200 MeV.

- Light charged particle production induced by protons (lcp = p, d, t, ^{3}He and α) were measured at 65 MeV at UCL and 135 MeV at KVI on the three target elements. Light charged particle production induced by neutrons were measured between 20 and 65 MeV at UCL and at 100 MeV at TSL. Almost no neutron-induced reaction cross sections had been previously measured in this energy region.
- Neutron production has been measured in (p,xn) on Pb and U at 65 MeV, while neutron elastic scattering was studied at 100 MeV as a preparation to (n,xn) experiments at the same energy. Finally, total cross sections of neutron-induced fission has been measured from 30 to 180 MeV at the same facilities.
- The production of residuals induced by protons between 30 and 70 MeV and induced by neutrons between 20 and 200 MeV on a large set of elements in this project, completes a global study of direct residual production between 20 MeV and 2 GeV initiated by the ZSR (Hannover) laboratory. Combining off-line γ-spectrometry with Accelerator Mass Spectrometry (at ETH-Zürich) allows the detection of long-lived radio-nuclides.

A large effort has been devoted in the **theoretical work at intermediate energies** to upgrade all the nuclear models in one nuclear reaction code – TALYS - under initiative of NRG – Petten and CEA – Bruyères-le-Châtel. The TALYS code predicts total and partial cross sections, energy spectra, angular distributions, double differential cross sections of n- and p-induced reactions, which is a difficult challenge. It also predicts excitation functions for residual nuclides, fission and γ production. Comparisons of the theoretical predictions with the new HINDAS data have produced very promising and some excellent fits to the data, even in the case of DDXS of n- and p-induced reactions.
On the other hand, new proton and neutron data libraries have been elaborated for selected materials up to 200 MeV.

The **experiments at high energies** were performed at 3 accelerators : COSY-Jülich, GSI-Darmstadt and SATURNE before its closing. Similarly to the intermediate energies, a coherent set of experimental data of reactions producing charged particles, neutrons and residues has been measured between 200 and 2000 MeV.

- The neutron double differential cross sections on Fe, Pb and Th on thin and thick targets between 800 and 1600 MeV, measured at SATURNE before the start of the present project, have been analyzed and compared to the theory. The Intra-nuclear cascade model (INCL) improved at ULg-Liege and CEA-Saclay, has provided a clear improvement in the fit of the data on thin targets. The implementation of INCL4 with the new evaporation and fission model ABLA, written at GSI-Darmstadt and Santiago, in the Los Alamos High Energy Transport code (LAHET3) produced excellent fits to the data obtained with thick targets.
- Neutrons and charged-particles have been measured with two 4π detectors: the Berlin Silicon Ball and the Berlin Neutron Ball at COSY-Jülich. Thin targets (between 1200 and 1800 MeV) and thick targets (from 400 to 2500 MeV) have been used. Neutron multiplicity distributions have been obtained from the thin target experiments and a fair agreement with the Saclay data has been observed. The production cross sections of H and He yield important information to estimate the damages and the lifetime of target and structural materials of future ADS systems.

Measurements on thick targets have produced neutron energy spectra and multiplicities. Comparison of the high energy transport codes show significant discrepancies. Improvements of the fits are obtained by introducing pre-equilibrium reactions in the INCL4 model.

- Residue isotopic distributions have been measured at GSI-Darmstadt in inverse kinematics. Acceleration of heavy ion beams of Pb (0.5 and 1 GeV.A) and U (1 GeV.A) on H and D-liquid targets allows the in-flight identification of the reaction products in mass and atomic number by means of a high-resolution spectrometer. At the same time, information on the reaction kinematics is obtained. More than 1000 elements have been identified in each reaction, covering most of the elements between oxygen and uranium. Velocity distributions of the nuclides have been determined. The elements produced by spallation-fission and spallation-evaporation reactions are clearly distinguished. These data are of primary interest for ADS design and allow to calculate the short- and long-term radioactivities induced in the target material. Moreover, the kinetic-energy distributions will allow to evaluate the atomic displacements in structural materials. The new data will help to improve the predicting power of the models for spallation reactions involving highly fissile materials.

Finally, the measurements in direct kinematics of residual nuclide production by proton-induced reaction on heavy elements by the ZSR-Hannover group, has produced excitation function from the threshold to an energy of 2.6 GeV on series of targets. Some spectacular fits have been obtained by simultaneous use of the new code TALYS from threshold to 200 MeV and by the INCL4+ABLA code from 200 to 2600 MeV.

List of the partners and the contact persons

Université catholique de Louvain - Louvain-la-Neuve (B) – Institut de Physique Nucléaire
J.P.Meulders et al.
Coordinator

Université de Nantes (F) – Labor. de Physique subatomique (SUBATECH).
Ph.Eudes, H.Haddad et al.

CNRS Laboratoire de Physique Corpusculaire de Caen (F).
J.Fr.Lecolley, Fr.R.Lecolley et al.

Rijksuniversiteit Groningen (Nl) – Kernfysisch Versneller Insituut.
H.Beijers et al.

Uppsala Universitet (S) – Departement of Neutron Research**.**
N.Olsson, J.Blomgren et al.

Universität Hannover (D) – Zentrum für Strahlenschutz une une Radiökologie.
R.Michel et al.

Phys.Techn..Bundesanstalt. (D) Braunschweig – Department of Ionizing Radiation.
H.Schuhmacher, R.Nolte et al.

Swisss federal institute of Technology (ETH) Zürich (CH) – Institute of Particle Physics.
A.Synal, D.Schumann et al.

Paul Scherrer Institute (CH) – Laboratory of Radio- and Enviromental Chemistry.
R.Weinreich et al.

Forschungzentrum Jülich Gmbh (D) – Institut für Kernphysik.
D.Filges, F.Goldenbaum et al.

C.E.A. Saclay (F) -DSM/DAPNIA- Service de Physique Nucléaire.
S.Leray et al.

C.E.A.-Bruyères-le-Châtel-(F) -Service de physique Nucléaire.
O.Bersillon et al.

Gesellschaft für Scwherionenforschung mbH (D) – Accelerator department.
K.H.Schmidt et al.

Universidade de Santiago de Compostela (E) – Depatamento de Fisica de particulas.
J.Benlliure et al.

Université de Liège (B) – Institut de Physique.
J.Cugnon et al.

Nuclear Research and consultancy Group – Petten (Nl) – Fuel, Actinides and Isotopes.
A.Koning et al.

1. Introduction

HINDAS (High and Intermediate energy Nuclear Data for Accelerator Driven systems) is an European FP5 project in the framework of partitioning and transmutation of radioactive waste. The well-balanced choice of an accelerator-driven system (ADS) as an adequate transmutation option, including its physical, technical, environmental and economical aspects, depends on the detailed knowledge of the involved nuclear-reaction processes. Therefore, accurate nuclear data are required to ensure that simulations of such a future innovative system are of high quality and allow to present well based options to the policy makers for their decision.

As a first, though significant, step the HINDAS-project focused on high- and intermediate-energy data that are specific to an ADS, in particular the energy region between 20 and 2000 MeV with the objective to have a much better control of nuclear data beyond the classical 20 MeV region. This was accomplished by launching an European-wide collaboration of experimentalists, theoreticians and data evaluators who merged their complementary expertise to meet basic nuclear-data requests for transmutation.

Various European experimental facilities were at the disposal of the project: TSL Uppsala, KVI Groningen and UCL Louvain-la-Neuve for intermediate energies up to 200 MeV, and GSI Darmstadt and FZJ Julich for energies above 200 MeV. An important prerequisite for the success of HINDAS was that the infrastructure was already present: all included facilities had proven their ability to deliver nuclear data in previous projects. For each experiment the best-suited facility within Europe was used. On the other hand, the HINDAS-project has been restricted to the study of a few key elements of particular interest for ADS: Fe as representative element of structural materials, Pb as target element and U as actinide element.

Three types of experiments were performed both at intermediate energies, between 20 MeV and 200 MeV, as at high energies, between 200 MeV and 2 GeV.

- Neutron production induced by protons and by neutrons. The source neutrons that will drive the sub-critical reactor are produced by (p,xn) reactions in the target, then multiplied by (n,xn) intermediate and low energy reactions in the target and next by fission in the fissile material. The precise knowledge of the number of neutrons produced in high-energy reactions is therefore important, as are their energy and spatial distributions for the detailed prediction of material damage and thermo-hydraulics in the target and sub-critical core. The (n,xn) multiplicities have been measured at high energies; they will shortly be measured at lower energies, around 100 MeV at TSL.

- Light charged particle production (from protons to alphas) induced by protons and by neutrons. A large set of new double differential cross sections of light charged particle production have been measured, which allows very sensitive tests of the nuclear models with the use of thin targets and of the transport codes with the use of thick targets. These reactions produce radiation damage in solid materials and hydrogen and helium bubble formation, which can lead to swelling and embrittlement of structural materials.

- Residual nuclide production induced by neutrons and by protons. Two complementary methods have been used : by direct irradiation of the element with proton or neutron beams, where the produced isotopes are analyzed off-line or by inverse kinematics, where relativistic heavy ions beams of U and Pb have been accelerated at 1GeV-A on a liquid H-target. In the last case, all the produced residuals are recorded simultaneously by a sophisticated spectrometric assembly. A large variety of isotopes are formed by spallation reactions. Many

of them are radioactive and the long-lived radio-isotopes may cause concern for radioprotection. The long-term radio-toxicity induced in the target and the surrounding materials may drastically influence the choice of the target element, the structural and the shielding materials of future ADS.

For the detailed design of a future ADS, all these quantities will have to be reliably predicted in order to choose the best and most economic configuration and materials. Simulation codes exist to predict any of those quantities. They generally consist of the coupling of high-energy transport codes, which handles the transport and interactions of the incoming proton and all the produced particles down to 200 MeV, with an intermediate energy transport code, utilizing evaluated nuclear-data files. If the experimental value of the elementary cross-sections are not available, they are calculated by nuclear physics models. It is therefore crucial that the nuclear models be reliable enough, that is, provide correct elementary cross-sections validated on an extensive set of experimental data.

In the theoretical part of the HINDAS project, new data libraries were produced for Fe, Pb and U isotopes from the unresolved resonance region up to 200 MeV, for both incident protons and neutrons. In the same energy region, a new European nuclear model code TALYS has been developed which describes basically the HINDAS experiments up to 200 MeV, ranging from elastic scattering distributions, double differential spectra, residual production cross sections to fission yields. Above 20 MeV, the increasing importance of the pre-equilibrium part of the reaction mechanism, clearly put in evidence in the experiments, has requested particular attention in the code.

In the high energy region from 200 MeV up to 2 GeV, significant improvements have been obtained with the new version of the intra-nuclear cascade code from Liège, INCL4, which have resulted in much better predictions of total reaction cross-sections and peripheral reactions. On the other hand, the ABLA model, which describes the de-excitation stage of the reaction, gives a much better description of the isotopic distributions and fission yields than other well known models. The INCL4-ABLA combination has been compared to the data obtained in HINDAS and to earlier results: an overall good agreement has been obtained. Finally, the INCl4-ABLA code has been introduced in different classical transport codes and are available to the whole community.

In addition to the previously mentioned impact of the work done during the HINDAS project for what concerns the ADS design, several studies have been conducted like simulations of the activity produced in thick Pb and Pb-Bi targets, evaluation of the neutron leakage energy spectra from thick targets and Helium production and damage cross-section in ADS windows. More applications of the results of the cross section measurements in HINDAS are expected in the near future.

The project contains 8 Workpackages :

-WP1, WP2, WP3 are devoted to experiments and WP7 to the theory at Intermediate energies (between 20 MeV and 200 MeV). They are presented in the chapter 2.

-WP4, WP5, WP6 are devoted to experiments and WP8 to theory at High energies (between 200 MeV and 2 GeV). They are presented in the chapter 3.

The chapter 4 presents some implications of the HINDAS results for ADS design and finally, the chapter 5 summarizes the main results and the conclusions of the project.

2. Experimental and Theoretical Results at Intermediate Energies between 20 and 200 MeV

2.1. Introduction

The required nuclear data for accelerator-driven systems at energies below 200 MeV are to be delivered to ADS design calculations in the form of ENDF-6 formatted data libraries. These libraries should contain tabulated data of cross sections, double-differential light-particle spectra and spallation product yields for a whole spectrum of nuclides. With these libraries, transport codes like MCNP and activation/burnup codes can simulate advanced ADS designs. To come to a complete library for applied use, nuclear data in the 20-200 MeV range should be combined with existing data libraries below 20 MeV. Preferentially, the 20 MeV libraries should be re-evaluated as well, to ensure a proper matching around 20 MeV. The latter has actually been done in the HINDAS project, though the theoretical and experimental emphasis has been on the 20-200 MeV region.
The total number of reaction channels in the intermediate energy region is so large that measurements alone can never cover the entire data request. For example, transport codes need for incident neutrons on a precise incident energy grid (say every 2 MeV between 20 and 200 MeV), outgoing spectra for all outgoing particles, energies and angles. It is clear that this can never be measured. To somehow interpolate between the measurements that do exists, only adequate nuclear reaction models will be successful. The data libraries are thus generated with nuclear model codes which contains a suite of nuclear reaction models whose parameters are tuned to carefully chosen experiments, and which subsequently produce the nuclear data on a pre-defined incident energy and emission energy/angle grid. This has been exactly the approach in HINDAS. To achieve this, three experimental workpackages and one theory/evaluation workpackage have closely worked together:

WP1 Light charged-particle production induced by neutrons or protons between 20 and 200 MeV

WP2 Neutron production induced by neutrons and protons between 20 and 200 MeV

WP3 Residual nuclide production induced by neutrons and protons between 20 and 200 MeV and production of long-lived radionuclides

WP7 Nuclear data libraries and related theory

The other workpackages WP4, 5, 6, 8 will be described in the next chapter.
This chapter will reveal several new experimental results, for reaction/nuclide combinations for which no data existed. Together with the theoretical developments, this has yielded sufficient intermediate energy information for the three central nuclides of HINDAS: Fe, Pb and U. For these nuclides, nuclear data libraries have been produced, and the methods developed during HINDAS can now be readily extrapolated to other nuclides.

2.2. The situation before and after the HINDAS project

To connect to the measurement requests, a High Priority Request List [HPRL,Kon98] has been designed in 1998, which for HINDAS has served as a guideline for necessary measurements for ADS research. As a result, the experimental database has been considerably improved. Table 2.1 shows the situation before and after the HINDAS project for energies up to 200 MeV. The collection of new measurements can be said to fall into three categories: (a) neutron elastic scattering, (b) double-differential particle production cross sections with both neutrons and charged particles as projectile and ejectile, (c) residual production cross sections, including fission, again for incident neutrons and protons. Clearly, many "desert" regions have been filled. A description of the methods used will be given in this Chapter.
These measurements have been used to guide theoretical calculations, which subsequently have been used to produce nuclear data libraries. Also in the field of modelling and data file creation, a significant step forward has been made during the HINDAS project. A new computer code, TALYS, has been constructed that gives a simultaneous prediction of all open nuclear reaction. This idea is not new: Well-known examples of all-in-one codes from the past decades are GNASH[You96], ALICE[Bla92], STAPRE[Uhl76], and EMPIRE[Emp01]. They have been, and are still extensively used, not only for academical purposes but also for the creation of the nuclear data libraries that exist around the world. For TALYS, many ideas have been adopted from these and other codes, but it is new in the sense that it has recently

E (MeV)	Tot	El	n,n'	n,2n	n,γ	n,f	n,xn	n,p	n,α	n,xp	n,xα	n,x	p,xn	p,xp	p,xα	p,x	p,f
0 - 1	X	X	X		X	X						X					
1 - 2	X	X	X		X	X						X					
2 - 4	X	X	X			X		X	X			X					
6 - 8	X	X				X		X	X			X					
8 - 10	X	X				X		X	X			X					
10 - 15	X	X	X	X	X	X		X	X			X				XH	
15 - 20	X	X		X		X	X	X	X			X				XH	x
20 - 30	X	X		X		x	X	X	X	H	H	XH	X		X	XH	x
30 - 40	X	X				xH				H	H	H				XH	x
40 - 60	X					xH				xH	xH	H	X		X	XH	x
60 - 80	X					xH				H	H	H	XH	XH	XH	XH	x
80 - 100	X	H				xH				H	H	H	x	x	x	XH	x
100 - 120	X					x						H	x			XH	x
120 - 140	X					x						H		H	H	XH	x
140 - 160	X					xH						H	x			XH	x
160 - 180	X					x						H				XH	x
180 - 200	X					xH						H				XH	x

Table 2.1: *General availability of experimental data as a function of incident energy and reaction type: X denotes available experimental data, x denotes available data but scarce, and H denotes the contribution of the HINDAS project to the experimental database. Pb can be taken as a representative example of the current situation.*

been written from scratch, uses the latest theoretical models and modern programming techniques and is well validated against many measurements. Also other theoretical methods, as fission and multi-step direct models, have been improved in the HINDAS project. Moreover, the production of ENDF-6 data libraries is now handled automatically.
In sum, the HINDAS project has enabled that the European situation regarding intermediate energy experiments, theoretical modelling and data library production is now well under control. Thanks to the new measurements, model calculations are now much more physically constrained and high-energy data libraries of improved quality can be produced on a routine basis. The accomplishments reported here will facilitate future contributions to nuclear waste analyses, at both low and intermediate energies.

2.3. Models and codes

2.3.1. TALYS code

A significant part of the theoretical work in HINDAS has been devoted to the development of TALYS. This is a computer code system for the simulation and analysis of nuclear reactions, created by NRG Petten and CEA Bruyères-le-Châtel. The basic objective behind the construction of TALYS is the ability to give a complete description of nuclear reactions that involve neutrons, photons, protons, deuterons, tritons, ^{3}He- and alpha-particles, for target nuclides of mass 12 and heavier. To achieve this, a suite of nuclear reaction models has been implemented into a single code system. This enables to evaluate nuclear reactions from the unresolved resonance region up to intermediate energies.

The development of TALYS follows the “first completeness, then quality" principle. This should certainly not suggest that we use toy models to arrive at some quick and dirty results. On the contrary, several reaction mechanisms coded in TALYS are based on theoretical models whose implementation is only possible with the current-day computer power. It rather means that, in our quest for completeness, we try to divide our effort equally among all nuclear reaction types. Hence, we aim to enhance the quality of TALYS equally over the whole reaction range and always search for the largest shortcoming that remains after the last improvement. The reward of this approach is that with TALYS we can cover the whole path from fundamental nuclear reaction models to the creation of complete data libraries for nuclear applications.

There are two main purposes of TALYS, which are strongly connected. First, it is a nuclear physics tool that can be used for the analysis of nuclear reaction experiments. The interplay between experiment and theory gives us insight in the fundamental interaction between particles and nuclei. When the resulting nuclear models are believed to have sufficient predictive power, they can give an indication of the reliability of measurements. The many examples presented in this chapter confirm that this software project would be nowhere without a reliable experimental database.

After the nuclear physics stage comes the second function of TALYS, namely as a nuclear data tool: After fine-tuning the adjustable parameters of the various reaction models using available experimental data, TALYS can generate nuclear data for all open reaction channels, on a user-defined energy and angle grid, beyond the resonance region. The nuclear data libraries that are constructed with these calculated and experimental results provide essential information for existing and new nuclear technologies. The flowchart of TALYS is presented in Fig. 2.1. As specific features of TALYS we mention :

- In general, a non-approximative implementation of many nuclear models for direct, compound, pre-equilibrium and fission reactions.
- A continuous, smooth description of reaction mechanisms over a wide energy range (0.001- 200 MeV).
- Completely integrated optical model and coupled-channels calculations through the ECIS code, with incorporation of new (global and local) optical model parameterizations for many nuclei.
- Total and partial cross sections, energy spectra, angular distributions, double-differential spectra and an exact modelling of exclusive cross sections and spectra. Excitation functions for residual nuclide production, including isomeric cross sections.
- Automatic reference to nuclear structure parameters as masses, discrete levels, resonances, level density parameters, deformation parameters, fission barrier and gamma-ray parameters, mostly from the IAEA Reference Input Parameter Library [RIP98].
- Various phenomenological and microscopical level density models, such as Gilbert-Cameron, Ignatyuk and combinatorial state densities built on Hartree-Fock-Bogoliubov based single-particle states.
- Semi-classical exciton model for pre-equilibrium reactions.
- Use of systematics if an adequate theory for a particular reaction mechanism is not yet available or implemented, or simply as a predictive alternative for nuclear models.
- Automatic creation of nuclear data libraries in ENDF-6 format, ready for use in nuclear applications.

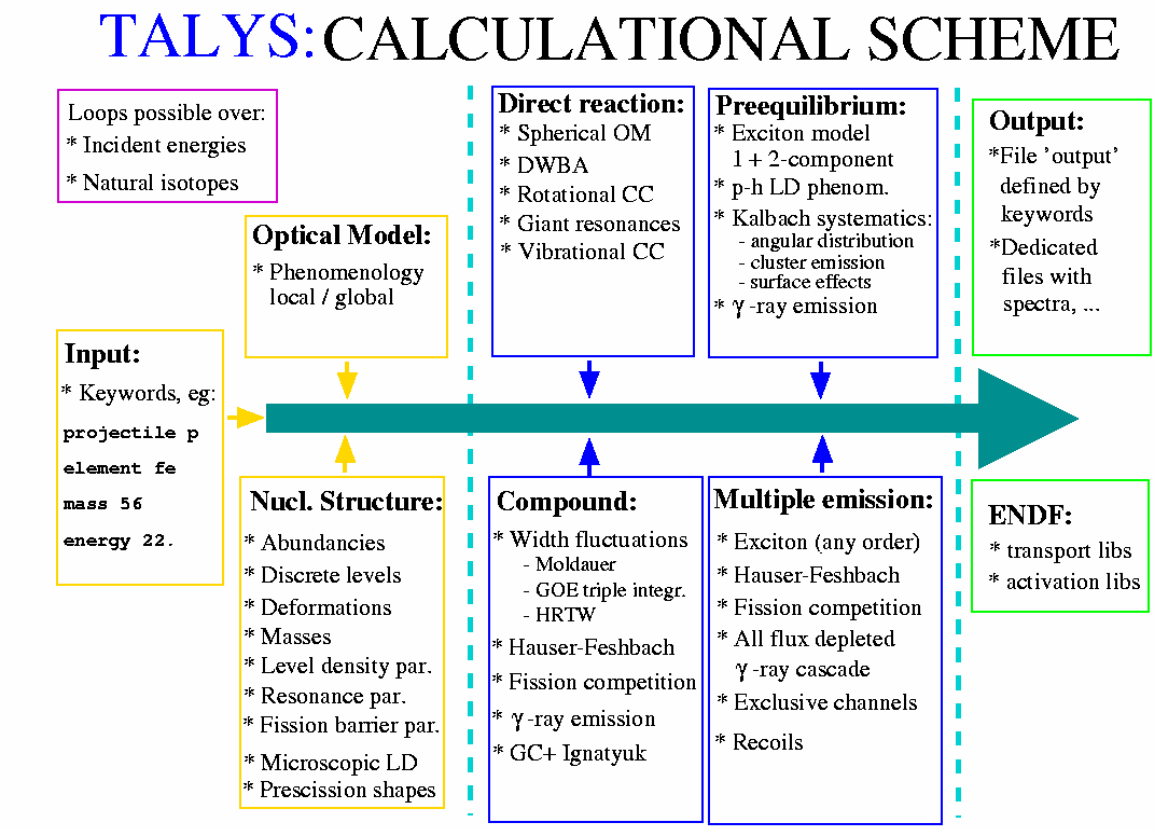

***Figure 2.1**: Flowchart of the TALYS code, showing all the included nuclear models and databases.*

TALYS is used for the analysis of all sub-200 MeV experiments in HINDAS, and has been improved over the whole range during the project. As specific contributions, we restrict ourselves here to the three nuclear models that are relevant to the experiments performed in HINDAS. The part of TALYS which is most relevant to transmutation of waste, namely the production of ENDF-6 formatted data libraries, is discussed later in this Chapter.

Optical model

The optical model has a significant impact on many branches of nuclear reaction physics. We have constructed new phenomenological optical model potentials (OMPs) for neutrons and protons with incident energies from 1 keV up to 200 MeV, for (near-)spherical nuclides in the mass range 24 <A <209. They are based on a smooth, unique functional form for the energy dependence of the potential depths, and on physically constrained geometry parameters. For the first time, this enables one to predict basic scattering observables over a broad mass range and over an energy range that covers several orders of magnitude in MeV. Thereby, the necessity of using different OMPs in different energy regions has been removed. Using extensive grid searches and a new computational steering technique, we have obtained optical model parameters for many isotopes separately. From these parameterizations, we have also constructed asymmetry-dependent neutron and proton global OMPs that are superior to all other existing phenomenological ones, not only with respect to the description of observables, but also as they cover larger mass and energy ranges. These (nucleon) global OMPs, we believe, may be used with some confidence in other studies whenever one of our local OMPs does not exist. To constrain our parameterization as much as possible and to assess the performance of our OMPs, we have compared our calculated results with an extensive experimental data set. This data set includes average resonance parameters, total and non-elastic cross sections, elastic scattering angular distributions and analyzing powers. The numerous local OMPs we have obtained allow us to disentangle asymmetry, Coulomb correction and mass-dependent components of our global OMPs. All results have been published [Kon03]. Here, we restrict ourselves to isotopes that are considered in the HINDAS project. Fig. 2.2 shows the elastic scattering distributions for all existing experimental data on Fe and Pb (apart from the new HINDAS results from Uppsala which will be discussed later). In [Kon03] it is shown that a similar quality of fit is obtained for the total cross section. Hence, the starting point of our nuclear model calculations, delivered by the optical model, is well under control.

Pre-equilibrium model

A first requirement for a proper description of spectra and production cross sections at intermediate energies is the control over the pre-equilibrium process. A full two-component exciton model has been implemented in TALYS, and an extensive database of experimental double-differential cross sections has been assembled. Comparison with TALYS calculations then enables a proper parametrization of the matrix element that determines the damping to more complex exciton states. As a novelty, multiple pre-equilibrium emission, in a two-component approach, has been generalized to an arbitrary numbers of reaction steps (so far, other nuclear reaction codes only included two reaction steps), which substantially increases the energy validity range of TALYS. Our new exciton model has been successfully tested against the double-differential data measured in the HINDAS project, as can be seen from the various comparisons given in this Chapter, and the associated publications. A comparison with all existing experimental data for all nuclides, similar to our study for the optical model, is in its final stages [Kon04].

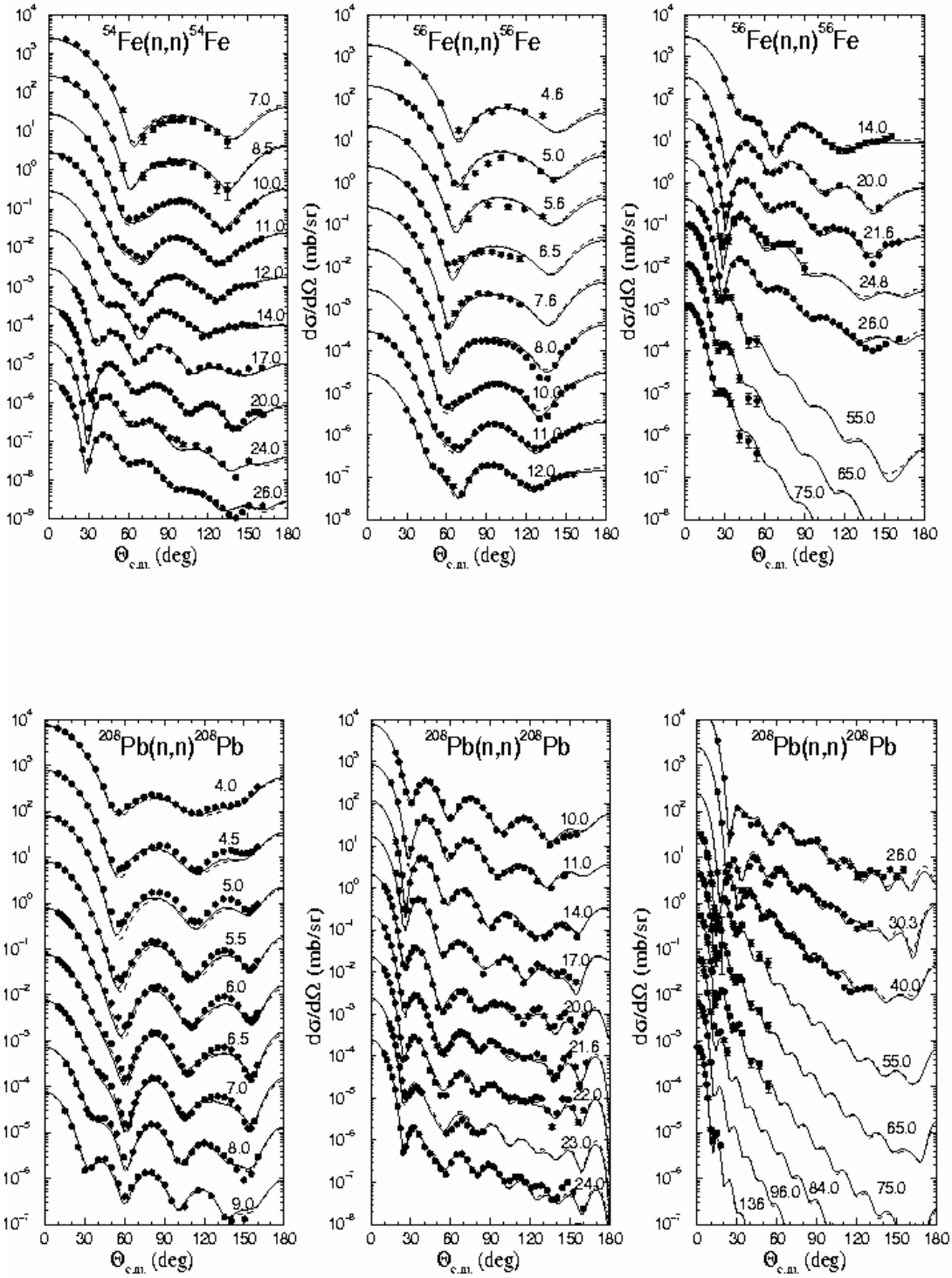

Figure 2.2*: Elastic scattering distributions for Fe and Pb isotopes. Comparison between optical model and experimental data.*

TALYS simultaneously produces double-differential spectra and residual production cross sections. Also for the latter, some TALYS results are compared with experimental data later in this Chapter. Apart from the above-mentioned pre-equilibrium ingredients, we have included energy-dependent shell effects in the level density, multiple compound emission treated with the Hauser-Feshbach model, and collective effects for direct reactions, see Fig. 2.1. Models for gamma-ray strength functions have been implemented. Every possible residual nucleus is characterized by its own set of discrete levels, which is automatically included in the decay scheme. This enables a prediction of (long-lived) isomer production.

Intermediate energy fission

For the prediction of the fission cross section in a Hill-Wheeler type of calculation, two main ingredients must be provided: the fission barrier parameters and the level density on top of the fission barriers. Their combination gives a measure of the fission probability that can be directly compared to the probability for all the competing processes like the evaporation of neutrons, photons and light charged particles.

Several models have been included in TALYS for the fission barrier heights and curvatures: the rotating liquid drop model (RLDM) [Coh74], the rotating finite range model (RFRM) [Sie86], the generalized liquid drop model [Roy00], and barrier parameters from the RIPL database [RIP98]. Additionally, the user can provide his own input. In the case of the RLDM and RFRM, the barrier heights are corrected for the ground-state shell correction as well as the shell correction on top of the barrier.

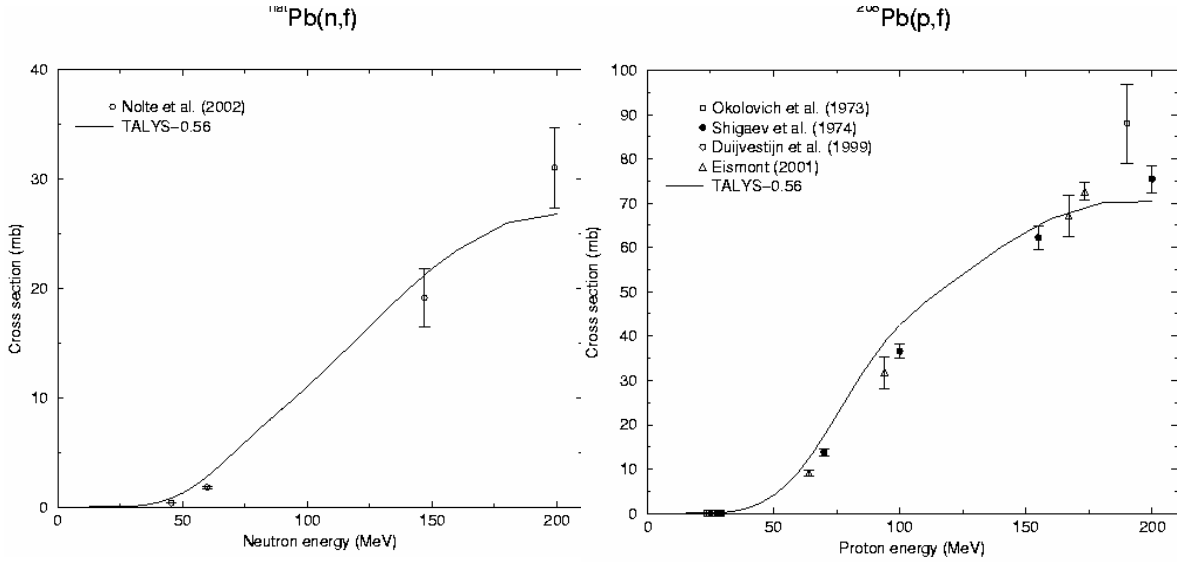

Figure 2.3 *Neutron-induced and proton-induced fission cross sections on Lead. Results from TALYS calculations are compared to experimental data by Nolte [Nol], Okolovich [Oko74], Shigaev [Shi73], and Duijvestijn [Dui99].*

The level density on top of the fission barriers differs from the one in the ground state for two aspects: the shell correction and the collective enhancement. For subactinide nuclides, the fission barrier shell correction is assumed to be zero and for actinide targets the shell correction on the inner and outer barriers is taken to be 2.5 and 0.6 MeV, respectively [RIP98]. Since shell corrections wash out at higher excitation energies, the intrinsic level densities in the ground state and on the barrier will tend towards the same value above a few tens of MeV. The collective enhancement of the level density is related to the deformation of

the nucleus. This factor also vanishes with higher excitation energies, but the rate at which it disappears is smaller for higher deformations. Consequently, the collective enhancement on the barrier persists up to much higher excitation energies (a few hundreds of MeV) than the one in the ground state. In order to enable the correct treatment of this effect, the collective effects have been taken into account explicitly in the description of the level density in TALYS. Hence, new level density parameters have been obtained by a fit to D0-values from RIPL including the collective effects explicitly. Results for subactinide target nuclides are depicted in Fig. 2.3.

As a next step TALYS has been extended with the random neck rupture model [Dui01]. This makes the prediction of the pre-neutron emission mass yields of the fission fragments possible. A detailed description of how the barrier parameters per fission mode are obtained (needed to determine the relative yields of each fission mode), how the prescission shapes are calculated, and the way the RNRM works can be found in [Dui01]. An example of its capabilities for a default TALYS run is illustrated by Fig. 2.4 for some reactions on subactinide targets.

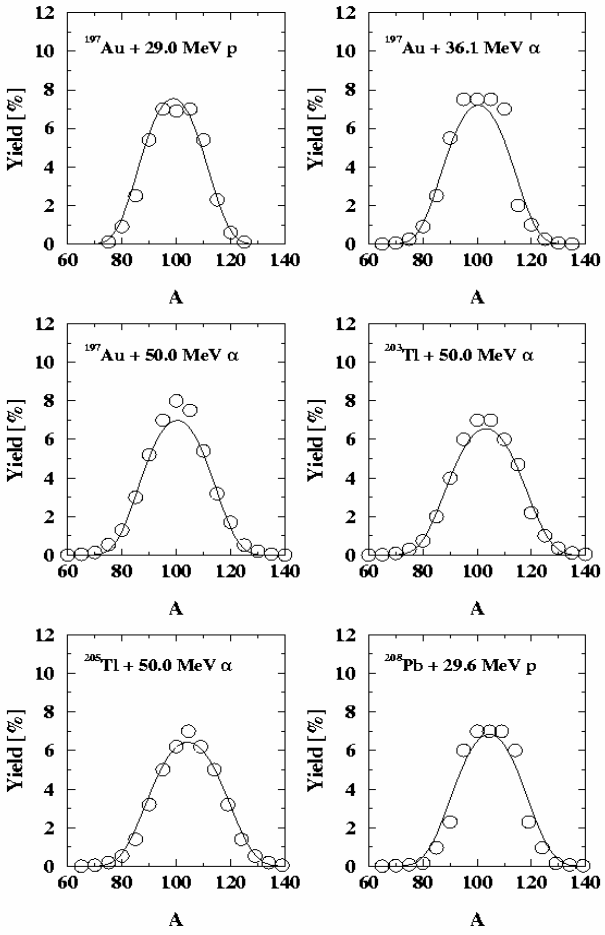

Figure 2.4 : *Normalized pre-neutron emission mass yields for the reactions specfied in each graph. The experimental data are taken from Itkis [Itk85,Itk88], the lines correspond to TALYS calculations.*

2.3.2. Calculation of nucleon production spectra in nucleon-induced reactions with the Tamura-Udagawa-Lenske model

Several reaction mechanisms contribute to the production of the continuous spectra of nucleons in nucleon induced reactions at intermediate energies. The two extremes of nucleus reaction models are those of the direct and the compound reactions, respectively. The angular distributions of the former are strongly forward peaked while those of the latter one are isotropic in the centre-of-mass system. Thus much can be learnt about the reaction mechanisms by studying the energy spectra at different angles. Intermediate processes, which are also mostly forward peaked, are described by preequilibrium reaction models, which thus can be looked upon as the conceptual link between the two extremes. Accordingly a proper understanding and application of models for the pre-equilibrium processes must be essential for the appropriate description of the spectra and production cross sections for nucleon induced reactions at intermediate energies, which have been measured in WP1 and WP2. In the TALYS code developed within the HINDAS project by Koning et al. [Kon03a], a full two-component exciton model has been implemented for these processes. However, in addition to the classical exciton models different statistical quantum-mechanical models exist derived for the desciption of the preequilibrium processes,. Thus with few exceptions, calculations of the multistep processes for nucleon induced preequilibrium reactions have up to now been carried out using two such approaches: the Feshbach. Kerman, and Koonin (FKK) theory [Fes80] and that of Tamura, Udagawaa, and Lenske (TUL) [Tam82, Len92]. A third approach by Nishioka, Weidenmüller, and Yoshida (NWY) [Nis88] relaxes some of the statistical assumptions in FKK and in TUL but is more difficult to implement. The differences and similarities between the FKK model, which is by far the up to now most commonly used model in applications, and the TUL model were discussed in detail at a workshop in Trento,1998 [Cha99] .

In this part of WP7 the quantum-mechanical multistep direct reaction model according to Tamura-Udagawa-Lenske (TUL) will be used to describe nucleon-induced reactions at intermediate energies[Ram04]. Thus the TUL model will be applied for the calculation of the double-differential cross sections measured in WP1 and WP2. There are several reasons for this choice of model. Thus a characteristic property of the the above mentioned experimental data especially at small angles and low excitation energies is that collective phenomena like giant resonances of different multipolarities are superimposed on an almost structureless background. This indicates that collective and statistical features are competing. This behaviour can't be properly described by the exciton model . However, a statistical approach in which characteristic structural aspects of the nuclei are retained would be appropriate to use for the description of these experimental data. This is the case with the TUL model in which the differential cross sections are given as the product of a part describing the nuclear structure and a part for the reaction dynamics. QRPA response functions are used for the structure part and DWBA cross sections are describing the reaction dynamics.

For applications the predictive power of the model is very important, since it should be used for predictions of unmeasured data at intermediate energies. Thus it is important that the magnitude of the calculated cross sections is free of any adjustable parameters and strictly related to known physical parameters and quantities such as effective interactions. In the calculations presented here the global optical model potential of Koning et al. [Kon03b] was used for the calculation of incoming and outgoing distorted waves in the DWBA calculations. Furthermore, the derivative of the real part of the same potential was used as the energy independent phenomenological formfactor in these calculations.

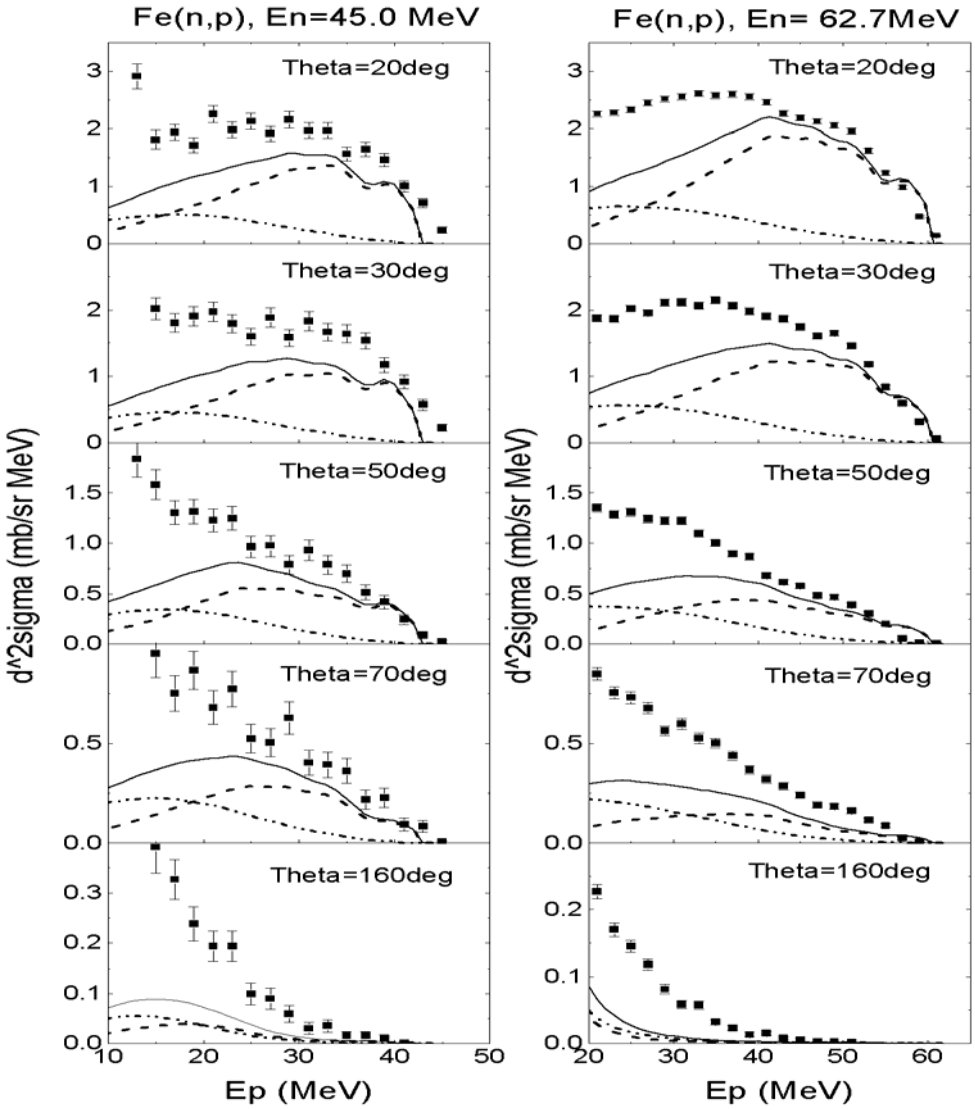

Figure 2.5 : *Double-differential cross sections of the Fe(n,p) reaction at 45 and 62.7MeV incident neutron energies. Experimental data are taken from ref [Sly93]. The solid lines represent the sum of the cross sections for the 1ststep(dashed lines) and 2ndstep (dashed-dot-dot lines) calculated with the TUL model.*

As mentioned above charge exchange and inelastic response functions are described microscopically in the quasiparticle random phase approximation (QRPA), thus including pair correlations in the ground state. In the present work a residual interaction derived from a G-matrix, based on the Paris potential, was used [Ana83]. Single particle wave functions and energies were calculated using Woods-Saxon potentials with parameters adjusted in order to reproduce the single particle levels known from experiments and theoretical calculations. The continuum was discretized by Fourier expanding the wavefunctions into box eigenstates.

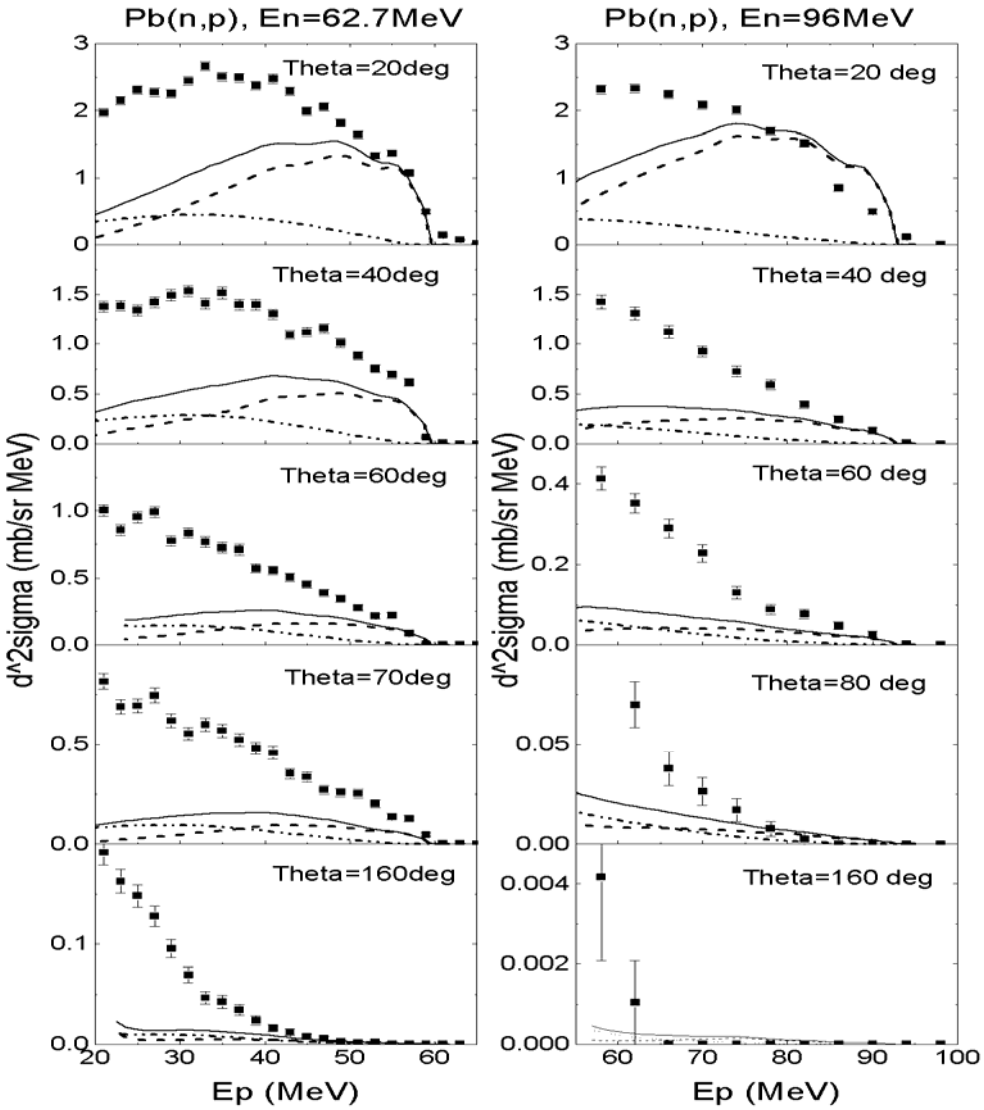

Figure 2.6 : *Double-differential cross sections of the Pb(n,p) reaction at 62.7 and 96.0 MeV incident neutron energies. Experimental data are taken from refs [Ker02,Lec03]. The solid lines represent the sum of the cross sections for the 1ststep(dashed lines) and 2ndstep (dashed-dot-dot lines) calculated with the TUL model.*

In Fig. 2.5 the double differential cross sections calculated with the TUL-model for the charge exchange reaction ^{56}Fe(n,p) at two different incident neutron energies, viz. 45.0 and 62.7 MeV, are shown together with experimental data measured with a target of natural iron at Louvain-la-Neuve [Sly93] within the HINDAS project. The dashed and dotted curves represent the contributions from the first step and second step, respectively, while the solid lines show the results of the full MSDR calculations (first plus second step). The first step was calculated as a direct charge exchange (n,p) reaction. To get the contribution from the second step, two different reaction chains were taken into account; firstly charge exchange (1 step) plus inelastic (2nd step), i.e. (n,p)+(p,p') reactions and secondly inelastic (1st step) plus charge exchange (2nd step) i.e. (n,n')+(n,p) reactions.

In Fig. 2.6 the corresponding cross sections for the ^{208}Pb(n,p) reaction at two different incident neutron energies, viz. 62.7 and 96.0 MeV, are shown. Also here the experimental

data are taken from measurements within the HINDAS reported from Subatech [Ker02] and Caen [Lec03], respectively.

It has to be emphasized that all these calculations have been performed without any adjustments of parameters in order to give a better fit to the data. As shown in Figs. 2.5 and 2.6 the TUL model for multistep direct reactions describes rather well the experimental data for excitation energies below 20MeV and angles smaller than 70 degrees for both the Fe(n,p) and the Pb(n,p) reactions at intermediate incident neutron energies. At higher excitation energies and larger angles other reaction mechanisms such as multistep compound and knock out reactions play a larger role, which is obvious when looking at the measured angular distributions. Thus the inclusion of these mechanisms into the model is planned. The goal is then to include this new option of the model in the code system TALYS in the future.

2.3.3. New evaluation of neutron-induced cross sections for ^{238}U up to 200 MeV

Introduction

The results of the evaluation of neutron-induced cross sections for ^{238}U up to 200 MeV of incident energy are reported. In a first step, the various cross-sections have been analyzed using models in the 1 keV-200 MeV energy range. In the second step, the model predictions obtained before 10 keV have been replaced by evaluated data from the ENDF/B6.7 library. The evaluation has been realized by the help of three main nuclear reaction models: Optical Model and Statistical+Exciton Model. The first model is contained in the ECIS code [Ray94] and the two last models are included in a modified version of the GNASH code [You96] that we have used. Each of these models is used to describe the different mechanisms of the interaction between nucleons and nuclei: the shape elastic and direct inelastic interaction, process that takes place in the first 10^{-21} s, the pre-equilibrium, that is the intermediate process before getting the equilibrium and finally, the compound nucleus formation in the last $10^{-19\text{-}16}$ s. In this report, a rapid description of the different models is presented with a more detailed presentation of the fission model that we have improved.

These models are phenomenological which means that parameters are adjusted and optimized on the experimental data. The consistency of our approach is to use the same set of parameters for different exit channels in competition, and only one set of parameters to characterize a nucleus as target or as residual nucleus.

n+^{238}U : Direct Interaction

The first step of the reaction is interpreted in terms of the Dispersive Optical Model [Rom96]. It provides the total and elastic cross sections and the reaction or absorption cross sections by the difference between them. This last one is the sum of cross sections corresponding to the non-elastic mechanisms where the incident particle either is absorbed by the target (compound-nucleus formation) or it transfers only a part of the energy to the target nucleus leaving it in an excited state (direct inelastic interaction). For deformed nuclei, the high number of excited states at low energies permits the incident particle to excite the nucleus relatively easily. The first excited states are considered coupled to the ground-state. Usually, only 3 excited states of the ground-state band are used in the coupling of ^{238}U, but we have observed recently from experimental data that many other states from other collective bands were also responsible for the direct interaction. A total coupling of 19 states from 6 octupolar- and quadrupolar-bands has been used, written in red, on the top of the figure. The Dispersive Optical Potential (DOP) is then obtained in a Coupled Channel Approach (CCA) [Tam65]

that takes into account the coupling to these states of the deformed nucleus. The neutron-induced total cross section for ^{238}U from the calculations is compared to experimental data in Fig. 2.7.

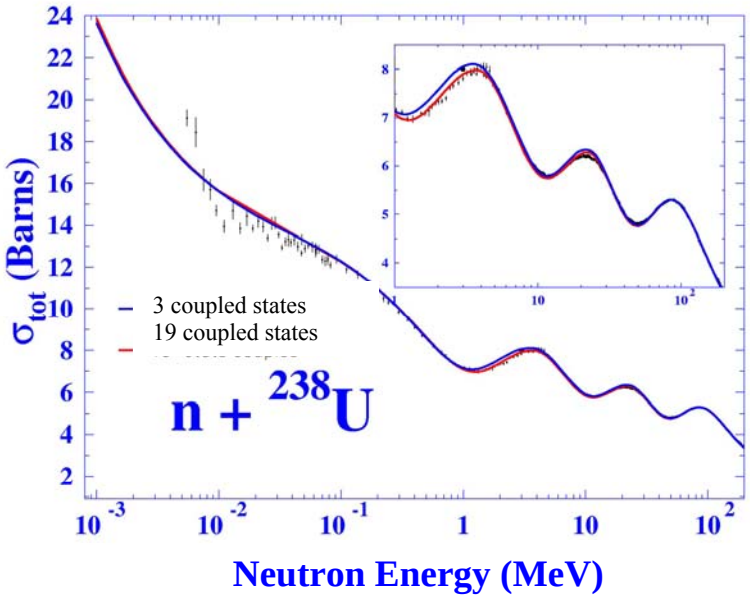

Figure 2.7 : *Total cross section of n + ^{238}U. Experimental data are in dots and calculations in full lines. Blue color corresponds to calculations with a standard coupling of only 3 states from the ground-state band. Red color corresponds to calculations with a large coupling of 19 states belonging to 6 collective bands.*

Compound Nucleus

(n,γ) and (n,xn) cross sections

In the second step, the slower process of compound nucleus formation is considered. The different deexcitation channels of the compound nucleus are treated with the Statistical Model (and the Exciton Model [Gru86] for the pre-equilibrium component, beyond 10 MeV). The corresponding cross section are calculated with the Hauser-Fesbach formula. The width fluctuations correction factor [Hil03] has been introduced in the cross section expression to takes into account the correlation between the entrance and exit channels at low energies. The transmission coefficients included in the formula are obtained from different models depending on the exit channel: for the radiative capture, we use Kopeky-Uhl [Kop90] model, for the emission of light particles (n, p and α) we use the Optical Model and for the fission channel, we use a penetrability model, as explained below.

The sum of all the partial cross sections are equal to the total inelastic cross section, see Fig. 2.8 where the experimental values are compared to calculations. In the same figure, the *(n,xn) [(n,2n), (n,3n), (n,4n)]* cross sections are also represented. The level densities of the residual nuclei produced by the emission of a supplementary neutron plays a crucial role in the calculations of the (*n,xn*) cross section. In order to be consistent in our method, the corresponding parameters should be the same to calculate the fission cross section.

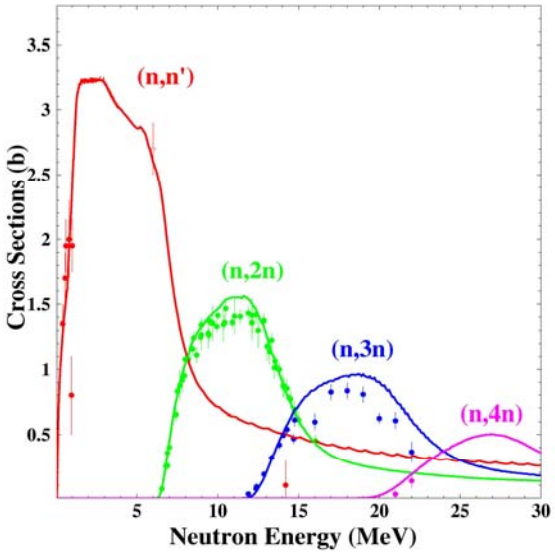

Figure 2.8 : **(**n,xn*) cross sections, calculations compared to experimental data for the system* $n + {}^{238}U$

Fission channel

In order to calculate the fission cross section, the fission process is interpreted as a potential energy barrier penetrability. For actinide nuclei, the fission barrier may display two or three humps as function of the nucleus deformation. These humps are represented in our calculations by inverted parabola of harmonic oscillators. The transmission coefficient through one of these humps is given by the Hill and Wheeler formula [Hil53]. Following the Bohr hypothesis [Boh55], in order to represent new fission paths, additional barriers are overlapped to the ground-state barrier with energy positions corresponding to the so-called *transition states*. In the general case, the penetrability is given by the sum of the transmission coefficients through all these barriers. In the energy range where the sum of discrete levels is not possible, a representation in terms of level density is needed. As formulated by Gilbert and Cameron [Gil65], at low excitation energies, a constant temperature level density formula is used and matched, at higher excitation energies, to a Fermi gas formula corrected by a collective enhancement factor. For a double-humped fission barrier, the penetrability coefficient is given by one combination of the transmission coefficients through both humps. The non-resonant formula is given by the expression $T_2=T_AT_B/(T_A+T_B)$ (it could be found in reference [Mic73]), where T_A and T_B are, respectively, the transmission coefficients of the first and second humps of the fission barrier. Between the first and the second hump, a (second) minimum of stable deformation exists where class II or Super-Deformed (SD) states are lying.

Similarly, for a triple-humped fission barrier, the penetrability coefficient is given by one combination of the transmission coefficients through the three humps. We have deduced the non-resonant expression (see [Lop04] for the demonstration) which takes a form similar to that of a double-humped fission barrier $T_3=T_2T_C/(T_2+T_C)$, with T_2 defined before and T_C being the coefficient transmission through the third hump. In the third well, class III or Hyper-Deformed (HD) states could lay. All these states (SD and HD) are particle-hole or vibrational excitation states and rotational band states built over them. These states of stable extreme deformation might induce a resonant transmission through the fission barrier that provides peaks in the sub-barrier fission cross section. (The expression of the resonant transmission

coefficients could be found in the same mentioned paper [Lop04]). The spacing of class III rotational states is smaller than that of class II rotational states because the deformation is larger. Also in the third well, doublets of positive and negative parity with the same K-head value could be found due to the mirror broken symmetries in the octupolar shape. These characteristics have been deduced, many years ago, from experimental studies of the fission cross section of Th and U isotopes [Blo82].

In the case of ^{238}U, the experimental neutron-induced fission cross section presents many transmission resonances that could belong to both class II and class III states, as it was already suggested by Blons [Blo82]. This led us to use a triple-humped fission barrier in our fission treatment, in order to calculate and reproduce correctly the first chance fission cross section. It should be noted that it is the first time that a HD shape is assumed in the calculations for this nucleus and a carefull study of the transmission resonances has been made in support of this assumption[Lop04] **.**

The first, second, … and n-chance fission cross section up to 50 MeV is shown in Fig. 2.9 and compared to experimental data. To calculate the first chance fission, we have introduced in the model the parametrical barrier of the Compound Nucleus (CN) ^{239}U. In the second chance, it is not only ^{239}U that undergoes fission but also the ^{238}U nucleus that is produced by the emission of a neutron (above ~5 MeV). The ^{238}U barrier parameters have been obtained from the study of the system n+^{237}U. This illustrates the consistency of our method that we use always the same set of barrier parameters for the same fissioning nucleus even if it is for different induced reactions. For the third, fourth, fifth, etc chances, we have used the same method, i.e. we have calculated the fission cross section with barriers obtained from the study of neutron-induced reaction of the corresponding residual nucleus.

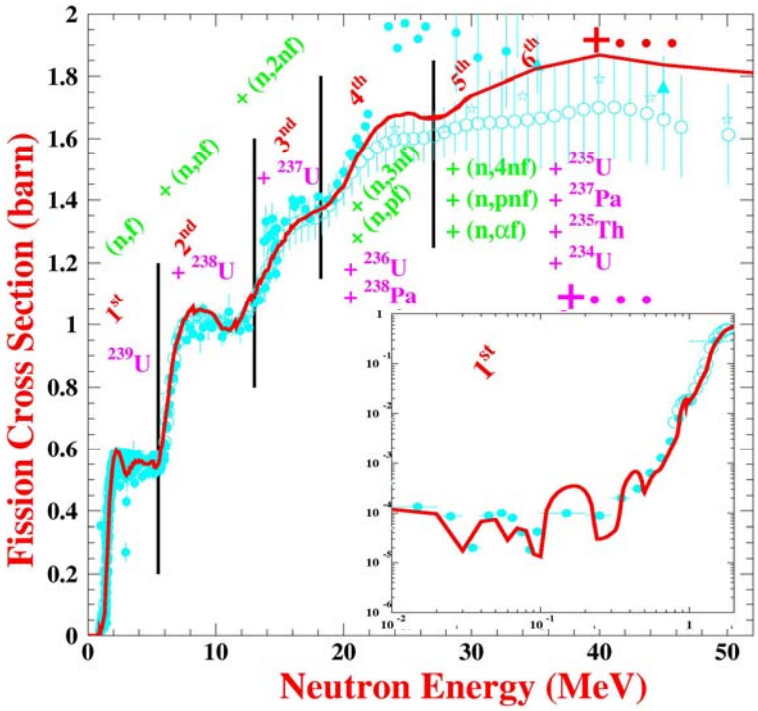

Figure 2.9 : *Neutron-induced fission cross section of ^{238}U from 1 keV up to 50 MeV. Experimental data in blue, results of our calculations are in red. Note the different plateau corresponding to the first, second, third chance, etc.*

The method described before has been used up to 50 MeV that corresponds to the seventh chance, where the residual ^{233}U contribution is added to the total fission. ^{232}U is the lighter U

isotope for which neutron-induced reactions are studied experimentally. So that for energies above 50 MeV, this method cannot be employed anymore. Thus, we have established a systematics of the fission barrier parameters for U nuclei lighter than ^{233}U based on extrapolations from the heavier U isotopes. We were able to obtained the fission cross section up to 200 MeV, Fig. 2.10. Moreover, above 20 MeV, the emission of light charged particles *(p,d,t,α)* is possible and we have to take into account different residual nuclei which contribute to the fission like Pa and Th isotopes. The fission parameters for these nuclei have not been optimized by calculating the corresponding fission cross section. We have simply introduced in our calculations experimental values found in the literature. The contribution of these nuclei becomes important above 100 MeV, where it amounts to be of the order of 30 % of the total fission cross-section. The multi-pre-equilibrum components are also considered.

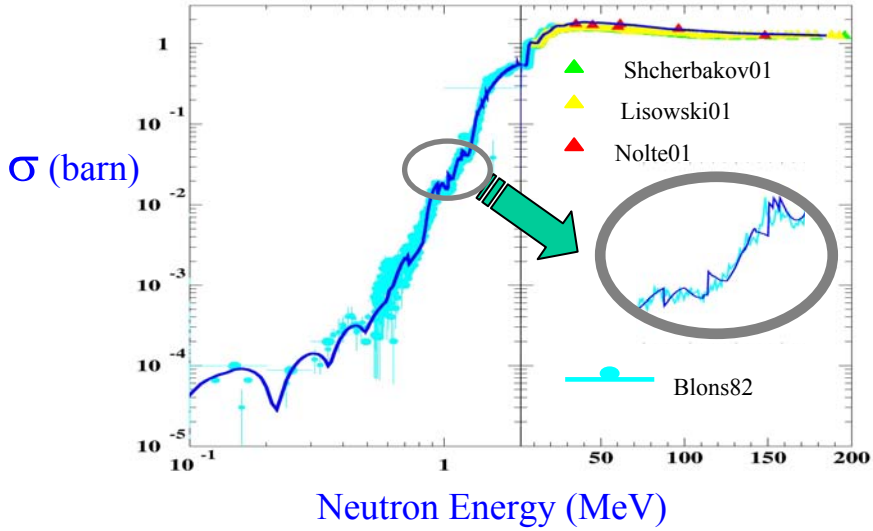

Figure 2.10 : *Neutron-induced fission cross section of ^{238}U from 1 keV up to 200 MeV.*

In Fig. 2.11 (a), the nth chance individual fission cross section are represented up to 130 MeV. We can see that the fission decreases in function of the neutron energy. For each residual nucleus the width of the fission cross section is about 40 MeV that corresponds to a temperature equal to 1 MeV. Then, the information that we can take from this figure is that the fission of these nuclei takes place at temperatures less than 1 MeV.

Prompt fission neutrons

The individual cross section permits to calculate the neutron prompt multiplicity, that is the number of neutrons per fission in function of the neutron energy, Fig. 2.11 (b). This value is deduced from an energetic balance ratio and calculated with the Madland-Nix-Vladuca-Tudora model [Vla01]. This model is available up to about 30 MeV. For higher energies, BRIC [Dua99], an Intra-cascade Model developed at CEA/Bruyères-le-Châtel is combined to the evaporation code of Bruyères-le-Châtel and the fission model of Atchison (RAL model [Atc94]) to get the average neutron multiplicity and the neutron spectra (n, xnf). Results are displayed in Figure 2.12.
BRIC returns the energy-momenta of produced particles and the excitation energy, recoil energy, charge and mass of the nucleus at the end of the first part of the reaction as a pre-equilibrium model does. The physical quantities describing the nucleus are than used as inputs of the evaporation-fission stage. The fission fragments undergo their own evaporation if necessary.

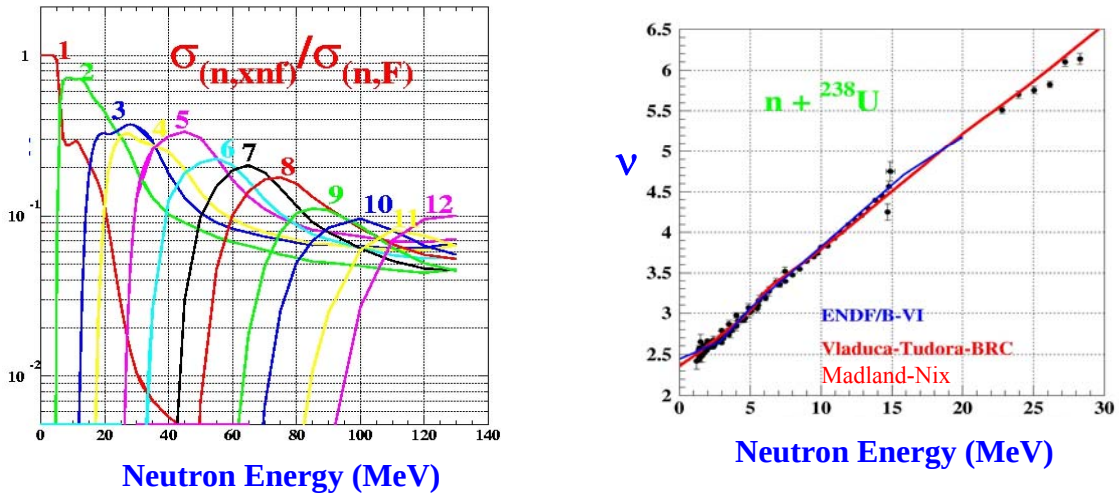

Figure 2.11 : *(a) Ratio of the n-chance fission cross section divided by the total fission cross section. (b) Multiplicity (ν) of neutron fission prompt calculated with the Madland-Nix-Vladuca-Tudora model.*

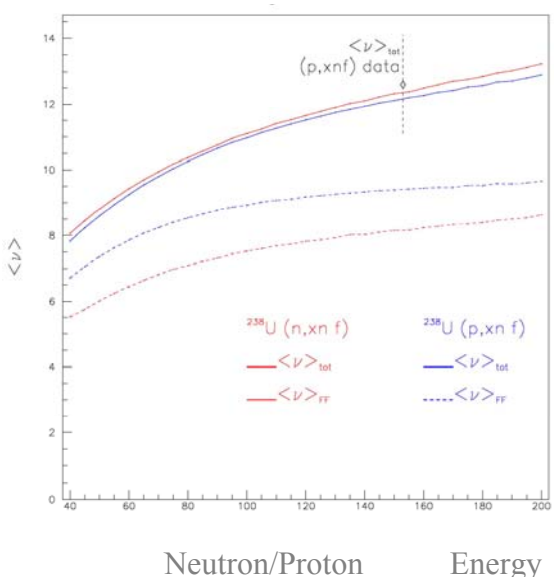

Figure 2.12 : *Multiplicity of fission prompt neutrons and protons between 40 MeV and 200 MeV calculated with the combination of the BRIC code, the evaporation code of Bruyères-le-Châtel and the RAL model of Atchison.*

2.3.4. A microscopic description of nucleon-nucleus reactions at intermediate energies within the DYWAN model

In nucleon-nucleus reactions at incident energies between 20 and 200 MeV, experimental data [Bli03] evidence that dynamical [Gue01] and quantum effects play an essential role on the emission mechanisms and the fragment yields. Unlike what happens at higher incident energy, the production of composites is important, at least 30% of the total number of emitted particles. In this range of energy, ADS simulation codes [Fo02] usually attempt to take care of quantum and out-of-equilibrium effects by coupling different models, which are adapted to the description of selected physical aspects. The conceptual and practical difficulty of this procedure lies in the ways the various specialized theoretical approaches can be interconnected. It is then worthwhile to investigate a theoretical framework, free from adjustable parameters, providing a unified description of different physical effects**,** having signatures on the experimental observables. In this prospect, the basis of such a theoretical

investigation has been developed within the DYWAN model. Owing to the current difficulties to predict the angular and energy cross sections of the emitted composites [Bli03], a special attention has been devoted to a new way to address the mechanisms of cluster formation. Particularly, it has been studied whether the phase space topology induced by the fluctuations of the self consistent nuclear mean field was able to provide the qualitative and quantitative behaviours of double differential cross sections.

The DYWAN model [Jo98] is derived from the quantum N-body problem. In this approach, stringent approximation schemes can be defined in order to treat the available information. The extraction of the relevant information in phase space is accomplished within the framework of the mathematical theory of wavelets [Dau92], which is the current most suitable tool to deal with the loss of information, inherent to the huge amount of degrees of freedom involved in many-body problems. The dynamics of the relevant variables is obtained from the Projection Methods of out-of-equilibrium Statistical Physics [Ba86]. The Projection Methods and the Wavelet theory rely on common concepts, for example the splitting in orthogonal spaces, and the treatment of the relevant information through entropy criteria. In this framework, the description of a complex system like a nucleus, compatible with our incomplete knowledge of its state, is given in terms of the projection of the N-body density operator onto the subspace associated with the available information. In the case where the relevant variables are one-body observables, the projection is done on the one body subspace while preserving two-particles correlations in order to include dissipative and fluctuating effects. The evolution of the density operator is then given by the ETDHF equation which is governed by a self consistent one-body Hamiltonian and a collision term resulting from two-body correlations.

Outlines of the model

Initial Conditions

The initial conditions of the nucleon-nucleus reactions are obtained from a self-consistent research of the target ground state. At the end of the iterative process, the Hartree Fock stationary one-body wave functions are evaluated according to the decomposition schemes in wavelets. The projectile is described as an incoming wave whose characteristics are defined with respect to the experimental constraints related to the incident beam. The incoming wave is decomposed in wavelets within the same scheme used for the target. The number of scales involved in the wavelet decomposition depends on the expected description quality of the dynamics and on the computational cost.

Dynamics

As the wavelet families are special sets of generalized coherent state [Ali95] , it is possible to use their group properties to translate, via a variational principle, the ETDHF equation into a set of coupled differential equations which rules the time evolution of the moments of the wavelets. Thus, the essential information on the nuclear mean field is contained in the spreading and correlations of the wavelets. The two-body correlations are introduced thanks to the master equation for the single-particle occupation numbers, which can be viewed in our approach as transitions of wavelets between energy levels. In current simulations, the transition rates are obtained in the framework of the Born approximation, by using the free nucleon-nucleon elastic cross section, without medium effects.

N-body information

In order to describe clusters production and the dispersion of observables, it is necessary to define the least biased N-body information associated with the approximation scheme of the model. Since the N-body wave function of the system is a linear combination of Slater determinants of single-particle wave functions, when these latter are expanded onto a wavelet basis, the N-body wave function can be expressed as a linear combination of Slater determinants of wavelets. According to the theoretical framework of statistical physics, the N-body density operator is derived from a random phase approximation. Thus, the time evolution of the N-body density matrix is due to both the mean field and the correlations: the former causes the evolution of the characteristics of the wavelets contained in the Slater determinants, and the latter lead to the population or depopulation of the Slater determinants. Each Slater determinant represents a fluctuation (an event) around a mean behaviour, described by the one-body density matrix.

Clusters formation

The study of the formation of bound systems (heavy fragments or clusters) is based on the topology of the phase space induced by the fluctuations of the mean-field caused by the two-body correlations. Even if the current treatment is still simplified, the formation of composites relies on the fundamental principle of the wave packets overlap. Thus, at the end of the dynamics, the wavelets of each Slater determinant are scanned in order to find the formed clusters. More than two-body irreducible correlations are not introduced in the collision term, and consequently the direct formation of clusters (pick-up for example) is not taken into account currently. In order to compare the theoretical results to the experimental ones, the momentum of the emitted particles are sampled accordingly to their distribution given by the structure of the wavelets packets. The asymptotical conditions are evaluated by a classical coulombian treatment which allows to follow their trajectory.

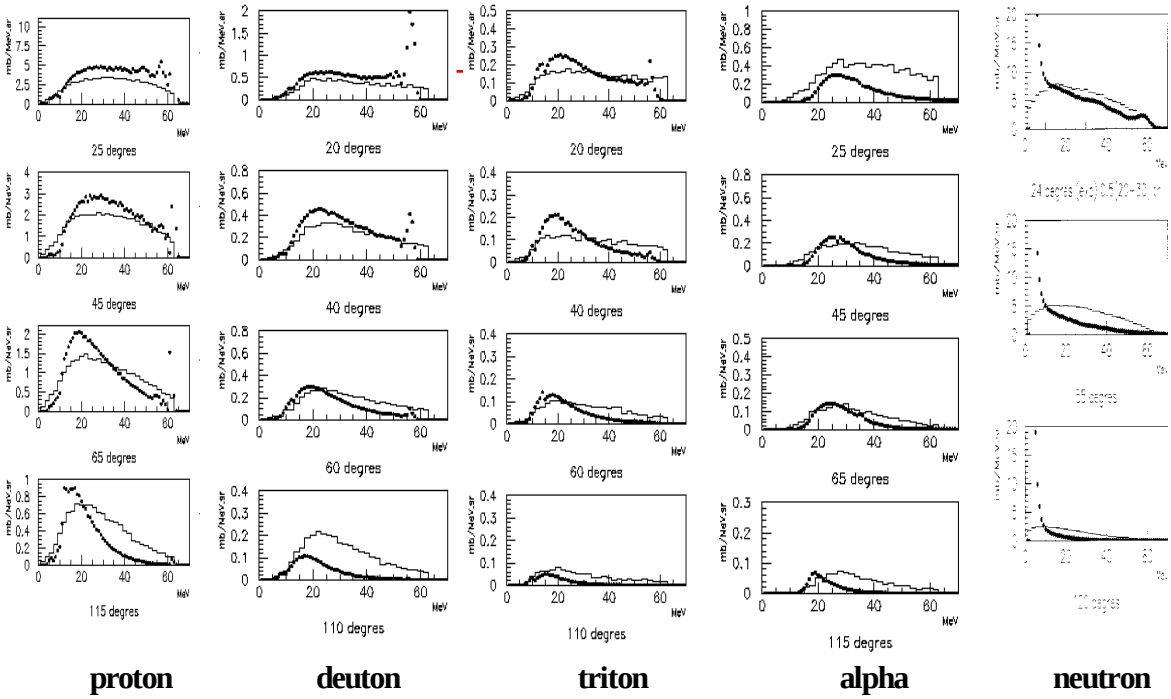

Fig. 2.13 : *Double differential cross sections of emitted particles in proton on lead reactions at 63 MeV of incident energy, the experimental results correspond to the black dots, the theoretical results are exhibited with histograms ([Gue01]).*

First results

Preliminary results are exhibited in Fig. 2.13 and Fig. 2.14 in comparison with experimental data obtained within the HINDAS project. Proton and neutron projectiles are respectively considered in these figures. The first figure points out the cluster spectra, whereas the second underlines the behaviour of the proton spectra for different incident energies and targets. The current implementation of the model correspond to the lowest order of approximation, either in the physical description (nuclear mean field, residual interactions,…), or in the mathematical representation. In addition, only the pre-equilibrium stage of the reaction contributes to the calculated cross sections. In general, all calculated cross sections fall within 70% of the experimental data. This agreement is somewhat less than that obtained by phenomenological approaches, but nevertheless promising, given the microscopical nature of the theory.

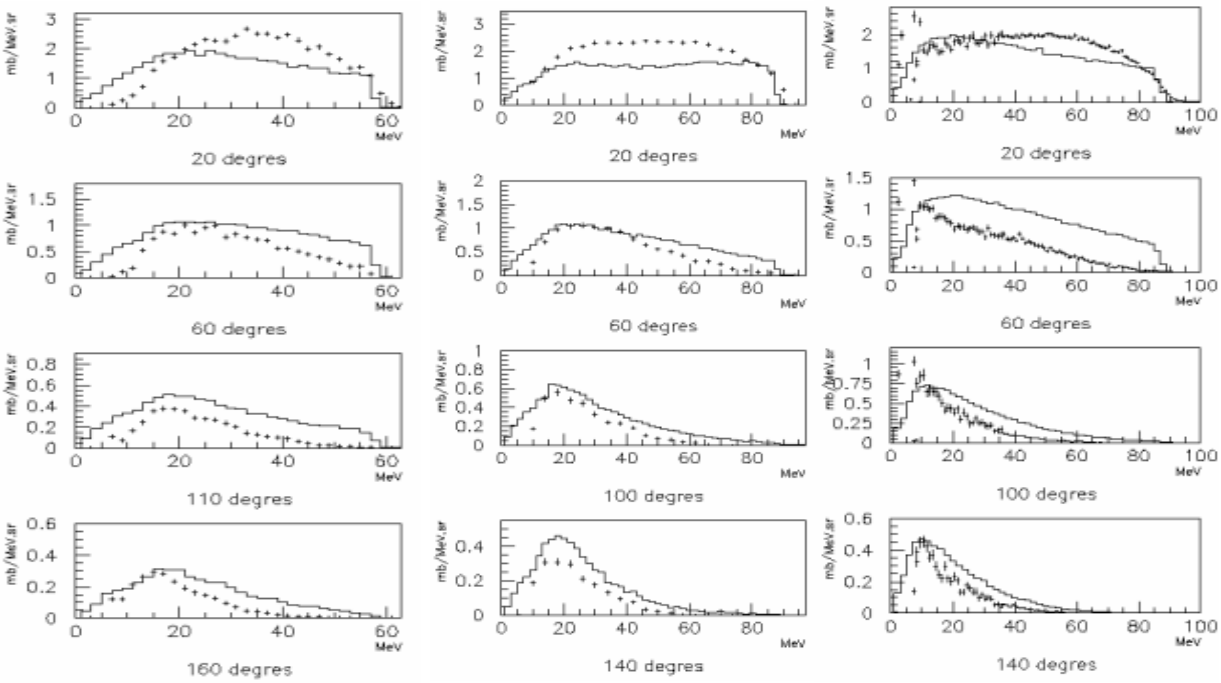

Pb(n,p) 63MeV **Pb(n,p) 96MeV** **Fe(n,p) 96MeV**

Figure 2.14 : *Double differential cross sections of emitted proton on different reactions : neutron on lead at 63 Mev and 96 MeV and neutron on iron at 96 MeV, the experimental results correspond to the crosses, the theoretical results are exhibited with histograms ([Ker02],[Bli03])*

Actual situation and prospects

The DYWAN model includes quantum effects which are necessary to a microscopic description of the nucleon-nucleus collision : the constituent of the nucleus are bound by a self-consistent mean-field, and, in the initial conditions, distributed along a discrete energy spectrum. Spin and isospin degrees of freedom are explicitly taken into account. The model gives the possibility to introduce different effective interactions and therefore to study physical aspects such as the non-locality of the nuclear interaction or its isospin dependence. These effects are expected to have an impact on the observables, in particular on the double-differential cross-section of light charged particles. It must be remarked that neither the total cross-section reaction nor the angular distribution of emitted particles are introduced as input data (as it is the case for most phenomenogical models). In the DYWAN model, the

distribution of emitted particles results from the properties of the nuclear interaction, by means of the collective effects via the mean field, as well as by means of the two-particle diffusions via two-body correlations.
The fact that this approach is based upon an accurate hierarchy of approximations, both for the physical description and for the mathematical representation, constitutes its main interest. It can therefore potentially be improved in order to be more suited to the physical processes under study. In the case of the nucleon-nucleus collision at intermediate energy, it has been remarked that the centre of the target is only slightly perturbed. It should therefore be interesting to consider a coarser representation of the central part of the target but with a finer description of the wave functions corresponding to the higher energy levels. As these levels are dominant at the surface of the nucleus, the preciseness of their description should have an influence over the quality of the calculated emission spectra. The description of the fragment formation, currently in a simplified version, can be strongly improved. The striking feature is the simultaneous and consistent treatment of the emission process of the different kind of particles.

2.4. Experiments

2.4.1. Elastic neutron scattering

Why elastic neutron scattering?

For ADS applications, improved understanding of neutron interactions are needed for calculations of neutron transport and radiation effects. It should be emphasized that what is primarily needed is not raw data, because for these applications, it is beyond reasonable efforts to provide complete data sets. Instead, the nuclear data needed for a better understanding must come to a very large degree from nuclear scattering and reaction model calculations, which all depend heavily on the optical model, which in turn is determined by elastic scattering and total cross section data.

The data situation before HINDAS

Before HINDAS, very little high-quality neutron elastic scattering data existed above 20 MeV energy (which is the upper energy limit of the established evaluated data libraries for fission and fusion applications). Neutron energies up to about 25 MeV are accessible with electrostatic accelerators, but above 30 MeV neutron energy, only two experiments have produced data with an energy resolution adequate for resolving individual nuclear states, an experiment from MSU at 30 and 40 MeV [DeV81, DeV83], and from UC Davis at 65 MeV [Bra84,Hjo94]. Recently, experiments at 55, 65 and 75 MeV have been reported, having energy resolutions in the 10-20 MeV range [Iba00,Bab02]. In addition, a few measurements in the 0-30 degree range, between 80 and 350 MeV, are available; all with energy resolution of 15 MeV or worse [Bra50, Sal60, Zyl56, Har58, Ash57].

The HINDAS experimental efforts

To remedy the absence of high-quality elastic neutron scattering data above 65 MeV, a dedicated campaign was undertaken at the neutron beam facility at the The Svedberg Laboratory (TSL), Uppsala, Sweden. A facility for measurements in the 50-130 MeV has been developed, SCANDAL (SCAttered Nucleon Detection AssembLy). The performance of SCANDAL has been corroborated by measurements and calculations. The different performance parameters, like resolutions, efficiencies, etc., are all understood and close to

their design values, and the instrument is now in frequent and regular operation. A technical description has been published in Nucl. Instr. Meth. A [Klu02].

SCANDAL has been used not only for elastic neutron scattering, but also for (n,xp) reactions and has thereby turned out to be a device of general usefulness. The multiple use of it has been very fruitful for the development of the facility itself, because it has resulted in a wide range of performance tests, which neither reaction itself could have provided. Finally, SCANDAL will also be used as one major component of the (n,xn') reaction studies initiated in HINDAS. The use of SCANDAL for measurements of other data than elastic scattering cross sections is described elsewhere in this report.

Results and discussion

Angular distributions of elastic neutron scattering from ^{12}C and ^{208}Pb at 96 MeV incident neutron energy are presented in Fig. 2.15. This experiment represents the highest neutron energy where the ground state has been resolved from the first excited state in neutron scattering. The measured cross sections span more than four orders of magnitude. Thereby, the experiment has met – and surpassed – the design specifications.

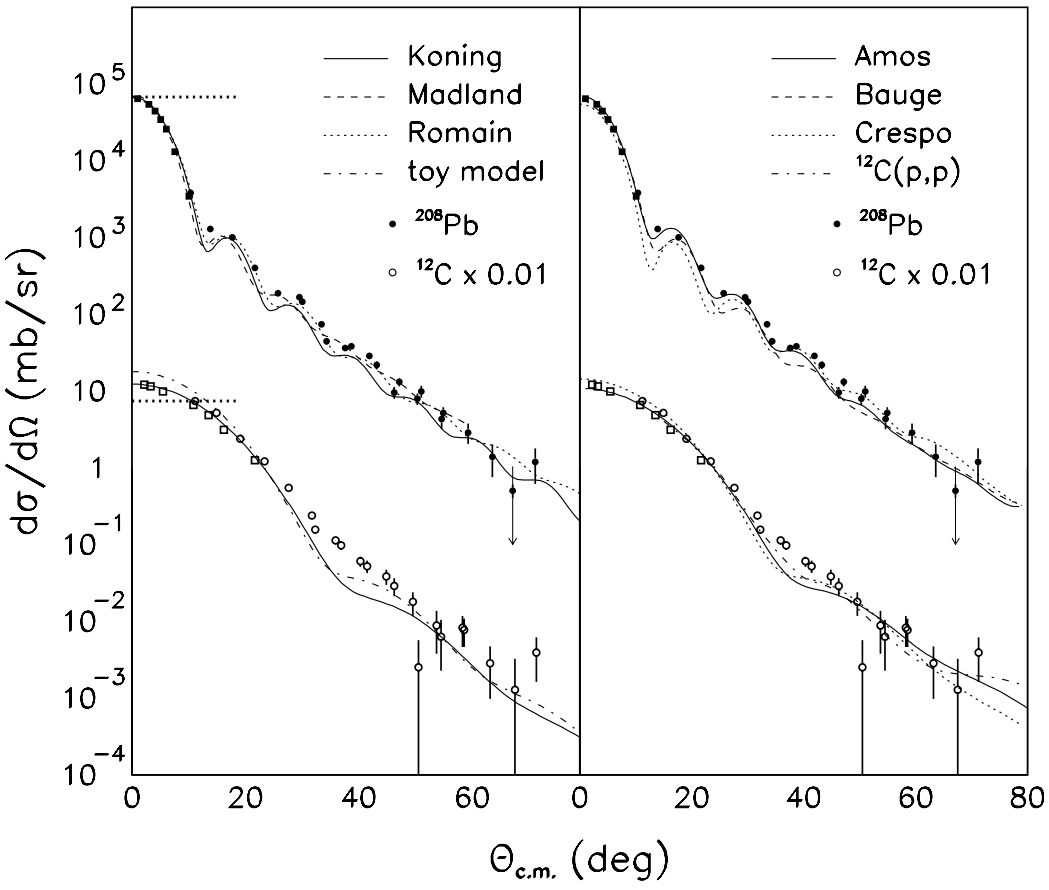

Figure 2.15 : *Angular distributions of elastic neutron scattering at 96 MeV for ^{208}Pb (solid circles) and ^{12}C (open circles), and comparisons with various models. The ^{12}C data and calculations have been multiplied by 0.01. For details, see refs. [Klu03a,Klu03b].*

Measuring neutron-induced cross sections on an absolute scale with experimental methods only is extremely difficult. In fact, there have up to now been essentially only two methods used, tagging and combinations of neutron-proton scattering measurements. Part of the present project has been devoted to the development of a third purely experimental technique for absolute neutron-induced cross section measurements. By combining data on total and reaction cross sections, as well as elastic scattering data, a purely experimental normalization with an estimated uncertainty of 3 % has been achieved.

The data have been compared with phenomenological and microscopic optical model calculations, all being performed before data were at hand. A general observation is that the shapes of the angular distributions provided by all models are in reasonable agreement with the data, but on an absolute scale, they all are 0-30 % below the data. In fact, no model exceeds the measured angular distribution.

A brief account of the data and theory interpretation has been published as a rapid communication [Klu03a] and a detailed publication has recently been accepted [Klu03b]. Data on elastic scattering from ^{1}H, ^{2}H, ^{16}O, ^{56}Fe and ^{89}Y have also been measured with SCANDAL, and are under analysis. As a side-effect of the present project, data for biomedical and electronics reliability applications have been produced. Last but not least, one PhD has already been examined and additionally three will have data from the present project as part of their theses.

Conclusions and outlook

After completed analysis of the data taken during HINDAS, the general picture should be reasonably well known for elastic neutron scattering at about 100 MeV. For a future transmutation demonstrator or production facility, some additional measurements might still be motivated to address particular issues, but a broad understanding should now be at hand. The experimental techniques developed within HINDAS have been analyzed, and it seems feasible to extend the present techniques up to 200 MeV, i.e., it is feasible to double the energy range of high-quality data.

2.4.2. Neutron, proton and light charged particle production induced by neutrons or protons between 20 and 200 MeV

(a) Light charged particle emission induced by fast neutrons with energies between 25 and 65 MeV on Iron and Uranium.

<u>The situation before the HINDAS project</u>

Results of measurements on light charged particle (lcp) production for fast neutron induced reactions in the incident energy range of 20 to 80 MeV were dramatically scarce in the literature due to specific experimental difficulties. Indeed, experiments of this type are affected by relatively low neutron beam intensities as well as low cross sections and, the target thickness is a compromise between the statistical accuracy, the acquisition time and the corrections to be applied on the charged particle spectra due to the energy losses in the target. In the 80's, only some incomplete measurements existed on light nuclei (^{12}C, ^{14}N, ^{16}O) [Sub83, Sub86]. Later, in the 90's, complete angular distribution of double-differential cross sections on light nuclei (^{12}C, ^{14}N, ^{16}O, ^{27}Al) were measured in Louvain-la-Neuve [Sly00, Duf00, Ben98a, Ben98b, Ben99a, Sly00, Ben98c]. However, no experimental data were available for medium-weight and heavy targets. During the concerted action "Physical aspects

of lead as a neutron producing target for accelerator transmutation devices" (contract N° F141-CT98-0017), measurements were performed on lead. Results of this measurement are now published for a 62.7 MeV incident neutron energy [Ker02]. On the other hand, experimental data on light charged particle production in proton-induced reactions on iron at comparable incident energies 28.8, 38.8 and 61.5 MeV exist in the literature [Ber73].

Experiments, data reduction procedure and results

The measurements were performed at the fast neutron beam facility of the Louvain-la-Neuve cyclotron CYCLONE (Fig. 2.16). The 65 MeV accelerated pulsed proton beam is focused on a 3 mm thick natural lithium target. After transmission through the lithium target, the proton beam is deflected into a water-cooled graphite beam dump (faraday cup). The integrated charge is used for the relative beam monitoring (first monitor). The ^{7}Li(p,n) reaction (Q = -1.64 MeV) produces, at 0° laboratory angle, a neutron energy spectrum consisting of a high-energy well defined peak followed by a flat continuum of lower-energy neutrons [Sch99]. In the main peak, located at 62.7 MeV, there are about ten times more neutrons/MeV than in the neutron lower energy continuum. The collimated neutron beam strikes the iron target placed in an evacuated reaction chamber 3.28 m downstream from the neutron producing target. With a proton beam current of 10^{-5}A, about 10^{5} neutrons/cm^{2}/s are available on the iron or uranium targets. Nine angles (from 20° to 70° in 10° steps, 110°, 140° and 160°) are chosen for the measurements [Nic02].

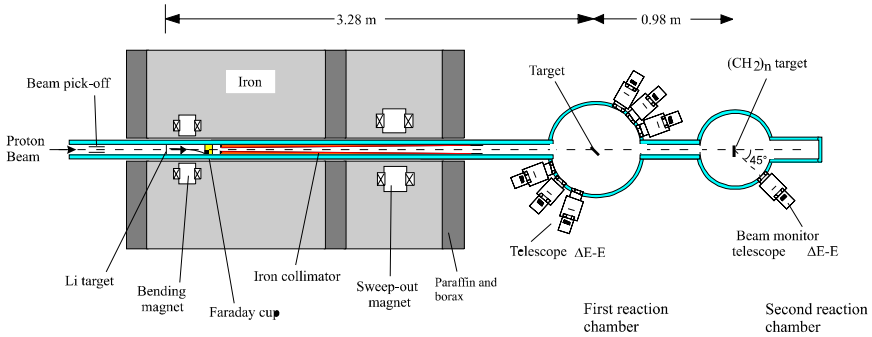

Figure 2.16 : *Global view of the experimental set-up.*

Light charged particles emitted from the target are detected simultaneously by six ΔE-E telescopes. Each of them is composed of a 0.1 mm thick NE102 plastic scintillator as ΔE and a 22 mm thick CsI(Tl) as E, each coupled to a photomultiplier. The E detector can stop 80 MeV protons. A coincidence is required between ΔE and E detectors in order to suppress an important part of the background always produced in such experiments.
For charged particle discrimination, a two-sequence separation procedure is applied by using: (i) the energy information from ΔE-E telescopes and (ii) two different charge integration of the CsI signal. Their combined use allows a reliable low energy background elimination and a good separation of the reactions products over their entire energy range [Nic02]. The alpha-particle spectra contain as well the ^{3}He products, which cannot be properly separated. Nevertheless, theoretical estimations show that the ^{3}He contribution is very small compared to alpha-particle emission.
Natural iron and uranium targets of 6x6 cm^{2} surface and respectively 0.5 mm and 0.18 mm thick are used for the measurements. The angle between the target and the neutron beam is chosen to minimize the thickness of the target material traversed by the emitted charged

particles in their way to the detector telescopes.
For energy calibration, the recoiling protons and deuterons are obtained from respectively a 1 mm thick polypropylene and a 0.6 mm thick deuterated polypropylene target and recorded at laboratory angles from 20° to 70° (in steps of 10°), with each of the six telescopes. An extra calibration point is obtained with a 5.5 MeV α-source. The complete set of calibration points is used together with a three-free-parameter analytical formula that relates the CsI light response to the energy, mass, and charge of the detected particles [Hor92]. In this way, the obtained energy calibration is consistent for all of the four particle species. Moreover, the n-p scattering is registered with good statistics, for a precise determination of differential cross sections [Ben97] to be subsequently used as reference.
Downstream from our reaction chamber and coupled to it, there is a second reaction chamber in which a 1 mm thick polypropylene target is placed perpendicular to the incident neutron beam. A ΔE-E telescope detects at 45° laboratory angle the emitted particles (mainly recoil protons). The integral of the recoil protons serves as second relative neutron beam monitor. Both monitoring procedures were in agreement (within 2 %) during the data taking.
A total time-of-flight (TOF) between a capacitive beam pick-off, located upstream from the neutron producing target (Fig. 2.16), and the ΔE detector is measured for each charged particle event in a telescope. Knowing the energy of the charged particle (from the energy calibration) and its flight path (distance from the target to the ΔE detector), one calculates the time-of-flight for each charged particle event which, when subtracted from TOF, gives the neutron time-of-flight, hence the energy of the corresponding incident neutron [Nic02]. In this way, the incident neutron energy spectrum corresponding to each particle type is reconstructed at each detection angle. In Fig. 2.17 the inset presents an incident neutron energy spectrum reconstructed from all the proton events recorded at 20° laboratory with the uranium target. Based on the time resolution in the experiment (0.8 ns), a selection of only those charged particles induced by a specific incident neutron energy bin is performed. As an

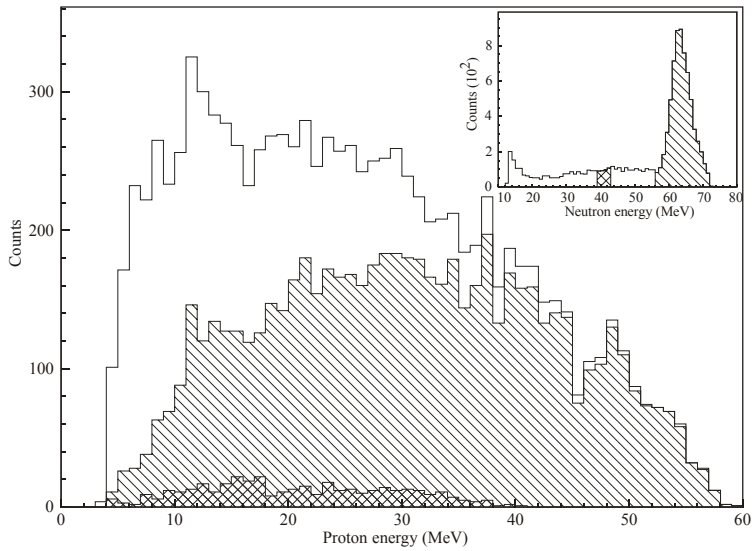

Figure 2.17 : *All proton events (white histogram) and selection of proton events incident neutron energies of the 62.7 MeV main peak (hatched area) and of the 41.0 ± 2.0 MeV bin from the continuum (double hatched area). The inset shows the incident neutron energy spectrum reconstructed from all proton events at 20°.*

example Fig. 2.17 illustrates the selection of the proton events induced by respectively the neutrons of the main peak (hatched area) and the neutrons of 41.0 ± 2.0 MeV energy (double hatched area). The statistics in the iron and uranium experiments corresponds respectively to a

total acquisition time of 35 and 97 hours for the forward angles and 70 and 185 hours for the backward angles, with a mean proton beam of $12x10^{-6}$ A on the lithium target.
The charged particle spectra are presented in 2 MeV energy bins for protons and deuterons and 3 MeV bins for tritons and alpha-particles. These widths are chosen to take into account the energy resolution in the experiment and the precision of the energy calibration.
Double-differential cross sections ($d^2\sigma/d\Omega dE$) were measured at nine laboratory angles between 20° and 160° for protons (p), deuterons (d), tritons (t) and alpha-particles (α) at the following neutron energies: 25.5 ± 1.5, 28.5 ± 1.5, 31.5 ± 1.5, 34.5 ± 1.5, 37.5 ± 1.5, 41.0 ± 2.0, 45.0 ± 2.0, 49.0 ± 2.0, 53.5 ± 2.5 and 62.7 ± 2.0 MeV. The overall relative uncertainties of the experimental points in the spectra are about 6 %, 9%, 20 and 25% for respectively p, d, t and α on the iron target and 7, 12, 20 and 22 % on the uranium target at 62.7 MeVneutron energy. They are mainly given by the statistics in the spectra. At lower ejectile energies, the thick target corrections (PERTEN code [Sly94]) contribute with supplementary uncertainties. For all the other incident neutron energies (continuum), these values are two to three times higher as a consequence of a lower incident neutron flux.
The uncertainty of the cross section absolute scale is about 7 – 8 %, due to uncertainties on the measured H(n,p) reference cross sections (5 %), statistics in the H(n,p) recoil proton peak (2-5%), beam monitoring (2 %), solid angle corrections (1 %), number of target nuclei (1%) etc. The detection energy thresholds in the experiment are mainly given by the thickness of the ΔE detector and correspond to about respectively 6 MeV protons and deuterons and 12 MeV for tritons and α-particles. The respective values of the Coulomb barriers are about 15 and 28 MeV for the uranium nucleus.
Fig. 2.18 present the double-differential cross sections (filled dots) measured at 20° laboratory angles for protons and deuterons on respectively iron and uranium, at different incident neutron energies. Open dots represent data from a similar experiment performed on Cobalt [Nic02] with the same set-up. Experimental results from proton-induced reactions [Ber73] are represented as follows: stars for ^{56}Fe at 61.5 MeV, and triangles for ^{54}Fe at 38.8 MeV incident proton energy. The data are also compared with calculations from two nuclear reaction codes GNASH [You92] and TALYS (see part 2.1) . Details about parameters used for GNASH calculations are given in ref. [Rae03a] and [Sly03]. The dashed lines show calculations with the GNASH code while continuous lines show calculations with the TALYS code. For both GNASH and TALYS, the calculations were performed on ^{56}Fe and ^{238}U. In general, for both targets, GNASH and TALYS calculations give a fair description of the proton spectra. Nevertheless, below 15 MeV proton energy, differences between the two codes are important on the iron target and the GNASH calculations describe better the experimental cross sections. The situation is quite different for the U(n,px) reactions: TALYS calculations describe well the absolute magnitude of the experimental cross sections for all incident neutron energies while GNASH underestimates the cross sections at the lower incident neutron energies.
For the emission of complex ejectiles, it is necessary to distinguish between data from the medium-weight targets (Fe [Sly03] and Co[Nic02]) and the heavier targets (Bi [Rae03b] and U [Rae03a]). In the case of the iron and cobalt data, both calculations are in fair agreement with the experimental data. On the other hand, for the heavier targets and for increasingly complex ejectiles (deuterons, tritons and alphas), GNASH underestimates strongly the experimental data while TALYS calculations reproduce the order of magnitude and the shape of the spectra except for the low ejectile energy part (particularly in the α-particle case).

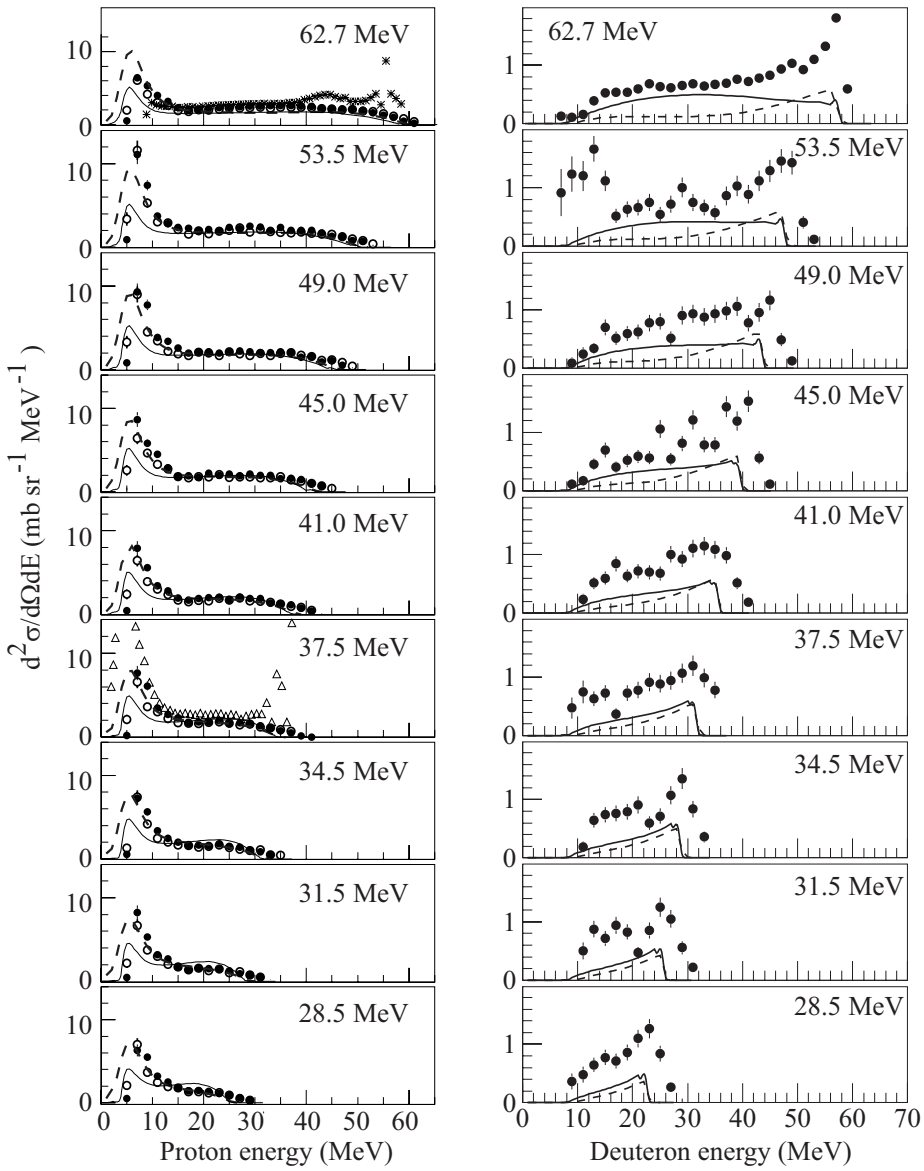

Figure 2.18 : *Double-differential cross sections ($d^2\sigma/d\Omega dE$) for (n,px) and (n,dx) reactions at 20° laboratory angle, for the indicated ten incident neutron energies on respectively iron and uranium targets (filled dots). Open dots represent data on cobalt [Nic02]. Corresponding experimental data from proton-induced reactions [Ber73] for the target nuclei ^{56}Fe (61.5 MeV at 20°, stars) and ^{54}Fe (38.8 MeV at 20°, triangles) are presented. GNASH (dashed lines) and TALYS (continuous lines) code calculations are shown.*

For each energy bin of the outgoing light charged particle spectra, the experimental angular distribution is fitted by a simple two-parameter formula [Kal88], $a \exp(b \cos\theta)$. This allows the extrapolation of the double-differential cross sections at very forward (2.5° and 10°) and very backward (170° and 177.5°) angles, and the interpolation for the missing angles. In this way, a good covering of the laboratory angular range 0° to 180° is obtained. For each incident neutron energy, the corresponding energy-differential cross sections ($d\sigma/dE$) are obtained by integration over the angle of the above mentioned angular distributions.
Some resulting energy-differential cross sections on uranium are shown in Fig. 2.19.

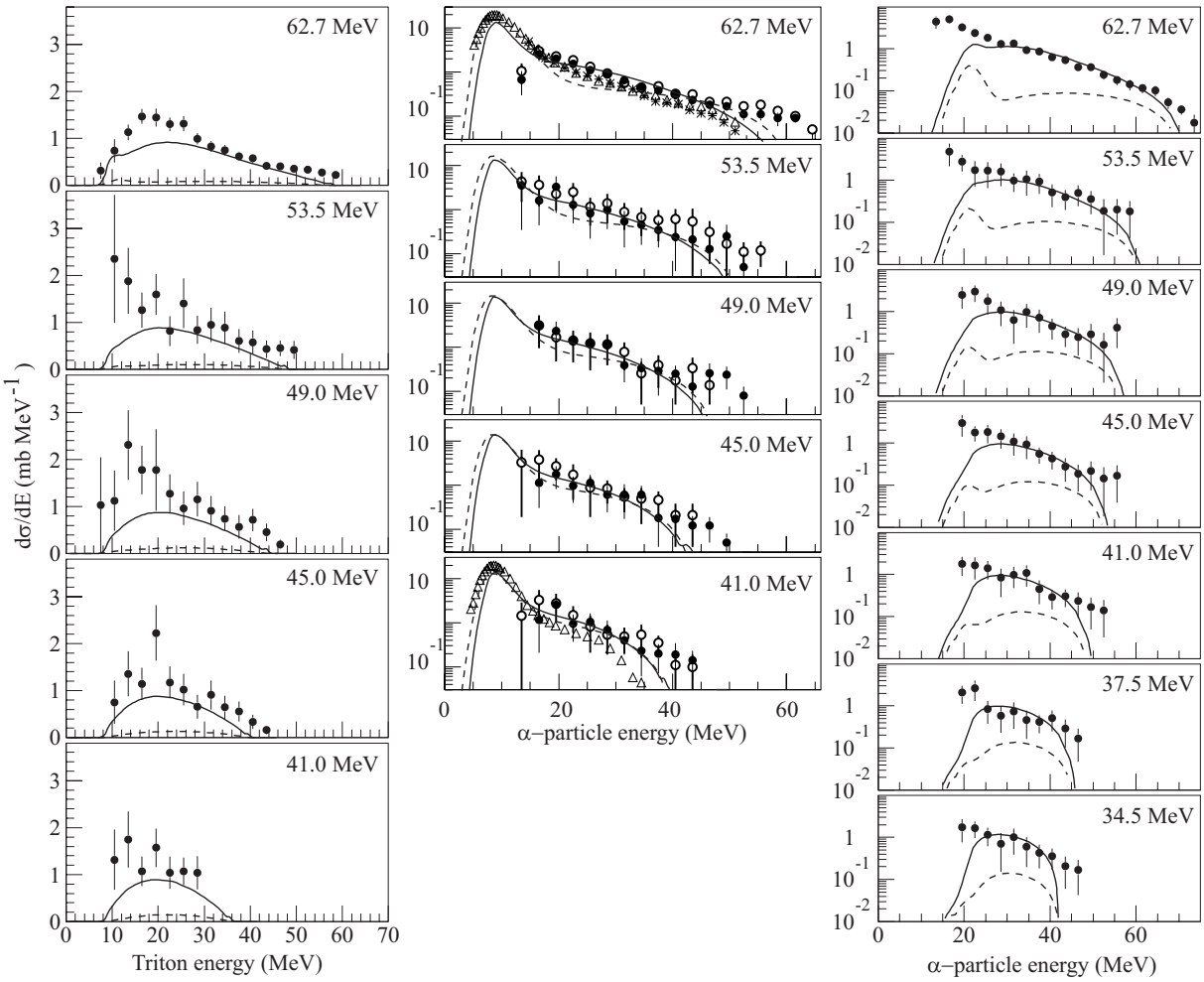

Figure 2.19 *: Energy differential cross sections (dσ/d*E*) for (n,tx) reactions on uranium (left) and (n,αx) reactions on iron (centre) and uranium (right) (filled dots). Open dots represent data on cobalt [Nic02]. Data from proton-induced reactions on ^{56}Fe (61.5 MeV, stars) and ^{54}Fe (61.5 and 38.8 MeV, triangles) [Ber73] are also presented. GNASH (dashed lines) and TALYS (continuous lines) code calculations are shown.*

What has been mentioned above concerning the comparison of the two theoretical calculations with experimental data on heavy targets is clearly illustrated here in Fig. 2.19. For the iron data, both the two codes describe well the four ejectile energy-differential cross sections resulting directly from the agreement observed in the double-differential cross sections.

By integration of the energy-differential spectra, the total production cross sections are obtained. The dependence of the total production cross sections for the four ejectiles vs. incident neutron energy is compared on Fig. A.20 with theoretical values calculated by GNASH and TALYS code (for iron, bismuth and uranium targets). For the iron data, the big discrepancies between the theoretical calculations and the measured alpha data come mainly from the huge evaporation peak predicted below 12 MeV and not seen experimentally (please see Fig. 2.19) [Sly03]. For uranium and bismuth targets, the TALYS code shows a dramatic improvement especially for complex particle emission, compared to GNASH nuclear reaction code.

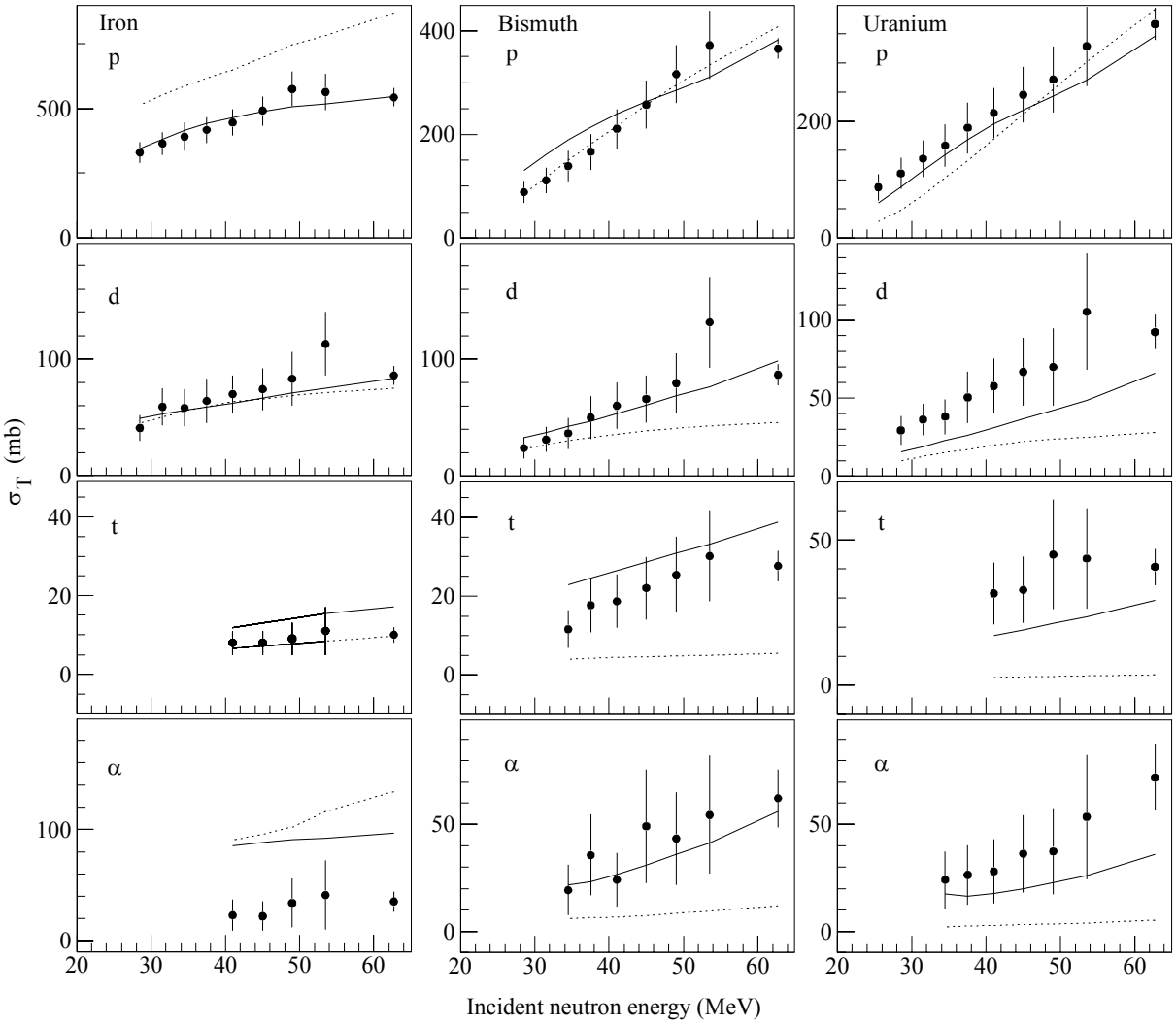

Figure 2.20 : *Experimental total cross sections (filled dots) for (n,px), (n,dx) ,(n,tx) and (n,αx) reactions on natural iron, bismuth and uranium vs. incident neutron energy, compared to values calculated by GNASH and the TALYS nuclear reaction code.*

All experimental data on iron and uranium and their comparisons with theoretical calculations have already been published [Sly03, Rae03a]. Data on cobalt and bismuth (Fig. 2.20) have also been measured with the same experimental set-up and are also published [Nic02, Rae03b]. It is also worth to mention the uranium and bismuth data are part of the PhD thesis of E. Raeymackers.

Conclusions and outlook

Inside the HINDAS project, we report for the first time, proton, deuteron, triton and α-particle energy spectra ($d^2\sigma/d\Omega dE$) in a wide incident neutron energy range of 28 to 63 MeV on iron and uranium. These results, together with those on cobalt and bismuth represent a self-consistent set of data important for benchmarking nuclear reaction models and for different applications in nuclear technology.

For a future transmutation demonstrator or production facility, some additional measurements might still be motivated to address particular issues, but a broad understanding should now be at hand.

(b) Proton and light charged particle emission from the interaction of 96 MeV neutrons on natural iron, lead and uranium targets

The experimental set up

The measurements were done at the TSL neutron beam facility in Uppsala. A detailed description of the facility has been provided in previous works [Con90].

The MEDLEY set-up has been used for the detection of protons and light charge particles (d, t, He-3 and alpha particles) and consists of eight Si-Si-CsI telescopes covering the angular range from 20° to 160°, located in a 100 cm diameter vacuum chamber. The front ΔE detectors (ΔE_1) are 60μm and 50μm thick for the telescopes located in the forward and backward hemispheres respectively, while the second ones (ΔE_2) are 500 or 400μm. The E detectors have a total length of 5 cm (sufficient to stop 100MeV protons) and the diameter of front sensitive area of 40 mm. The reaction target is located at the chamber centre. The $\Delta E - \Delta E$ or $\Delta E - E$ technique allows a good particle identification and a low threshold in the energy spectra.

The energy resolution for each telescope was found to be about 60, 45 and 500 keV for the ΔE_1, ΔE_2 and E detectors respectively.

A detailed description of the MEDLEY set-up is given in ref. [Dan00].

The SCANDAL set-up (SCAttered Nucleon Detection AssembLy) has been used in our experiment for proton detection only and it consists of two identical systems, located on each side of the neutron beam. Each arm consists of two ΔE plastic scintillators for triggering, two drift chambers for proton tracking, and an array of CsI detectors for proton energy determination. In order to improve the count rate, rather than using a thick target which could affect the energy resolution, a multi-target system consisting of thin target layers interspaced by nine MWPC (Multi-Wire Proportional Chambers) is used, allowing the identification of the proton emission target and energy loss corrections in the subsequent targets. During the experiment, the two arms were placed one in the forward and the other in the backward direction, covering scattering angles of interest. The set-up is located in air and the energy losses of the created particles from production target to CsI detectors gives a threshold in the proton energy spectra of about 30 MeV.

The energy resolution of the set-up, which has contribution from the neutron beam, the plastic scintillators and straggling in non-detector material is estimated to be about 3.7 MeV (FWHM) [Klu02].

Cross-section measurement

The cross-sections normalization has been done using the recently measured [Rah01] np elastic scattering cross-section. The different error sources give a total systematical uncertainty of about 5%. Statistical errors are shown on the figures.

The light charged particle Double Differential Cross-Sections for iron, lead and uranium were measured for 96 MeV neutrons. Starting from the double differential cross sections, it is possible to calculate the integrated cross-sections in angle or in energy. The angular differential cross sections are determined by integrating over the energy the Double Differential Cross Sections while the energy differential cross-sections were calculated using the Kalbach systematic [Kal88]. The energy differential cross-sections are shown in the Fig. 2.21 for proton and light charged particles emitted in 96 MeV neutron induced reactions on natural iron, lead and uranium. With the iron target, we were able to measure helium 3

production while with the heaviest target; this production was too weak to be measured. Finally, the integral yields were determined by integrating the energy differential cross sections and are reported in Table 2.2.

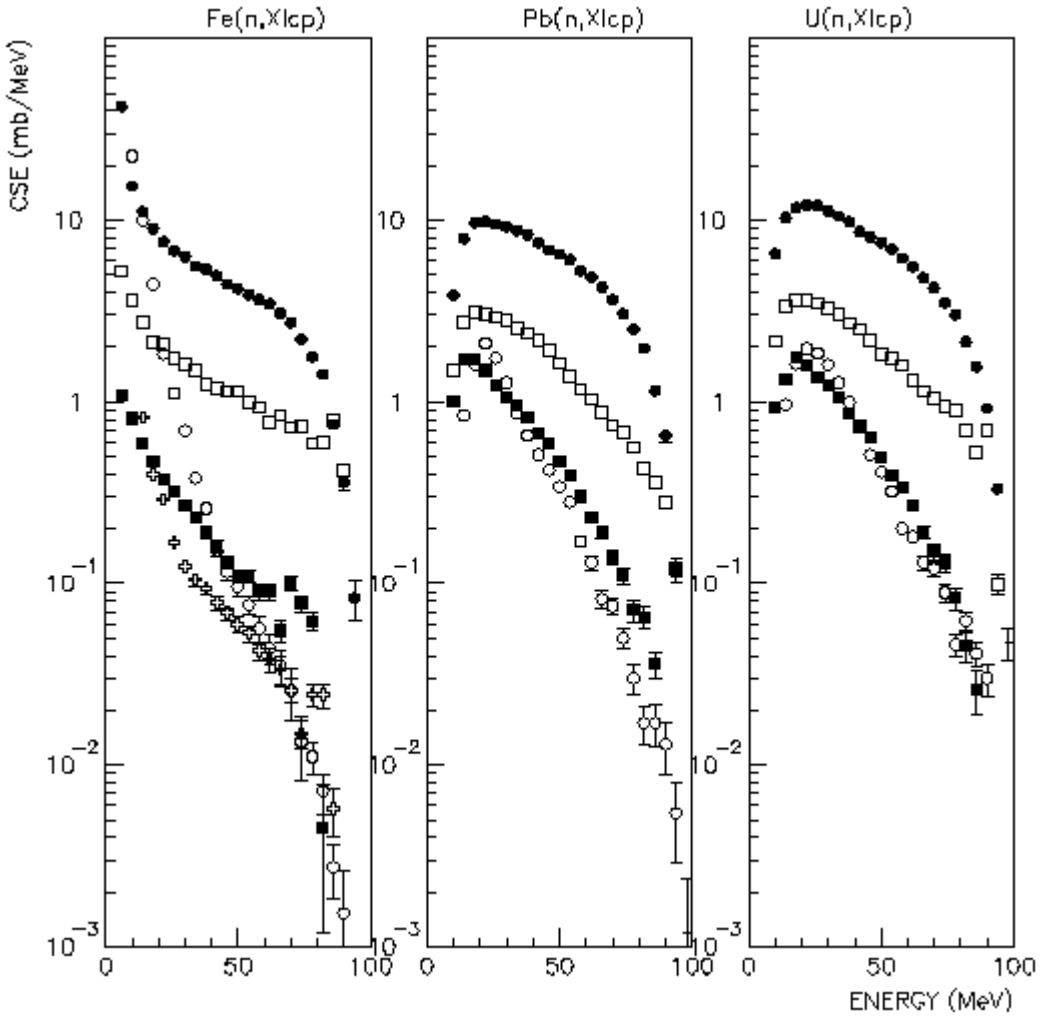

Figure 2.21 : *Cross-Sections in Energy for light charged particles emitted in 100 MeV neutrons induced reactions on respectively natural iron, natural lead and natural uranium (proton : black circle, deuteron : open square, triton : black square, helium 3 : open cross, alpha particle : open circle)*

Table 2.2 *: Integral yields (mb) for neutrons induced reactions at 96 MeV*

Emitted particle	**^{nat}Fe**	**^{nat}Pb**	**^{nat}U**
p	584 ± 29	485 ± 24	589 ± 29
d	131 ± 06	137 ± 07	170 ± 08
t	21 ± 01	53 ± 03	54 ± 03
He3	10 ± 01	---	---
He4	167 ± 08	45 ± 02	52 ± 03

(c) Neutron productions in neutron induced reactions on lead at 96 MeV

The experimental set up

The measurements were done at the TSL neutron beam facility in Uppsala. A detailed description of the facility has been provided in previous works [Con90].

The setup, which has been operated successfully in March'03, is made of two separated devices (see Fig. 2.22):

- DECOI & DEMON is devoted to the low energy part (10–50 MeV) of the neutron spectra. The detection principle is based on H(n,n) conversion. Incoming neutrons interact with the hydrogen nuclei of the plastic scintillator DECOI, scattered neutrons are then detected in DEMON cell. Neutron identification is achieved via the well-known pulse-shape analysis while energy is derived from the time-of-flight of the scattered neutron between DECOI and DEMON. The upper threshold of 50 MeV is a consequence of the path-flight (100 cm) while the lower one is mainly due to the low energy (~ 50 keV) of the recoiling proton detected in DECOI.
- CLODIA & SCANDAL is devoted to the high energy part (40–100 MeV) of the neutron spectra. CLODIA is made of 7 neutron converters interspaced by 8 drift chambers. The detection principle is based on H(n,p) study. Incoming neutrons interact with the hydrogen nuclei of the neutron converters located in the CLODIA box, recoiling protons are then detected and identified using SCANDAL and the well-know ΔE-E method. Neutron identification is achieved via rejection of incident charged particles using information coming both the veto scintillator and CLODIA drift chamber n°1. The energy is derived from the tracking of the recoiling proton by several plastic scintillators and drift chambers; the residual energy of those protons is measured in a CsI detector. The low energy threshold of 40 MeV is due to recoiling proton energy losses in the several plans of the setup before they reach the CsI.

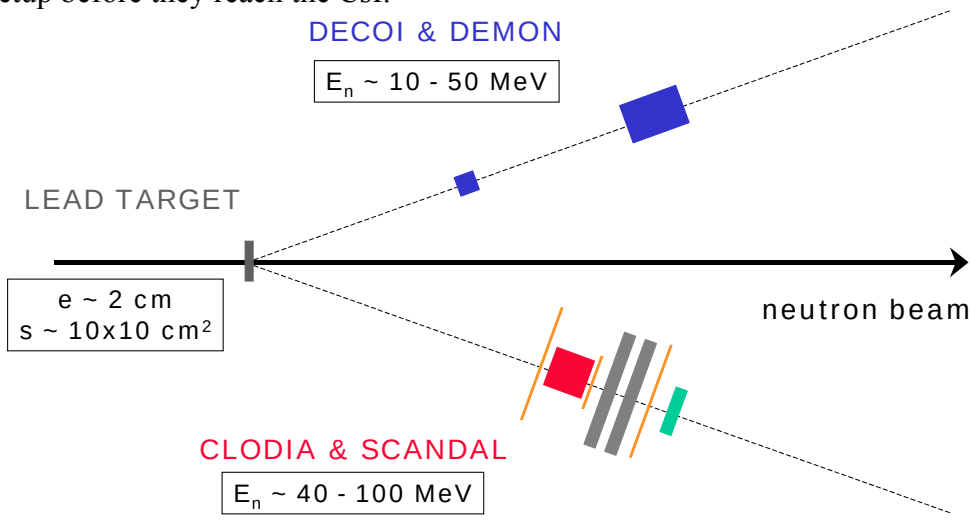

Figure 2.22 *: Experimental setup. In March'03, the two devices were located at 15° in respect to the beam axis.*

Preliminary results

To obtain cross-section from raw spectrum, there are two steps: the first one is to take into account the neutron detection efficiency of each device, the second one to normalise results in order to obtain cross-section. Neutron detection efficiency was determined using GEANT simulation (Fig. 2.23) while normalisation was derived from neutron beam intensity measurement [Klu02, Smi95].

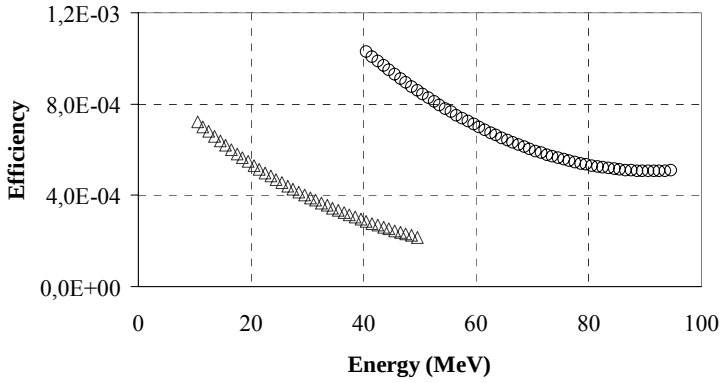

***Figure 2.23* :**

Neutron detection efficiency

The neutron detection efficiency has been determined using GEANT simulation for the two devices :

DECOI & DEMON (open triangle) and CLODIA & SCANDAL (open circle) with one neutron converter.

Preliminary results are presented in the Fig. 2.24; they were obtained taking into account only one neutron converter in CLODIA. Error bars are not yet available. Nevertheless, the good agreement in the energy region where the two devices overlap can be consider as a test of all the whole procedure. Moreover, the elastic cross-section Pb(n,n) derived from our preliminary results is in good agreement with previous measurement performed at Uppsala [Klu03]. Besides, MCNPx calculation using evaluated cross-section calculated by GNASH and incident neutron at 95 MeV with a Gaussian distribution (σ_E = 1.5 MeV) reproduce our preliminary results with a very good accuracy (Fig. 2.24).

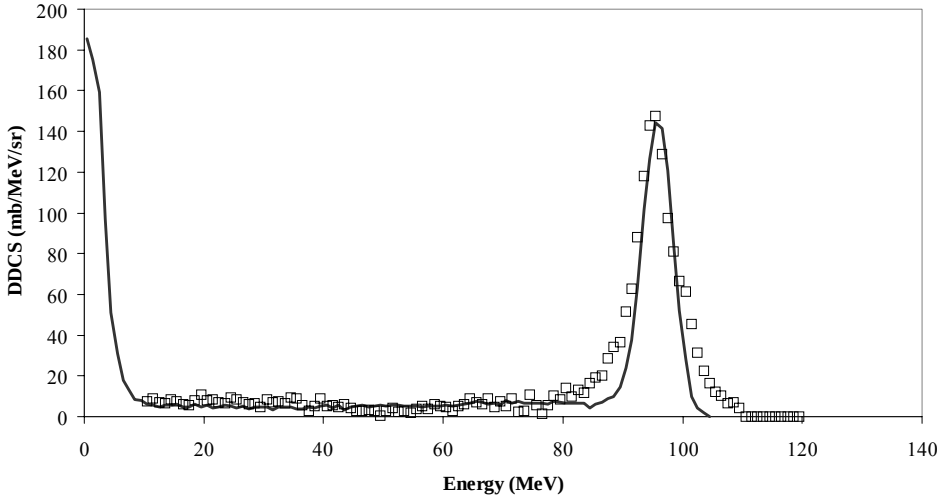

Figure 2.24 *: Preliminary results. Comparison between our preliminary results (open square) and MCNPx prediction (black line). Pb (n,xn) at 95 MeV at 15°*

Conclusion

A large amount of new data has been obtained within the HINDAS project. Our data combined with data obtained by other groups within the HINDAS collaboration (see contributions in WP1 & WP2 to this Final Report) in 20-200 MeV neutrons or protons induced reactions on iron, lead and uranium will help code developers in this energy region, in particular the codes developed in the framework of the HINDAS project (WP7 & WP8).

In addition, with the development of a dedicated set-up (CLODIA-SCANDAL), we are now able to measure neutron productions in neutrons induced reactions. In that way in the forthcoming years using the new neutron beam facility [Blo03] at TSL (Uppsala – Sweden)., we will study Fe(n,xn) reactions and Pb(n,xn) reactions at 96 MeV and measure double Differential Cross-Sections from 15° up to 100°.

(d) Secondary particle emission from the interaction of protons on iron (^{56}Fe), Lead (^{208}Pb) and uranium (^{238}U) targets.

In order to predict neutron production, shielding requirements, activation and material damage of accelerator driven systems, it is necessary to make macroscopic simulations that rely on basic nuclear reaction data. These data can be obtained directly from experimental results when they exist or using theoretical models. Below 20 MeV, extensive sets of data exist and are available within nuclear data libraries [ENDF, JEFF]. Above 200 MeV, the intra-nuclear cascade model is reliable and can be used to estimate accurately the needed cross sections (see WP8 or [Cug02]).

In the energy region between 20 MeV and 200 MeV, where few experimental results are available (see for example [Ber73], [Sak80], [Wu79], [Ric92], [Ric92], [Ric92], [Seg82], [Ric92], [Ric92]) in particular for complex particle emission, the situation is much more complicated since several reaction mechanisms contribute to the particle production. In addition, new reaction channels appear, implying the creation of composite particles. All these effects require a quite complex theoretical treatment especially to describe the production of Light Charged Particles (LCP), i.e. protons, deuterons, tritons, helium 3 and alpha particles.

By combining neutron and proton reactions, one should put enough constraints on theoretical models. One goal of HINDAS is to collect a large set of data for few nuclei that can be used as benchmark points by code developers helping them to enhance the predictive power of their theoretical models.

Double differential production cross sections in nucleon induced reactions are among HINDAS requested observables. These data are of great importance since the information contained in the Double Differential Cross Sections (DDCS) is much more stringent than energy differential cross sections due to the strong angular dependence of pre-equilibrium processes which are playing a crucial role in the 20-200 MeV energy region.

Measurement of neutrons and light charged particle production cross-sections in 62.9 MeV proton induced reactions

The double differential production cross sections of neutrons, protons, deuteron, triton, ^{3}He and ^{4}He were measured in reactions induced by a proton beam, impinging on a target at 62.9 MeV. These measurements were done using two independent experimental set-ups ensuring respectively neutron and light charged particle detection. It was then possible to do two complementary measurements in a single experiment[Gue02]. The 62.9 MeV proton beam was delivered by the 18 MHz cyclotron of Louvain-la-Neuve.

The experimental set up

Neutrons were detected using five DEMON cells (16 cm diameter and 20 cm deep cylinder, filled with NE213 liquid scintillator coupled with a photomultiplier [Til95]). Detectors were placed at 24°, 35°, 55°, 80° and 120° and their time-of-flight path lengths were respectively 534.7 cm, 388.7 cm, 303.9 cm, 250.7 cm and 296.0 cm. In order to reject background neutrons and gamma rays, each DEMON cell was surrounded by a 4 cm thick lead cylinder and installed inside a “bombarde” barrel filled with paraffin and boron. A very good discrimination between neutrons and gamma rays was achieved by pulse shape analysis of the liquid scintillator response. Neutron energies were determined with the time-of-flight method.

Light charged particles were detected using a set of triple telescopes (Si-Si-CsI) settled inside a vacuum chamber. Each telescope consisted of two silicon detectors (80 μm thick (Si1) and 300 or 500 μm thick (Si2) respectively), backed by a one inch diameter and 80 mm thick CsI(Tl) crystal. The identification of charged particles was obtained using the well known ΔE-E method. Most of the background coming from γ–rays was suppressed using a pulse shape analysis of the CsI energy signal. It allowed us to identify and to measure light charged particles over their entire energy range. A copper collimator was placed in front of each telescope to precisely define the detection solid angle. One detector was set at a fixed position (30^o at 62.9 MeV and 47^o at 135 MeV) to be used as a second beam monitor along with the Faraday cup. The others were separated into 2 groups which were mobile independently, allowing us a broad angular coverage from 15° to 165 °.

Cross-section measurement

Absolute normalisation has been obtained using the information coming from the Faraday cup and (p,p) cross-section measurements made during the experiment using a CH2 target. The different error sources give a total systematical uncertainty of about 20% for neutrons and does not exceed 10% for light charged particles.

Particle spectra show the same structure and angular evolution. Three different componants can be extracted from these spectra: a direct componant at high energy, an isotropic componant with a Maxwellian shape at low energy (the so-called evaporation componant [Wu79]) and the preequilibrium componant which is found highly non isotropic.

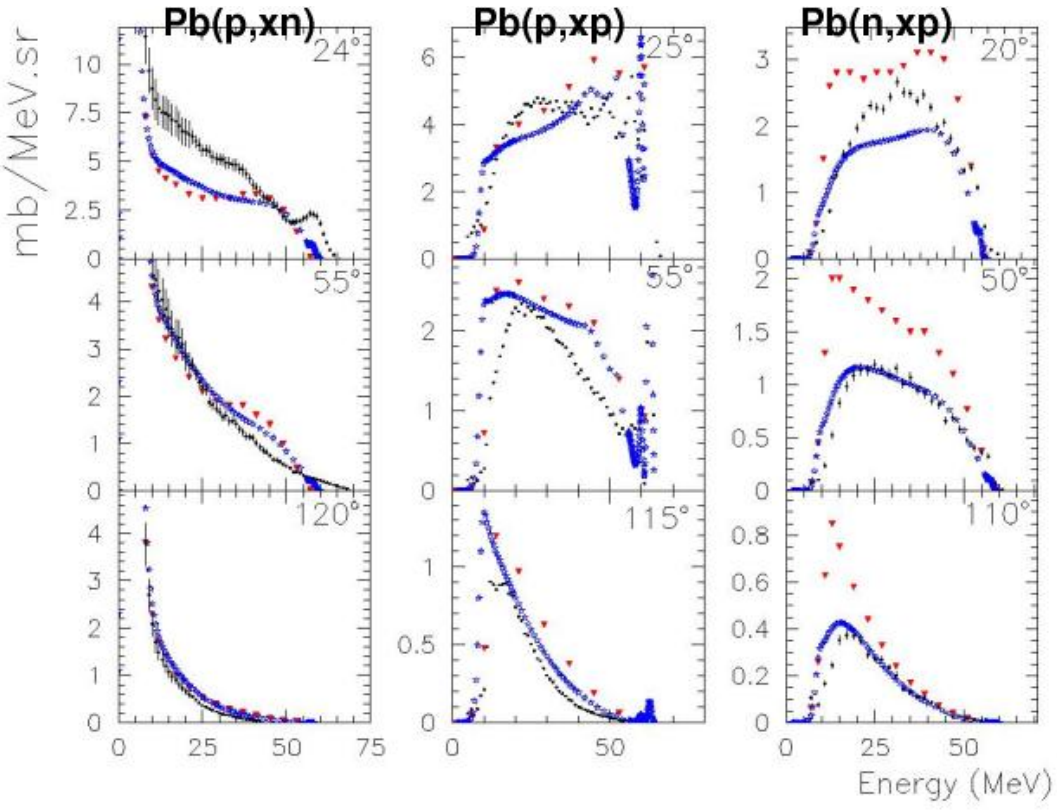

Figure 2.25 : *Proton and neutron double differential production cross sections for lead in neutron and proton induced reactions. The data are represented using full black circle, TALYS results using stars and GNASH results using triangles.*

Data obtained in nucleon induced reaction at 63 MeV are compared with TALYS in Fig. 2.25 for proton and neutron at 3 different angles. An overall good agreement is obtained with

TALYS even if discrepancies can be observed at forward angles. For composite particles, the TALYS code is not able to reproduce our differential and double differential cross sections. Nevertheless, it gives an integrated production cross sections compatible with our measured ones as can be seen in Tables 2.2-2.3.

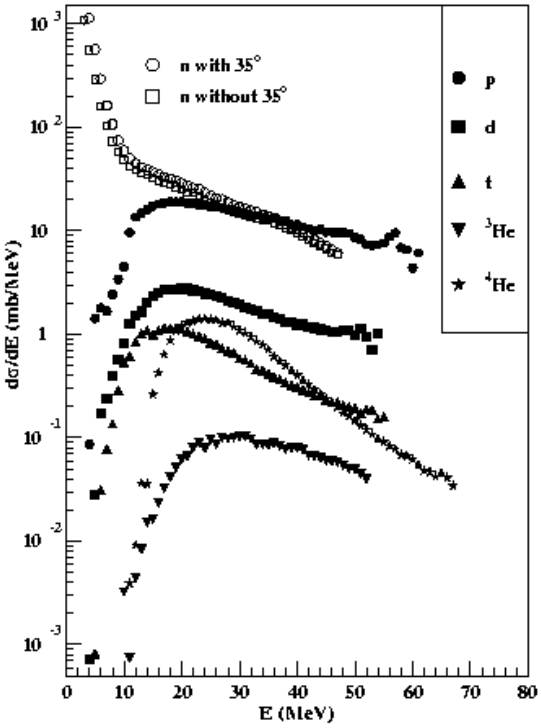

Figure 2.26 : *Energy differential cross-sections for neutrons and light charged particles emitted in 62.9 MeV protons induced reactions on lead. For neutron energy differential cross-sections, calculations were performed taking into account or not the measured double differential cross-sections at 35°.*

Starting from the double differential cross sections, it is possible to calculate the integrated cross-sections in angle or in energy. The angular differential cross sections are determined by integrating over the energy the Double Differential Cross Sections while the energy differential cross-sections were calculated using the Kalbach systematics [Kal88]. Results obtained with the lead target are shown on Fig. 2.26.

Finally, the integral yields were determined by integrating the energy differential cross sections.

Table 2.3 : Integrated production cross sections for composite particles at 62.9 MeV.

particule type	Experimental cross section (mb)	TALYS (mb)
deuterons	80.5	68.4
tritons	27.0	22.7
^{3}He	2.7	2.4
^{4}He	27.9	34.5

As an example, we have obtained a neutron production cross-section of 3218 ± 203 mb in 62.9 MeV protons induced reactions on lead, and a neutron production cross-section of 9076 ± 579 mb on uranium.

Measurement of light charged particle production cross-sections in 135 MeV proton induced reactions.

The data at 135 MeV were collected at KVI (Groningen - the Netherlands). Three different targets have been used: ^{208}Pb, ^{56}Fe and ^{natural}U. Charged particles were measured using the experimental set up developed in Nantes and previously presented (see section D-1.1).
At such a high energy, corrections for hadronic reactions on the detection system have to be made. Indeed, such effects induced an underestimation of the particle energy for almost 18% of the particles produced at 135 MeV. This contribution decreases steeply with energy and is almost negligible below 65 MeV [Klu02]. The correction is of great importance for forward angles since a deformation of the spectra is induced by this bad energy measurement. This correction is important for Z=1 charged particles and is no longer necessary for Z=2 particles. The absolute normalization has been obtained by combining the information coming from the Faraday cup and the (p,p) cross section values measured during the experiment using a CH_2 target. Taking into account the different contributions of errors, the systematic uncertainty in the absolute values of the cross section does not exceed 20%. The statistical errors correspond to 10% for 10 μbarn per steradian and per MeV.

Our double differential cross sections shows the same behaviour as at 62.9 MeV. For heavy target such as Pb or U, the large value of the Coulomb barrier inhibits the evaporation of low energy particles. The evaporation become small and its contribution is no longer visible at forward angles and can only be quantify by looking at the most backward angles.

From our data, it is possible to extract the angular differential by integrating over the energy the double differential cross sections. The energy differential cross sections were derived directly by fitting our data points using the Kalbach systematics [Kal88]. This systematics successfully accounts for a wide variety of experimental angular distributions of proton induced reactions at incident energies up to 200 MeV. However it does not take into account correctly direct processes and it is not efficient in energy regions where these processes are dominant. To prevent this effect, we have excluded from our cross section estimations the upper energy part of our spectra (see Table 2.4).

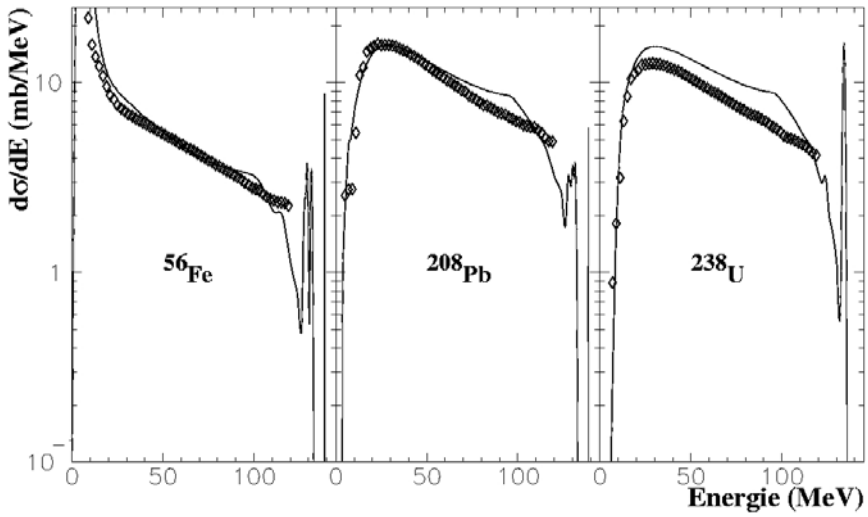

Figure 2.27 *: Energy differential production cross sections for proton obtained in proton induced reactions at 135 MeV. Experimental data are presented as symbols whereas TALYS calculations as line.*

In Fig. 2.27 our data (symbols) and TALYS prediction (line) are displayed as for iron, lead and uranium. An overall good agreement is obtained for proton energy differential cross section. Dicrepancies is found in the amplitude for the uranium target even if the shape of the spectra is correct.

Finally, the integral yields were determined by integrating the energy differential cross sections and are reported in Table 2.4.

Table 2.4*: Integral particle yield obtained for proton induced reaction at 135 MeV*

Target	Production cross sections (mb)				
	Proton (<131 MeV)	Deuteron (<121 MeV)	Triton (<127 MeV)	^{3}He (<109 MeV)	^{4}He (<119 MeV)
^{56}Fe	913,6	93	13,8	10	31,2
^{208}Pb	1174,5	169,3	59,2	10,5	84,9
^{nat}U	969,6	139	51	9,1	59,8

2.4.3. Multiplicity Studies of Light Charged Particles

Introduction

Here, we report on the measurement of multiplicity and differential cross sections of protons from ^{56}Fe, ^{208}Pb, and ^{238}U targets at an incident proton energy of 190 MeV. This experiment [Muk01] was performed at the superconducting cyclotron facility, AGOR (Accelerator Groningen Orsay) of the Kernfysisch Versneller Instituut (KVI). Singles proton spectra were obtained at a number of angles between 5^{o} - 32^{o} and 91^{o} - 160^{o}. The results [Muk02] are compared with modern optical model predictions and with Intra-Nuclear Cascade (INC) calculations.

Experimental Procedure

The experiment was conducted with several targets placed in the scattering chamber of the *p*-line associated with the SALAD (Small-Angle Large-Acceptance Detector) setup at KVI. The 190-MeV incident proton beam from the AGOR cyclotron lost a negligible amount of energy while traversing the target. Beam current varied between 0.1 and 0.2 nA and was limited by acceptable counting rates in the detectors. Beam halo, which may in principle be severe at forward angles, was monitored by a comparison of the count rate of particles scattered from an empty target frame with that of particles scattered from the target. Results reported here correspond to background rates of typically 0.5% to 1%, and were corrected for this effect wherever required.

Scattered protons were detected by two different detection systems, Plastic Ball [Bad01] and SALAD [Kal01], for two different angular domains, as is shown in Fig. A.28. Its spatial resolution and thus the number and dimensions of individual modules of Plastic Ball, is suitable to resolve the multiplicity distribution of particles from proton-induced reactions. Consisting of 340 ΔE-E particle identifying detector modules, it covers a solid angle of up to nearly 50% of 4π, ranging in polar angle from $\Theta = 91^{o}$ to 160^{o}, with respect to the beam axis. Seven geometrical annular rings, each one defining a Θbin of approximately, 10^{o}, hold the detector modules around the target position. The setup of SALAD, covering a solid angle of approximately 655 msr, detected the protons in the forward angles, as is schematically shown in Fig. 2.28. In this experiment, SALAD consisted of a ΔE plane of 24 thin scintillators, and

an *E* plane of 24 thick scintillators. Protons are detected at polar angles between 5^{o} to 32^{o} with full azimuthal coverage below 26^{o}. The 112.5 mm thick plastic scintillators in the *E* plane, ensuring a complete stop for 135 MeV protons, are aligned in two rows, each containing 12 of them. These strips are aligned in such a way that they form part of a cylinder with a radius of 71.5 cm around the target position. The Δ*E* and *E* planes of SALAD were mounted such that they formed a grid among themselves, thereby acting effectively as a set of 144 Δ*E*-*E* telescopes in the forward angle. Since the energy loss for protons was considerably greater in the Δ*E* detector of SALAD than in the target, it is primarily the thickness of the Δ*E* detector that determines the low-energy cut-off, which comes around 20 MeV for protons. Proton with energy smaller than (approximately) 20 MeV will not be detected as this would completely stop in Δ*E* plane. Similarly, protons with energies larger than 135 MeV (high-energy cut-off) punch through the *E* scintillator, and therefore, it becomes more difficult to identify them in SALAD. For 190 MeV proton beam, it guarantees that all the elastically-scattered protons will be detected but not identified on-line as they will not follow the conventional Δ*E*-*E* energy loss pattern. However, in the off-line analysis, elastically-scattered protons are recognized by their typical energy deposition spectrum in the *E* detector. In this experiment, the individual scintillator rates of SALAD were around 10 kHz, while the Plastic Ball modules were operating at a rate of around 1 kHz. The SALAD CFD (Constant-Fraction Discriminator) signal was down-scaled and OR-ed with the down-scaled Plastic Ball signal, to generate the master trigger for data acquisition, with a rate of about 250 Hz.

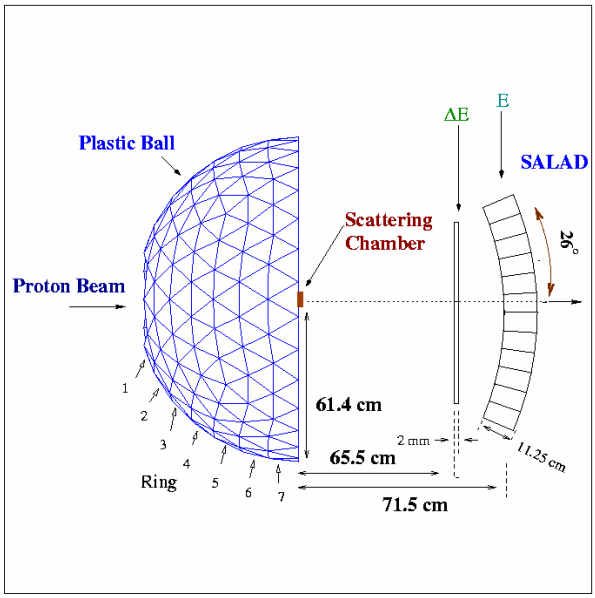

Figure 2.28 : *A schematic top view of the experimental setup, showing both Plastic Ball (left) and SALAD (right). The beam pipe goes through the center of the entire detector setup.*

Data Analysis

With an effective 24-hour beam time, a total of 4.1, 8.6, and 4.2 million events were recorded, respectively, for ^{56}Fe, ^{208}Pb, and ^{238}U targets. Subsequently in the off line analysis, we exploited the energy and time information of each detector, in order to identify and isolate protons from γ's and other detected particles, like leptons, neutrons, deuterons or high-*Z* particles. In the analysis of Plastic Ball data, the events were selected with a prompt (self trigger and/or coincidence) time window and a well-defined energy window for identifying protons.

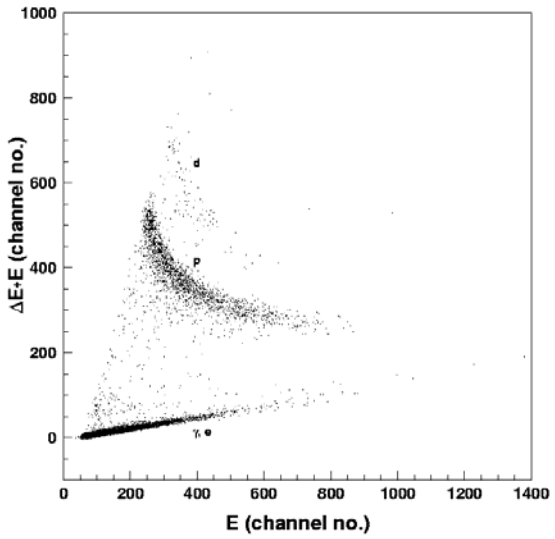

Figure 2.29 : *A two-dimensional plot of ΔE+E versus E, revealing the excellence of the Plastic Ball to discriminate protons and other light charged particles (deuterons, in this case) from the mostly abundant γ's and leptons produced in this reaction.*

In Fig. 2.29, a typical Δ*E*-*E* spectrum shows the quality of Plastic Ball for having an excellent identification and separation of protons from the background. It is the energy loss of the particles (lower branch in Fig. 2.29), traveling with the speed of light (photons and leptons), that determines the cleanliness of separation from the relatively heavier protons and deuterons (respectively, middle and upper branches in Fig. 2.29). The scattered events in the overlapping region between two neighboring branches, determine the major source of uncertainty in this singles measurement. However, as it is evident from this spectrum, we found that the uncertainty of misidentifying a proton as a photon, or as a lepton is as low as nearly 2%, while that for a proton as a deuteron is less than a percent. This limit ensures the major source of systematic uncertainty in particle identification, to be much below 5% for Plastic Ball. On the other hand, for the analysis of the SALAD data, we selected those events for which at least one Δ*E* and the corresponding *E* scintillators have fired within the proper time window, thereby selecting protons which had either reached or punched through the *E* scintillator.

Results and Comparison with Model Calculations

After correcting the data with the detector efficiencies and applying the normalization for covering the phase space, multiplicity of protons per each event was determined. Here, the multiplicity distributions of protons per each event are compared with the theoretical predictions folded with the detector acceptance. As the Plastic Ball and SALAD, covering two different phase-space regions, have different detecting thresholds for protons and also because they acquired data in OR mode, we analysed the registered multiplicities in SALAD and Plastic Ball separately. Therefore, this distribution is disentangled in two different angular regions. In Fig. A.68 (top panel), the multiplicity distribution of protons for Plastic Ball is shown, while Fig. A.68 (bottom panel) shows the same for SALAD. The error bars depicted here are the sum of the statistical and systematic uncertainties. In the Intra Nuclear Cascade (INC) calculations [Kun01], the energy of protons is restricted to E>25 MeV for Plastic Ball and E>20 MeV for SALAD data. In Fig. 2.30, the measured data points (open circles) are compared with INC calculations (solid histograms). Overall, each measured spectrum is characterized by an exponential line (not shown in the figures), starting with a huge

contribution at multiplicity one, mainly attributed to the elastic contribution for forward angles, while completely non-elastic for backward angles. A maximum multiplicity, five protons per event at backward angles, in contrast to four at forward angles, is found for the ^{208}Pb target. For ^{56}Fe, the maximum comes at four protons per event for both angular ranges, while for ^{238}U it is three and five, respectively, in the forward and backward angular ranges. This difference in maxima of multiplicity, for two different angular regions, is probably due to the difference in the phase-space coverage of the two detection systems. For high-multiplicity proton events, when one proton is detected in the Plastic Ball, there is a fair chance that a large portion of the rest of the protons in that event are also detected in it because of its large phase-space coverage. Therefore, in backward angles we expect a full multiplicity distribution. Whereas in case of SALAD, because of its relatively small phase-space coverage, the probability of one or more protons escaping detection is high, thereby, the high-multiplicity proton-events would effectively appear as low-multiplicity events in SALAD. This perhaps explains why we fail to observe an event with five protons in SALAD

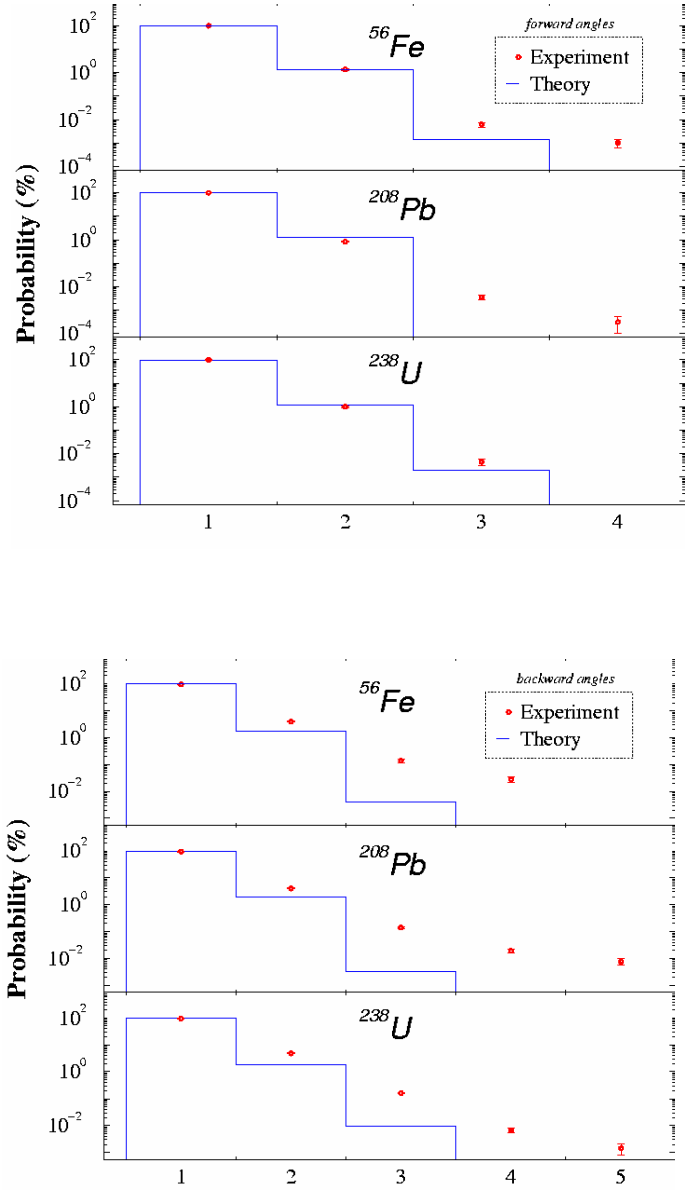

Figure 2.30 : *Multiplicity distribution of protons observed in Plastic Ball (top) and SALAD (bottom), compared with the INC model predictions.*

in contrast with the Plastic Ball. To understand and interpret the observed multiplicity distributions in both angular ranges, we have carried out an extensive study with INC model [Cug01]. In this model, the cascade process is seen as a time ordered sequence of binary collisions occurring as in free space (except for Pauli blocking) between classical nucleons. Recently, it has been tested at lower energies (from 40 MeV to 250 MeV) as well, resulting in a good agreement in most of the cases [Cug02]. This model has reproduced the measured values of multiplicity one very accurately for all targets in the angular coverages in both systems, although it should be pointed out that this model does not take into account the coherent elastic scattering. That probably explains why the intensity of multiplicity=1 event is so different between all the experimental data and calculations. Moreover, the two- and three-proton events are also reasonably well accounted for by the INC calculations. The major disagreement comes from the fact of underestimation of highest multiplicity proton events for all the targets except for ^{238}U at forward angles, where it exactly reproduces the highest multiplicity(=3) proton events. Overall, the INC underevaluates any event with more than four protons, with the situation becoming more striking for the case of ^{208}Pb at forward angles, where it even predicts a two-proton event to be the highest multiplicity event, in contrast to four from the experiment. However, the lack of high-multiplicity events from INC calculations should not be overemphasized because of its Monte-Carlo identity in nature. With a total number of 500,000 events, this calculations give a very good statistical accuracy for highly frequent events, but are notoriously insufficient to predict good results on less frequent events.

As already outlined in the previous section, the angle-differentiated cross sections are obtained by integrating over the azimuthal angle, Φ. After correcting the data with the detector efficiencies and applying the normalization for covering the phase space, these values of cross-section are determined. These distributions of protons emitted from three targets, ^{56}Fe, ^{208}Pb, and ^{238}U, respectively, are presented in Fig. 2.30. The data are compared with modern Optical-Model Potential (OMP) calculations using CHUCK3 [Kun01], and with the INC calculations to account for all possible reaction-channels contributions. As the theoretical curves are not folded with the experimental angular resolution, comparisons are rather qualitative. Moreover, the distributions presented here have not been corrected for reaction losses and multiple scattering in the target, all of which contribute negligibly small in comparison to the total. Therefore, the absolute normalization of the data has not been possible. However, the accuracy of the present normalization is rather fair as can be judged by comparing to the total elastic cross section calculated for these systems. The data points (open diamonds) are compared with model predictions in Fig. 2.31, where the solid and dotted lines represent the INC and OMP calculations respectively. A variation of the energy threshold for proton detection, within ±5 MeV in the INC calculation leads to a relative change by approximately ±5% of the calculated cross-section values.

We have performed a series of OMP calculations with CHUCK3, employing a global nucleon-nucleus optical-model potential for ^{56}Fe, ^{208}Pb, and ^{238}U [Kon01]. This OMP is valid for incident nucleon energies between 1 keV and 200 MeV and masses from 24 to 209. It is based on a smooth functional form for the energy dependence of the potential depths, and on physically constrained geometry parameters. An extensive collection of experimental data-sets for different types of observables was used to determine the parameters of the OMP. When comparing these predictions with the data, a few striking features appear evident. First, optical-model calculations for elastic scattering are in reasonably good agreement at small angles, as they should with all the data set. It should be pointed out that none of the predictions of the optical model uses parameters adjusted to the present experiment. In fact, they were all made available before the data were obtained. Even the absolute scale seems to be under remarkably good control. Particularly, for ^{208}Pb and ^{238}U data sets, the first two data

points at small angles are in good agreement with the OMP calculations, thereby increasing the confidence of good normalization of the data. However, in ^{56}Fe a large discrepancy is observed at the smallest angle, maybe, arising from the global OMP, which has been used for this nucleus. At relatively larger angles, contribution from the elastic cross section drops sharply, and therefore, becomes completely insignificant for Plastic Ball data at backward angles. Around 20^{o} - 30^{o}, the optical model predicts an oscillatory structure for ^{56}Fe (cf. Fig. 2.31 : panel a), which is not evident from the data. In this region and further backward non-elastic channels start dominating over the elastic one.

Second, the INC model calculations are, more or less, in good agreement with the experiment. Particularly, for ^{56}Fe data the INC calculation accounts well for the backward-angle cross section values. However, there exist some overestimations, at most by a factor of two to three, for some experimental points at 91^{o} - 120^{o}. But at the most backward angles, the calculation smoothly converges with the experimental values. The most noticeable feature of these calculations is that for forward angles they are reasonably in good agreement with the data, since the elastic scattering contribution dominates in this region. The disagreement between INC model and the experiment for the backward angles is not expected as is reported in Referencc [Cug02]. For the heavier targets, like ^{238}U, its general pattern in our calculations indicates that proton emission is too much forward peaked, which translates into an overestimation of the differential cross-section values. This discrepancy should not be overemphasized because of the fact that the INC model, which assumes mean-field properties of nuclei to be dominant, can have problems in describing deformed nuclei. This model assumes spherical nuclei. Although the nuclei considered here are known to be spherical in nature, except ^{238}U, a co-existence of deformation degrees of freedom in spherical nuclei might result in deviations from the results predicted by INC. The same remark should probably be made for the events where the multiplicity is equal to four or more. These events are rare and the results obtained with the INC model are possibly underestimated.

Conclusions

In short, a study of proton-induced reactions is carried out at KVI with the Plastic Ball + SALAD configuration, measuring the multiplicity and differential cross sections of protons over a broad angular region. The present investigation has resulted in a data set for three nuclei, namely, ^{56}Fe, ^{208}Pb, and ^{238}U at 190 MeV of proton energy, for the first time in this energy range. The measured cross sections span more than three orders of magnitude, thereby, the experimental setup has met the design specifications. The overall agreement with model predictions, both OMP and INC, is reasonably good. In particular, the agreement with the global optical model calculations is impressive. However, a detailed account of all aspects of INC calculations shows that, particularly at backward angles, it disagrees with the experiment by at most a factor of two to three, which triggers a need for improvement of INC model, at least to reproduce the smooth angular distribution pattern over the range investigated. Moreover, this could perhaps shed light on the reasons for the higher multiplicity pattern observed in this experiment.

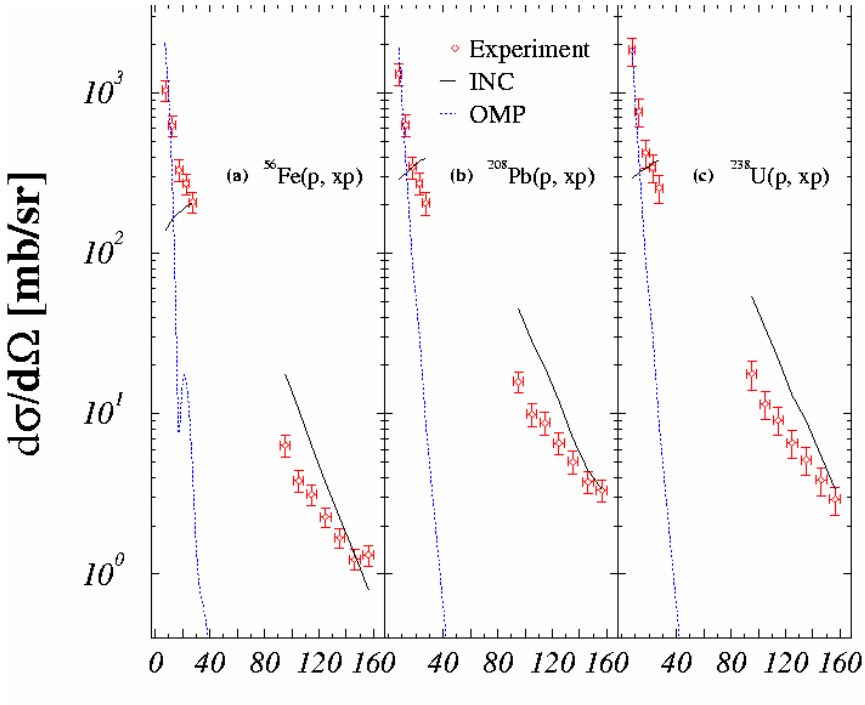

Figure 2.31 : *Differential cross sections of proton scattering from ^{56}Fe (panel a), ^{208}Pb (panel b), and ^{238}U (panel c) at 190 MeV incident proton energy.*

2.4.4. Residual Nuclide Production by proton-induced and neutron-induced reactions

This part of the HINDAS project deals with the investigation of residual nuclide production by proton-induced reactions for energies up to 2.6 GeV and by neutron-induced reactions up to 180 MeV. In this chapter, only the results below 200 MeV will be discussed. Proton-irradiation experiments were performed at PSI, neutron-irradiations at UCL and TSL. Targets irradiated previously at TSL and Saturne were investigated using accelerator mass spectrometry (AMS) at ETH Hönggerberg and rare gas mass spectrometry at ETH Zurich. Further, this work includes measurements of fission cross sections of ^{238}U, ^{235}U, ^{209}Bi, and ^{nat}Pb for energies from 19 MeV to 200 MeV. The experiments for these measurements were performed at UCL and NAC.

(a) Residual Nuclide Production by proton-induced reactions

For proton-induced reactions, the efforts of the HINDAS project aimed to further developing and completing the cross section database which was established by our collaboration in recent years; [MIC97] and references therein. During the HINDAS project the data base was extended to the heavy target elements Ta, W, Pb, and Bi [GLO01, MIC02, MIA02]. Further, about 560 new cross sections for the production of 19 radionuclides from the target element iron have been measured from thresholds up to 2.6 GeV. For the target element lead a comprehensive set of excitation functions published recently [GLO01] was completed by AMS-measurements of cross sections for the production of the long-lived radionuclides ^{10}Be, ^{36}Cl, and ^{129}I and by mass spectrometric measurements of for stable and radioactive rare gas isotopes of He, Ne, Ar, Kr, and Xe. Irradiation experiments with natural uranium were performed at the injector cyclotron at PSI using the stacked-foil technique and subsequent gamma-spectrometry. About 400 cross sections for the production of 18 radionuclides for energies from 21 MeV to 69 MeV were measured.

These investigations are complimentary to those using inverse kinematics where the primary residuals can be studied. While inverse kinematics allows to study in detail the isobaric and isotopic production cross sections at certain energy points, the classical kinematics allows studying the energy dependence from thresholds up to the highest energies which are 2.6 GeV for proton-induced reactions of this work.

All these data allow for stringent tests of nuclear models and codes when calculating cross sections for residual nuclide production from thresholds up to 2.6 GeV. The new codes are the TALYS code for energies up to about 200 MeV and the INCL4+ABLA code for higher energies. In this chapter, only the comparison with TALYS will be discussed. Comprehensive tests of the new codes, TALYS and INCL4+ABLA, for Fe, W, Ta, Pb, Bi, and U for energies from thresholds up to 2.6 GeV are underway. Fig 2.32 gives an example of an excitation for the production of $^{52m+g}$Mn from iron.

For proton-induced reactions on uranium, we measured cross sections for the production of ^{91}Y, ^{95}Zr (Fig. 2.32), ^{95m}Nb ^{99}Mo, ^{103}Ru, ^{112}Pd, ^{115}Cd, ^{124}Sb, ^{126}Sb, ^{127}Sb, ^{132}Te, ^{131}I, ^{134}Cs (Fig. A.72), ^{136}Cs, ^{137}Cs, ^{140}Ba, ^{141}Ce, ^{144}Ce, ^{147}Nd, and ^{238}Np from natural uranium for energies between 21 MeV and 69 MeV. The new experimental results were compared with model calculations using the TALYS code. There were not too many cross sections for the proton-induced production of residual nuclides from uranium available in literature. Moreover, they were mostly old and neither systematic nor comprehensive with respect to the product nuclide and energy coverage. To improve this situation, further collaborations were initiated during the HINDAS project.
As an example for the new low-energy results we use ^{95}Zr (Fig. 2.33) where only one earlier measurement existed for energies up to 300 MeV. The TALYS calculations are in excellent agreement with our measurements and with the only earlier data point by Yokoyama [YOK96] at lower energies. The agreement between theory and experiment seen in Fig. 2.33 is typical for all product nuclides with masses up to 115.

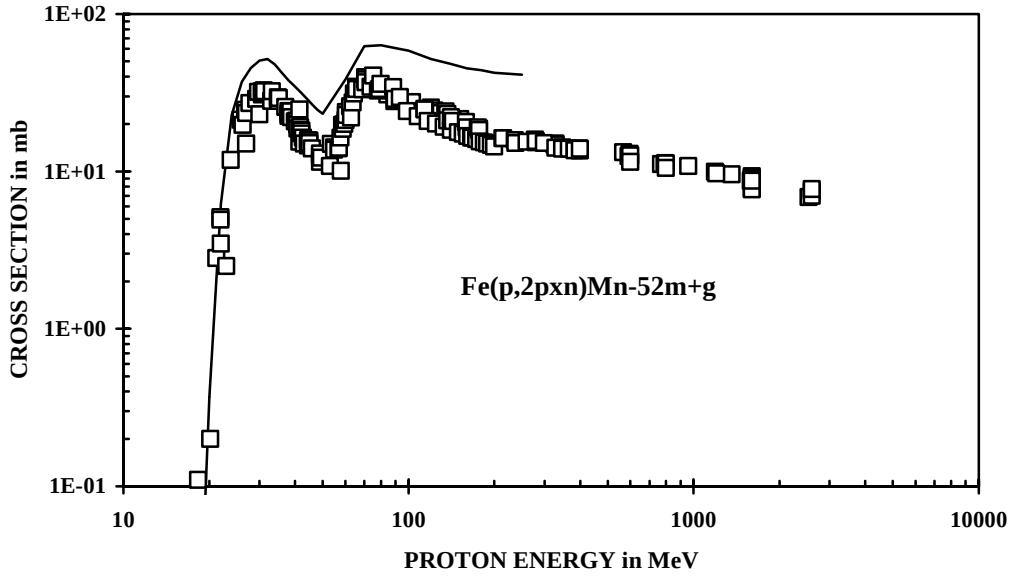

Figure 2.32 *: Comparison of experimental cross sections from this work and previous work of our group for the reaction ^{nat}Fe(p,2pxn)$^{52m+g}$Mn with theoretical ones calculated by the TALYS code.*

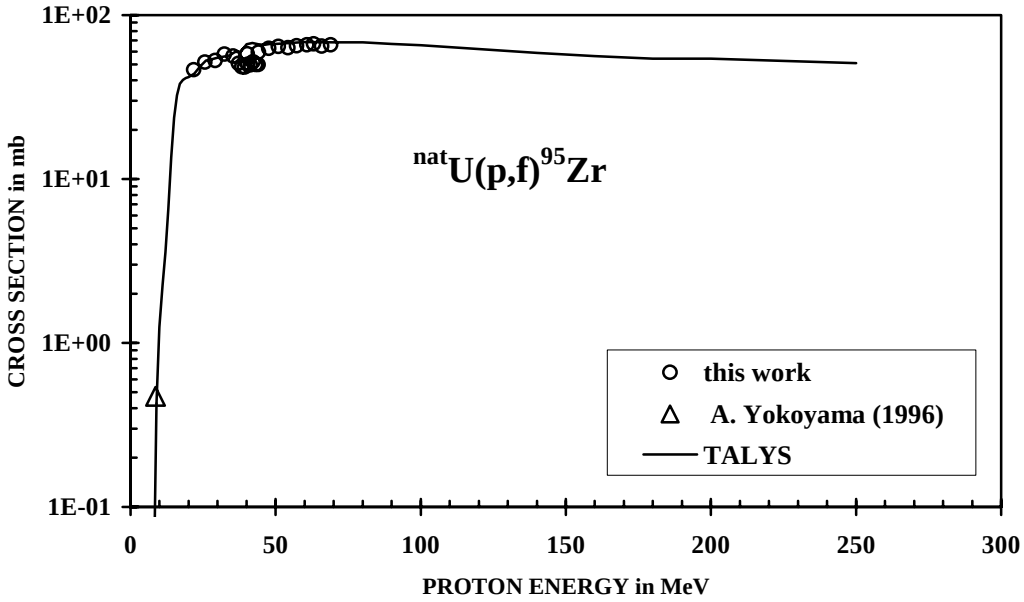

Figure 2.33 *: Comparison of experimental cross sections from this work and from Yokoyama [YOK96] with theoretical ones calculated by the TALYS code for the cumulative production of ^{95}Zr in proton-induced fission of natural uranium.*

Due to the efforts of the HINDAS project there now exists a comprehensive and consistent database of cross sections for the production of residual nuclides by proton-induced reactions on the heavy target elements Ta, W, Pb, and Bi from thresholds up to 2.6 GeV. Some examples for the target element bismuth are given in Figs. 2.34 and 2.35. This database allows validating the newly developed codes TALYS and INCL4+ABLA by systematic comparisons.

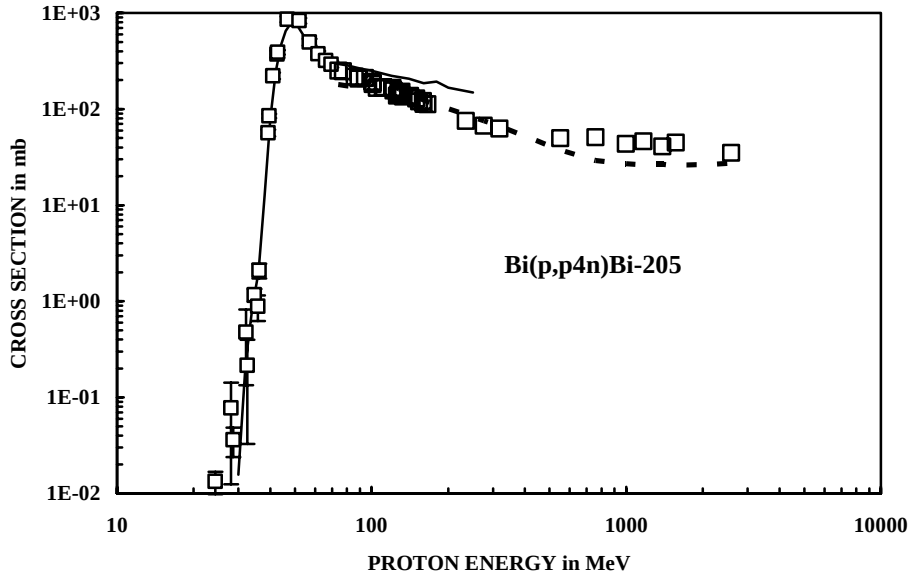

Figure 2.34 *: Production of ^{205}Bi from bismuth by proton-induced reactions. Comparison of experimental results (squares) with theoretical cross sections calculated with INCL4+ABLA (broken line) and TALYS (solid line).*

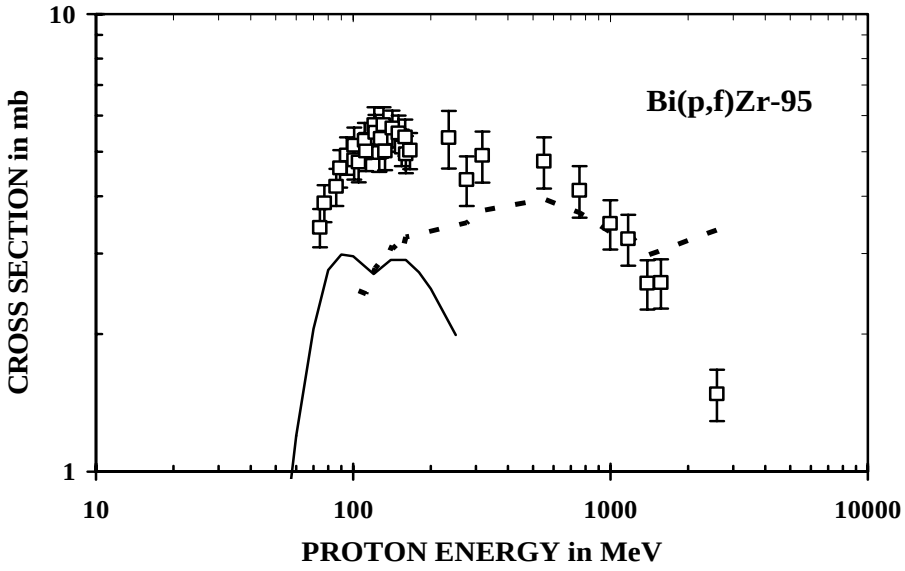

Fig. 2.35 *: Production of ^{95}Zr from bismuth by proton-induced reactions. Comparison of experimental results (squares) with theoretical cross sections calculated with INCL4+ABLA (broken line) and TALYS (solid line).*

(b) Residual nuclide production by neutron-induced reactions

Within the HINDAS project, activation experiments with quasi mono-energetic neutrons produced by the ^{7}Li(p,n)^{7}Be reaction were performed at the neutron beam lines at TSL [CON90, NEU98] and UCL [SCH99] in order to determine excitation functions for the production of residual radionuclides from a variety of target elements up to 175 MeV.

A total of 10 activation experiments covered proton energies of 36.4, 48.5, and 62.9 MeV at the UCL and of 69.1, 76.4, 98.5, 136.7, 148.4, 162.7 and 178.8 MeV at TSL. The target elements C, N, O, Mg, Al, Si, Fe, Co, Ni, Cu, Ag, Te, Pb, and U were irradiated with the highest beam currents available. Residual radionuclides with half-lives between 20 min and 5 years were measured by off-line γ-spectrometry. In spite of the long irradiation times and high beam currents applied, the measurement of the irradiated targets is a low-count-rate problem and requires close-to-detector geometries. This results in particular problems with respect to efficiency determination and to necessary corrections for systematic coincidence. In addition, γ-self-absorption in the targets has to be corrected for. Therefore, a new method for the determination of detector efficiencies was developed which takes into account all these effects simultaneously [GLA02].

The γ-spectrometry of the activated target foils yields activities proportional to production rates P in s^{-1} g^{-1}. A production rate P of a nuclide produced is given by:

$$P = \frac{N_L}{A_T} \int \sigma(E) \cdot J(E)\, \mathrm{d}E \quad \text{with} \quad J(E) = \frac{\mathrm{d}^2 \Phi(E)}{\mathrm{d}E\, \mathrm{d}t} \tag{1}$$

with N_L being Avogadro's number and A_T the atomic mass of target element. $\sigma(E)$ are the neutron cross sections, $J(E)$ the spectral neutron flux densities and $\Phi(E)$ the neutron fluences. The integral is taken over all neutron energies E.

Information on the energy dependence of the neutron spectra in the targets was obtained by modeling the neutron spectra by Monte Carlo techniques using the LAHET/MCNP code

system [PRA89, BRI97]. These transport calculations started either from the experimentally determined neutron spectra (at UCL) or from the systematics of experimentally measured neutron emission spectra of the ^{7}Li(p,n)-reaction [PRO02] (at TSL). The calculations described the transport of the neutrons into the target stacks and into the individual targets as well the production and transport of secondary particles inside the massive target stacks which cannot be neglected [KOL03].

Cross sections cannot be directly calculated from these response integrals since the neutrons used are just "quasi mono-energetic" with only about 30 to 50% of the neutrons in the high-energy peak with a width of a few MeV. The neutron cross sections $\sigma(E)$ have to be extracted from production rates P_i (i = 1,..., n) determined in a series of n irradiation experiments with different neutron energies by iterative procedures [KIM99] or by unfolding using the STAYS´L formalism [PER77, MAT79]. The unfolding needs a guess function to start with and which in our case was calculated using the ALIPPE code [SHU95]. But, the unfolding procedure is rather independent from the guess functions. The feasibility of the unfolding method was successfully demonstrated in the analysis of thin-target and thick-target data [SCH92, NEU99, LEY00]. The advantage of this evaluation method is that it gives as results complete excitation functions together with their uncertainties and that evaluations can be repeated with improvements of the excitation functions as soon as new experimental information becomes available. In those few cases where the new data can be compared with the results of earlier work our excitation functions are in excellent agreement with the earlier data; e.g. for ^{nat}Cu(n,2pXn)^{56}Co where data were reported earlier by Kim et al. [KIM99].
The importance to distinguish proton- and neutron-induced reactions in residual nuclide production is emphasized in Fig. 2.36.

The excitation functions for the proton- and neutron-induced production mostly differ strongly with respect to shapes and absolute values. These figures also demonstrate the partially severe deviations of the final neutron excitation functions from the theoretical guess functions.

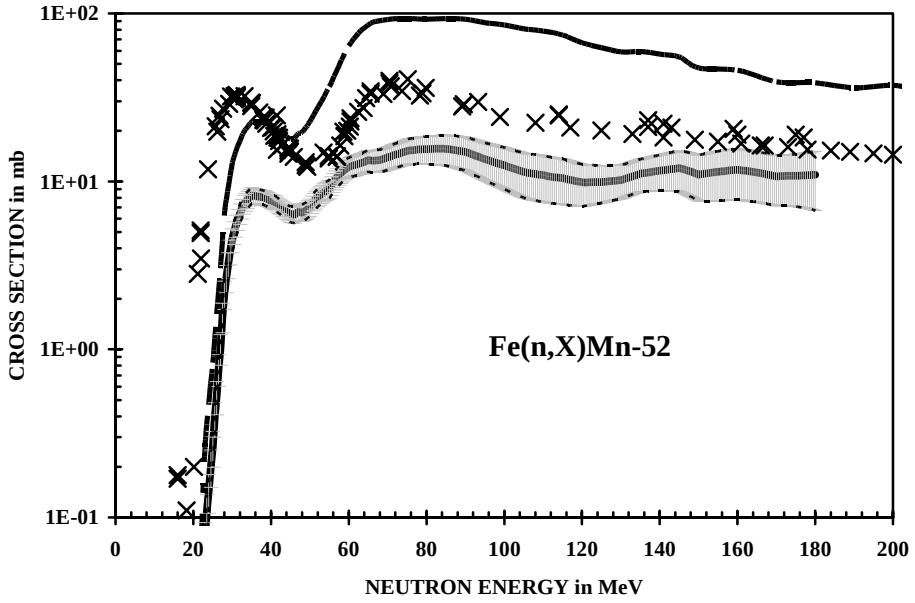

Figure 2.36 : *: Unfolded cross sections (solid line) with their uncertainties (shaded area) for the reaction ^{nat}Fe(n,pXn)$^{52m+g}$Mn compared with the cross sections from [MIC97] and this work for the production of $^{52m+g}$Mn by proton-induced reactions via ^{nat}Fe(p,2pXn)$^{52m+g}$Mn (crosses). The broken line is the guess function calculated by ALIPPE.*

(c) Measurement of ^{238}U, ^{235}U, ^{209}Bi, and ^{nat}Pb fission cross sections using quasi-monoenergetic neutrons with energies from 19 MeV to 200 MeV

Fission of pre-actinide and actinide nuclei induced by high-energy neutrons will contribute significantly to neutron multiplication in a future accelerator-driven subcritical demo reactor, both in the target material (Pb, Bi) and in fuel elements (U, Pu and minor actinides) located close to the target region. In neutron metrology, the fission cross sections for ^{235}U, ^{238}U, and ^{209}Bi are also used as secondary standards. Despite their importance, the experimental data base for these cross sections is rather scarce at neutron energies above 20 MeV. Out of the experimental cross section available from EXFOR or as unpublished data, only the comprehensive data set of *Lisowski et al.* [LIS91] for ^{235}U(n,f) and some data for ^{238}U(n,f) by *Eismont et al*. [EIS96] were determined relative to the differential n-p scattering cross section which is the primary reference for cross section measurements. All other experiments were carried out relative to other standards, mostly fission cross sections themselves.

This is why measurements of neutron induced fission cross sections relative to n-p scattering were included in the HINDAS project to extend the experimental data base. The measurements at neutron energies below 60 MeV were carried out at the neutron beam facilities of the Université Catholique de Louvain (UCL) in Louvain-la-Neuve/Belgium. Above 60 MeV the neutron beam facility of the former National Accelerator Laboratory (NAC) in Cape Town/South Africa, now renamed the iThemba Laboratory for Accelerator Based Sciences (iTL), was used. The quasi-monoenergetic collimated neutron beams available at these facilities are produced using the ^{7}Li(p,n) reaction. Hence the same techniques for beam specification could be used as for the experiments on the production of residual nuclei mentioned above. Actually, the same beam time was used for both experiments for neutron energies up to 60 MeV. In addition, a measurement at 19 MeV was carried out at the PTB neutron beam facility in Braunschweig/Germany using monoenergetic neutrons produced with the T(d,n) reaction.

Parallel plate fission ionization chambers (PPFC) equipped with thin fissile layers of ^{235}U, ^{238}U, ^{209}Bi and ^{nat}Pb were used for the measurements of the fission cross sections. The latter two PPFC's were especially manufactured within the HINDAS project for the measurements at higher neutron energies while the two U-PPFC's were already used in several international intercomparisons at neutron energies below 20 MeV. Due to the small rise time of the PPFC signals, the time-of-flight (TOF) technique could be applied to separate fission events caused by neutron from the high-energy peak from those caused by continuum neutrons. The efficiency of the PPFC's for detection of fission fragments is close to unity. It was calculated using a dedicated Monte Carlo program which included the effects of anisotropic fragment emission and incomplete transfer of linear momentum to the fragments. The experimental data were corrected for dead time, loss of events with pulse-heights below threshold, contributions from fission events caused by residual neutrons from the low-energy continuum, background from charged particles produced in the electrodes of the PPFC's and neutron absorption and multiplication in the electrodes. The latter correction was calculated using MCNPX [HEN03] and caused a decrease of the ^{235}U(n,f) cross section by up to 6% while the effect on the ^{238}U(n,f) cross section is much smaller. This is because the ^{235}U(n,f) cross section is finite in the energy range of evaporation neutrons while the ^{238}U(n,f) has a threshold at about 1 MeV.

Fig. 2.37 shows the results for ^{235}U(n,f) and ^{238}U(n,f) together with the data set recommended by INDC [CAR97] for neutron energies above 20 MeV and with the ENDF-B/VI data below 20 MeV. In addition, a data set [NEL98] resulting from the measurements of *Lisowski et al.* [LIS91] is shown. While the data for ^{235}U are consistent with the recommended data, the cross

sections for ^{238}U(n,f) are about 7% higher in the energy range between 30 MeV and 60 MeV. The deviating data points at 100 MeV are probably due to an experimental normalization problem. It is foreseen that these measurements will be repeated in the near future.

To summarize, the measurements carried out within the HINDAS project have led to an extension of the experimental data base for fission cross sections for materials relevant for neutron metrology as well as accelerator driven technologies. While the available amount of data for the potential spallation target materials Bi and Pb, either in unpublished form or from EXFOR, could be considered satisfactory, new measurements for the metrologically relevant U(n,f) cross sections relative to n-p scattering and with smaller systematic uncertainties are still highly desirable.

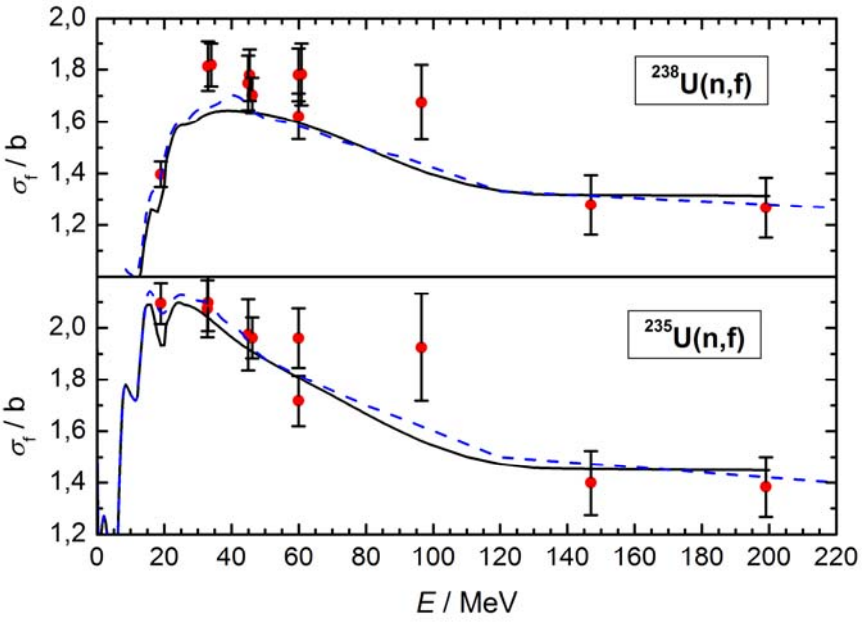

Figure 2.37 *: Experimental fission cross sections for ^{238}U (closed circles, upper panel) and ^{235}U (closed circles, lower panel). The black lines show the INDC data [CAR97] (neutron energies above 20 MeV) and the ENDF-B/VI data (below 20 MeV). The dashed blue lines represent data sets [NEL98] resulting from the measurements of* Lisowski et al. *[LIS91]. The deviation of the data point at 100 MeV is very likely due to an experimental normalization problem*

2.5. Nuclear data libraries

The evaluated data files for the Fe- and Pb-isotopes are based primarily on nuclear model calculations by the TALYS code, version 0.56. The nuclear model parameters of TALYS have been adjusted to reproduce the existing experimental data, from HINDAS and other resources. The resulting data files provide a complete representation of nuclear data needed for transport, damage, heating, radioactivity, and shielding applications over the incident neutron energy range from 1.0E-11 to 200 MeV.

Though the HINDAS project is meant to deal with energies in excess of 20 MeV, completely revised data files were created, including low energies. Each file is part of a larger collection of isotopic evaluations, all created by running TALYS with input parameters that do not or slightly deviate from the default values. The mutual quality of these isotopic evaluations is

thus relatively consistent. The same set of nuclear models is used and, equally important, the same ENDF-6 formatting procedures for each isotope. We have intended to make these evaluations complete in its description of reaction channels, and use a method to store data that resembles that of various recent Los Alamos evaluations.

For reactions and energy ranges where TALYS is not used, usually the resonance range or low energy total cross sections, because e.g. the directly available experimental data is of better quality, we have adopted the best possible data from an existing library. All transport data for particles, photons and residual nuclides are filed using a combination of MF1,2,3,4 and 6. This includes cross sections, angular distributions, double-differential spectra, discrete and continuum photon production cross sections, and residual production (activation) cross sections. Moreover, isomeric production data are stored in MF8 and MF10. These evaluations can thus be used as both transport and activation libraries. The data files have been created automatically using the ENDF-6 format generator TEFAL, written at NRG Petten.

For the Fe- and Pb-isotopes that were evaluated, the following output of TALYS is stored in the data files:

- Total, elastic and non-elastic cross sections
- Elastic scattering angular distributions
- Inelastic cross sections to discrete states
- Inelastic scattering angular distributions to discrete states
- Exclusive channel cross sections, e.g. (n,g), (n,2n), (n,np), etc.
- Exclusive channel energy spectra
- Exclusive channel double-differential spectra
- Exclusive gamma production for discrete states and continuum
- Isomeric and ground state cross sections
- Residual production cross sections
- Total particle cross sections, e.g. (n,xn), (n,xp), etc.
- Total particle energy spectra
- Total particle double-differential spectra

We will now give a more detailed description of the used nuclear models, their comparison with experimental data, the ENDF-6 formatting techniques, and finally a comparison with integral experiments.

2.5.1. Used nuclear models

Optical model:

All optical model calculations are performed by ECIS-97 [ray94], in TALYS used as a subroutine. The default optical model potentials (OMP) used are the local and global parameterizations of Koning and Delaroche [kon03]. These are phenomenological OMPs for neutrons and protons which in principle are valid over the 1 keV - 200 MeV energy range, though the low energy boundary of validity may differ from nucleus to nucleus (e.g. for the total cross sections, experimental data are included directly in the file for energies below that). Solving the Schroedinger equation with this OMP yields the total cross section, the shape-elastic cross section, the shape-elastic angular distribution, the wave functions for the direct reaction cross sections (see below), the transmission coefficients for the compound nucleus model (see below) and the reaction cross sections for the pre-equilibrium model (see below).For neutrons and protons, the used parameterization is given in Eq. (7) of [kon03]. To calculate the transmission coefficients and reaction cross sections for deuterons, tritons,

helions and alpha particles, weuse OMPs that are directly derived from our nucleon potentials using Watanabe's folding approach [mad88].

Direct reactions:

The built-in ECIS-97 is used for coupled-channels or DWBA calculations for rotational or vibrational nuclides. For the nuclides under consideration, DWBA was used to compute the direct cross sections to several low-lying discrete levels. In addition, a macroscopic, phenomenological model to describe giant resonances in the inelastic channel is used. For each multipolarity an energy weighted sum rule applies and a DWBA calculation with ECIS-97 is performed for each giant resonance state and spread the cross section over the continuum with a Gaussian distribution.

Compound nucleus:

For binary compound nucleus reactions we use the model of Moldauer [mol80], i.e. the Hauser-Feshbach model [hau52] corrected for width fluctuations. The transmission coefficients have been generated with the aforementioned OMPs and the full j,l-dependence of the transmission coefficients in the Hauser-Feshbach model is used. For each nucleus that can be reached through a binary reaction, several discrete levels and a continuum described by level densities are included simultaneously as competing channels.
The compound nucleus angular distribution is calculated with the Blatt-Biedenharn formalism [bla52], leading to compound nucleus Legendre coefficients that are added to their direct counterparts. For incident energies above the neutron binding energy, the width fluctuation correction is automatically disabled. For multiple compound emission, i.e. emitted particles after the binary emission, we use the Hauser-Feshbach model. Again, for each nucleus several discrete states are included as well as a continuum described by level densities. Multiple compound emission is continued until all reaction channels are closed and all residual nuclides end up in the ground state or an isomer.
For the level density, we take the composite formula proposed by Gilbert and Cameron [gil65], consisting of a constant temperature law at low energies and a Fermi gas expression at high energies. For the level density parameter a we use the energy dependent expression proposed by Ignatyuk [ign75] to take into account the damping of shell effects at high excitation energy. We have obtained the parameters for the Ignatyuk formula from a simultaneous fit to all experimental D_0 values as present in the RIPL library.

Gamma-ray transmission coefficients are generated with the Kopecky-Uhl generalized Lorentzian for strength functions [kop90], with giant dipole resonance parameters taken from the RIPL library [rip98], and normalized with experimental radiative widths [gar84].

Pre-equilibrium reactions:

For pre-equilibrium reactions, which become important for incident energies above about 10 MeV, we use the two-component exciton model [kon04b], in which the neutron or proton types of particles and holes are followed throughout the reaction. For energies above 20 MeV, multiple pre-equilibrium emission up to any order of particle emission was included in the calculations.

For deuterons, tritons, helions and alpha-particles, an extra contribution was added from the pick/up and knock-out reaction model by Kalbach [kal01].
For photons, the model of Akkermans and Gruppelaar [akk85] was applied, to simulate the direct and semi-direct capture processes.

The angular distribution systematics by Kalbach [kal88] were used to describe the angular distributions for all continuum particles.

2.5.2. Example of comparison with experiment: Pb-208

The evaluation was performed simultaneously with other adjacent isotopes, both for incident neutrons and protons. This enables, when compared with a single-isotope effort, to put stronger constraints on the produced calculated data, i.e. a globally good comparison between TALYS and experimental data is requested for all isotopes at the same time, while nucleus-specific input parameters are consistently used for all isotopes. Also, experimental data that is not available for the isotope under study may be present, and tested, for adjacent nuclides or for other projectiles. Examples are the (p,xn)....(p,xa) spectra for Pb-208 and Pb-nat and the (n,xn) excitation functions up to 200 MeV for Bi-209. A similar performance is then expected for the present nucleus.

Total and reaction cross sections and elastic scattering

The spherical OMP was tested against experimental data [Car91, Fow62, Fos71, Fin93]. Consult [Kon03] for the complete experimental database of elastic scattering angular distributions and for a comparison of calculations and measurements over the whole energy range. In addition to that work, the recent experiment for 96 MeV neutron elastic scattering [klu03], from the HINDAS project, was used to validate the model at higher energies.

Inelastic cross sections

For the total inelastic cross section, the calculated results were compared with two available experimental data sets [dic77, sim93]. For inelastic scattering to the first excited state, the calculations have been tested against the available experimental data sets [tow63,alm74]. They are also validated, for the first few MeV, with experimental data on the specific gamma ray, from the first level to the ground state, produced by the (n,n') reaction [von94]. For inelastic scattering to the second and third state, the calculations have also been tested against the available experimental data set [tow63]. No further renormalization was necessary to describe the experiments. Inelastic scattering angular distributions for the first 3- and 5- states were tested against the available data at 11 MeV [bai77] (reasonable fit, underestimation at forward angles), 22 MeV [fin84] (good fit), and 26 MeV [bai77] (good fit).

Other partial cross sections

(n,gamma):

The calculated capture cross section is renormalized, by overruling the default renormalization to the s-wave strength function, to the available experimental data, all taken from the EXFOR database. A normalization factor of 0.35 was used. Further, the E1 giant resonance energy was changed to 12 MeV to better describe the direct/semi-direct peak around an incident energy of 14 MeV. The pre-equilibrium gamma cross section was adjusted to the data by multiplying the calculated result by a factor of 2.2.

(n,2n):

The calculated results have been validated with the experimental (n,2n) cross section of Frehaut [fre80], taking into account a necessary 10-15 % renormalization of the experimental data that was recently reported [ber03]. Independent tests come from specific gamma rays

produced by the (n,2n) reaction [von94], and the simultaneous description of the differential energy spectra at 14 MeV [sch97]. For this reason, the 14 MeV value of Simakov [sim93] has not been used to guide our (n,2n) cross section.

(n,3n):

Validated with experimental data on a specific gamma ray produced by the (n,3n) reaction [von94].

(n,p):

Old [bas68] and new [cos00, plo02] experimental data for (n,p) were used to validate the calculation. Above 30 MeV, the calculation overestimates the data of [cos00] by a factor of 2. Since this only amounts to a few millibarns, no attempt was made to describe the data by adjusting parameters.

Particle spectra

For Pb-208, no adjustment of the default matrix element parameterization of [kon04b] for pre-equilibrium reactions was needed, to describe the aforementioned cross sections and emission spectra [sch97]. For high-energy neutron and charged particle spectra, the average quality is likewise determined by the pre-equilibrium model and its global parameterization. Two experiments from the HINDAS project, for neutron induced reaction spectra at 63 MeV [ker02] and 96 MeV [lec03], have enabled us to better constrain the results, through the aforementioned matrix element, for particle yields and double-differential spectra for all ejectiles up to alpha particles.

2.5.3. ENDF-6 data file information

A short description of the directory of the data file for Pb-208 follows. This gives an impression of the techniques to store the data.

For the lowest energies, Reich-Moore resolved resonance parameters covering the energy range 1.0e-5 eV to 1 MeV were adopted from the ENDF/B-VI.8 evaluation. They are based on [hor86] and [lar89] (>70 keV), and [mug81] (<70 keV).

Below 6.5 MeV, total cross sections are adopted from ENDF/B-VI.8. The experimental total cross sections from [hor86] are used above the resonance range (> 1 MeV). The rest of the data file is completely generated with TALYS.

For energies above 20 MeV, MT5 contains the non-elastic cross section. Using the relative yields of MF6/MT5, the particle production cross sections can be recovered.

For elastic scattering angular distributions at incident energies below 20 MeV, the Legendre coefficients are given on a sufficiently precise energy grid. They are a sum of calculated Legendre coefficients for compound nucleus and shape-elastic scattering. For incident energies above 20 MeV, relative angular distributions are tabulated on an angular grid.

File checking and processing

All data files have been checked successfully by the BNL checking codes CHECKR-6.12, FIZCON-6.12 and PSYCHE-6.12 [dun01] and have been processed successfully into an MCNP library by the processing code NJOY99.81 [mac00].

2.5.4. Validation of the data files

Once processed into an application library, our evaluated file can be used in applied calculations. The lack of relevant high-energy integral experiments poses a problem here. All we can do is search for integral experiments in which a sizeable amount of lead is present and presume its relevance for ADS calculations. Our files have been used already in ADS calculations, within the MUSE and PDS-XADS project, though these are obviously of a theoretical nature. A comparison with other methods and libraries can however be provided, and we will do that here. All our calculations have been performed with the MNCPX transport code from Los Alamos.

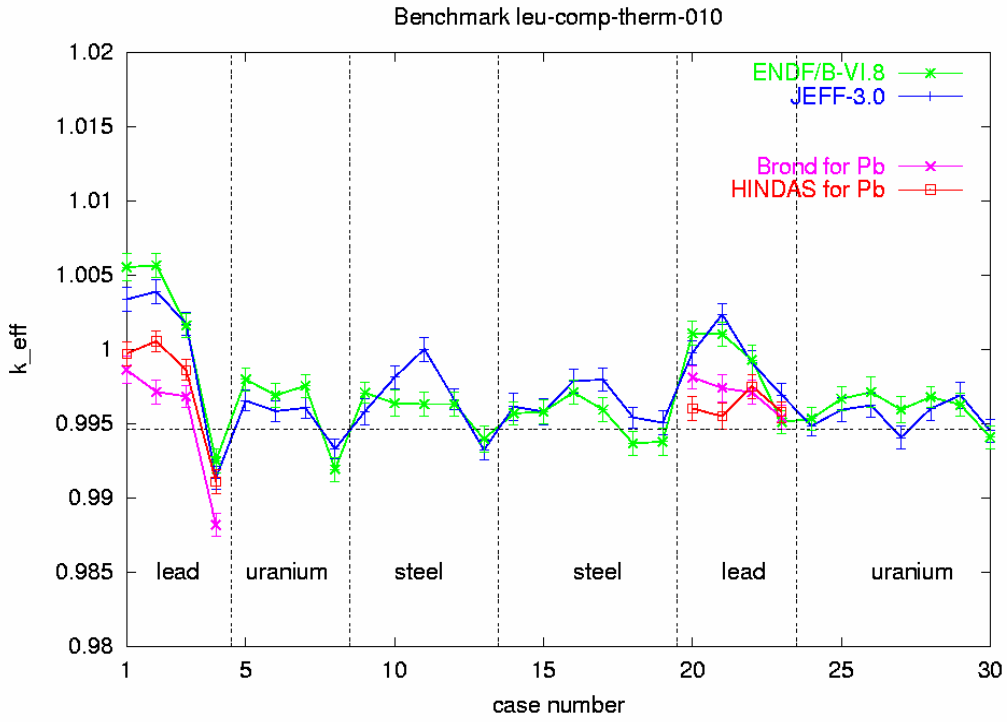

Figure 2.38 : *ICSBEP benchmark LCT-010: Comparison between experiment, HINDAS and other data libraries.*

First, Fig. 2.38 shows a low-enriched uranium compound thermal benchmark from the NEA ICSBEP criticality benchmarks series. Though this shows merely the impact of the new files for low energies, it is already an indication of the effect of the HINDAS library.

In Fig. 2.39 a fusion experiment is shown together with the calculations with various libraries. Since all high-energy neutrons will eventually also pass 14 MeV, it is interesting to note here that the high-energy tail of the spectrum is best described by the HINDAS data library.

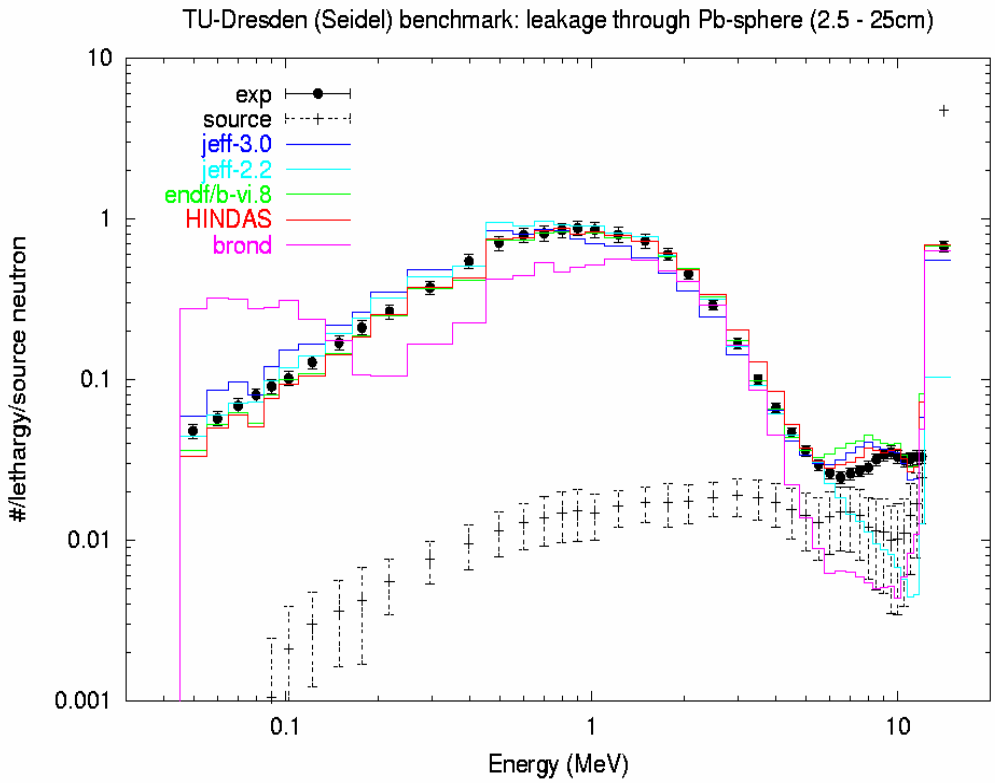

Figure 2.39 :*Fusion source experiment of a Pb sphere. Comparison between experiment HINDAS and other data libraries.*

Fig. 2.40 concerns a simulation of a 150 MeV proton beam on a lead buffer is shown .Both the proton and the neutron HINDAS files are used in this calculation. The spectrum of the total neutron production just outside the lead is calculated for the HINDAS file, the LA150 data file [cha98] and the LAHET intranuclear cascade code. Clearly, the latter deviates from the library approaches.

In summary, new proton and neutron data files from 0 to 200 MeV are constructed. The data present in these libraries are based on consistent model calculations and give a better description of microscopic available data over the whole energy range. Apart from this microscopic validation, several integral benchmarks have proven that the new HINDAS libraries can be used with some confidence over the same energy range. More tests with transmutation-relevant calculations and experiments will reveal whether good is good enough. More precision experiments, especially in the sub-20 MeV area may be necessary for Pb.

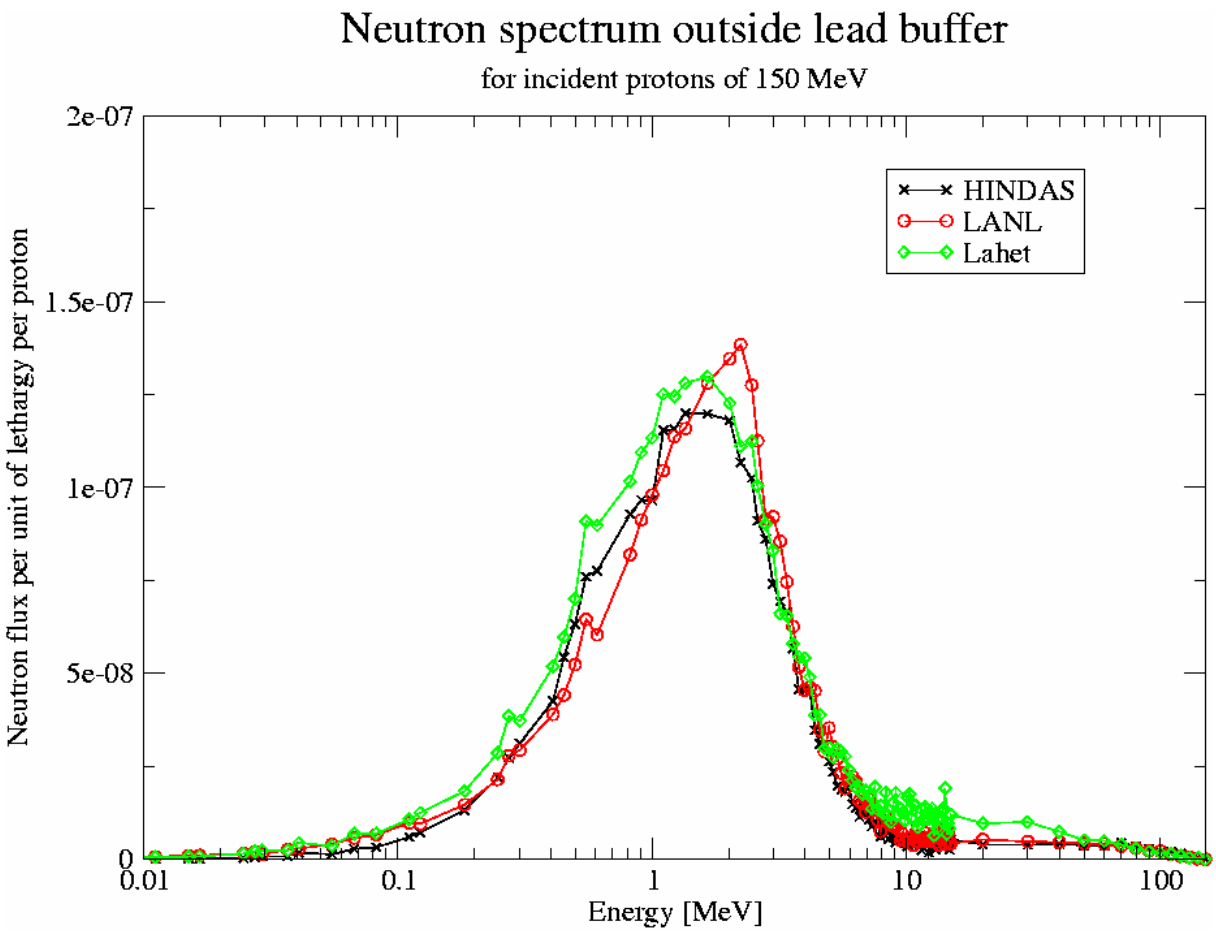

***Figure 2.40**: Neutron spectrum just outside the lead target, calculated with MCNPX. Comparison between HINDAS library, LA150 library and LAHET*

Nevertheless, on the basis of the new HINDAS measurements, the performance of TALYS in describing microscopic data, and the available integral data, we already recommend the HINDAS data files to be the reference libraries for target/coolant analyses in transmutation systems. We wish to mention here that the files for Pb are already used in the other FP5 projects MUSE and PDS-XADS.

3. Experimental and Theoretical Results at High Energies between 200 and 2000 MeV.

3.1. Introduction

3.1.1. General motivations

In an Accelerator-Driven System, high-energy reactions play a major role for the optimization of the neutron-source performance and assessment of induced radioactivity and material damage in the spallation module. They are induced essentially by the primary proton beam in the target and in the window separating the accelerator vacuum and the target, but also by a few energetic secondary neutrons that can reach the target surrounding.

The source neutrons that will drive the sub-critical reactor are produced by the spallation reactions then multiplied, first by (n,xn) intermediate- and low-energy reactions in the target, and next, by fission in the fissile material. The precise knowledge of the number of neutrons produced in high-energy reactions is therefore important, as are their energy and spatial distributions for the detailed prediction of material damage and thermo-hydraulics in the target and sub-critical core. A few high-energy neutrons also escape the system and have to be taken into account for the shielding of the facility.

Light charged particles (mainly protons and alphas) are produced in spallation reactions with rates much larger than usual in reactors. They will be responsible for radiation damage (as atom displacements) in solid materials and hydrogen and helium bubble formation that can lead to swelling and embrittlement of structural materials. This is particularly important for the prediction of the lifetime of the window.

A large variety of isotopes is produced by spallation reactions. Many of them are radioactive and could be a source of concern for radioprotection. For instance, it is important to know the time evolution of the target activity to determine when it is possible to approach it for maintenance or unplanned intervention. Long-lived isotopes are produced which will be responsible for the long-term radiotoxicity of the target after operation. In addition, the chemical modifications due to the build-up of impurities could lead to corrosion problems on the structure materials in contact with the liquid metal of the target or loss of cohesion of alloys in the window. The recoil energy of the spallation products, which will induce heat deposition and atom displacements, in particular in the window, has also to be known.

For the detailed design of a future ADS, all these quantities, specific for high-energy reactions, will have to be reliably predicted in order to choose the best and most economic configuration and materials, which, in addition, satisfy all the safety regulations. Simulation code packages exist, which make it possible for spallation source designers to predict any of the above-mentioned quantities. They generally consist of the coupling of a high-energy transport code, which handles the transport and interactions of the incoming proton and all the produced particles down to 200 MeV, and a low-energy neutron transport code utilizing evaluated nuclear-data files (which are the subject of the intermediate-energy part of HINDAS) below. In the high-energy transport codes, the elementary cross-sections are calculated by nuclear physics models. It is therefore crucial that the nuclear models be reliable enough, that is, provide correct elementary cross-sections validated on an extensive set of experimental data.

3.1.2. The status before starting the HINDAS project

When the interest for ADS began to raise, several inter-comparisons between high-energy experimental data and nuclear models and codes were performed under the auspices of OECD/NEA [Bla94, Fil95, Mic97b]. The main features that were pointed out were:
- the existence of discrepancies between different sets of experimental data, in particular concerning neutron production
- the general lack of high-quality data above 800 MeV
- the particular lack of experimental data concerning light charged-particle production
- the lack of information on residue production due to the limitation of the experimental techniques to the detection of certain types of isotopes
- the large dispersion between the predictions of the models and codes
- the absence of one model or code able to predict correctly the whole set of available experimental data
- the difficulty to identify how to improve the existing models

This led to the proposal of a series of new experiments initiated in the course of the Concerted Action "Lead for ATD" [Meu00] which preceded the HINDAS project. During this Concerted Action, first results of the study of spallation reactions induced by protons on lead were obtained and innovative experimental methods, as the reverse kinematics technique, were developed. Simultaneously, a work on theoretical models was undertaken. It was shown that a combination of high-quality experimental data regarding all the possible reaction channels could be obtained, which should allow for a better understanding of the physics of spallation reactions and, therefore, an improvement of the physics models.

3.1.3. Objectives of the HINDAS high-energy program

As a step towards the more remote final goal of disposing of a high-energy transport code capable of reliably predicting any quantity related to spallation reactions in ADS, the first objective of HINDAS was to study a limited number of selected key reactions, representative of target (Pb), fuel (U) and structure (Fe) material, in full detail. The second objective was to use these experimental data to benchmark, improve and develop nuclear-reaction codes so that these codes can be used to calculate the reactions occurring in the accelerator-driven system in their full variety. This was realized through the following work:

- Measurements for a few targets (Fe, Pb and U) of experimental data covering all the reaction channels in the whole energy range at the best suited facility
    - Light charged-particle production above 200 MeV at COSY (Jülich)
    - Neutron production (multiplicity distributions and double-differential cross-sections) in thin and thick targets at SATURNE and COSY
    - Residual nuclide production: isotopic distributions in inverse kinematics at GSI and excitation functions measured by γ- and mass spectrometry
- Comparison of the experimental data to nuclear models in order to assess their success and deficiencies
- Improvement of nuclear physics models on the basis of the best possible physics ingredients
- Validation of the models on the new experimental data
- Implementation of the high-energy models into High-Energy Transport Codes
- Assessment of implications of HINDAS results for ADS design.

To achieve those objectives, the work has been divided into three experimental workpackages (WP4 to WP6) and one theoretical workpackage (WP8).

WP4 : Light charged-particle production above 200 MeV

WP5 : Neutron production induced by protons above 200 MeV in thin and thick targets

WP6 : Residual nuclide production above 200 MeV in inverse kinemetic.

WP8 : High energy models and codes.

All along the project, there has been a close collaboration between the workpackages since some of the scientists were involved in several different workpackages and, in particular, between the experimental workpackages and the theoretical one. In the following sections the workpackage WP5, dedicated to neutron production, is presented before WP4, devoted to light charged particles, mainly because historically most of the neutron experiments were done first and some of the physics conclusions drawn from these experiments are used in the analysis of the charged particle workpackage.

3.2. The results obtained in the HINDAS project

3.2.1. Experimental results on neutron production

The goal of the workpackage 5 of HINDAS was to collect both thin- and thick-target data on neutron multiplicities (by the NESSI[1] collaboration) and energy spectra at different angles (measured at SATURNE[2]). The thin-target data served as benchmark data for the improving of high-energy nuclear models: they were first compared with the predictions of the models commonly used within high-energy transport codes in order to assess their deficiencies. Meanwhile, a new set of models was developed in workpackage 8 (see section 2.1) that tried to cure the pointed out deficiencies. These new models were then compared to the neutron data.
Both the NESSI and SATURNE experiment allowed not only for studying the neutron production in thin targets, but also the measurement of neutrons produced in thick targets. In this case the codes have not only to describe the intra-nuclear cascades correctly, but also the propagation of the hadronic showers caused by the reaction products of secondary or higher-order reactions have to be considered. The NESSI thick-target data give direct information on the mean neutron number expected from a spallation target, while SATURNE energy spectra of escaping neutrons are important for shielding. Furthermore, they have been compared also with the old and new models implemented into high energy transport codes, so that their predictability could be estimated.

(a) Thin target data

(i) <u>Double differential cross-sections measured at SATURNE</u>

During the HINDAS project, the neutron production double-differential cross-sections measured at the SATURNE synchrotron induced by 0.8, 1.2 and 1.6GeV protons impinging on different thin targets, among which Fe, Pb and Th [Ler02], were compared to different intra-nuclear cascade models implemented into high-energy transport codes, the Pb data

[1] The NESSI collaboration was constituted from FZJ Jülich, GANIL Caen, HMI Berlin.
[2] The collaboration working at the Laboratoire National SATURNE accelerator in Saclay was joining CEA/Saclay, CEA/Bruyéres-le Châtel, LPC Caen, IPN Orsay, ULB Bruxelles.

[Led99] having already been reported on in the Concerted Action FI4I-CT-98-0017 [Meu00]. The details of the experimental method can be found in [Bor97] and [Mar97]. Actually, the targets were a few centimeter thick but can be considered as thin since the rate of secondary reactions is small enough. In fact, secondary reactions contribute for about 10% to the total neutron production but mainly below 2 MeV, that is, below the detection threshold.

The high energy part of the neutron spectra allows directly probing the INC models. Low energy neutrons, which are the majority of the neutrons produced in spallation reactions, are emitted during the evaporation process. However, their number mainly depends upon the INC stage since the cascade determines the initial excitation energy of the decaying hot residue and, therefore, the number of evaporated particles. Calculations have been done using different INC models implemented into high-energy transport codes (in which the actual thickness and diameter of the targets have been taken into account), using always the same Dresner-Atchison evaporation-fission model with the default parameters.

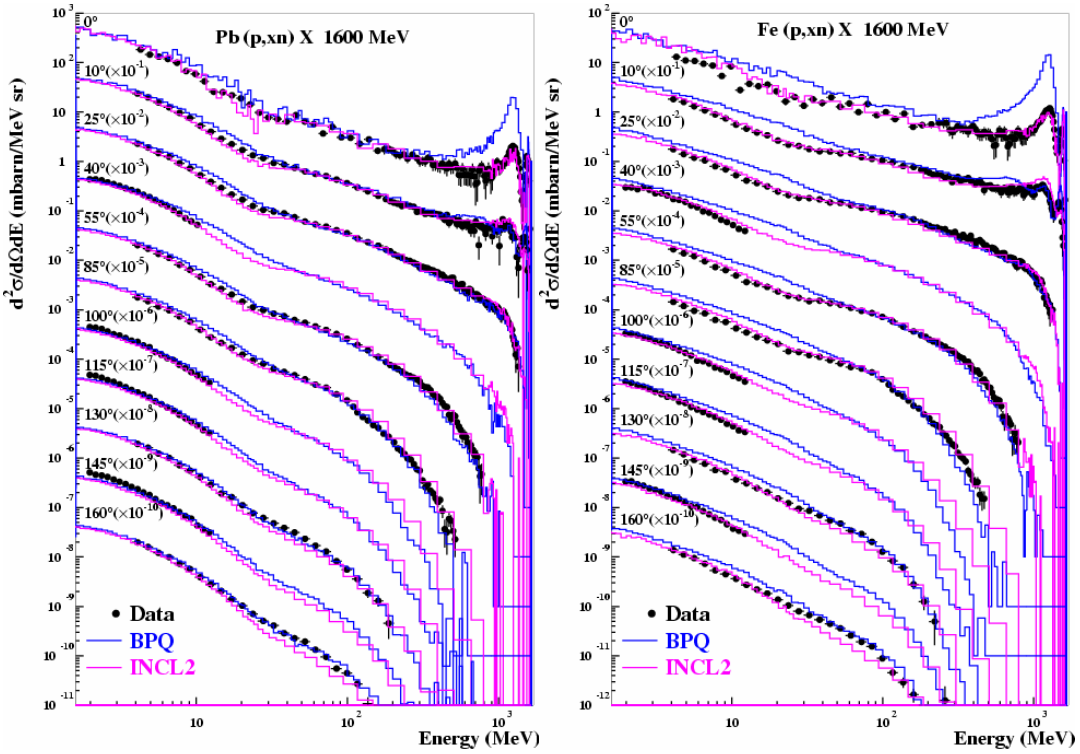

Figure 3.1 : *Experimental p (1600 MeV) + Pb (right) and Fe (left) neutron double-differential cross-sections compared with calculations performed with LAHET using either Bertini plus pre-equilibrium (blue line) or INCL2 (pink line) INC model. From [Ler02].*

In [Led99], for lead, calculations were performed with the TIERCE [Ber96] code system developed at Bruyères-le-Châtel using either the Bertini or the INCL2 model [Cug87, Cug97a] which is the original version of the Liège INC, available before HINDAS. Since the INCL2 model does not predict a correct total reaction cross-section mainly because the diffuseness of the nuclear surface is not taken into account, the INCL2 calculations were renormalized to the experimental total reaction cross-sections. It was shown that, at the three measured energies, the Bertini model was largely overpredicting the experimental data while INCL2 was giving a rather good agreement, well reproducing the shape of the angular and energy spectra of the emitted neutrons. This was ascribed to the higher excitation energy, E*, obtained at the end of the cascade stage with the Bertini calculation than with INCL2. Several

reasons were invoked to explain the difference in E* between both models: first, INCL2 produces more pions than Bertini. Second, it seems that the cut-off energy stopping criterium of Bertini leads to a larger excitation energy than the thermalization time in INCL2. Third, as mentioned in [Led99], the Pauli blocking is treated in a different way. In Bertini, only collisions of nucleons with momentum larger than the Fermi momentum are allowed while, in INCL2, the actual phase space occupation rate is taken into account. This leads to a less stringent condition; therefore more cascade particles can escape and make the energy remaining in the nucleus lower.

In [Ler02] the data at the three energies have been compared with LAHET [Pra89] using the default option, i.e. Bertini followed by pre-equilibrium, referred to as BPQ, and INCL2 calculations. Actually, the pre-equilibrium stage is expected to reduce the excitation energy of the nucleus by emission of intermediate energy particles prior to the evaporation. An example is shown in Fig. 3.1, for the Pb and Fe targets at 1600 MeV. For Pb, both BPQ and INCL2 models were found to give a very good agreement with the data at 800 MeV. At higher energies, BPQ tends to overestimate the production of intermediate energies neutrons, as it can be seen in Fig. B.1. Since the high energy part of the spectra is always rather well reproduced (except at 0°), this seems to point out a wrong dependence of the pre-equilibrium emission with incident energy. The discrepancy at 0° for the peak corresponding to the excitation of the Δ resonance, in the case of BPQ, is due a deficiency of Bertini INC model, already pointed out in [Cug97b] as due to a bad parameterization of the N N → N Δ reaction angular distribution. As the target becomes lighter, the trends are amplified and BPQ begins to also overpredict low energy cross-sections. In fact, it seems difficult to obtain the correct evaporation neutron cross-sections without overestimating intermediate energy, i.e. produced by pre-equilibrium, ones. On the contrary, INCL2 reproduces quite well the data for all the targets at all the energies, proving that the model has correct energy and mass dependences. Only for the Fe targets at very backward angles, the high energy neutron production is underpredicted.

Also available in LAHET or MCNPX [Hug97] is the ISABEL [Yar79, Yar81] model which can be used only up to 1 GeV. Calculations with ISABEL have been performed at 800 MeV for the Pb and Fe targets. A rather good agreement was found, except that they underestimate cross-sections at backward angles in the intermediate energy region, especially for iron.

(ii) Inferred mean neutron multiplicities

Because the double-differential cross-section data nearly cover the full angular range with sufficiently close measurements, it was also possible to infer from the data mean neutron multiplicities per reaction above the energy threshold of the detectors [Ler02]. In all cases, INCL2 was shown to agree with the data within the error bars while BPQ tends to overpredict 2-20 MeV neutron multiplicities, i.e. evaporation neutron production, especially at 1200 and 1600 MeV. For high energy neutrons (above 20 MeV) the sensitivity to the models was found less important because of compensating effects, BPQ predicting more intermediate energy neutrons because of pre-equilibrium while INCL2 spectra often extend to higher energies. However, a significant deviation from the experiment was found at the highest energy for iron with BPQ.

In [Ler02] the mean kinetic energies carried away by the neutrons, extracted from the energy weighted double-differential cross-sections (i.e. multiplied by neutron energy) using the same procedure as for the multiplicities were compared with the calculations. For the 2-20 MeV bin, conclusions similar to what was stated for multiplicities were drawn, reflecting the fact

that ExM_n is governed by M_n as far as the same evaporation model is used in both calculations and thus gives an identical energy spectrum for the low energy neutrons. For the high energy bin, the compensating effect noticed for the multiplicities seems to be even stronger and, regarding the uncertainties, it was not possible to discriminate both models. It is interesting, nevertheless, to remark that these high energy neutrons carry out the major part (from 80% for Th to 98% for Al) of the emitted neutron energy and a large amount (about 30%) of the incident proton energy. In a thick target this will play an important role in the spatial distribution of the energy deposition and particle production.

(iii) Neutron multiplicity distributions measured by the NESSI collaboration

Neutron multiplicity distributions have been measured by the NESSI collaboration on really thin targets [Her01] and, amongst others, for cm thick targets [Fil01, Let00] that are similar to the ones used for double-differential cross-section measurements at SATURNE. However, in the NESSI experiments the measurements of the kinetic energy of the neutrons was not possible since the detector is mainly sensitive to low energy (below 20 MeV) neutrons while at SATURNE the detection threshold was between 2 and 4 MeV.

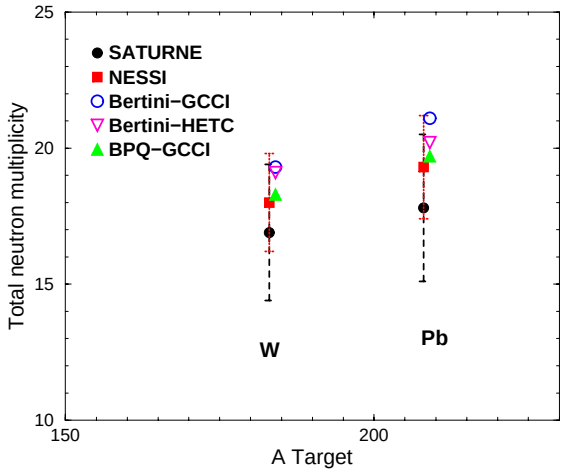

Figure 3.2 : *Experimental mean total neutron multiplicities per primary reaction for 15 cm diameter, 2cm thick Pb and 1 cm thick W targets from SATURNE (extrapolated from 3 to 15 cm diameter) and NESSI (corrected by detector efficiency and secondary reactions in the liquid scintillator) compared to calculations using LAHET with the Bertini INC (without pre-equilibrium) and the GCCI level density parameterization in the Dresner-Atchison evaporation model (open circles), Bertini and the original HETC level density parameterization (open triangles) or adding a pre-equilibrium stage between INC and evaporation with GCCI (full triangles). For the sake of clarity the calculation symbols have been slightly shifted.*

The comparison of the mean neutron multiplicities measured by NESSI and at SATURNE at 1200 MeV on 1 cm (resp. 2cm) thick W and Pb targets was made in [Ler02]. It is not straightforward because of the respective thresholds, efficiencies of the detectors and diameter difference, but, after corrections to make the data comparable, it can be concluded that the two results are compatible within the error bars, as shown in Fig. 3.2. However, there is a tendency for the NESSI multiplicities to be slightly larger that the ones obtained from the double-differential cross-section integration.

Table 3.1 [Fil01] shows the mean neutron multiplicities for 2 cm thick Pb and 1 cm thick W targets measured at different energies and calculated taking into account the detection efficiency. Calculations were done with LAHET and HERMES using in both cases the Bertini INC (without pre-equilibrium) and Dresner-Atchison evaporation-fission model with the original HETC level density parameterization. In the case of the calculations, the mean neutron multiplicities before detector efficiency are also given. It can be seen that generally the experimental values are in a somewhat better agreement with simulation calculations using HERMES than LAHET. The difference between LAHET and HERMES is not fully understood but likely originates from differences in the parameters of the evaporation model. However, there are systematic trends in quality of the agreement between calculations and data. In particular for the higher proton energy, theoretical calculations predict slightly higher mean multiplicities than experimentally observed. Discrepancies seem to become larger for even higher energies [Pie97]. The origin of these trends is presently not fully understood. Since high neutron multiplicities are essentially due to evaporation, overestimation of the neutron multiplicities by the models may be caused by an overestimate of the nuclear excitation energies as will be discussed below or too high Coulomb barriers. In [Fil01] it is also observed that the codes are also unable to reproduce the experimental data in the low-multiplicity region representing peripheral reactions. In this low M_n region both codes appear to overestimate the probabilities especially for the 2.5 GeV incident proton energy. On the one hand the experimental precision for low neutron multiplicities is limited by threshold effects and accuracies in background corrections and on the other hand the description of the nuclear density profile of the nucleus has a large influence on the distributions for low M_n. For the Pb target the deviation of theoretical predictions with respect to experimental data increases with increasing incident energy. The maximum discrepancies are found at 2.5 GeV, namely 13 (9.1) % for M_n with LAHET (HERMES). Observations similar to those for lead were made for the tungsten target.

Table 3.1 : *Mean neutron multiplicities for cylindrical 2 cm thick Pb and 1 cm thick W targets of 15 cm diameter bombarded with protons of different energies measured, $<M_n^{exp}>$, and calculated taking into account the detection efficiency with HERMES and LAHET, $<M_n^{eff}>$. The mean neutron multiplicities before detector efficiency, $<M_n>$, are also given. From [Fil01].]*

Target	Energy	LAHET		HERMES		Experiment
		$<M_n^{eff}>$	$<M_n>$	$<M_n^{eff}>$	$<M_n>$	$<M_n^{exp}>$
Pb	1.2 GeV	15.1	21.0	14.6	20.3	14.5
Pb	1.8 GeV	18.9	26.5	18.0	25.3	17.7
Pb	2.5 GeV	22.3	31.7	21.3	30.3	19.4
W	1.2 GeV	16.3	22.2	15.0	20.5	14.8
W	1.8 GeV	20.6	28.3	18.8	25.9	17.9
W	2.5 GeV	24.9	34.2	22.8	31.7	20.5

A study of the sensitivity of the predictions to the level densities used in the evaporation model and to the adding of a pre-equilibrium stage was performed [Fil01]. The Gilbert-Cameron-Cook-Ignatyuk (GCCI) level densities instead of the original HETC ones were used (see Fig. 3.4) and preequilibrium model was turned on in LAHET. In general, improved agreement between experimental data and theoretical predictions is achieved when the preequilibrium model is used together with the GCCI description, as noticed also for the SATURNE results. Note that in the LAHET code the recommended and default parameter setting is indeed the GCCI option and pre-equilibrium switched on.

Neutron multiplicity distributions have also been measured on a large variety of really thin targets at 1200 MeV [Her01]. In Fig. 3.3 the measured distributions are compared to calculations made with INCL2 coupled to the GEMINI [Cha88] evaporation model after folding with the detector efficiency (shaded area). The dashed curve shows the distribution before taking into account the detector efficiency. It can be seen that generally the INCL2 calculations agree very well with the measured distributions. For heavier targets and low neutron multiplicities there exists however a discrepancy between experiments and calculations. A similar discrepancy was reported previously [Pie97] and was ascribed to the sharp cut off modeling of the nuclear density distribution in INCL2.

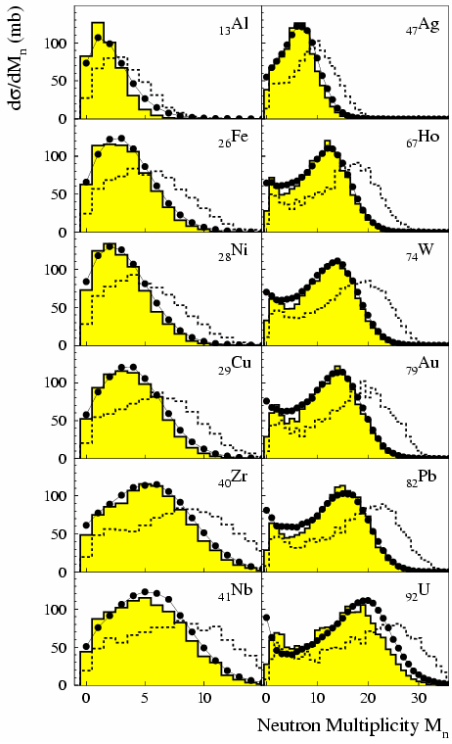

Figure 3.3 : *Experimental (solid points) and calculated (histograms) mean neutron multiplicities as a function of the target atomic number Z_T at 1.2 GeV. The calculated distributions are shown before (dashed line) and after (shaded area) folding with the detector efficiency. From [Her01].*

From the preceding sections, it is clear now that using Bertini-like INC codes leads to too large excitation energy. In fact, the NESSI neutron multiplicities can be converted (provided that a formalism described in [Gol96] is applied) into excitation energy and compared to model predictions. In [Enk99] it has been shown that ISABEL and INCL2 calculations, once renormalized to the reaction cross-section, coincides with the reconstructed experimental distributions while Bertini extends to much larger E* values. The deviation for higher E* is all the more pronounced as the energy of the incident proton increases. One assertion which could explain the disagreement is the way the originally transferred energy is being exhausted or carried away by the different exit particles. While the INCL2 code predicts many relatively highly energetic particles during the INC, the Bertini code produces not only fewer, but also less energetic pions following the reaction. The appraisement of the quality of pion spectra

and production cross-sections is however difficult due to the lack of experimental data in the energy regime beyond 1 GeV. It should be noted that INCL2 fails to reproduce the low excitation energies because of the bad description of the nuclear density.

In the Dresner-Atchison code the Coulomb barriers are reduced with increasing E*. It has been found (see 2.2.2) that the production cross-sections for H (all targets) and He isotopes (for heavy targets) are generally overestimated by a factor of approximately two for Bertini-Dresner based codes, while the INCL2 code coupled to the statistical evaporation model GEMINI [Cha88] gives reasonable agreement with the NESSI experimental data [Enk99]. Actually this has been interpreted [Hil00b] by the fact that the Coulomb barriers are considerably smaller in Dresner than in GEMINI: both because they are smaller at E*=0 and because they decrease with increasing E*. The latter effect is amplified by the fact that Bertini gives a larger E* than INCL2. In [Fil01] the effect of the scaling down of barriers with excitation energy was tested by, in the LAHET code system, applying the ORNL fission/evaporation formalism which does not contain the scaling down of the Coulomb barriers with E*. It was found that the H (except proton) and He-production cross-sections are then reduced drastically, the proton not being much affected. This problem of too low Coulomb barriers in the Bertini-Dresner model was also suspected as the cause of its bad predictions of the isotopic distributions measured at GSI [Wla00]. Actually, this leads to a feedback on the neutron kinetic energy spectra and multiplicities, because changing the emission width for charged particles effects at the same time the emission probability for neutrons, the two emissions being in competition. The influence of modifying the Coulomb barriers on the M_n is demonstrated in Fig. 3.4 for 1.2 GeV proton induced reactions on the different thin targets. It can be seen that, for the same excitation energy at the end of the cascade (Bertini), M_n is larger when the Coulomb barriers is kept constant (LAHET-ORNL dashed line) than when it is reduced with E* (LAHET-RAL dotted line). However, the INCL2-GEMINI calculation for which the excitation energy is lower and the barrier similar to the ORNL case gives an even lower multiplicity closer to the experimental values.

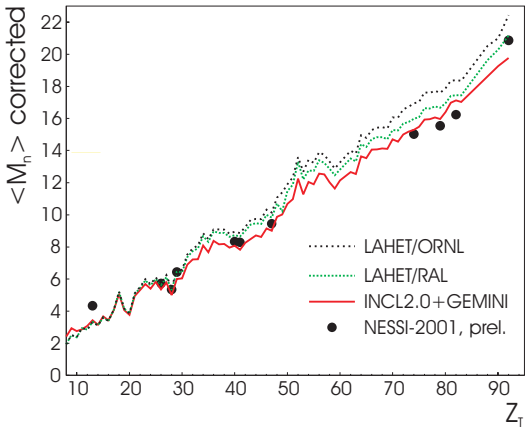

Figure 3.4 : *Measured, after correction by the detector efficiency, (solid points) and calculated (lines) average neutron multiplicity values for different thin targets at 1200 MeV. The dashed (resp. dotted) lines are obtained by LAHET calculations using the Bertini INC followed by Dresner with ORNL (resp. Atchison (RAL)) fission model. The solid line is given by the INCL2+GEMINI model combination. From [Her01].*

Conclusion

A comprehensive comparison of the whole set of thin target data collected within WP5 with some of the high energy models commonly used in high energy transport codes for applications has been made. It showed that the combination of the Bertini-Dresner-Atchison models, which is the default option of most of the codes, presents serious deficiencies, although less important when used in the HERMES package. It is clear that the Bertini INC predicts too large excitation energy at the end of the cascade stage, therefore overestimating, especially at high incident energies, the number of evaporated neutrons. The adding of a pre-equilibrium stage improves the prediction of the code, in particular for low energy neutron multiplicities. However, discrepancies tend to remain for neutrons produced at intermediate kinetic energy for high incident energies and grow larger as the target becomes lighter. The ISABEL model was also tried, when possible, and was found to give a good agreement with both the double-differential cross-sections and the multiplicity distributions. Only for iron, the predictions were less good. Finally, we have shown that the use of the Cugnon intranuclear cascade model, INCL2 is able to fairly reproduce the whole bulk of our results. However, it should be recalled that this model still suffers from serious defects mostly due to the fact this it does not treat correctly the diffuseness of the nuclear surface. This obliges to renormalize the calculations to the correct total reaction cross-section. Also, it makes it impossible to have a correct prediction of the most peripheral collisions. The new version of the Cugnon model, INCL4 [Bou02], under progress in WP8 is expected to solve this problem. The influence of the level density parameterization and Coulomb barriers (which are suspected of being too low in the Dresner-Atchison model to predict charged particle and residue data) was also tested and found to have an influence on the neutron multiplicities. The ABLA evaporation-fission model [Jun98] also under development in WP8 is intended to give better level densities and Coulomb barriers.

(b) Thick target data

(i) NESSI data on multiplicities

- *Neutron multiplicity*

During the NESSI experiments, neutrons were detected with the so called BNB (Berlin Neutron Ball), described in details in [Hil98,Gal94], which is a spherical, gadolinium loaded liquid scintillator ball. The operation of the BNB is based on the detection of gadolinium γ-rays from the capture of neutrons thermalized within the scintillator liquid. The thermalization of the reaction neutrons is a relatively fast process, occurring on a 0.1 μs time scale. It is accompanied by a light flash generated mostly by the interaction of the recoiling nuclei (mostly hydrogen, but also carbon and oxygen) with the scintillator. A prompt light flash indicates an energy deposit in the detector by any reaction product. As it is detected with virtually unit efficiency, it can be used to measure the total reaction cross section, including reactions without neutron emission. The above fast thermalization process is followed by a slow diffusion of the neutrons through the scintillator, before they are eventually captured by the gadolinium nuclei present in the scintillator. There is a statistically-distributed time lapse for a thermalized neutron to "find" such a gadolinium nucleus and be captured, which occurs on a μs scale. The subsequent capture γ-ray cascade, with a total energy of approximately 8 MeV, produces a delayed light pulse. Due to the statistical nature of the thermalization and diffusion process, individual neutrons entering the detector volume at the same time instance are captured at different times, spread over several tens of μs. It is this spread in capture times

that allows one to count one-by-one the individual light pulses produced in different capture events and thus, (ideally) the number of neutrons that have entered the detector volume[1].

The measured neutron multiplicity distributions were corrected for background and deadtime. The correction of the experimental data due to the detector efficiency (see Fig. 3.5) can not be performed because the information of the kinetic energy of the neutron is lost in the experiment.

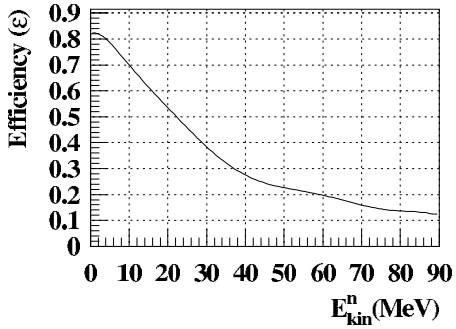

Figure 3.5 : *Efficiency of the BNB as a function of the kinetic energy of the neutrons.*

- Monte Carlo Simulations
Monte Carlo simulations were performed using three code packages: The Jülich code system HERMES [Her00], (High Energy Radiation Monte Carlo Elaborate System), the Los Alamos code package LCS [Pra89] (LAHET Code System), and the MCNPX code [Hug97]. HERMES is a collection of Monte-Carlo codes simulating the transport of particles through and the interaction with matter. To simulate the NESSI experiments three modules were applied. HETC-Jülich and MC4 were used to simulate the spallation process with the intra-nuclear cascade (INC) and the evaporation process. The transport of charged particles and high energetic neutrons (>20 MeV) through the target material are also described by these codes. Because of the large target geometries the lower energetic neutrons below 20 MeV were transported with MORSE-CG. In contrast to the HERMES system, which provides an analysis for the neutron multiplicity, LCS and MCNPX do not include such a feature. In this case we had to analyze the history tapes. To consider the experimental trigger conditions we used two different methods, which lead to exactly the same results. One possibility is to consider only those events, where the excitation energy of the nucleus after the first INC is greater than zero. This condition indicates an inelastic collision. The second way is to trigger on any particle leaving the target surface, except the source particles. As mentioned earlier it is not possible to correct the experimental data for the detector efficiency. In the simulated data exists the information of the kinetic energy of the neutrons leaving the target surface. To compare experimental and theoretical data the statistical weight of the neutrons were multiplied with the energy dependent detector efficiency.

- Survival probability
Because of the same trigger condition in experiment and simulation we are able to compare the measured and calculated survival probability $1\text{-}P_{reac}$, where P_{reac} is the reaction probability. In Fig. 3.6 the measured (symbols) and the calculated (lines) survival probability are plotted for different target materials. It can be seen that the measured data are in accordance to the predicted values of the HERMES code. These data are for an incident

[1] This principle of neutron detection dates back to the investigations of Frederic Reines. In 1995 he got the Noble-Price for the recovery of neutrinos

proton energy of 2.5 GeV. The simulated, as well as the measured data, follow quite accurately the exponential law $1-P_{reac}=exp(-L/L_{reac})$, where L is the target length and L_{reac} is the hadronic interaction length. The predicted interaction lengths are 10.0 cm, 14.1 cm, and 17.9 cm for W, Hg, and Pb, respectively. The published data [Let00] obtained with the NESSI experiment are 10.8±0.2 cm, 15.1±0.3 cm, 18.0±0.3 cm, respectively. The experimental reaction cross sections deduced from the measured P_{reac}, amount to σ_{reac}=1.46±0.03 barn, 1.64±0.05 barn, and 1.69±0.03 barn for the three W, Hg, and Pb targets, respectively. These values are slightly smaller than the HERMES calculations of 1.62 barn, 1.71 barn, and 1.73 barn for W, Hg, and Pb, respectively. An agreement of the same order of magnitude was found when confronting the experimental data with the predictions of LCS and MCNPX.

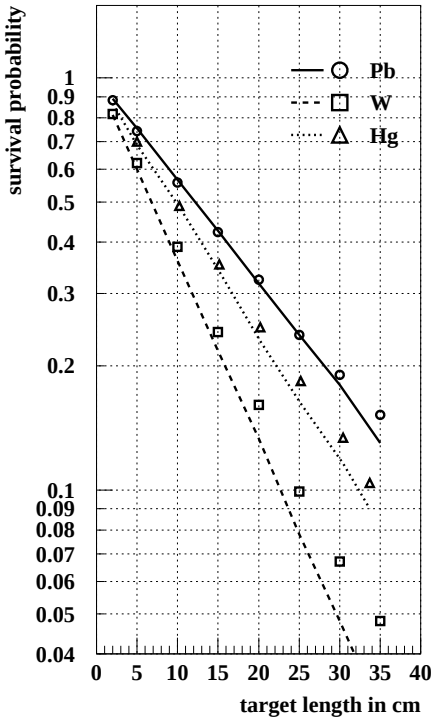

Figure 3.6 : *Comparison of the measured (symbols) and with HERMES calculated (lines) survival probabilities for Pb, Hg, and W.*

- *Mean Neutron Multiplicity*

The term neutron multiplicity means the mean number of neutrons leaving the target surface per incident source particle. In the simulations we used the neutron current detector to count for these neutrons. In Fig. 3.7 the mean neutron multiplicity M_n/p is plotted for different target lengths and incident proton energies of 1.2 and 2.5 GeV. The symbols represent the experimental data and the solid lines the HERMES simulations. The dashed lines are HERMES simulations folded with the detector efficiency.

As can be seen in Fig. 3.7 the calculations agree very well with the experimental observations, over a wide range of target geometries and target materials. The agreement between calculation and experiment for the second moment of the distributions within a few percent gives additional confidence to the program packages under consideration. The statistical error of calculated mean values is typically of the order of 1 %. In case of the mercury target simulations the calculations account for the 1 mm thick wall of stainless steel encapsulating the liquid mercury. The increase of the mean neutron multiplicity with increasing target length is due to an increase of the reaction probability P_{reac} and, to a lesser extent, to an increase of secondary reactions with the target length.

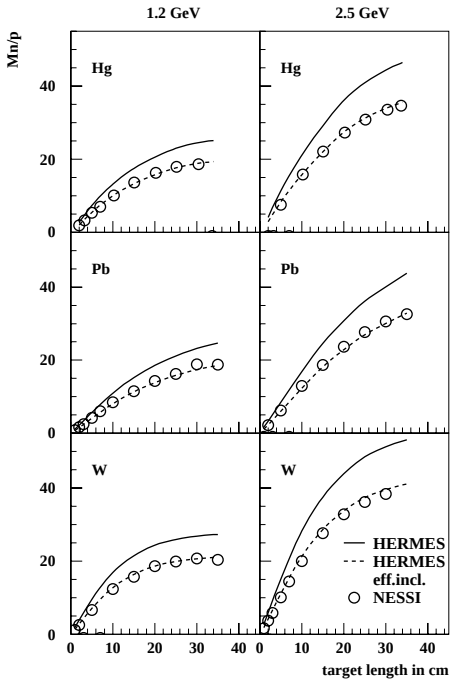

Figure 3.7 : *Mean neutron multiplicity per incident proton M_n/p as a function of target thickness for 1.2 and 2.5 GeV. Solid line: HERMES simulation, dashed line: HERMES simulation including detector efficiency, open circles: NESSI data.*

- *Neutron Multiplicity Distributions*

The advantage of the NESSI experiment is the possibility to measure the neutron multiplicity eventwise, which lead to the measuring of the neutron multiplicity distributions. A typical, bell-shaped, experimental neutron multiplicity distribution is shown as open circles in Fig. 3.8. Here, P_{reac} is plotted versus the number of neutrons leaving the target surface per incident proton. The presented Monte-Carlo simulation was performed with LCS. In this simulation the Gilbert-Cameron-Cook-Ignatyuk (GCCI) level density description was applied [Gil65]. This diagram illustrates further the influence of the detector efficiency on the theoretical results. Fig. 3.9 shows the Monte-Carlo simulations performed with HERMES and MCNPX for incident proton energy of 1.2 GeV. But not only for this energy, but also for higher energies a good agreement was achieved, as can be seen in Fig. 3.10. Discrepancies between model calculations and experimental data are generally less than 5 %. The maximum discrepancy is 7.4 % in case of the 5 cm Pb target bombarded with 2.5 GeV protons. In this case the deviation from the measurements is 18 %. Fig. 3.10 points out the agreement of the HERMES simulations and the shifted shape of the LCS simulations towards higher neutron multiplicities.

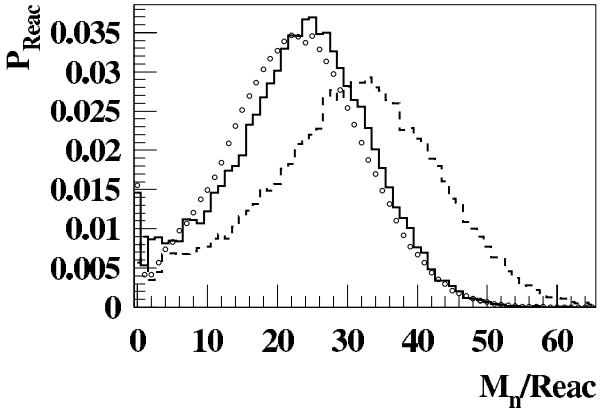

Figure 3.8 : *Influence of the detector efficiency on the theoretical data obtained with GCCI (LCS) for a 15 cm long Pb rod (diameter 15 cm) bombarded with 1.2 GeV protons. The dashed histogram represents MC-data while the solid histogram shows efficiency folded data. The open circles are the experimental data corrected for acquisition deadtime and background, but not for efficiency.*

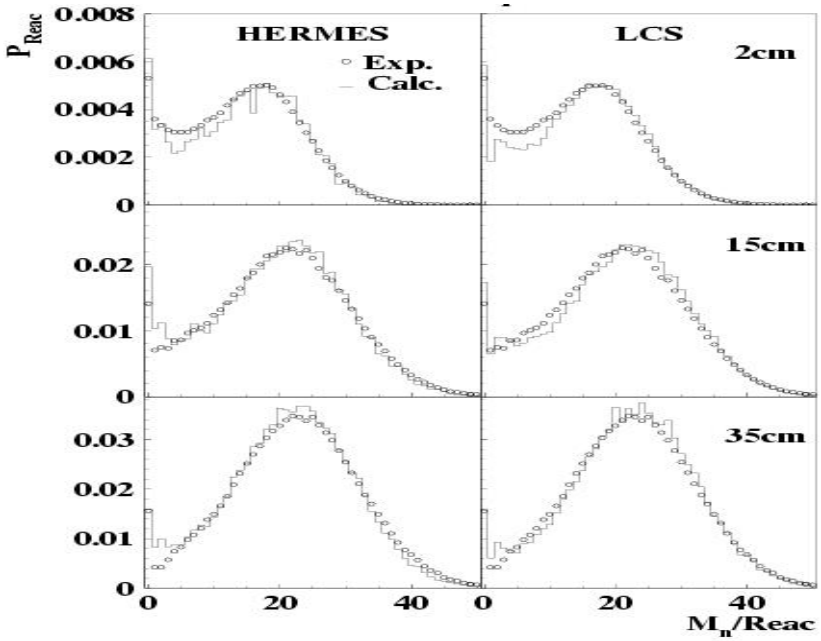

Figure 3.9 : *Comparison of HERMES (left), MCNPX (right) and experimental data (o) for Pb targets of various lengths bombarded with 1.2 GeV protons. Experimental data from [Let00].*

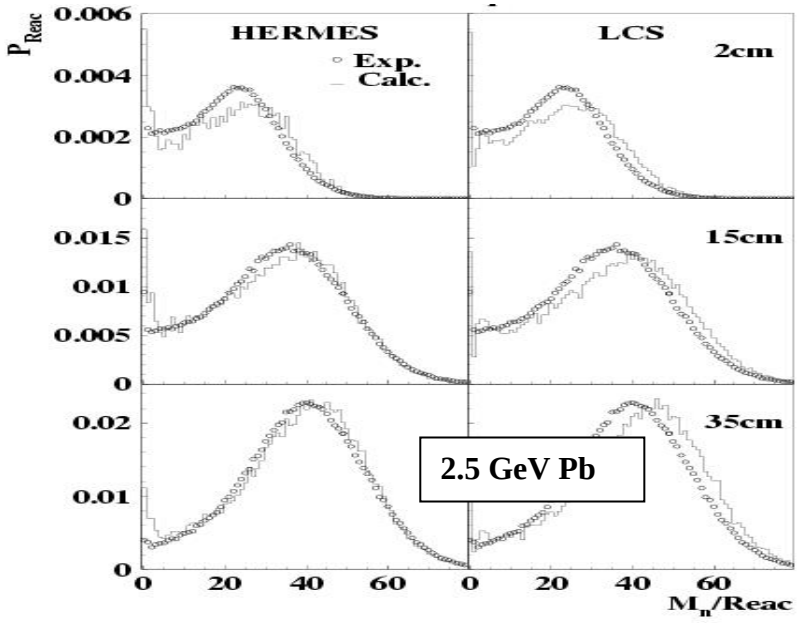

Figure 3.10 : : *Comparis on of HERMES (left), MCNPX (right) and experimental data (o) for Pb targets of various lengths bombarded with 2.5 GeV protons. Experimental data from [Let00].*

- Parameter Discussion

As in section 3.2.1 for thin targets, results of simulations are influenced by the parameters which can be chosen in the codes, like e.g. pre-equilibrium model, Coulomb barriers, INC models, or fission. Behaviours similar to those found for thin targets are observed. When pre-equilibrium is included in the LCS and MCNPX codes, it results in a slightly shifted neutron multiplicity distribution towards lower neutron multiplicities as compared to simulations with a standard parameter set. This is due to the emission of higher energetic neutrons in an energy range between 20 and 100 MeV. Also, as discussed in section 3.2.1, the choice of the Coulomb barriers, to which –in contrast to neutrons - charged particles are subject during their evaporation, modify the predictions of the codes. Calculations using either the ORNL/Dresner description [Dre62] or the RAL [Atc80] formalism, in which the Coulomb barrier are further downscaled depending on the excitation energy E^* of the nucleus were performed with the MC4 code of the HERMES package. Fig. 3.11 shows the influence of the reduced Coulomb barrier on the neutron multiplicity distributions for a 2 and 35 cm long Pb target bombarded with 1.2 GeV protons. It can be seen that the shape of the neutron multiplicity distributions agree better when using the method of reduced Coulomb barriers, as shown in 2.1.1 and contrary to what happen for helium production.

One interesting point was to exchange the INC model, describing the fundamental spallation process. Beyond the classical approach of Bertini [Ber63] we studied the influence of the Liège INCL2 [Cug87, Cug97a] on the neutron production. INCL2 was implemented into MC4 to simulate not only thin target experiments, but also thick target experiments. To achieve a better agreement with the experimentally determined total reaction probability, the external radius of the nucleus was set to r_0^{ext}=1.3 fm. In Fig. 3.12 the calculated neutron multiplicity distributions using the INCL2 model are shown. The shift towards lower neutron multiplicities is due to a higher transparency of the nucleus in the INCL2 code. A further difference between Bertini and the INCL2 model is the description of the nuclear density.

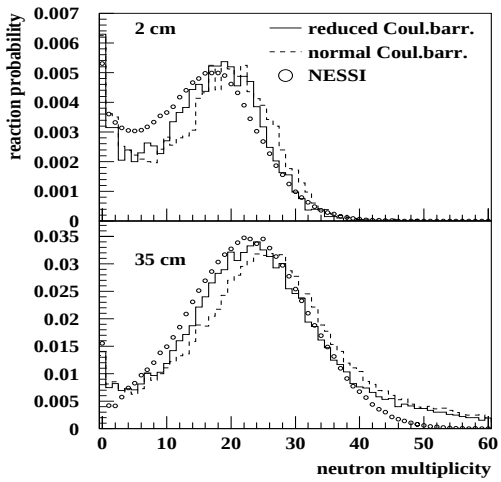

Figure 3.11 : *Agreement between experimental data (o) and simulation using reduced Coulomb barriers (solid line). The dashed line represents the theoretical values without reduction of the barriers. The targets used for this comparison were Pb targets.*

Whereas in the Bertini model the nuclear density is an approximation by a three step function of the Hofstaedter curve [Ber63], INCL2 assumes a spherical nucleus with a constant nuclear density. This crude approximation in INCL2 (which will be removed in INCL4) could explain the discrepancies with the data.

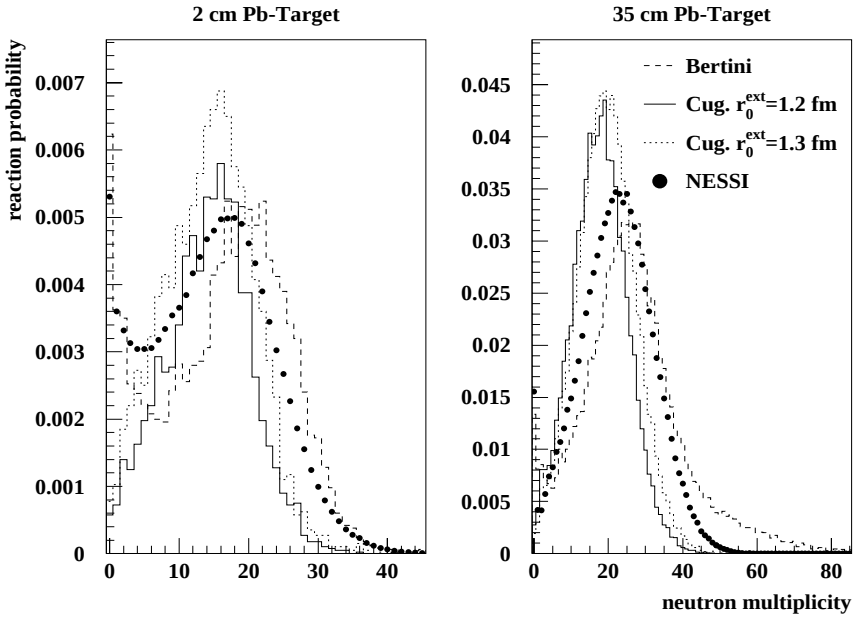

Figure 3.12 : *Comparison of the neutron multiplicity distributions with the Bertini code (dashed line) and INCL2.0. The solid line represents the simulation with the standard parameters and the dotted line with r_0^{ext} adjusted. The simulations are performed for a 2 cm and 35 cm Pb target bombarded with 1.2 GeV protons.*

All three considered codes – HERMES, LCS, and MCNPX - are able to describe the experimental data over a broad range of incident energies, target geometries, and target materials. The achieved agreement is better than 10 %. Currently the HERMES code package seems to be the best suited package to describe the neutron production in spallation targets. The mean neutron multiplicity coincides within ±4 % and fullfills the accuracy requested to design target stations for spallation neutron sources. LCS and MCNPX show some

discrepancies when describing the neutron production of tungsten targets at high incident proton energies. These discrepancies can be eliminated by considering the pre-equilibrium process using the multistage exciton model. Many details of the experimental measurements and investigations together with Monte Carlo validations are given in the Refs. [Fil01, Nün01].

(ii) Energy spectra measured at SATURNE

Results concerning the neutron energy spectra measured on thick iron and lead targets [Mén98, Var99] bombarded by 800, 1200 and 1600 MeV protons at SATURNE have been delivered and compared to simulations made with the LAHET code in which the new INCL4-ABLA models have been implemented. The experimental set-up (Fig. 3.13) was the same as the one used for the thin target measurements, discussed in section 2.1.1, except that, because very few neutrons are expected to have energies higher than 400 MeV, only the time-of-flight method was used [Bor97]. Measurements with various lengths and diameters of cylindrical targets were conducted on the different targets. The collimators and the possibility to longitudinally translate the target allowed the selection of neutrons coming from different emission zones, thus enabling to test the propagation of the cascade along the target. Measurements were performed at 0° and every 15° from 10 to 160°. The detail (diameter, length and measurement position for each target) of the different measurements is given in the Table 3.2.

Because of the collimators, the target area seen, totally (full exposition zone) or partially (penumbra zone), by a detector depends on the angle of the collimator and on the target diameter and longitudinal position. Therefore, on each figure and for each angle a diagram showing the full exposition and penumbra zone has been added. All data presented here are number of neutrons per incident proton, MeV and cm^2 of detector. The systematical errors on the data are the same as for thin target measurements, as discussed in details in [Ler02], and are always less than 12%.

Table 3.2 : *Characteristics of the different measurements performed on thick Pb and Fe targets irradiated with protons at SATURNE.*

Target	**Target dimension (Φ x l)**	**E beam (MeV)**	**Position (cm)**
Pb	10 cm x 40 cm	800	10 30
Pb	20 cm x 40 cm	800	10 30
Pb	20 cm x 65 cm	800	10 30
Pb	20 cm x 65 cm	1200	10 30 50
Pb	20 cm x 105 cm	1200	50 70
Pb	10 cm x 105 cm	1200	10 30 50
Pb	10 cm x 105 cm	1600	10 30 50
Pb	20 cm x 105 cm	1600	10 30 50
Fe	10 cm x 40 cm	800	10 30
Fe	20 cm x 40 cm	800	10 30
Fe	20 cm x 65 cm	1200	10 30 50
Fe	10 cm x 65 cm	1200	10 30 50
Fe	10 cm x 105 cm	1600	10 30
Fe	20 cm x 105 cm	1600	10 30

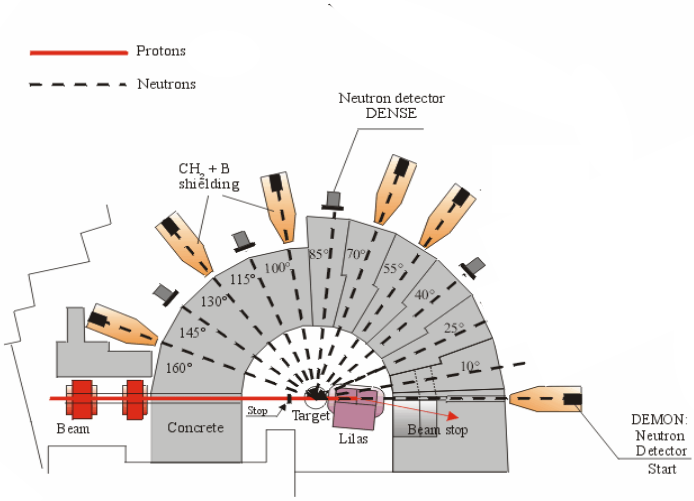

Figure 3.13 : *Experimental setup.*

- *Comparison with KEK data*

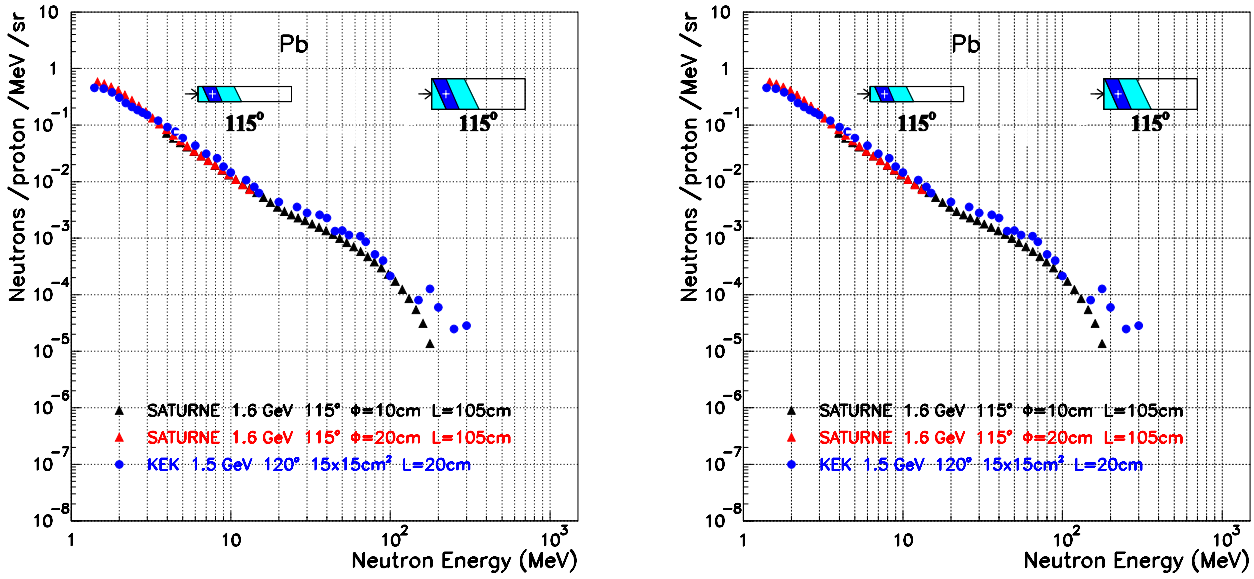

Figure 3.14 : *Neutron spectra from a cylindrical lead target measured at SATURNE at 1.6 GeV (black points: Φ=10cm; red points: Φ=20cm) and parallelepiped target at KEK at 1.5 GeV (blue points) at 10° or 15° (left side) and 115° or 120° (right side). The enclosed schemes show the region of the target seen by the detectors at SATURNE in the case of the 10 cm and 20 cm diameter targets respectively.*

A similar experiment has been carried out at KEK [Mei99]. The experimental set up used at KEK to measure neutron spectra produced from a thick lead target bombarded with 1.5 GeV protons is approximately the same one used at SATURNE. The main differences between the experiments are the target geometry (a 15*15*20 cm^3 parallelepiped) and the positions of the detectors. Nevertheless, we can compare the behaviour of the spectra. This is done on Fig. 3.14 where the results obtained at KEK (at 15° and 120°) are shown together with the ones

from SATURNE for the cylindrical targets L=105cm, Φ=10 and 20 cm at angles 10° (left) and 115° (right) respectively. The enclosed schemes show the region of the target seen by the detectors at SATURNE in the case of the 10 cm and 20 cm diameter. For the forward angle, a much larger number of neutrons is found in the case of the KEK experiment. This can be understood from the difference between the lengths of the two targets and transport through the target. Actually, in such targets most of the protons interact in the first 20 cm leading to the emission of high-energy, forward-peaked neutrons. In a long target, as in SATURNE, the transport, i.e. secondary reactions, tends to scatter and consequently decrease the neutron flux for forward angles, while at KEK a large part of the primary neutrons are detected.

On the contrary, at 115-120°, the primary neutrons pass through too little matter to be affected by secondary reactions and, therefore, the number of emitted neutrons does not depend on the target diameter or shape. That is why both experiments give practically the same results.

- *Comparisons with models*

The model combination INCL4/ABLA has been shown in [Bou02] (see also section 2.4.3) to give rather good results with thin targets, especially for neutron spectra. It was, therefore, interesting now that ABLA have been implemented into the high energy transport code LAHET3 (see section 2.4.4) to test this combination on thick targets. All the target configurations have been simulated with LAHET3, the neutrons below 20 MeV being passed to MCNP for the low energy transport [Dav03]. In order to minimise the computer time, only the target geometry is taken into account in LAHET and MCNP. The created neutrons that leave the target are stored in libraries and another code is called to transport these neutrons from the target surface to the detectors.

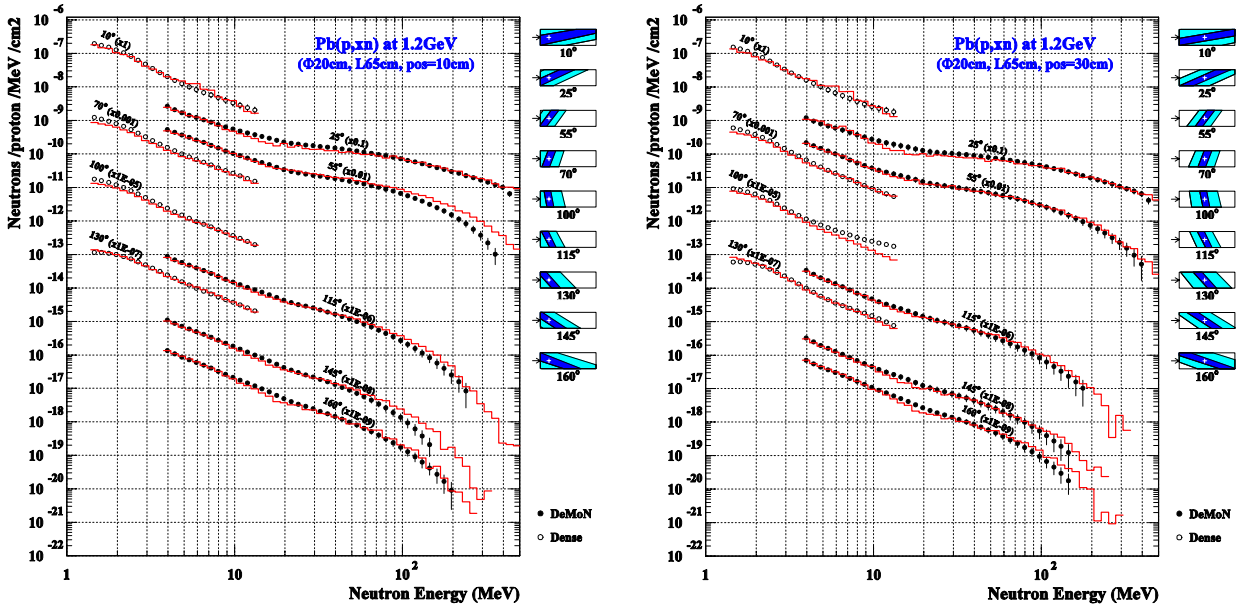

Figure 3.15 : *Neutron spectra measured at SATURNE on a 20 cm diameter lead target at 1.2 GeV (black points) compared with calculations made with the LAHET3/MCNP code using the INCL4/ABLA model combination (red line). The two figures correspond to two different longitudinal positions of the target with respect to the collimators.*

In general, INCL4/ABLA reproduces well the SATURNE data whatever the material, geometry and angle, with a few discrepancies. The energy dependence of the model seems rather good since the quality of the agreement is the same at the three energies. In Fig. 3.15

examples of the obtained results are shown for a 20 cm diameter lead target at 1.2 GeV for two different longitudinal positions of the region aimed at by the collimators. The agreement is very good, except for the position 10 cm, where the neutrons from the cascade (above 70-80 MeV) are overestimated at some angles. This behaviour is consistent with what has been observed for thin targets [Bou02]. If we move the same target to the position 30 or 50 (not shown) cm these discrepancies disappear. An explanation could be that the neutrons detected in this case come from an interaction occurring further in the target (see the schemes on the right of the figures), consequently at a lower energy and that the model predicts more correctly the spectra at lower energies.
Results obtained with different target diameters or lengths are well understood with the simulations. For instance, the behaviour observed in Fig. 3.14 concerning the comparison of two different diameters is perfectly reproduced by the calculations. It is found that a smaller diameter (10 compared to 20 cm) has little effect on the sideward emitted neutrons while it leads to an important increase (about a factor 2) of the neutrons emitted in the direction of the beam. This could be a problem for shielding considerations. The models allow predicting the total amount of neutrons which are 29.7 (resp. 23.5) n/p for the 20 (resp. 10) cm diameter target.

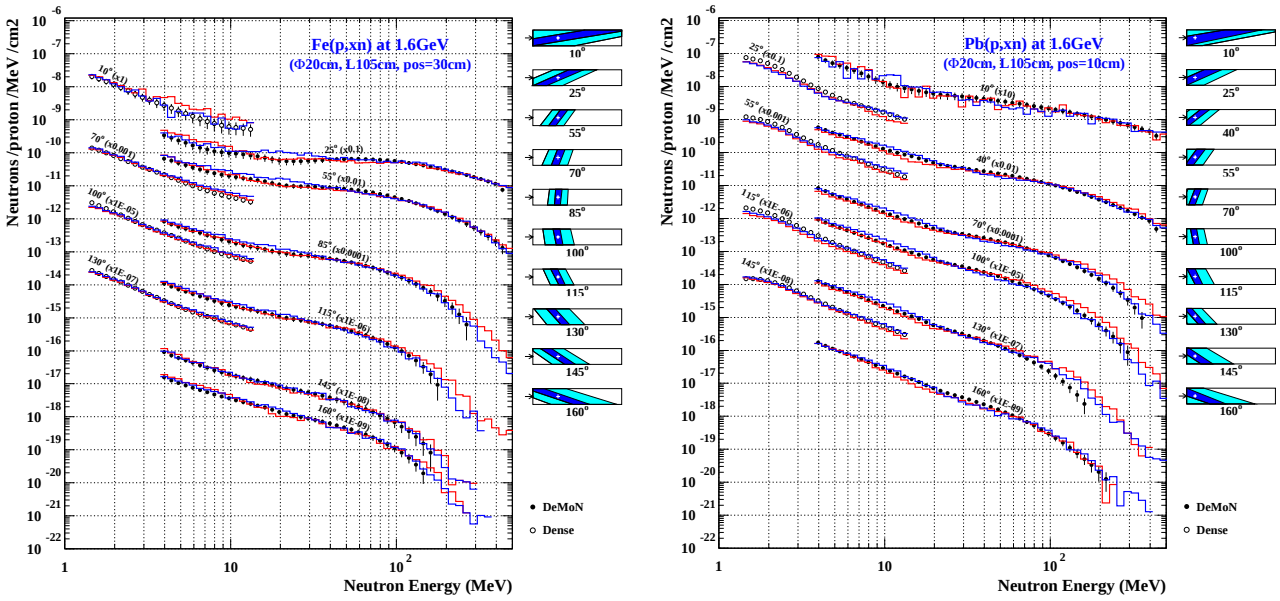

Figure 3.16 : *Neutron spectra comparisons between SATURNE data (black points), INCL4/ABLA model (red line) and Bertini/Dresner model (blue line) for a lead and an iron target at 1.6 GeV.*

In Fig. 3.16, data at 1.6 GeV for a lead and an iron target are compared with INCL4/ABLA (red curve) and also to the Bertini(+preequilibrium)/Dresner combination, which is the most common combination used, up to now, for thick target calculation or simulations. Actually, whatever the material, diameter or length of the target, or beam energy, the agreement obtained with the two combinations is of similar quality. In general, small discrepancies are observed which corresponds to the ones already pointed out with thin targets: Bertini/Dresner is less good in the intermediate energy region (around 100 MeV) especially for iron while INCL4/ABLA tends to overestimate the high energy neutrons at angles close to 90°.

Conclusion

In conclusion, HINDAS has permitted the collection of a wide set of data on thick targets covering the energy range foreseen for ADS and the main target and shielding materials. Both

neutron multiplicities and energy spectra are rather well predicted by either the standardly used high energy transport codes as LAHET, MCNPX or HERMES/MC4 with the default options or the newly developed INCL4/ABLA implemented in LAHET3 and MCNPX. The accuracy of the code predictions can be assessed to be of the order of magnitude of the experimental uncertainties, that is around 10-15% for global quantities, but can be larger in some regions of the angle or energy spectra.

3.2.2. Experimental results on light charged particle production

(a) Light charged particle production with the NESSI experiment

The international collaboration NESSI[2] has initiated measurements at the proton accelerator facility COSY in Jülich in order to study secondary particle production created in structural-, window- and target-materials by proton beams up to 2.5 GeV incident kinetic energy. Event-wise correlation measurements of charged particles and neutrons on thin targets give extensive insight of the complex spallation process and the different phases on the excitation and the subsequent deexcitation of hot matter.

(i) The experimental apparatus

Neutrons and charged particles are measured by means of two 4π detectors (BNB-Berlin Neutron Ball and BSiB - Berlin Silicon Ball [Jah03, Her03]) schematically shown in Fig. 3.17.

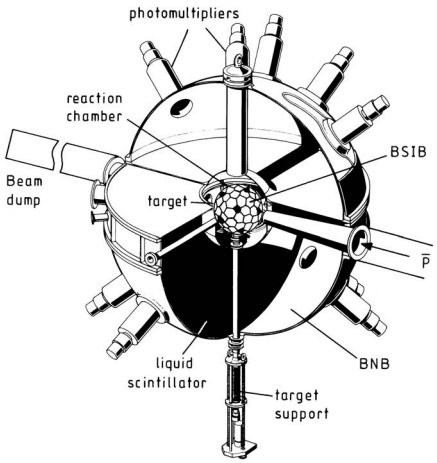

Figure 3.17 : *Schematic drawing of the BNB and the BSiB in the reaction chamber.*

In addition to the neutrons, in the thin-target experiments, charged reaction products were detected. Light charged particles (LCP: H- and He-isotopes), intermediate mass- (IMF), and

[1]The NESSI-Collaboration
M. Enke[3], D. Filges[1], J. Galin[2], F. Goldenbaum[1], C.-M. Herbach[3], D. Hilscher[3], U. Jahnke[3],A. Letourneau[2], B. Lott[2], R.-D. Neef[1], K. Nünighoff[1], N. Paul[1], A. Péghaire[2], H. Schaal[1], G. Sterzenbach[1], A. Tietze[1], M. Wohlmuther[1]
[1]FZJ, IKP, D-52425 Jülich, Germany, [2]GANIL, F-14076 Caen, France, [3]HMI, D-14109 Berlin, Germany

fission-fragments (FF) were detected and identified by the Berlin Silicon Ball (BSiB) inside the BNB. The BSiB is composed of 158 independent, 500-μm thick silicon detectors approximating a 20-cm diameter sphere and covering a solid angle of about 90 % of 4π. Due to absorption of LCPs in the target material, the overall detection efficiency for LCPs, calculated with Monte Carlo simulations, is about 79-84 %, depending on the atomic number Z of the particle. Charged particles (CP: H+He+IMF+FF) were identified by means of time of flight *TOF* versus energy *E* correlations with a mass resolution of ± 3 units for A=20 and ±15 units for A=100. Protons and α-particles with energies larger than 8.2 and 32.2 MeV respectively are not stopped anymore in the 500 μm silicon detectors. Consequently the lower detection threshold of 2.3 MeV represents at the same time an upper limit for detecting highly energetic protons of more than 26 MeV kinetic energy. For the same reason minimum ionizing particles, pions and kaons fall below detection threshold. For α-particles on the other hand practically no such upper limit exists. Six of the Si-ball detectors have recently been replaced by ΔE-E telescopes. They consist of two fully depleted ΔE silicon detectors (80 μm and 550 μm thick) backed by a 7cm thick CsI-scintillator. These telescopes allow a fully isotopic separation up to about A=20.

(ii) H – and He – production cross sections

In particular the H- and He-production cross sections are of great importance for estimations of damages of target- and structure-materials of the planned spallation source since the life-

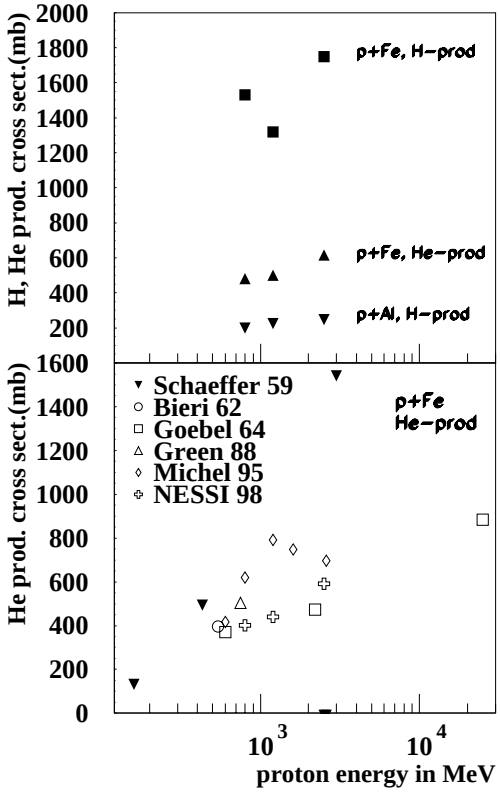

Figure 3.18 : *Hydrogen- and helium-production cross sections for p+Fe and p+Al (upper panel) as a function of incident proton energy measured by the NESSI collaboration. Lower panel: Comparison between He production cross sections following NESSI measurements and data from literature for proton induced reactions on Fe. The year of the publication is also indicated. (References: Schaeffer [Sch59], Bieri [Bie62], Goebel [Goe64], Green [Gre88], Michel [Mic95], NESSI [Her00]).*

time for window and target materials is directly associated to those cross sections. Exactly these H- and He- measurements show large discrepancies not only between experiment and theory, but also between different experiments. Partly, these discrepancies within the models are understood: On the one hand the energy originally transferred to the nucleus during the intra nuclear cascade is differently re-distributed in various exit channels [Gol00] and on the other hand strongly different Coulomb barriers lead to differing production cross sections of charged particles [Her00, Enk99].

H- and He-cross sections of recent NESSI data are also shown in the upper panel of Fig. 3.18 for p+Fe and p+Al as a function of incident proton energy. The large spread in experimental cross sections found in literature is also demonstrated in Fig. 3.18 (lower panel) for He-production cross sections following proton-induced reactions on Fe. As for example, for p+Fe the measured helium production cross sections in the NESSI experiment are about a factor of two smaller than from other experiments [Mic95] .

Table 3.3 : *Hydrogen cross sections from the NESSI – Experiment*

Target	Proton energy (MeV)	ejectile	A ejectile	Cross section (mb)	reference
Fe	800	H	1	1531	[Her00]
Fe	1200	H	1	1320	[Her00]
Fe	2500	H	1	1749	[Her00]
Al	800	H	1	481	[Her00]
Al	1200	H	1	502	[Her00]
Al	2500	H	1	617	[Her00]

Table 3.4 : *Helium cross sections from the NESSI – Experiment*

Target	Proton energy (MeV)	ejectile	A ejectile	Cross section (mb)	reference
Fe	800	He	4	401	[Her00]
Fe	1200	He	4	440	[Her00]
Fe	2500	He	4	592	[Her00]
Al	800	He	4	199	[Her00]
Al	1200	He	4	226	[Her00]
Al	2500	He	4	248	[Her00]

Table 3.5 : *Hydrogen cross sections in Fe and Al for energies between 600 and 2600 MeV.*

Target	Proton energy (MeV)	ejectile	A ejectile	Cross section (mb)	reference
Al	600	H	1	670	[Ala75]
Al	600	H	3	44	[Ala75]
Fe	600	H	1	2680	[Ala75]
Fe	600	H	3	46	[Ala75]
Fe	800	H		1531	[Her00]
Fe	1200	H		1320	[Her00]
Fe	2500	H		1749	[Her00]

Table 3.6 : *Helium cross sections in Fe and Al for energies between 600 and 2600 MeV.*

Target	Proton energy (MeV)	ejectile	A ejectile	Cross section (mb)	reference
Al	800	He	3	47.7	[Mic95]
Al	1200	He	3	52.4	[Mic95]
Al	1600	He	3	68.5	[Mic95]
Al	2600	He	3	63.2	[Mic95]
Al	800	He	4	371	[Mic95]
Al	1200	He	4	427	[Mic95]
Al	1600	He	4	450	[Mic95]
Al	2600	He	4	430	[Mic95]
Fe	600	He	3	36.6	[Mic95]
Fe	800	He	3	63.9	[Mic95]
Fe	1200	He	3	86.8	[Mic95]
Fe	1600	He	3	99.8	[Mic95]
Fe	2600	He	3	91.8	[Mic95]
Fe	600	He	4	379	[Mic95]
Fe	800	He	4	556	[Mic95]
Fe	1200	He	4	705	[Mic95]
Fe	1600	He	4	648	[Mic95]
Fe	2600	He	4	604	[Mic95]

Table 3.7 : *Hydrogen cross sections in Pb, Ta and W for energies between 800 and 2500 MeV.*

Target	Proton energy (MeV)	ejectile	A ejectile	Cross section (mb)	reference
Pb	800	H	1	1923	[Her00]
Pb	1200	H	1	2270	[Enk99]
Pb	1800	H	1	3130	[Enk99]
Pb	2500	H	1	4972	[Her00]
Ta	800	H	1	1740	[Her00]
Ta	1200	H	1	2200	[Enk99]
Ta	1800	H	1	3300	[Enk99]
Ta	2500	H	1	4544	[Her00]
W	800	H	1	2069	[Her00]
W	1200	H	1	2210	[Enk99]
W	2500	H	1	4257	[Her00]

Table 3.8 : *Helium cross sections in Pb, Ta and W for energies between 600 and 1800 MeV.*

Target	Proton energy (MeV)	ejectile	A ejectile	Cross section (mb)	reference
Pb	600	He	4	361	[Goe64]
Pb	800	He	4	793	[Her00]
Pb	1200	He	4	1220	[Her00]
Pb	1800	He	4	1640	[Her00]
Ta	800	He	4	823	[Her00]
Ta	1200	He	4	1100	[Her00]
Ta	1800	He	4	1600	[Her00]
W	750	He	4	762	[Gre88]
W	800	He	4	726	[Her00]
W	1200	He	4	1150	[Her00]

A compilation of currently available data on H- and He-cross sections in the energy regime up to 2.5 GeV are given in Tables 3.3 - 3.8. Further analysis and future experiments at NESSI are dedicated to the completion of the production cross sections of the n, p, d, t, He-isotopes and the IMF for light structure materials (C, Al, Fe, Cu, Nb...) and for heavy target materials (W, Pb, Hg...).

(iii) Emission of composite particles in the 2.5 GeV p + Au spallation reaction

The previous investigations, however, were restricted to particles with Z≤3 and to sufficient heavy target nuclei because of the lower energy thresholds of the telescopes. The H- and He-production cross sections in thin targets have been delivered in form of a comprehensive data base for hydrogen and helium production cross sections as Deliverable 8 of WP4. The H- and He- production cross sections as published in the HINDAS annual report 2001 have been evaluated not only for Fe as originally offered in the work package description, but have been extended to p-induced reactions on targets of Al, Pb, Ta, W. The resulting data base available on the web is being discussed in detail in the HINDAS 2002 annual report. In this contribution we show first results from recent measurements on IMF's at COSY with upgraded telescopes, using protons of 1.2 GeV and 2.5 GeV incident energy and target nuclei from Al up to U. We present here, as a typical example, data from the emission of ^{3,4}He and ^{7,9,10}Be in the reaction p(2.5GeV)+Au to demonstrate the experimental features.

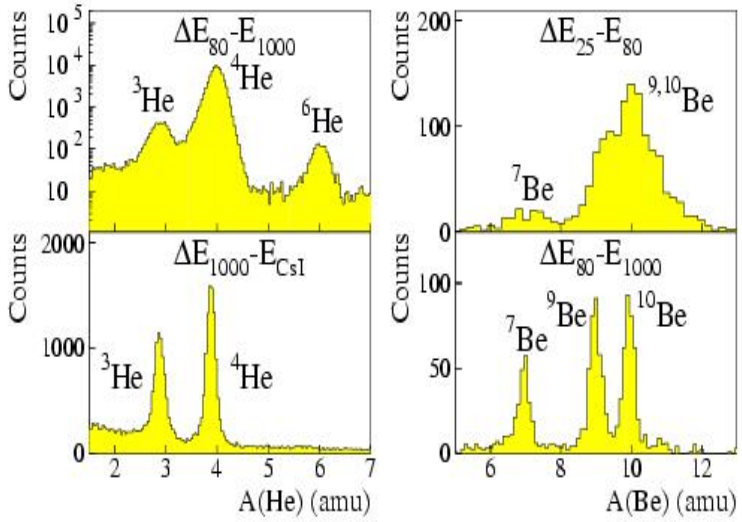

Figure 3.19: *Mass distributions of He (left panels) and Be (right panels) in the reaction p(2.5GeV)+Au measured by the detector telescope at the angle of 30^o.*

The modified telescopes consist of three silicon detectors (25, 80 and 1000 μm) backed by a 7 cm long CsI crystal and allow for identification of ^{1,2,3}H, ^{3,4,6}He, $^{6,7.8,9}$Li, ^{7,9,10}Be, ^{10,11}B, and further IMFs up to Mg with mass resolution of ΔA≤0.2 amu for E/A > 3.5 MeV/A and ΔA≤0.4 for E/A < 3.5 MeV/A (see for examples Fig. 3.19). Kinetic energy spectra detected at the angle of 30^o are shown in Fig. B.20, summed over all Be isotopes (filled circles), and separately for ^{7}Be (open squares). The ^{7}Be contribution in the low-energy range, which is dominated by statistical evaporation, is small compared to ^{9,10}Be (right panel of Fig. 3.20), while the high-energy yield arising from pre-equilibrium emission turns out to be very similar for all three Be-isotopes. This result is also shown in Fig. 3.21, which exhibits the angular distribution of He and Be for kinetic energies below (left panel) and above (right panel) 60 MeV.

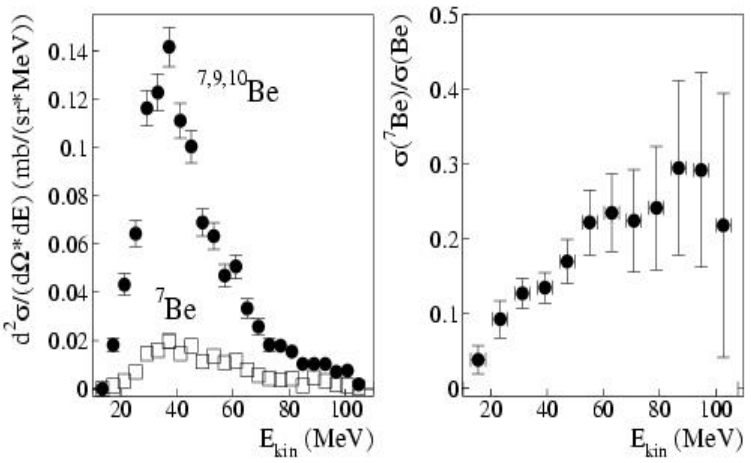

Figure 3.20 : *Kinetic energy spectrum of Be detected at 30^o (left panel) and relative contribution of ^{7}Be (right panel).*

The sharp decline of the angular distributions for the faster particles (right panel) is almost the same for all He and Be isotopes, and the isotopic yields of particles with equal charge do not vary strongly with the particle mass. As expected, the angular distribution of the particles emitted with smaller kinetic energies is weaker, and again, the slopes are similar for the various isotopes (left panel). The isotopic low-energy yields, however, differ considerably, since they are governed by the binding energies of the composite particles.

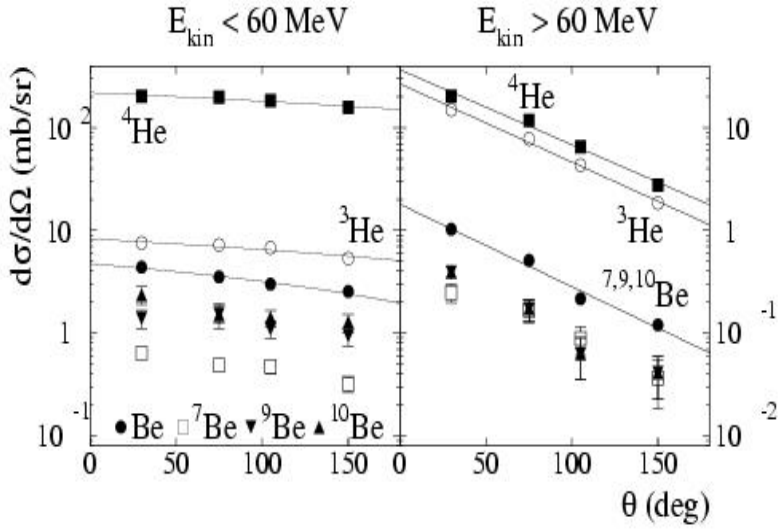

Figure 3.21 : *Angular distributions of ^{3,4}He and ^{7,9,10}Be emitted in the reaction p(2.5GeV)+Au. The yield with E<60 MeV (left panel) and E>60 MeV (right panel) are dominated by evaporation and pre-equilibrium emission, respectively.*

The ratio of the overall yield for Be and He amounts to 0.02, and the total production cross-sections for ^{7}Be, ^{9}Be and ^{10}Be result to 8 mb, 20 mb and 20 mb, respectively.

The investigation of composite-particle emission in spallation reactions has been pursued in detail with the help of the complementary tools of the NESSI experiment as discussed in this section as well as employing the PISA experiment being subject of Deliverable 28 and also described in both annuals reports 2002 and 2003. First data from the PISA experiment, double differential p, d, He and IMF light charged particle production spectra will be discussed in the subsequent section.

On the one hand, the 4π coverage for neutron and light charged particle (lcp) detection at NESSI allows an event-wise determination of the excitation energy E* of the heated target nucleus, on the other hand, a set of six low-threshold telescopes providing A and Z identification for the lcp (essentially H, He and Li isotopes) allows a precise characterization of all these particles as a function of E*. The experimental multiplicities for lcp´s, ranging from p to ^{7}Li are shown as function of E* in Fig. 3.22 and are compared with the result of a two-step simulation including an intra-nuclear cascade model, code INCL2 [Cug97a], followed by a statistical decay, code Gemini [Cha88].

This simulation which is restricted to evaporation can certainly not account for the observed yield of most particle species at low E*. The discrepancy between experiment and simulation is narrowing down, however, with increasing E*. At high E* some particles (e.g. ^{2}H, ^{3}H, ^{4}He, ^{6}Li) are mostly issued from a statistical emission, whereas others (^{1}H or ^{3}He) are emitted both, prior and past to the attainment of thermal equilibrium. Among all particles the two neighbouring isotopes of He, ^{3}He and ^{4}He, exhibit extreme behaviours: the strongly bound ^{4}He is shown to be almost exclusively evaporated whatever E*, while ^{3}He is mostly of non-evaporative character whatever E*, with at best 50% of evaporative component at high E*.

This comparison thus reveals the strong deficiency of the intra-nuclear cascade models which do not consider pre-equilibrium emission of composite particles, direct emission prior to evaporation being a common feature of all ejected particles. Direct emission amounts to 61, 44, 34, 68 and 11% of the total emission for the most abundant lcp´s: p, d, t, ^{3}He and ^{4}He, respectively. The non-evaporative component of ^{3}He, together with that of ^{2}H and ^{3}H has been satisfactorily accounted for by building up composite particles by coalescence during the INC process [Let02]. In Fig. 3.23 we show for 3He that not only the integrated cross section can thus be reproduced but also the doubly differential ones (at 4 emission angles) for several E* bins. While a similar good agreement is reached also for d and t, the coalescence concept in its present version seems to fail for the strongly bound ^{4}He.

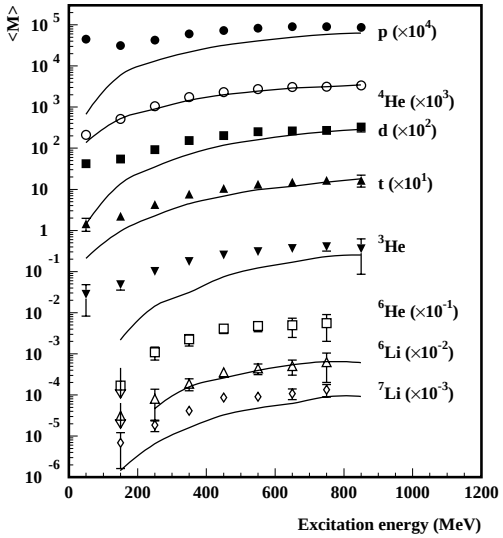

Figure 3.22: *Comparison of experimental (symbols) and calculated (solid lines) multiplicities of various H, He and Li isotopes as function of the excitation energy E*. A two-step model, INCL2 [Cug97a, Let02] combined with Gemini [Cha88], has been used for the calculation which, however, does not allow for pre-equilibrium emission of composite particles. For protons direct emission is suppressed here for comparison.*

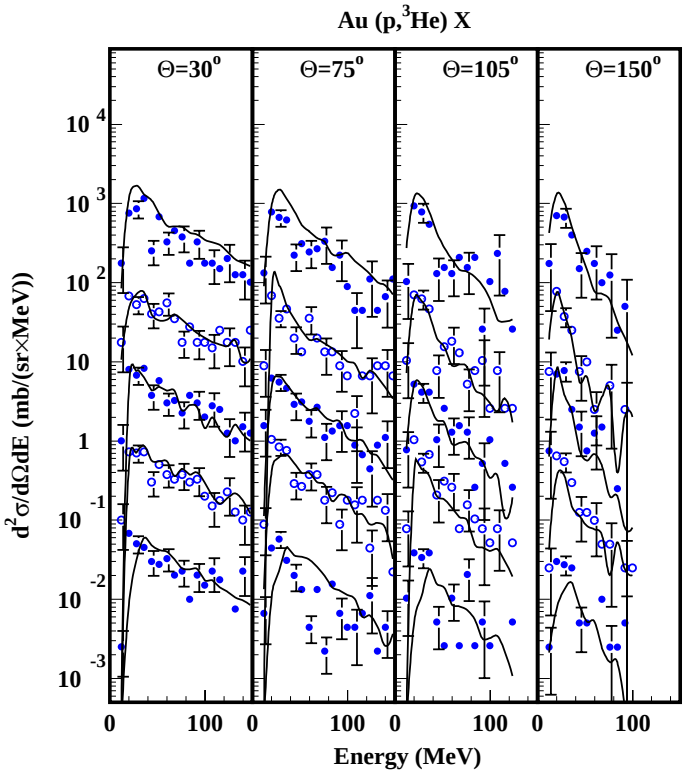

Figure 3.23 : *Doubly differential cross sections for the emission of ^{3}He, observed at Θ=30°, 75°, 150° and for five bins in E^* (from top to bottom: E^*=0-220, 220-370, 370-470, 470-570,>570 MeV). The experimental data are indicated by dots, the simulation which now includes coalescence is shown as lines. A scaling factor 10^i, i=0-4 has been applied to the spectra in each panel, beginning with i=0 at the bottom.*

In summary the experimental data from NESSI represent strong constrains on the comparison with state of the art model calculations and therefore provide an important benchmark for obtaining key parameters necessary to design and construct of ADS systems and future spallation sources.

(b) The PISA experimental setup

The international collaboration PISA (Proton Induced SpAllation) has built a detector system and has initiated measurements of total and double-differential cross-sections for products of spallation reactions on a wide range of target nuclei (C-U) at the proton accelerator COSY in Jülich (Germany) in order to study secondary particle production created in structural-, window- and target-materials by proton beams up to 2.5 GeV incident kinetic energy. Residual nuclei---as H, He up to intermediate mass fragment (IMF)---production cross sections are of great importance for estimations of damages of target- and structure-materials of the planned spallation neutron sources since the lifetime of window and target materials is directly associated to those cross sections.

The achievements we managed to reach with the PISA experiment at the COSY accelerator went far beyond the originally offered design, construction and final layout of the experimental facility. After a quick and successful installation of the PISA scattering chamber and the complex detector devices at the internal ring of the cooler synchrotron first preliminary measurements were taken as already reported on in the HINDAS annual report 2002 providing an extensive set of benchmark data in the GeV incident p-energy range where few and moreover quite diverging data exist. With the PISA experiments the aims were:

- understanding the complex reaction mechanism itself by a comprehensive and systematic description of all nuclear reactions and measurement of kinetic energies and angular distributions of the ejectiles.
- testing and increasing the reliability of physical models describing both the fast intranuclear cascade (INC) phase as well as the subsequent statistical decay from an equilibrated or thermalized hot nucleus.
- developing new models for the description of highly energetic *composite* particles (there exist no models being capable of reliably predicting production cross sections, energy spectra or angular distributions).
- planning and construction of high intense neutron spallation sources, since the production cross sections are of particular interest for studying radiation damage in target-, window- and structural-materials. Helium, for instance, is known to destroy the mechanical strength of solids, which limits the lifetime of window and target (if solid). The production of tritium as a radioactive gas of considerable toxicity has bearings on radiation safety provisions.
- providing the Li, Be and B data in proton-induced reactions on light targets (up to Fe), which are of crucial importance for understanding the anomalous abundance of light elements in the cosmic rays (compared to solar system) and astrophysical questions of nucleosynthesis of the light nuclei in general.

The mass dependence of the production cross sections (for full range of targets from Carbon to Uranium) should shed light on the competition of various mechanisms of interaction of protons with nuclei and fill the currently existing lack of systematical data on the evolution of the production process as a function of bombarding energy and mass of the decaying system. Therefore one of the main tasks of the PISA investigations is the determination of various IMF yields in their full kinetic energy range for several targets and incident proton energies. The PISA set up---allowing for rather low (<1 MeV/A) energy thresholds---is perfectly suited as an experimental detection system

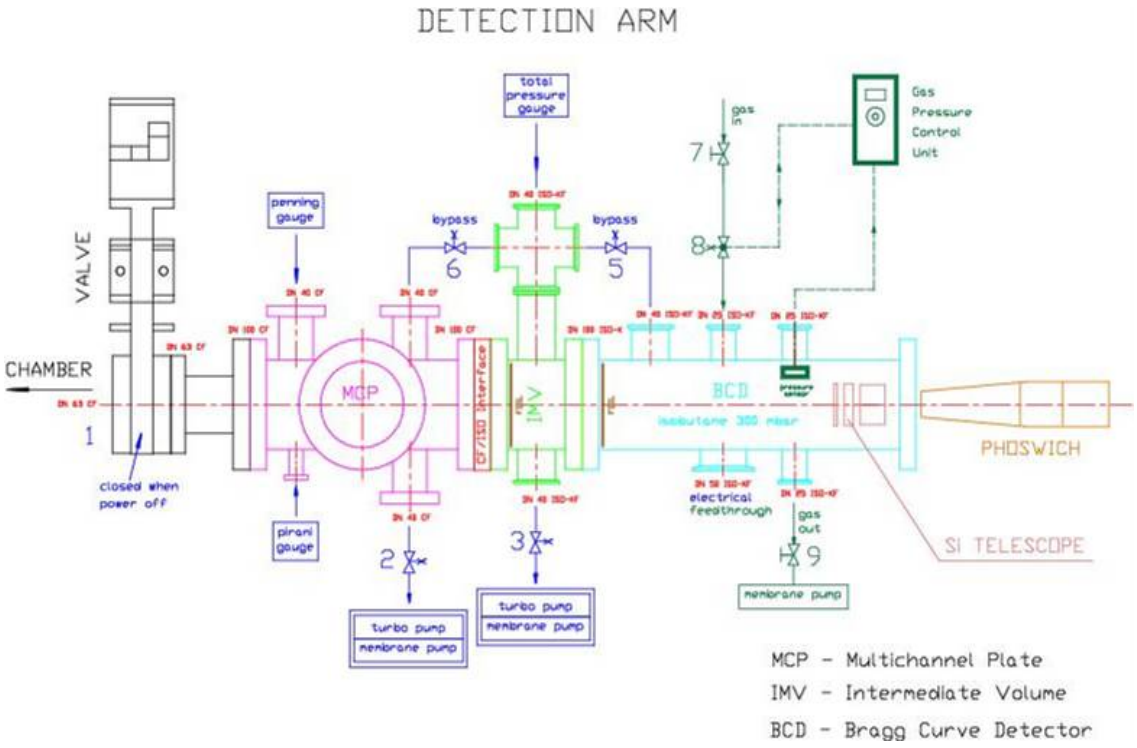

Figure 3.24 : *Full detector arm mounted as mounted at 15 and 120^{o} equipped with Bragg curve-, channelplate- and phoswich-detectors.*

Each of the eight (currently only the most forward and the most backward detection arms are mounted) detection arms mounted at the scattering chamber (see Fig. 3.24) of the PISA experiment consists of two Multichannel Plates (MCP) working as “Start” and “Stop” detectors for the time of flight measurement, a BCD followed by three silicon detectors of 100, 300 and 4900 μm thickness for particle identification using ΔE-E techniques and kinetic energy measurement of intermediate-mass spallation products, and a set of double layer scintillation detectors - fast and slow (phoswich) - in order to identify light charged evaporation and spallation products like p, d, t, He. It is shown that the TOF plus BCDs provide identification of light heavy ions with mass up to 20 - 30 and kinetic energy starting from less than 1 MeV/amu.

These results op the PISA experiments are the first of a programme that will extend beyond the scope of the HINDAS project. Together with the SPALADIN project, described at the end of section 3.2.3.(d), it will allow a more detailed understanding of the reaction maechanisms.

3.2.3. Experimental results on residue production

In addition to the detailed understanding of the neutronics and the complex transport phenomena of light particles, the production of heavy residues by proton- and neutron-induced fragmentation and fission reactions needs to be known for the design of ADS, because it has decisive consequences for the shielding and the activation of the installation, the radiation damages of construction materials and the chemical properties of the spallation target.

(a) Status before starting the HINDAS project

The conventional experiments on residual-nuclide production in proton- and neutron-induced reactions are performed by bombarding various target materials with protons or neutrons of the energy of interest and by analyzing the produced species after irradiation, e.g. by their radioactive decay or by off-line and on-line mass spectrometry [Ros83, Cun47, Wol56, Fri63, Kla69, Sau83, Glo01]. These methods can only give a limited insight into the reaction mechanism, because short-lived products, which form the dominant production in most cases, cannot be observed due to the time delay between the irradiation and the measurement. Information on the reaction kinematics is also not easily accessible. In addition, stable nuclides could only be detected with much effort e.g. by off-line mass spectrometry. As documented in a comprehensive intercomparison [Mic97], the experimental information was insufficient to develop reliable models. In the course of the concerted action “Lead for ATD”, which preceded the HINDAS project, an innovative experimental method has been developed, which copes with this problem. This new approach is based on the bombardment of an hydrogen target with heavy projectiles. That means that the experiment is performed in inverse kinematics. The reaction products are identified in-flight in mass and atomic number in a high-resolution spectrometer. At the same time, information on the reaction kinematics is available. Using this technique, during the HINDAS project large sets of new experimental data with unprecedented quality have been accumulated.

Still, continued effort was invested using the conventional techniques, providing very important complementary information on the energy dependence of the production of specific nuclides. Such information, which is extremely valuable for the understanding of the energy dependence of the different reaction mechanisms, cannot easily be obtained by the inverse-kinematics technique due to the large effort for performing and analyzing these experiments. In addition, the experiments based on decay spectroscopy give a direct measurement on long-term activation. The combined information of these two techniques formed the basis for an

improved understanding of the nuclear-reaction aspects and for essential improvements of the nuclear models, which now allow for performing considerably more realistic calculations.

(b) Reverse kinematics measurements at GSI

We report here on the complete isotopic production cross sections for a long series of elements, measured in the inverse-kinematics spallation reaction of 1 GeV protons and 2 GeV deuterons with lead and uranium. In addition, the velocity distributions of all the produced isotopes were measured, giving crucial information on the reaction mechanisms involved. Most of these results have been published in scientific journals [Wla00, Enq01, Enq02, Tai03, Ber03]. Others are documented in PhD theses [Cas01, Per03, Ric03] and will be published soon.

- Experimental method

The experimental method and the analysis procedure have been developed and applied in previous experiments [Jon98, Enq99, Ben99b, Ben01, Rej01]. The primary beam of 1 *A* GeV ^{208}Pb and 1 *A* GeV ^{238}U, respectively, was delivered by the heavy-ion synchrotron SIS at GSI, Darmstadt. The dedicated experimental set up is shown in Fig. 3.25. The proton target and the deuteron target were composed of 87.3 mg/cm^2 liquid hydrogen [Che97] and of 206 mg/cm^2 liquid deuteron, respectively, enclosed between thin titanium foils of a total thickness of 36 mg/cm^2. The primary-beam intensity was continuously monitored by a beam-intensity monitor based on secondary-electron emission [Jun96, Jur02]. In order to subtract the contribution of the target windows from the measured reaction rate, measurements were repeated with the empty target. Heavy residues produced in the target were all strongly forward focused due to the inverse kinematics. They were identified using the Fragment Separator (FRS) [Gei92] and the associated detector equipment.

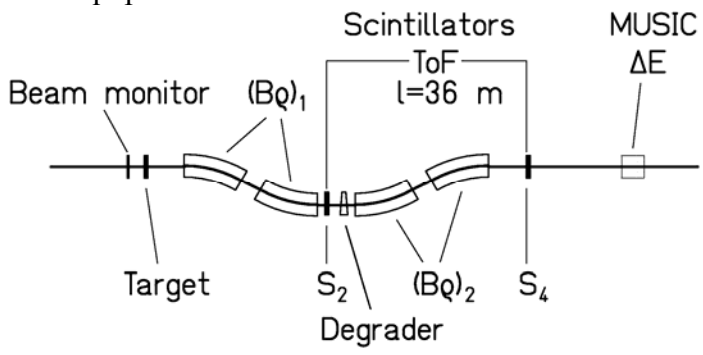

Figure 3.25 *: Schematic drawing of the fragment separator FRS with the detector equipment. For details see text.*

The FRS is a two-stage magnetic spectrometer with a dispersive intermediate image plane (S_2) and an achromatic final image plane (S_4) with a momentum acceptance of 3% and an angular acceptance of about 15 mrad around the beam axis. Two position-sensitive plastic scintillators placed at S_2 and S_4, respectively, provided the magnetic-rigidity ($B\rho$) and time-of-flight measurements, which allowed determining the mass-over-charge ratio of the particles. For an unambiguous isotopic identification of the reaction products, the analysis was restricted to ions, which passed both stages of the fragment separator fully stripped. The losses in counting rate due to the fraction of incompletely stripped ions and the losses due to secondary reactions in the layers of matter in the beam line were corrected for [Enq01]. To identify all residues in the whole nuclear-charge range up to the projectile, it was necessary to use two independent methods in the analysis. The nuclear charges of the lighter elements, mainly produced by fission, were deduced from the energy loss in an ionisation chamber (MUSIC) with a

resolution $Z/\Delta Z$ = 170 obtained for the primary beam. Combining this information with the mass-over-charge ratio, a complete isotopic identification was performed. A mass resolution of $A/\Delta A$ = 480 was achieved. Since part of the heavier reaction products was not completely stripped, the MUSIC signal was not sufficient for an unambiguous Z identification. Therefore, the identification of reaction products of elements above terbium was performed with the help of an achromatic energy degrader [Sch87] placed at the intermediate image plane of the FRS. Degrader thicknesses of about 5 g/cm^2 of aluminium were used. The nuclear charge of the products was deduced from the reduction in magnetic rigidity by the slowing down in the energy degrader. The MUSIC signal was still essential for suppressing events of incompletely stripped ions and from nuclei destroyed by secondary reactions in the degrader. The velocity of the identified residue was determined at S_2 from the $B\rho$ value and transformed into the frame of the beam in the middle of the target, taking into account the appropriate energy loss. More than 100 different values of the magnetic fields were used in steps of about 2 % in order to cover all the produced residues and to construct the full velocity distribution of each residue in one projectile-target combination.

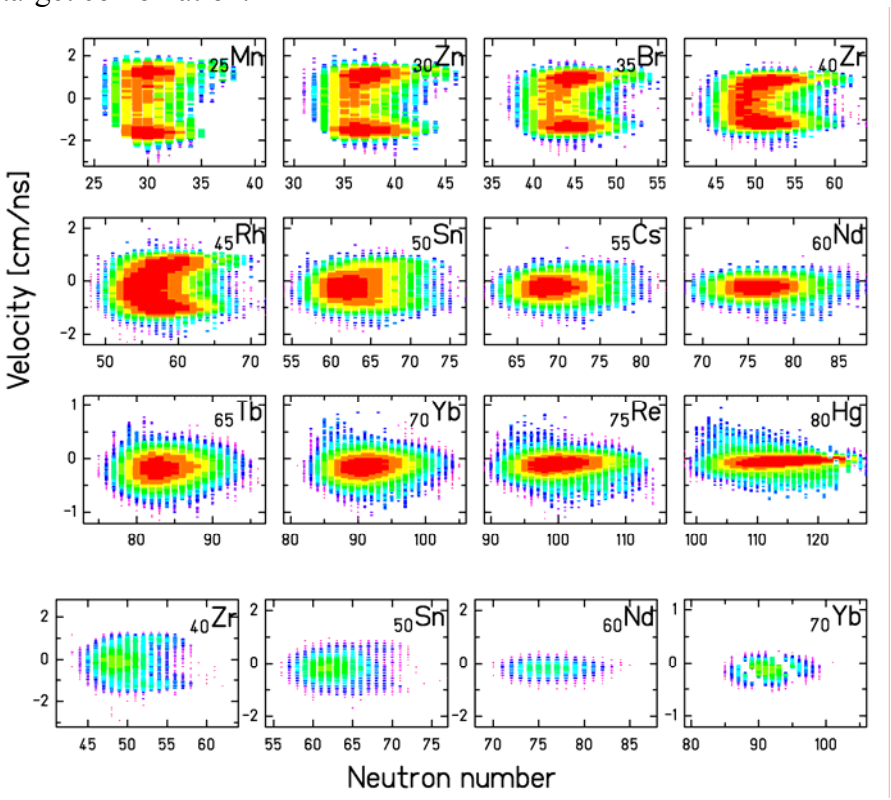

Figure 3.26 : *Two-dimensional cluster plots of velocity versus neutron number for 12 selected elements produced in the reaction ^{208}Pb + ^{2}H at 1* A *GeV. The three uppermost rows show the reaction rate with the full target and the lowest row with the empty target (target windows). The velocity is given in the centre-of-mass system of the primary beam in the middle of the target. The intensity scale is logarithmic and different for each element, the full and empty target contributions can directly be compared. The distribution of the ytterbium isotopes produced in the empty target was incompletely measured, the contributions of the three spectrometer settings are visible. Note also the different scales in velocity in different rows.*

The re-construction of the full velocity distribution allows for disentangling reaction products formed in fragmentation and fission reactions due to their different kinematic properties. The velocity distributions as a function of neutron number for 12 selected elements of one of the systems investigated are shown in Fig. 3.26 as cluster plots. It can be seen from the distributions that the reaction products can be attributed to different reaction mechanisms, i.e. spallation-evaporation and spallation-fission. For isotopes close to the projectile, one or two

settings are able to cover the whole distribution of one isotope. Around mass region 150, three or four settings are needed. For isotopes produced by fission, only those emitted either in forward or in backward direction with respect to the primary beam can be observed in a given setting of the FRS because the angular acceptance is too small for sideward emitted fragments [Ben02]. The production of lighter elements from fragmentation ($Z \leq 60$, and mean velocity centred close to the primary-beam velocity) seen in Fig. B.26, does not result from primary reactions in the liquid-hydrogen target, but from secondary reactions or from reactions in the titanium target windows.

- *Measured cross sections*

The production of residual nuclides has been investigated for four systems which are particularly relevant for the design of accelerator-driven systems. The production rates were measured for a total number of 1056 nuclides in the reaction ^{208}Pb + ^{1}H, for 1037 nuclides in the reaction ^{208}Pb + ^{2}H, for 1220 nuclides in the reaction ^{238}U + ^{1}H, and for 1369 nuclides in the reaction ^{238}U + ^{2}H. These data are depicted on a chart of the nuclides in Figs. 3.27 and 3.28. The velocity distributions of all these nuclides were determined at the same time. The different regions on the chart of the nuclides, produced by spallation-evaporation and by spallation-fission reactions, respectively, can clearly be distinguished. In the reactions with the deuteron target, which induce roughly a factor of two more energy into the system, the production of spallation-evaporation residues extends to appreciably lighter nuclides, while the fission distributions are much less affected. This can be also seen in Fig. 3.29, which compares the isotopic distributions for several elements measured in the reactions of ^{238}U in proton- and deuteron-target.

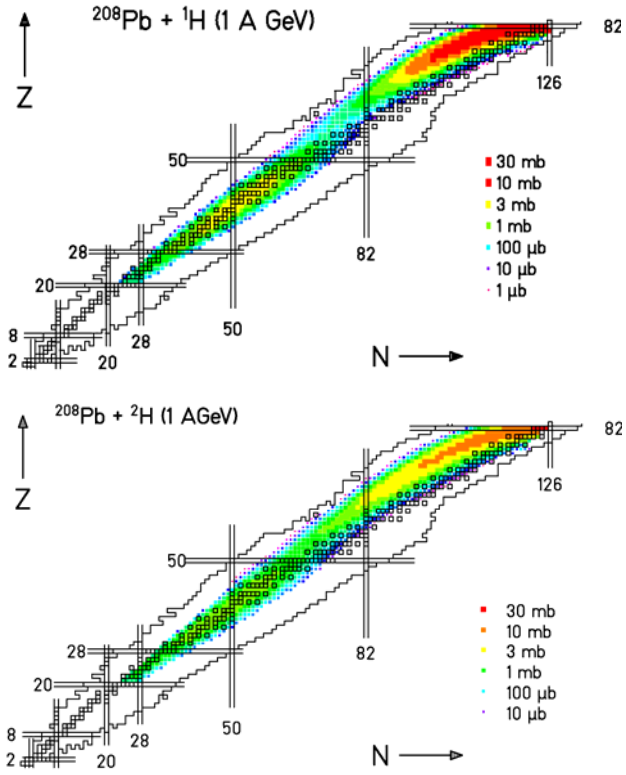

Figure 3.27 : *Residual nuclide cross sections for the reaction ^{208}Pb + ^{1}H and ^{208}Pb + ^{2}H at 1* A *GeV on a chart of the nuclides. Primordial nuclei are marked by open squares, the outer line gives the range of known nuclides, and the shell closures are indicated by double lines.*

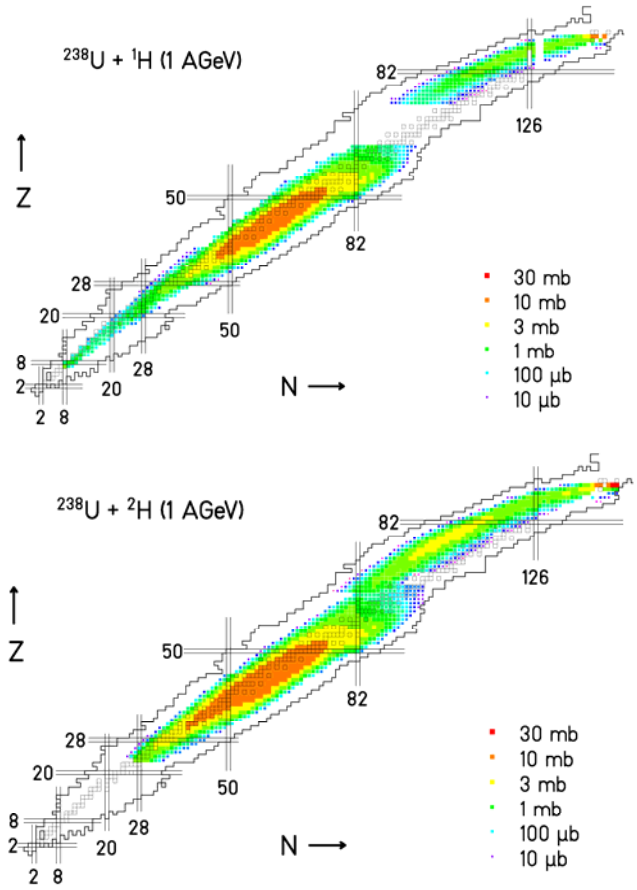

Figure 3.28 : *Residual nuclide cross sections for the reaction* $^{238}U + {}^{1}H$ *and* $^{238}U + {}^{2}H$ *at 1* A *GeV.*

For the elements close to the ^{238}U projectile, the production cross sections are almost the same. In fact, these isotopes are produced in very peripheral collisions, where in the case of the deuteron- induced reaction only one nucleon, i.e. the proton or the neutron, interacts with the projectile making then the reactions ^{238}U (1 *A* GeV) + p and ^{238}U(1 *A* GeV) + d looking similar. On the other hand, going away from the projectile (e.g. *Z*= 76, 80 in Fig. 3.29) deviations between these two reactions appear. This is a region, where both nucleons of the deuteron target interact with the projectile, thus introducing almost two times more excitation energy in the first stage of reaction compared to the proton-induced reaction. This would then results in not only higher cross sections for the production of light spallation-evaporation residues, but also in the production of lighter spallation-evaporation residues (see Fig. 3.28) in the reaction ^{238}U(1 *A* GeV) + d as compared to the reaction ^{238}U(1 *A* GeV) + p.

In fission cross sections, there are not so many differences to be expected between these two reactions, as can be seen in Figs. B.28 and B.29. In the case of lighter fission fragments (e.g. *Z*=44 in Fig. 3.29), the neutron-deficient isotopes are produced slightly more abundantly in the ^{238}U + d reaction, while the neutron-rich side seems to be equally populated. This difference can be understood as an indication that the prefragments from the reaction ^{238}U + d extend to higher excitation energies, and thus the evaporation chains extend to lighter and more neutron-deficient fission fragments. All this discussion is also valid for the ^{208}Pb + p,d reactions at 1 *A* GeV.

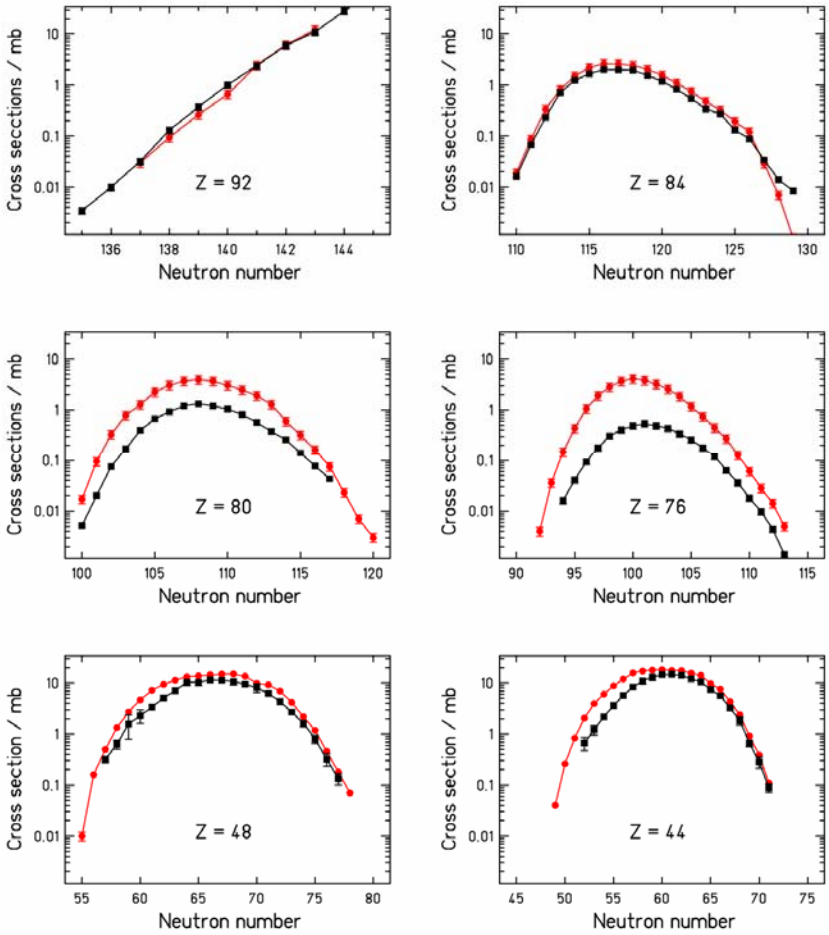

Figure 3.29 : *Isotopic distributions for several elements measured in the reactions of ^{238}U at 1* A *GeV with protons (black squares) and deuterons (red dots).*

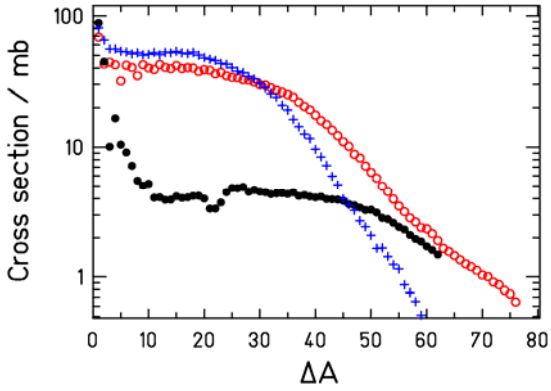

Figure 3.30 : *Isobaric cross sections as a function of mass loss for three reactions: The full symbols mark the system ^{238}U + ^{1}H at 1* A *GeV, open symbols represent the system ^{208}Pb + ^{1}H at 1* A *GeV, and the crosses result from the reaction ^{197}Au + ^{1}H at 0.8* A *GeV [Rej01].*

Another valuable information on the reaction aspects that these data can provide concerns the influence of dissipation on the fission dynamics at high excitation energies. Thanks to the measurement of the full isotopic chains, we are able to produce sensible isobaric cross sections, this means, cross sections summed up over the full isobaric chains. The associated plot is reproduced in Fig. 3.30, which shows the isobaric distributions for three reactions: ^{238}U

+ p, ^{208}Pb + p, both at 1 *A* GeV, and ^{197}Au + p at 0.8 *A* GeV from Ref. [Rej01]. The isobaric cross section is figured as a function of the mass loss.

As far as low-fissility nuclei are concerned (gold and lead), the trends are very much similar. The main difference can be observed for the lowest mass. The lighter evaporation residues are less produced in the gold experiment. The explanation appears clearly when one considers the difference in term of projectile energy. Within the frame of a two-stage model, the first phase of the interaction leads to the production of an excited nucleus. The excitation spectrum depends on the energy of the projectile. The fastest projectile leads to the highest excitation energy (as far as the so-called limiting fragmentation regime is not reached) inducing the longest evaporation chain and producing the lightest evaporation residues. The height of both distributions (spallation of gold and lead) is similar for the heaviest residues. Concerning the spallation of uranium, the shape and the height of the isobaric distribution is pretty different.

As far as uranium is concerned, we notice a slight dip for mass losses close to 22. This depression is due to the very fast alpha decay of N = 128 isotones toward the 126-neutron shell. In fact, several isotopes characterized by a number of 128 neutrons decay by α emission toward the 126-neutron shell. The decay period of those isotopes is of the order of the time-of-flight through the FRS (150 ns eigen-time). Therefore, part of the production is lost before being analysed and identified. Moreover, when the decay occurs at the very beginning of the flight path, the ion is ”seen” as the daughter nucleus. This effect causes the slight “hump” that can be observed. Below a loss of 60 mass units, the cross sections are notably lower in the uranium case than obtained for the two other experiments. The effect is stronger for the heaviest fragments. The explanation lies in the strong depletion effect of the fission process for actinide nuclei. During the evaporation phase, the fission probability is much higher for actinides than for rare earth nuclei, which are involved in spallation of gold or lead. Thus, in the case of uranium, the production of evaporation residues is paradoxically very much influenced by the fission mechanism.

Looking carefully at the isobaric cross sections shown in Fig. 3.30, the first qualitative observation is that the distributions associated to the lead and uranium experiments join for mass loss close to 60. The depletion effect observed on the cross section for the heaviest nuclei seems to vanish for the lightest evaporation residues. In the two-stage model, this observation seems surprising. Actually, the first step of the reaction leads to the production of an excited prefragment. The mass and nuclear charge of this nucleus is close to the one of the projectile (5 to 10 nucleons could be removed). Therefore, the light evaporation residues (for instance with a mass loss equal to 60 compared to the projectile) are consecutive to a very long evaporation chain starting in the actinide region. The fact that the light evaporation residues are not depopulated in the uranium case compared to the lead one indicates that the fission probability along the extensive de-excitation path is rather low. This rather astonishes considering that this path crosses the actinide and pre-actinide regions, where the fission barriers are low. The explanation lies in the inhibition of the fission process for highly excited nuclei. In such a case, the typical de-excitation times are rather short, always much shorter than the time needed for equilibrating the fission-degree of freedom. Consequently, the fission channel is not open for highly excited actinides. When the nucleus cools down, emitting nucleons and light charged particles, the typical emission time increases, allowing the fission process to occur. For more details, see the Theory report of the High-Energy contribution.

- *Velocity distribution*

The experimental set up allows determining the recoil-velocity properties of the produced nuclei. In this section, we present the results for the systems ^{238}U + p and ^{208}Pb+p. The values

for the system ^{238}U + d and ^{208}Pb + d turned out to be rather similar. For the spallation-evaporation residues, the velocity distributions are well represented by Gaussian distributions. The mean value and the standard deviation of the recoil-velocity distribution were determined for each ion. The slowing down in the target area, assuming that the nuclear reaction occurred in the middle of the target on the average, was accounted for.

In Fig. 3.31a are plotted the mean velocities normalised following the prescriptions of Morrissey [Mor89] for systems ^{238}U + p and ^{208}Pb + p. Thus, we introduce $p'_{\|}$, which is the longitudinal recoil momentum, normalized in the following way:

$$p'_{\|} = v_{\|} * M_p * (\beta\gamma/(\gamma+1))$$

This normalisation allows an inter-comparison of various measurements realised at different projectile energies. The location straggling is also unfolded for estimating the standard deviation of the velocity distribution. Note, however, that this contribution is negligible. Fig. 3.31a also includes the empirical systematics stated by Morrissey [Mor89], which predicts a linear dependence between the reduced recoil momentum ($p'_{\|}$) and the mass loss (relative to the mass of the projectile). We observe that the systematics describes reasonably well the measured data. The width of the longitudinal recoil momentum acquired in the spallation-evaporation reaction is shown in Fig. 3.31b for systems ^{238}U + p and ^{208}Pb + p. Again, the data are compared with the systematics of Morrissey, and also with the predictions of the Goldhaber model [Gol74]. While the systematics better represents the data for mass losses below $\Delta A = 20$, the experimental values increase more strongly for large mass losses and reach the prediction of the Goldhaber model for $\Delta A \approx 55$.

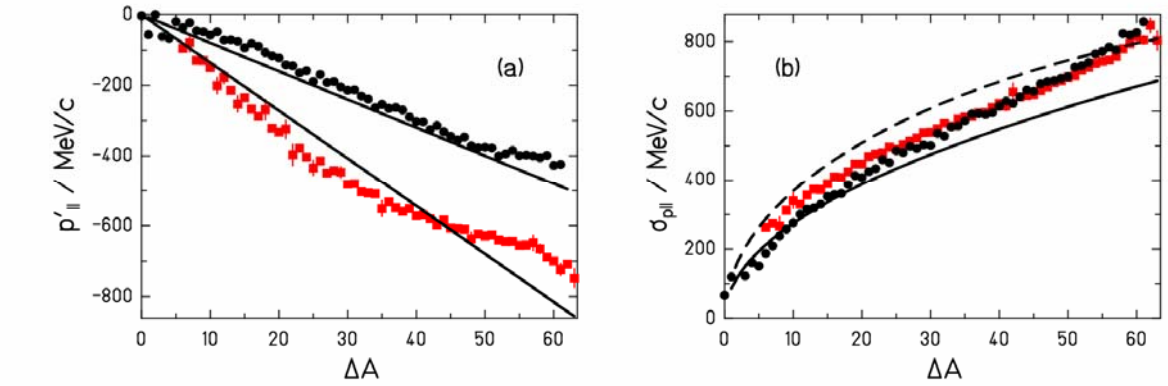

Figure 3.31 : *(a) Mean recoil momentum induced in the spallation of ^{238}U (black dots) and ^{208}Pb (red squares) by 1 GeV protons as a function of mass loss. The experimental data (symbols) are compared with the systematics of Morrissey [Mor89] (full line). (b) Standard deviation of the longitudinal momentum distribution of the spallation-evaporation residues produced in the bombardment of ^{238}U and ^{208}Pb with 1 GeV protons. The experimental data (symbols) are compared with the Goldhaber model [Gol74] (dashed line) and with the Morrissey systematics [Mor89] (full line). Since the measurement has been performed in inverse kinematics, the measured momenta and standard deviation are transformed into the frame of the beam.*

The mean velocity values induced in the fission process are shown in Fig. 3.32 for systems ^{238}U + p (left part) and ^{208}Pb + p (right part) both measured at 1 A GeV. The velocity values are obtained from the plots similar to Fig. 3.26, averaged over the mass and corrected for the effect of the finite angular acceptance of the FRS. All fission velocities are consistent with the binary decay of a heavy nuclear system between lead and uranium for the ^{238}U + p reaction,

and between hafnium and lead in the case of the ^{208}Pb + p reaction. The strong variation of the fission velocity with the atomic number of the fission fragment is mostly given by momentum conservation.

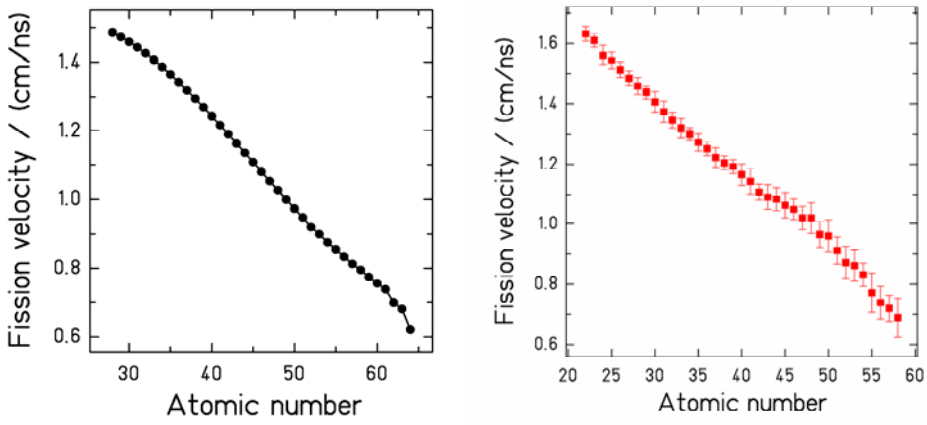

Figure 3.32 : *Measured mean velocities of the fission fragments produced in the spallation-fission reaction of ^{238}U (left) and ^{208}Pb (right) induced by 1 GeV protons as a function of the atomic number of the fission fragments. Since the measurement has been performed in inverse kinematics, the velocities are transformed into the frame of the beam.*

Conclusion

A total number of 4682 individual nuclide production cross sections and velocity distributions in the reactions of 1 *A* GeV ^{238}U and ^{208}Pb with proton- and deuteron-target have been studied, covering most elements between oxygen and uranium. The reaction products were fully identified in atomic number *Z* and mass number *A* using the magnetic spectrometer FRS. Moreover, the velocity distribution of each individual nucleus was measured.
The data, production cross sections and energies, are of highest interest for the design of accelerator-driven systems. Using the measured production cross sections, combined with the known decay properties, the short- and long-term radioactivities in the target material can be calculated. The number of atomic displacements being the reason for radiation damages in the structural materials can now be estimated from the measured kinetic-energy distributions. The data also allow estimating the admixtures of specific chemical elements in the liquid target, accumulated in long-term operation of the reactor, which enhance the corrosion of the walls or any material in the container.
The systems investigated provide stringent constraints to nuclear-reaction codes, in particular to the modelling of the fission competition and the nuclide production in fission. The new data will help to develop improved models with better predictive power for spallation reactions involving highly fissile nuclei.

(c) Excitation function of residual nuclide production by proton-induced reactions

For proton-induced reactions, the efforts of the HINDAS project aimed to further developing and completing the cross section database which was established by our collaboration in recent years; [Mic97a] and references therein. During the HINDAS project the data base was extended to the heavy target elements Ta, W, Pb, and Bi [Glo01, Mic02, Mia02]. Further, about 560 new cross sections for the production of 19 radionuclides from the target element iron have been measured from thresholds up to 2.6 GeV. For the target element lead a comprehensive set of excitation functions published recently [Glo01] was completed by

AMS-measurements of cross sections for the production of the long-lived radionuclides ^{10}Be, ^{36}Cl, and ^{129}I and by mass spectrometric measurements of for stable and radioactive rare gas isotopes of He, Ne, Ar, Kr, and Xe. Irradiation experiments with natural uranium were performed at the injector cyclotron at PSI using the stacked-foil technique and subsequent gamma-spectrometry. About 400 cross sections for the production of 18 radionuclides for energies from 21 MeV to 69 MeV were measured.

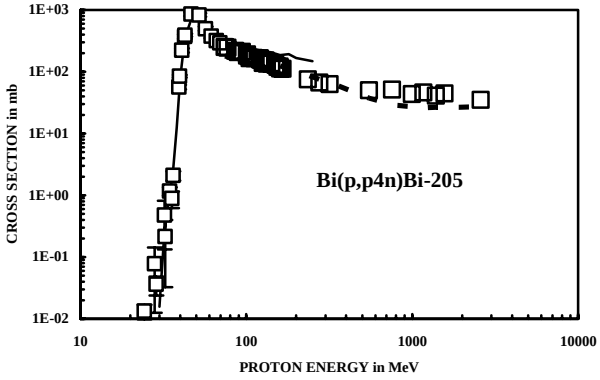

Figure 3.33 : *Production of ^{205}Bi from bismuth by proton-induced reactions. Comparison of experimental results (squares) with theoretical cross sections calculated with INCL4+ABLA (broken line) and TALYS (solid line).*

These investigations make use of classical kinematics and therefore are confined to residual nuclides with usually at least a few hours' half-lives which mostly reveal a cumulative production due to the decay of short-lived progenitors. These investigations are complimentary to those using inverse kinematics where the primary residuals can be studied. While inverse kinematics allows to study in detail the isobaric and isotopic production cross sections at certain energy points, the classical kinematics allows studying the energy dependence from thresholds up to the highest energies which are 2.6 GeV for proton-induced reactions of this work.

All these data allow for stringent tests of nuclear models and codes when calculating cross sections for residual nuclide production from thresholds up to 2.6 GeV. The new codes are the TALYS code for energies up to about 200 MeV and the INCL4+ABLA code for higher energies. Comprehensive tests of the new codes, TALYS and INCL4+ABLA, for Fe, W, Ta, Pb, Bi, and U for energies from thresholds up to 2.6 GeV are underway.

For proton-induced reactions on uranium, there were not too many cross sections for the production of residual nuclides available in literature. Moreover, they were mostly old and neither systematic nor comprehensive with respect to the product nuclide and energy coverage. To improve this situation, further collaborations were initiated during the HINDAS project. First results on the production of residual nuclides from natural uranium by proton-induced reactions at 600 MeV are available [Ada03] and evaluations of past irradiation experiments of thorium and uranium at SATURNE for energies between 200 MeV and 2.6 GeV are underway.

Due to the efforts of the HINDAS project there now exists a comprehensive and consistent database of cross sections for the production of residual nuclides by proton-induced reactions on the heavy target elements Ta, W, Pb, and Bi from thresholds up to 2.6 GeV. Some

examples for the target element bismuth are given in Figs. 3.33 and 3.34. This database allows validating the newly developed codes TALYS and INCL4+ABLA by systematic comparisons. Fig. 3.35 exemplifies such an intercomparison for light fission products from Ta, W, Pb, and Bi.

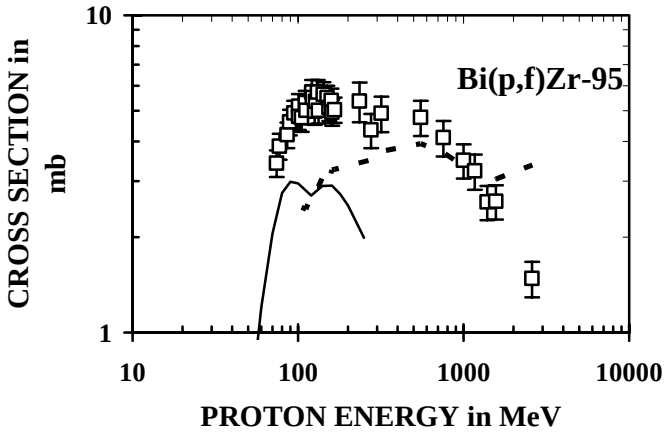

Figure 3.34 : *Production of ^{95}Zr from bismuth by proton-induced reactions. Comparison of experimental results (squares) with theoretical cross sections calculated with INCL4+ABLA (broken line) and TALYS (solid line).*

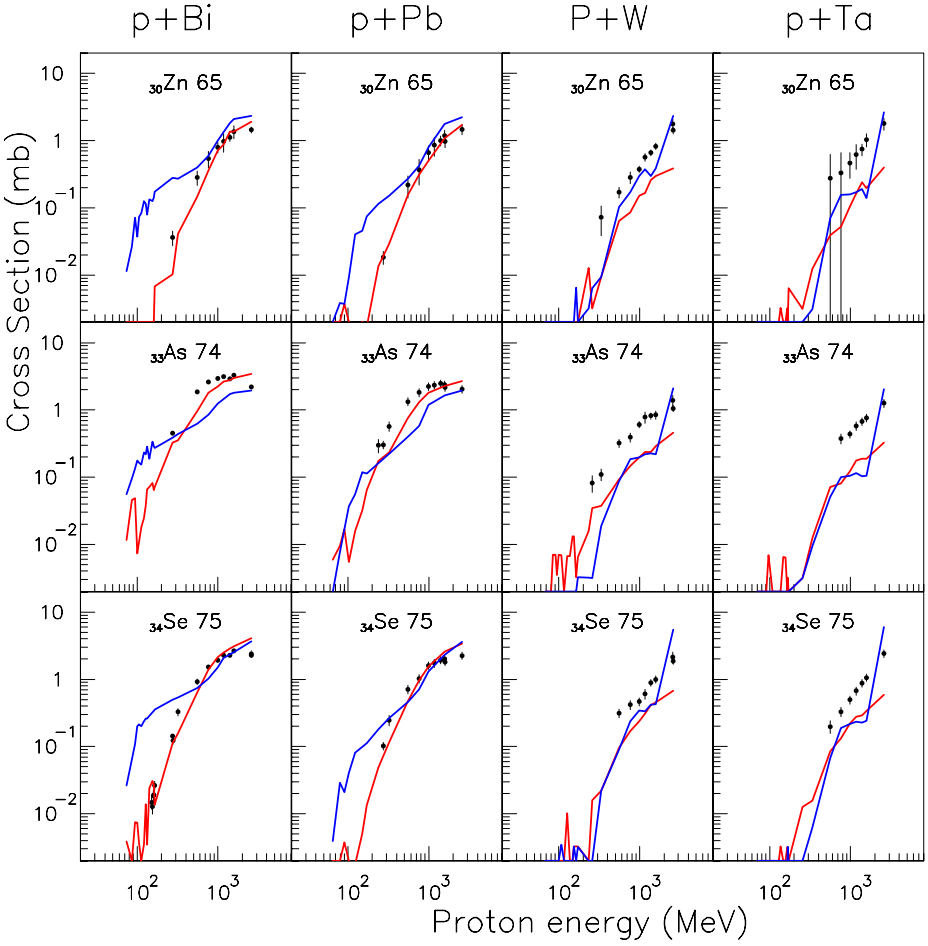

Figure 3.35 : *Production of ^{65}Zn, ^{74}As, and ^{75}Se from tantalum, tungsten, lead, and bismuth. Comparison of experimental results (squares) with theoretical cross sections calculated with INCL4+ABLA (red line) and a Bertini-Dresner code (blue line).*

Production of long-lived radionuclides and rare gas isotopes from lead

Long-lived residue nuclide production has to be considered as essential recording to waste management problems in ADS systems. About 60 radionuclides with half-lives over 10 years are known, which can be produced in spallation reactions. The cross sections for the production of these nuclides are scarcely known. Due to the long half-lives and the absence of measurable radiation the determination of ^{129}I ($T_{1/2} = 1.6 \times 10^7$ a), ^{36}Cl ($T_{1/2} = 3.0 \times 10^5$ a), ^{26}Al ($T_{1/2} = 7.2 \times 10^5$ a) and ^{10}Be ($T_{1/2} = 1.6 \times 10^6$ a) must be carried out by AMS-measurement, a method which is very sensitive but requires careful and time-consuming sample preparation. During the HINDAS project the excitation functions for the production of these long-live radionuclides by proton-induced reactions from natural lead were measured using AMS at ETH Hönggerberg. The chemical separation scheme developed for this purpose is given in Fig. 3.36. It also allows for further determinations of other radionuclides.

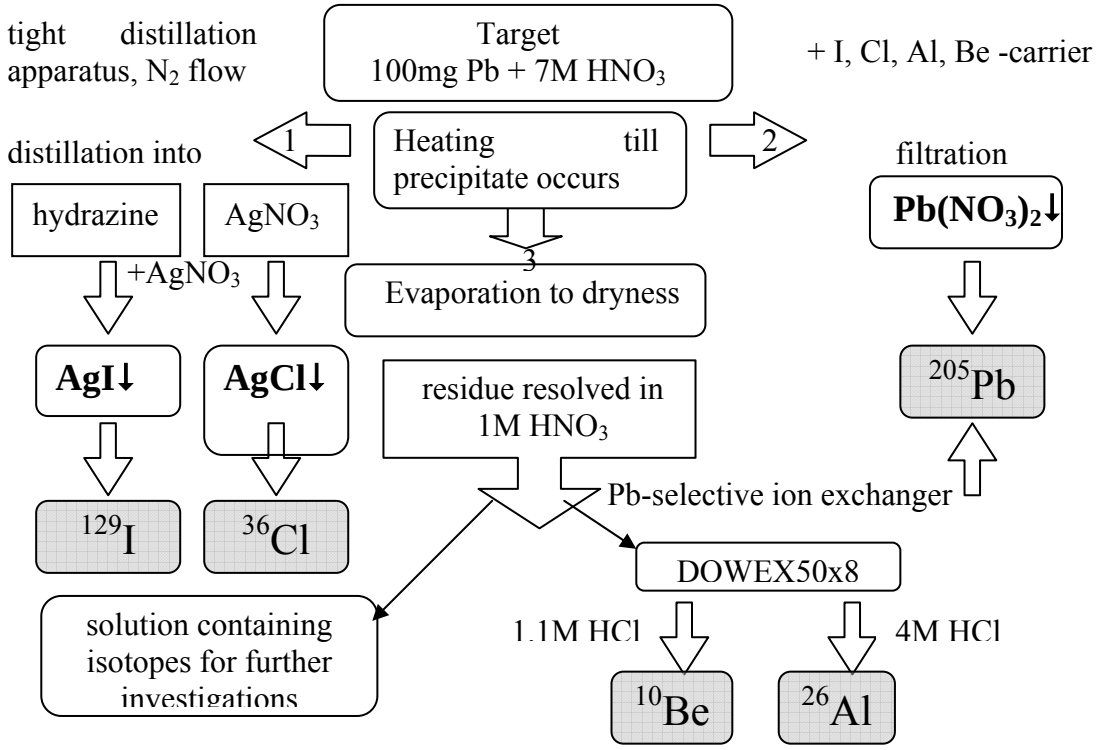

Figure 3.36 *: Chemical separation scheme for the isolation of the nuclides ^{129}I, ^{36}Cl, ^{26}Al, and ^{10}Be.*

The target material (ca. 200 mg) and the carrier for the 4 elements (10 mg I, 10 mg Cl, 2 mg Al and 2 mg Be) were filled into a three-neck flask and dissolved in half-concentrated HNO_3 under N_2-flow. The flask was heated slightly for better dissolving and to distil iodine into hydrazine-solution. After that, chlorine was distilled into $AgNO_3$-solution. The macro amount of $Pb(NO_3)_2$ was removed by filtration.

The solution in the flask was evaporated to dryness and the residue dissolved in 10 ml 1 M HNO_3. Remaining Pb was removed by adsorption onto a Pb-specific exchange column (Eichrom). The eluate was divided in two equal parts; one is stored for further investigations.

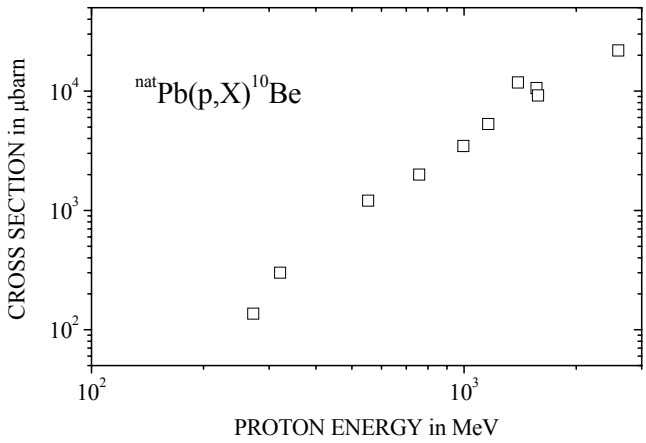

Figure 3.37 : *Cross section of ^{10}Be produced in the bombardment of ^{nat}Pb with protons, in dependence on the proton energy.*

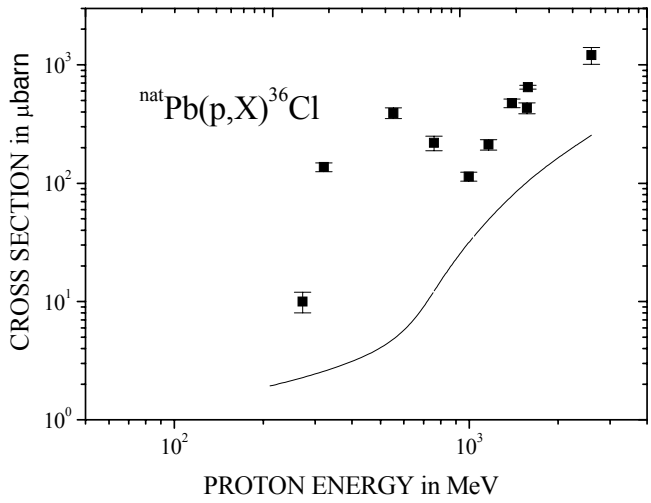

Figure 3.38 *: Cross section of ^{36}Cl produced in the bombardment of ^{nat}Pb with protons, in dependence on the proton energy. The solid lines are theoretical excitation functions calculated by INCL4+ABLA.*

The other part was feed onto a cation exchange column (0.5x3 cm, DOWEX 50x8, 150-200 mesh, H+-form). The column was washed with 20 ml 0.1 M HNO_3 to remove boron. Be was then eluted with 15 ml 1.1 M HCl, after that Al with 4 ml 4 M HCl. The individual elements were then treated as follows. For iodine, the hydrazine solution was acidified with HNO_3; AgI was precipitated, filtrated, and washed with bidistilled water. For chlorine, the precipitate of $AgNO_3$ was solved in NH_3, again precipitated, and washed with bidistilled water. The samples were dried at 80°C. For aluminum and beryllium, the hydroxides were precipitated with NH_3, washed with bidistilled water, and glowed at 800°C.

The cross sections for the production of ^{129}I, ^{36}Cl, ^{26}Al and ^{10}Be are shown in the Figs. 3.37 – 3.39. The lines represent calculations with INCL4+ABLA code. For the production of ^{10}Be, which is formed as a fragmentation product, up to now no nuclear reaction model exists.

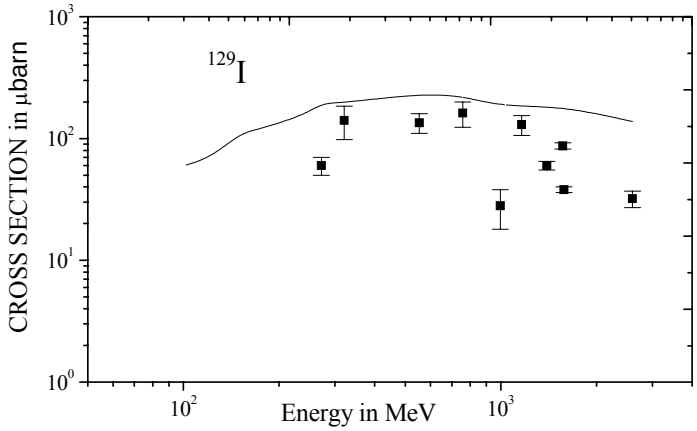

Figure 3.39 : *Cross section of ^{129}I produced in the bombardment of ^{nat}Pb with protons, in dependence on the proton energy. The solid lines are theoretical excitation functions calculated by INCL4+ABLA.*

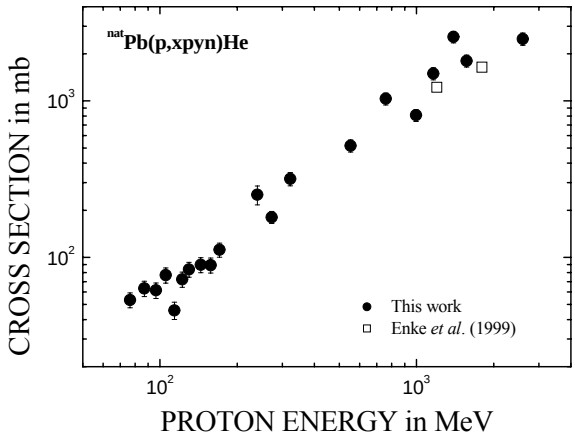

Figure 3.40 : *Excitation function for the production of total He,* i.e. *^3He_d + ^{4}He, from lead by proton-induced reactions. Solid symbols are the results from this work. Open squares are data from the NESSI collaboration [Enk99].*

The production of noble gas isotopes in lead by proton-induced reactions is of special importance for design studies of accelerator driven systems and energy amplifier. Such measurements were performed within the HINDAS project by direct measurement of light gas isotopes by the NESSI collaboration. In addition and in order to test the consistency with earlier mass spectrometric measurements the production of stable and radioactive rare gas isotopes of He-, Ne-, Ar-, Kr-, and Xe from natural lead by proton-induced reactions was investigated from threshold up to 2.6 GeV by rare gas mass spectrometry. Apart from some exceptions the database for the proton-induced production of noble gas isotopes from lead is consistent and nearly complete. In contrast to the production of He from Al and Fe, where the cross sections obtained by thin-target irradiation experiments are up to a factor of 2 higher than the NESSI data, both datasets agree for the He production from lead (Fig. 3.40). Fig. 3.41 gives in addition a comparison of the excitation function for the production of ^{38}Ar from

lead by proton-induced reactions and demonstrates the quality of the theoretical calculations with INCL4+ABLA.

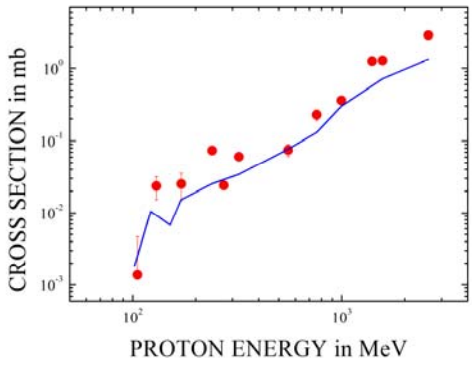

Figure 3.41 : *Production of ^{38}Ar from lead by proton-induced reactions. Comparison of mass spectrometric results (red dots) with theoretical cross sections calculated with INCL4+ABLA.*

(d) Preparative studies for the SPALADIN experiment

The data collected within HINDAS have led to improvements of nuclear models but also raised new questions which appear difficult to answer with inclusive experiments alone. This is why a more complete experiment, called SPALADIN, is in preparation, which aims at measuring as exclusively as possible the final states of the spallation reaction. Its main goal is to reconstruct as completely as possible, the primary fragment after the first stage of the reaction in mass, charge and excitation energy. For this, the heavy residues will be detected as well as the light particles, the nature and the energies of which will be determined to permit a calorimetry of the primary fragments. This experiment will concentrate on the study of the evaporative particles in coincidence with the residual nuclei. Nevertheless, the reconstruction of the residue characteristics before evaporation will allow checking of the modellisation of the first stage of the reaction, described by intra-nuclear cascade models and the various decay modes of the primary residue.

The SPALADIN experiment will use the reverse kinematics technique. The detection in coincidence of the beam fragment and of the light particles (neutrons and charged ones) will be performed event by event. This will enable the detection of the heavy and light charged particles in the same apparatus, the filtering-out of high-energy particles in the final state, leaving detected mainly evaporated particles. This is explained by the fact that the reverse kinematics focuses in the direction of the beam fragment the particles with a small energy in the final state, whereas the high energy particles in the center of mass frame, emitted at small angles with respect to the proton direction in this frame, are emitted, in the lab frame, at rather large angles and small energies.

The selection of particles from the evaporation stage, will allow, in principle, for the reconstruction of the compound nucleus produced at the end of the INC stage. Once this reconstruction is performed, whose result is independent of the evaporation models, a comparison of the mass, charge and excitation energy spectra of the compound nucleus with the predictions of the INC models can be done. Furthermore, a study of the different decay channels as functions of the mass, the charge and the excitation energy of compound nucleus is possible, with a comparison with evaporation codes independently of the INC models.

Experimental set-up and performances

The experimental set-up is sketched on Fig. 3.42. The beam is sent on a liquid hydrogen target (lH2). The t = 0 of the time of flight (ToF) measurements of each event is provided by a scintillator (START) in front of the lH2 target. ToF's are measured for beam fragments as well as for light charged particles (LCP) and neutrons.

In SPALADIN, the heavy fragments ($Z \geq 7$-8) are characterized by: their charged measured twice (in the MUSIC detector behind the target and in the TP MUSIC III downstream of ALADIN), their velocity determined by the RICH (Ring Imaging CHerenkov) and their magnetic rigidity – which gives their masse once their charge is known – by the combination of the information from the high resolution position detectors upstream of ALADIN and from the TP MUSIC III. LCP's are measured in the TP MUSIC III and in the HODOSCOPE planes in charge, magnetic rigidity and momentum (for the compound nucleus excitation energy reconstruction). Neutrons are detected in LAND in multiplicity and, for the low-neutron multiplicity events, also in velocity by ToF. The LCP's were initially thought to be identified in mass and charge and their momentum measured by a set of multiwire proportional chambers (MWPC's) and a scintillator array behind the ALADIN magnet. During two years, in-beam tests have been performed to check the capability of the various detectors on a step-by-step basis, each following step approaching the final design. It appeared that the MWPC's set-up originally planned was too challenging a device to detect LCP's in the heavy-ion environment with the beam passing through the detectors. Hence it was decided to use the TP MUSIC III with its ToF scintillator wall which represents the best alternative the original set-up. The physics trigger of SPALADIN is the coincidence between the START scintillator and LAND.

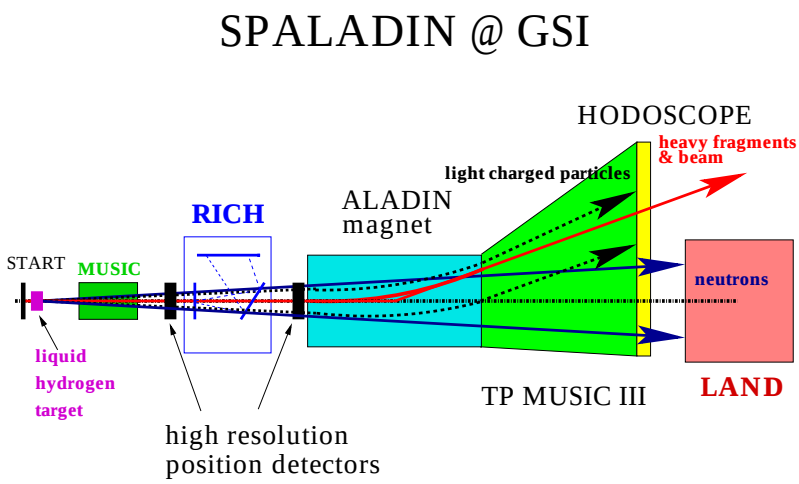

Figure 3.42 : *SPALADIN experimental set-up.*

Building of the experimental setup with, in particular, realization of the high resolution position detectors for the heavy fragments has been achieved during the HINDAS project. In-beam tests of the different part of the setup have been performed which led to the demonstration of the feasibility of the experiment. Achieved performances are the following:

- position resolution upstream of ALADIN: 50 µm (FWHM) in lab.
- position resolution in the TP MUSIC III: 100 µm in beam
- charge resolution in both MUSICs: ΔZ 0.7 (FWHM) in beam
- beam fragment velocity: $\Delta\beta/\beta$ 10^{-3} in beam
- data acquisition rate: 300 events per spill (4 s).

A first experiment with an iron beam will be conducted in 2004. Further experiments with aluminium, carbon and a beam with A around 100 are foreseen.

3.2.4. Model and code development

In the high-energy transport codes used to design ADS, cross-sections and characteristics of particles produced in elementary interactions above 200 MeV are generated by nuclear physics models. Generally, the reaction is described in two steps: a first stage of individual nucleon-nucleon collisions, generally described by Intra-Nuclear Cascade (INC) models, then, the decay of the excited remnant nucleus by evaporation-fission. The comparison of the experimental data to widely used models having shown severe deficiencies, during the HINDAS project, efforts have been devoted to the building of improved INC and evaporation-fission models. These models have been compared to the whole set of available data and implemented into high-energy transport codes so that they can be used for calculations of spallation modules.

(a) The new intranuclear cascade model INCL4

It is worth to first describe the main features of the Liège intranuclear cascade (INCL) model and the status of the corresponding numerical code prior to HINDAS. The basic premise of the INCL model is the description of the nucleon-nucleus interaction as a sequence of binary collisions (and decays) well separated in space-time. In fact, all the particles are followed as time evolves. They move on straight-line trajectories until two of them reach their minimum distance of approach (at which time collision between them is decided or not on a minimum distance of approach criterion), or until a particle hits the surface (where it can be transmitted or reflected on the basis of the usual transmission probability), after which straight-line motion is resumed, and so on. Collisions are subjected to Pauli blocking. The latter is implemented on a stochastic basis: the phase space occupancies f_i are evaluated on the neighbourhood of the positions occupied in phase space by the two partners in the candidate final state, just by counting alike particles in a reference volume centered on these positions. The collision is allowed only if two random numbers are found to be smaller than $(1-f_1)$ and $(1-f_2)$, respectively. This procedure enables to account for the depletion of the Fermi sea in a consistent manner. Elementary cross-sections are supposed to be the same as in free space. Pion and Δ-degrees of freedom are introduced. The target is supposed to occupy a sphere with a sharp surface, in which nucleons undergo the effect of a constant attractive potential.

An important aspect of the INCL model is the "self-consistent" determination of the stopping time, i.e. the time at which an evaporation model is to be cranked: the average evolutions of many physical quantities, like the excitation energy or the anisotropy of the emission pattern, exhibit a simultaneous change of rate roughly at the same time, which is chosen as the stopping time: before this time they vary rather rapidly, after this time they show characteristic time scales typical of evaporation.

At the beginning of the HINDAS project, the INCL model was cast into the INCL2 [Cug97a] and INCL3 numerical codes. They were shown to give good results, especially for neutron double differential cross-sections, but suffered from some shortcomings: (i) they failed on the quasi-elastic peak, (ii) residue cross-sections close to the target mass were underestimated and (iii) the statistical implementation of the Pauli blocking led to unphysical results. A new version of the model, leading to the new numerical code INCL4 [Bou02], has been developed within the frame of the HINDAS program.

Building of the INCL4 model

The following aspects have been introduced in INCL4:
- *Introduction of a smooth surface*
Target nucleons are positioned at random according to a Saxon-Woods distribution for the density $\rho(r)$, cut at $R_{max}=R_0+8a$, where R_0 and a are the nuclear radius and diffuseness parameter, respectively. Their momenta are randomly generated in a sphere of radius p_F; r-p correlations are introduced in order to account for the fact that fast nucleons travel farther out than slow nucleons. Nucleons with momentum between p and p+dp are assumed to contribute to the density $\rho(r)$ by the layer:

$$\delta\rho(r) = (\rho\,(R(p)) - \rho\,(R(p+dp))\,)\,\theta_H(R(p)-r),$$

where θ_H is the Heaviside function. This defines the correlating, monotonously increasing, function R(p). This prescription amounts to take, first momentum p at random, and then position at random in a sphere of radius R(p). Furthermore, particles of momentum p are feeling a potential of constant depth V_0 and of radius R(p). It is shown in Ref. [Cug97a] that this leads to a total stabilization of the target (in terms of r and p distributions), in absence of collisions. This procedure is basically equivalent to putting particles in a Saxon-Woods potential well, but preserves the simplicity of the straight-line motion, which allows propagating particles in a single time step between collisions.

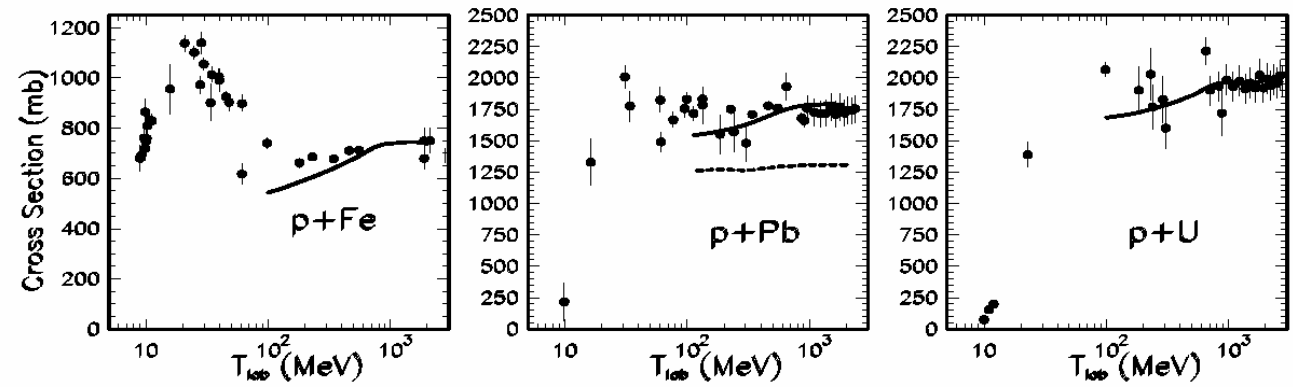

Figure 3.43 : *Total reaction cross sections for p on iron, lead and uranium as computed from INCL4 (full line) and compared with a compilation of experimental values from [Pra97, Bar93]. The dashed line is the calculation of INCL3 assuming a sharp spherical density.*

This now correct description of the nuclear surface leads to a very good prediction of the total reaction cross-section, as shown in Fig. 3.43. This is an important improvement compared to older versions of the model, INCL2 or INCL3, which always had to be renormalized to reproduce absolute cross-sections (see section B.2.1 thin target data for instance).

- *Consistent dynamical Pauli blocking*

The combination of the statistical generation of the initial state and the statistical implementation of the Pauli blocking leads to unphysical effects. Because of fluctuations the phase space occupancy f (measured by counting particles in a small phase space volume) can be smaller than one, even in the initial state. As a consequence, even the first collision made by the incoming particle may lead to a decrease of the energy of the colliding target nucleon, if the foreseen position of the latter in phase space is in a region where $f<1$. In such a case, the target excitation energy may become negative. In most events this deficiency is cured by

subsequent collisions. For a typical case, the amount of events with negative final excitation energy is of the order of a few percent. In INCL2, for those events, the excitation energy was simply set to zero. In INCL3, the excitation energy is checked at any binary collision and the event is terminated just before the first collision leading to negative excitation energy.

In INCL4, this undesirable effect is removed by forbidding collisions which could lead to a negative excitation energy of the current Fermi sea, i.e. the summed energy of all particles with momentum below p_F cannot be smaller than the ground state of the current Fermi sea, defined as the energy of the original Fermi sea minus the separation energy of the nucleons which have escaped from it.

-*Incident light clusters*
Incident light clusters, up to ^{4}He, can now be accommodated by the INCL4 code. Initial positions and momenta inside the cluster are determined from Gaussian laws with parameters taken from experiment.

- *Improved pion dynamics*
The dynamical picture of pion production has been improved on some points. In particular, a corrected detailed balance formula, which accounts for the finite lifetime of the Δ-resonances, is used to determine the N Δ→ NN cross-section.

- *Remnant angular momentum*
This quantity is provided as an output of the code. It is calculated as the difference between the initial angular momentum and the angular momentum carried by the ejectiles.

- *Spectators and participants*
Spectators are moving, which generates a physical rearrangement of the density, but are not allowed to collide among them.

The numerical code INCL4 is basically a parameter-free code. Input data are taken from experiment (target radius, cross-sections, etc) or fixed once for all (e.g. Fermi momenta and parameters determining the reference volume used to evaluate phase space occupancies). Baryon-baryon and pion-nucleon cross-sections are taken from accurate parameterizations of the existing data [Cug96], as far as possible. Technically, and in order to allow the users to make sensitivity analyses, three parameters are left free in the code: the potential depth, the stopping time and a parameter allowing the choice between a statistical or a strict implementation of the Pauli blocking. However, because of the physics arguments given above, the optional values appear as the most appropriate. All investigations within HINDAS have been carried out with these values.

(b) ABLA

In a spallation reaction, it is standard to distinguish between two separate stages. The first stage is usually modelled by individual nucleon-nucleon collisions with intra-nuclear-cascade codes, which ends with the formation of a thermalized excited nuclear system. The second stage is described in the statistical model of nuclear reactions. Several evaporation codes have been developed for this purpose. However, since most of these codes have been designed for fusion reactions, there is specific need for a code adapted to the deexcitation process of spallation residues:

- The large range of excitation-energies and the large variety of nuclear species demands for a consistent treatment of level densities as a function of excitation energy and nuclear shape. The treatments of shell effects [Ign75] and collective excitations [Jun98] are particularly important.
- Due to the low angular momentum induced in spallation reactions, approximations which have been used for fusion reactions are not adapted.
- The dynamics of the fission process and the onset of thermal instabilities at the highest temperatures have to be considered. This demands an explicit treatment of nuclear dynamics as a function of time.
- Modelling of fission requires considering a large variety of fissioning nuclei in a wide range of excitation energies. Available empirical formulations of nuclide distributions in fission of specific nuclei should be replaced by a model, which is based on more fundamental properties, like the potential energy landscape around saddle and scission.
- The application in complex transport codes demands for short computing times.

In the following, we first give a short overview of the ABLA code and the most important modifications, developed during the HINDAS project.

The ABLA code

ABLA is a dynamical code that describes de-excitation of the compound nucleus through the evaporation of light particles and fission. The probability that a compound nucleus with charge *Z,* neutron number *N* and excitation energy *E*, decay via channel ν is given by:

$$P_\nu(E) = \frac{\Gamma_\nu(Z,N,E)}{\sum_i \Gamma_i(Z,N,E)} \qquad (1)$$

where *i* denotes all the possible decay channels (specifically: neutron emission, proton emission, alpha emission, fission). The particle evaporation is considered in the framework of the Weisskopf formalism. The particle decay widths can be written as [Wei37]:

$$\Gamma_\nu(E) = \frac{1}{2\pi\rho_c(E)} \frac{4m_\nu R^2}{\hbar^2} T^2 \rho_d(E - S_\nu - B_\nu) \qquad (2)$$

where m_ν denotes the particle mass, S_ν is the particle separation energy, B_ν is the effective Coulomb barrier that takes into account the tunnelling through the barrier, *R* is the radius of the nucleus, *T* is the temperature of the residual nucleus after particle emission, ρ_c and ρ_d are the level densities of the compound nucleus and the daughter nucleus, respectively.

The density of excited states, ρ, is calculated with the well-known Fermi-gas formula [Hui72]:

$$\rho(E) = \frac{\sqrt{\pi}}{12} \frac{\exp(S)}{\tilde{a}^{1/4} E_{eff}^{\ 5/4}} \qquad (3)$$

with the entropy S:

$$S = 2 \cdot \sqrt{\tilde{a} \cdot E_{corr}} = 2 \cdot \sqrt{\tilde{a} \cdot \left(E_{eff} + \delta U \cdot k\left(E_{eff}\right) + \delta P \cdot h\left(E_{eff}\right)\right)} \qquad (4)$$

and the asymptotic level-density parameter $\tilde{a}$ as given in Ref. [Ign75]:

$$\tilde{a} = 0.073 \cdot A + 0.095 \cdot B_S \cdot A^{2/3} \tag{5}$$

where A is the mass of a nucleus, and B_s is the ratio of the surface of the deformed nucleus and a spherical nucleus. δU is the shell correction, which is for the ground state calculated as the difference between the experimental ground-state mass and the corresponding macroscopic value from the finite-range liquid-drop model [Sie86]. At the saddle point, shell corrections are assumed to be negligible. The function $k(E_{eff})$ describes the damping of the shell effects with excitation energy, and is calculated according to Ref. [Ign75] as $k(E_{eff}) = 1 - \exp(-\gamma E_{eff})$, with the parameter γ determined by $\gamma = \tilde{a} / (0.4 \cdot A^{4/3})$ [Sch82].
The effective pairing energy shift δP is calculated as:

$$\delta\ P = -\frac{1}{4} \cdot \Delta^2 \cdot g + 2 \cdot \Delta \tag{6}$$

with an average pairing gap $\Delta = 12/\sqrt{A}$, and the single-particle level density at the Fermi energy $g = 6 \cdot \tilde{a} / \pi^2$. $h(E_{eff})$ parameterises the superfluid phase transition [Ign79] at the critical energy $E_{crit} = 10$ MeV [Ign77]:

$$h(E_{eff}) = \begin{cases} 1 - \left(1 - \dfrac{E_{eff}}{E_{crit}}\right)^2, & E_{eff} < E_{crit} \\ 1, & E_{eff} > E_{crit} \end{cases} \tag{7}$$

The effective energy E_{eff} is shifted with respect to the excitation energy E to accommodate for the different energies of even-even, odd-mass, and odd-odd nuclei:

$E_{eff} = E$, for odd – odd nuclei
$E_{eff} = E - \Delta$, for odd mass nuclei
$E_{eff} = E - 2\Delta$ for even – even nuclei.

As it was shown in Ref. [Jun98], collective excitations can contribute considerably to the nuclear level density. In deformed nuclei, the most important contribution to the collective enhancement of the level density originates from rotational bands, while in spherical nuclei the collective enhancement is caused by vibrational excitations. In ABLA, the contribution of collective excitation to the level density is described in the following way: For nuclei with a quadrupole deformation $|\beta_2| > 0.15$, the rotational enhancement factor $K_{rot}(E_{corr})$ is calculated in terms of the spin-cutoff parameter $\sigma_\perp$:

$$K_{rot}(E_{corr}) = \begin{cases} \left(\sigma_\perp^2 - 1\right) \cdot f(E_{corr}) + 1, & \sigma_\perp^2 > 1 \\ 1, & \sigma_\perp^2 < 1 \end{cases}$$

$$\sigma_\perp^2 = \frac{\Im_\perp \cdot T}{\hbar^2}, \quad f\left(E_{corr}\right) = \left(1 + \exp\left(\frac{E_{corr} - E_c}{d_c}\right)\right)^{-1}$$

where E_{corr} is defined in Eq. (4), $\Im_\perp = \frac{2}{5} m_0 \cdot A \cdot R^2 \left(1 + \beta_2 / 3\right)$ is the rigid-body moment of inertia perpendicular to the symmetry axis, and m_0 is the mass unit. The ground-state quadrupole deformation β_2 is taken from the finite-range liquid-drop model including microscopic corrections [Möl95], while the saddle-point deformation is taken from the liquid-drop model as given in Ref. [Coh63]. The damping of the collective modes with increasing

excitation energy is described by a Fermi function $f(E)$ with parameters E_c = 40 MeV and d_c = 10 MeV.
The vibrational enhancement for spherical nuclei is generally smaller than the rotational enhancement for deformed nuclei. For nuclei with a quadrupole deformation $|\beta_2| < 0.15$, the vibrational enhancement factor is calculated as $K_{vib}(E_{corr}) = 50 \cdot \beta_{eff}^2 \cdot K_{rot}(E_{corr})$, where β_{eff} is a dynamical deformation parameter: $\beta_{eff} = 0.022 + 0.003 \cdot \Delta N + 0.005 \cdot \Delta Z$. ΔN and ΔZ are the absolute values of the number of neutrons and protons, respectively, above or below the nearest shell closure. More details about collective enhancement can be found in Ref. [Jun98]. Finally, the total level density is calculated as the product of the intrinsic level density given by Eq. (3) and $K_{vib}(E_{corr})$ and $K_{rot}(E_{corr})$.
To define the fission-decay width, apart from the level densities, the necessary ingredients are also dissipation effects that will be described in the next subsection and fission barriers. The angular-momentum dependent fission barriers are taken from the finite-range liquid-drop model predictions of Sierk [Sie86]. In order to describe the fission-fragments mass and charge distributions, as well as their kinetic energies, the ABLA code is coupled to the semi-empirical fission model PROFI described below.

Time-dependent fission width

The modelling of the fission decay width at high excitation energies requires the treatment of the evolution of the fission degree of freedom as a diffusion process, determined by the interaction of the fission collective degree of freedom with the heat bath formed by the individual nucleons [Kra40, Gra83]. Such process can be described by the Fokker-Planck equation (FPE) [Ris89], where the variable is the time- and dissipation-dependent probability distribution $W(x, p; t, \beta)$ as a function of the deformation in fission direction x and its canonically conjugate momentum p. β is the reduced dissipation coefficient. The solution of the FPE leads to a time-dependent fission width $\Gamma_f(t)$. The results for the case of ^{238}U at a temperature of 3 MeV for different values of reduced dissipation coefficient β are shown in Fig. 3.44 with solid lines.

However, these numerical calculations are too time consuming to be used in nuclear-reaction codes. Therefore, in most of the model calculations one of the following approximations for the time-dependent fission width $\Gamma_f(t)$ is used:

- A step function that sets in at time τ_f: $\Gamma_f(t) = \begin{cases} 0, t < \tau_f \\ \Gamma_f^k, t \geq \tau_f \end{cases}$ (8)
- An exponential in-growth function: $\Gamma_f(t) = \Gamma_f^k \{1 - \exp(-t / \tau)\}$ (9)

where $\tau = \tau_f / 2.3$, with τ_f beeing the transient time defined [Bha86] as a time in which $\Gamma_f(t)$ reaches 90% of its asymptotic value given by the Kramers fission width Γ_f^k [Kra40]. These approximations strongly deviate from the numerical solution and thus severely influence the results [Jur01]. Therefore, a new highly realistic description of the fission width based on the analytical solution of the FPE when the nuclear potential is approximated by a parabola was developed [Jur03].

The new analytical solution is based on the following assumptions: 1.) The shape of the probability distribution at the barrier deformation as a function of the velocity v is constant, and only its height varies with time, 2.) For $W_n(x = x_b; t, \beta)$ the solution of the FPE obtained using a parabolic nuclear potential [Cha43] can be used, and 3.) Zero deformation and zero velocity are considered as initial conditions. In addition, the zero-point motion was taken into account by shifting the time scale by the time needed to establish the initial shape of the probability distribution. A detailed description can be found in Ref. [Jur03]. As one can see in

Fig. 3.44, this analytical approximation reproduces the exact solution for the critical damping ($\beta = 2 \cdot 10^{21}$ s^{-1}) rather well. A similar agreement is reached in the over-damped regime ($\beta > 2 \cdot 10^{21}$ s^{-1}). The approximation also gives a rather good description of the slightly under-damped motion ($\beta = 1 \cdot 10^{21}$ s^{-1}). Even in the under-damped case ($\beta = 0.5 \cdot 10^{21}$ s^{-1}), the oscillations are reproduced very well, although the absolute magnitude of the fission width is somewhat underestimated.

In the previous investigation [Jur02], it was shown that the total suppression of the fission width for small time values and the gradual increase are the most critical features of a realistic in-growth function. Both features, missing in the previously used descriptions, are well reproduced by our analytical approximation. The actual version of the ABLA code explicitly treats the relaxation process in deformation space and the resulting time-dependent fission-decay width, using the described approximate solution of the FPE.

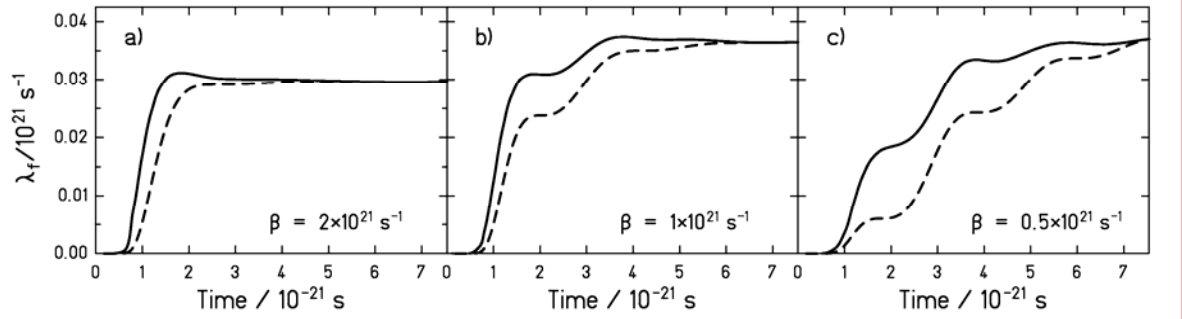

Figure 3.44 : *Fission rate* $\lambda_f(t) = \Gamma_f(t) / \hbar$ *as a function of time for three different values of the reduced dissipation coefficient* β *for* ^{238}U *at* $T = 3$ *MeV. The solid line is the numerical solution of the FPE while the dashed line is calculated using the new analytical solution as described in Ref. [Jur03].*

The fission code PROFI

The fission code PROFI [Ben98d] is a semi-empirical Monte-Carlo code developed to calculate the nuclide distributions of fission fragments. It is theoretically based on the application of the statistical model of nuclear reactions to the concept of fission channels. Within this model, the population of the fission channels is assumed to be basically determined by the number of available transition states above the potential-energy surface near the fission barrier. The barrier as a function of mass asymmetry is defined by three components: The symmetric one is defined by the liquid-drop potential. Two asymmetric ones are located at mass asymmetries corresponding to neutron numbers $N = 82$ (Standard I channel) and $N \approx 90$ (Standard II channel). Three parameters (position, strength and width) of each shell are taken from channel-specific fission cross sections [Vla03] and fixed for all systems. Shells are washed out with excitation energy [Ign75]. It is assumed that the mass-asymmetry degree of freedom at the fission barrier is on the average uniquely related to the neutron numbers of the fragments. The mean values of the neutron-to-proton ratios for the channels Standard I and Standard II are deduced from measured nuclide distributions after electromagnetic- induced fission of ^{238}U [Enq99]. Since the shell effects of the nascent fragments at scission, which are strongly deformed on the average, are not known experimentally, only macroscopic properties are included in the calculation of the charge polarisation of the symmetric fission channel. Consequently, the two fission fragments are obtained. Their excitation energies are calculated from the excitation and deformation energy of the fissioning system at the scission point. A full description of the model is given in [Ben98].

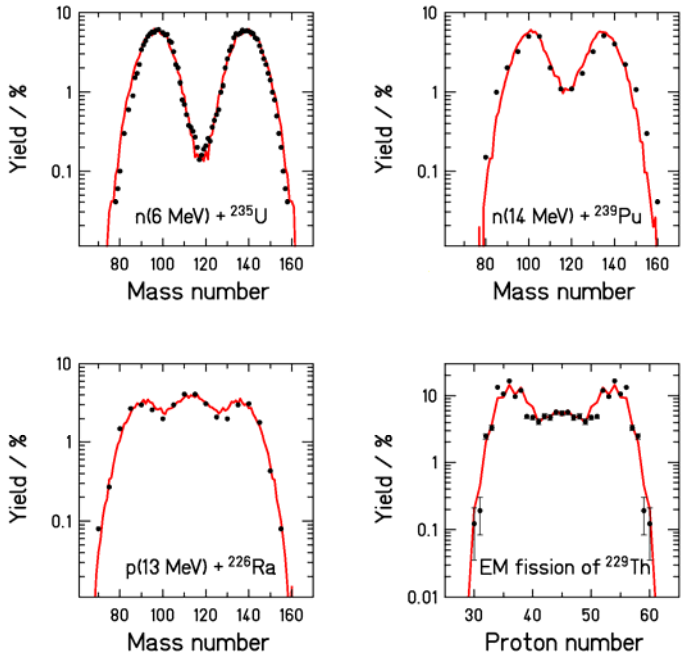

Figure 3.45 : *Comparison between experimental data (black dots) measured in the low-energy fission with the prediction of the PROFI code (red lines). Experimental data are taken from: n(6 MeV) + ^{235}U [Str87], n(14 MeV) + ^{239}Pu [Gin83], p(13 MeV) + ^{226}Ra [Per71], electro-magnetic induced fission of ^{229}Th [Sch00]. Yields are normalized to 200 %.*

In Figs. 3.45 and 3.46 we compare the fission mass and charge distributions measured in different reactions with the prediction of PROFI code. The agreement between data and calculations is very satisfactory. The actual version of PROFI requires slight adjustments of the parameters for the different fissioning systems. It is a possible plan for the future to extend the model with one or two more parameters in order to obtain a universal version with one parameter set for all systems (up to $A_{cn} = 250$).

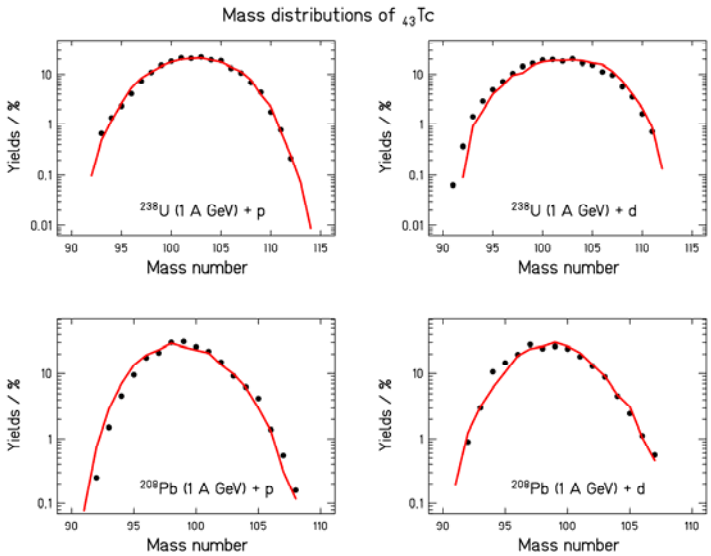

Figure 3.46 : *Mass distributions of $_{43}$Tc produced in the high-energy fission. Experimental data (black dots) measured in the frame of the HINDAS programme (see experimental contribution to the High-Energy part of the Final Report) with the prediction of our nuclear-reaction code including PROFI for the fission-fragment nuclide production (red lines). Yields are normalised to 200 %.*

The simultaneous break-up stage

As presented in Ref. [Sch02], the analysis of the isotopic distributions of heavy projectile fragments from the reactions of a ^{238}U beam in a lead target and a titanium target gave evidence that the initial temperature of the last stage of the reaction, the evaporation cascade, is limited to a universal upper value of approximately 5 MeV. This is consistent with results on the caloric curve from multifragmentation experiments [Hau00]. The interpretation of this effect relies on the onset of the simultaneous break-up process for systems whose temperature after the first stage of the reaction (e.g. the intra-nuclear cascade) is larger than 5 MeV. In ABLA, the simultaneous break-up stage is modelled in the following way: If the temperature after the first stage of reaction exceeds the value of 5 MeV, the additional energy is used for the formation of clusters and the simultaneous emission of these clusters and several nucleons. The number of protons and neutrons emitted is assumed to conserve the N-over-Z ratio of the projectile (or target) spectator, and an amount of about 20 MeV per nucleon emitted is released. The break-up stage is assumed to be very fast, and thus the fission collective degree of freedom is not excited. The major fragment left over from the projectile (or target) spectator undergoes the sequential decay. We actually investigate a more elaborate description of the break-up process on the basis of the Statistical Multifragmentation Model (SMM) [Bon95].

In the case of spallation reactions, the break-up stage plays an important role for light targets, while for heavy targets only a small fraction of the prefragments in the upper tail of the excitation-energy distribution is formed with temperatures exceeding 5 MeV. As the consequence, the production of intermediate-mass fragments through the simultaneous break-up is more enhanced for light targets (e.g. iron). This could explain the failure of a standard evaporation model to describe the cross section for the production of intermediate-mass fragments (e.g. ^{7}Be, ^{14}C…).

Conclusion and outlook

During the HINDAS project important improvements in the GSI evaporation code ABLA have been performed. These improvements have profited from the high-precision data measured at GSI also in the frame of the HINDAS project. By developing the new analytical approximation to the solution of the Fokker-Planck equation for the time-dependent fission width, ABLA is transformed from a pure statistical to a dynamical code. It is coupled to the semi-empirical fission model PROFI that calculates the characteristics of fragments formed in fission. A new stage, the simultaneous break-up, is introduced between the intra-nuclear cascade and the evaporation stages of reaction, which contributes to the production of intermediate-mass fragments.

For the future, we are planning some further development of the code, such as the inclusion of the evaporation of other light charged particles than protons and alpha, and the emission of gamma rays. The more detailed study of the dissipation effects in fission, e.g. influence of deformation and temperature, is also planned. The fission model PROFI could be extended with one or two more parameters in order to obtain a universal version with one parameter set for all systems (up to A_{cn} = 250). Finally, we are also planning to develop a more elaborate description of the break-up stage.

(c) Comparison of the INCL4/ABLA combination to HINDAS experimental data

The INCL4/ABLA predictions have been tested, during the second year of HINDAS, on a large body of experimental data including total cross-sections, neutron and proton differential cross-sections, neutron and charged particle multiplicities, residue mass and charge distributions, isotopic distributions, fission cross-sections and distributions, and residue recoil energy distributions. In particular, they have been compared with many data obtained by the

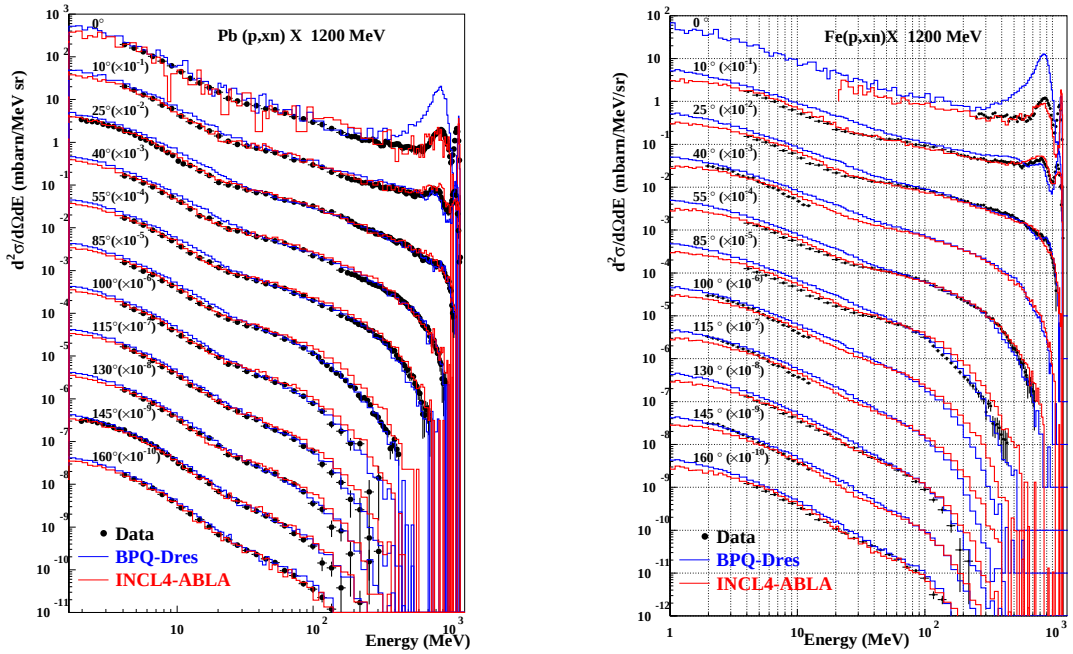

Figure 3.47 : *Comparison of the results of INCL4/ABLA model with experimental data from [Ler02] and predictions from Bertini+preequilibrium/Dresner: left (resp. right) for a lead (resp. iron) target at 1.2 GeV. The calculations have been performed with the LAHET3 transport code to take into account the effective thickness of the targets.*

HINDAS collaboration, a few examples have been shown in the preceding sections of this report. Furthermore, the INCL4 code has also been tested after inclusion in transport codes. The predictions have been compared with thick target experiments and have been used for activity calculations and gas production, as explained in section 4 of this report.

The details of the extensive comparison can be found in [Bou02]. A short summary and evaluation is given here. It is first to be underlined that, without any parameter fitting, the INCL4 turns out to give a remarkable overall agreement with all experimental data for proton and deuteron-induced reactions in the 200 MeV to 2.5 GeV range. Examples of comparisons with neutron production data discussed in section 3.2.1(a) subsection “thin target data” are presented in Fig. B.47. This overall agreement is substantially better than with INCL3, except on some details of the neutron double differential cross-sections. The shortcomings of this previous version have been overcome. The quasi-elastic peak is correctly reproduced in (p,p) reactions, and comes out with the correct amplitude, but slightly shifted, in (p,n) reactions. This improvement is mainly due to the introduction of a smooth surface, which enhances the weight of peripheral events, where single-scattering is very important. For these events leading to small excitation energy, the residue mass spectra is considerably improved for small mass loss, by the same token. The unphysical effects, linked with the implementation of the Pauli principle, are now removed, still preserving the account of the depletion of the Fermi sea.

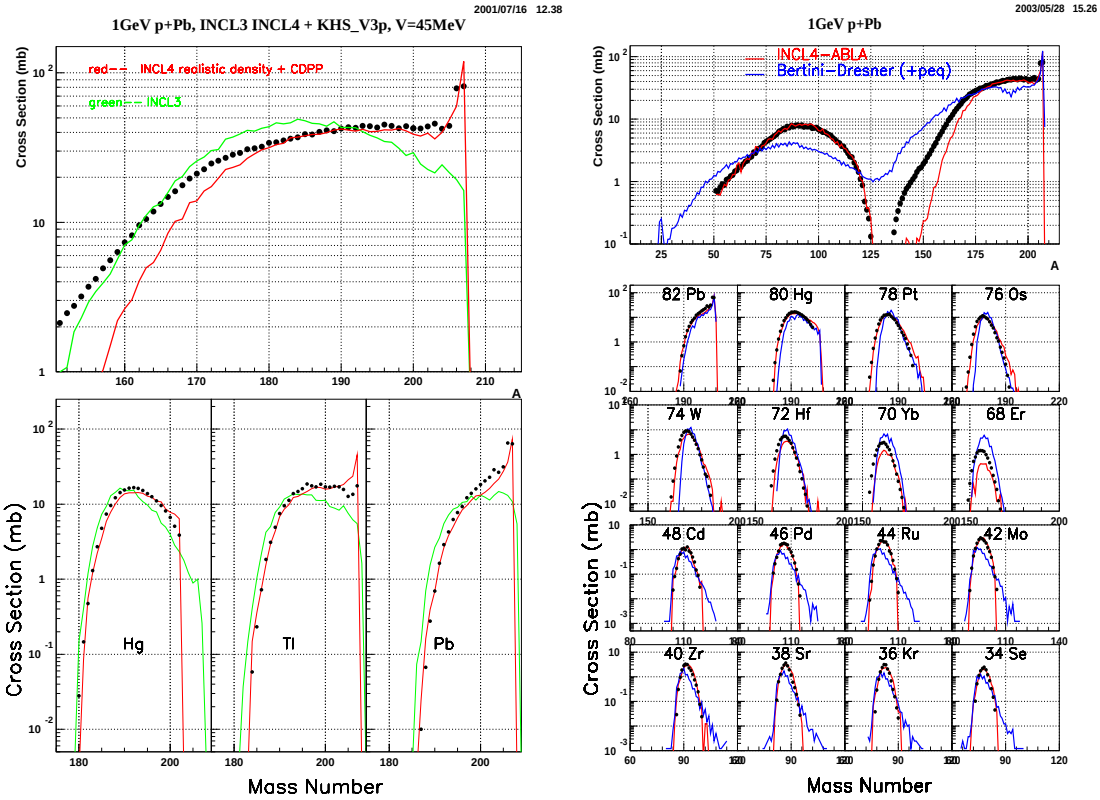

Figure 3.48 : *Mass and a few isotopic distributions of residues produced in Pb+p at 1* A *GeV, measured at GSI [Wla00, Enq01] compared with the INCL4-ABLA models. Left: comparison with the INCL3 version of the model for the heaviest evaporation residue. Right: comparison of the whole distribution with also calculations done with the Bertini+preequilibrium/Dresner model.*

For residue production, the improvement brought by the new version on the prediction of heaviest residue of the code is illustrated in Fig. 3.48 left. Here again, this is due to the correct taking into account of the surface diffuseness. Fig. 3.48 right shows in addition the comparison with the Bertini/Dresner model for the whole range of the mass distribution. It can be observed that INCL4/ABLA (mainly thanks to ABLA) reproduces perfectly the isotopic distribution shapes whatever the element and the fission fragment production cross-sections, which was a major failure of the Dresner model. On the other hand, the lightest evaporation nuclei are systematically under predicted. This has been also observed for the uranium target and could either indicate an excitation energy too low at the end of the cascade or problems of the de-excitation model at the highest excitation energies.

In addition, the INCL model has been tested at low incident energy, between 40 and 200 MeV, on the nucleon double differential cross-sections and residue production (as shown in Fig. 3.35). The results are encouraging. The shapes of the double differential cross-sections are rather well reproduced, sometimes better that with dedicated models, like multi-step direct models or even FKK calculations, but the total cross-section is definitely underestimated.

Evaluation and further improvement

In view of the overall good agreement with experimental data, no further run of improvements has been done. However, the numerical code INCL4 has been extended on two points: specific parameterizations are introduced for light targets (A<27) and results are normalized on the experimental total cross-sections for incident energies less than 100 MeV.

In spite of the overall good agreement reached with INCL4, some weak points have been identified. There are indications that INCL4 does not generate enough events with large excitation energy. More clearly, the model produces too many pions. These deficiencies have small consequences on the overall particle-energy flow and on the eventual neutron production in thick targets. A more serious problem arises from the fact that, by construction, INCL4 does not generate clusters with high kinetic energy. Although the multiplicity of these particles is low, they may contribute sizably to gas production in thick targets. Implementing cluster production in INCL4 has tentatively been carried out recently, leading to encouraging results [Bou03a].

Availability and inclusion in transport codes

The numerical codes INCL4 and ABLA have been included in a package (deliverables D16 and D18 of HINDAS), available to the physics community. This "user-friendly" oriented tool can generate, without any further manipulation, a large number of observables, under the form of histograms to be manipulated by the PAW++ package. A long write-up has been written under the form of a HINDAS report [Bou03b].

They also has been adapted and introduced in the transport codes HERMES (see below), LAHET3 and MNCPX. Applications within LAHET3 led to a comparison with thick target experiments carried at SATURNE [Dav03] (section B.2.1 subsection "thick target data") and to activity and chemical composition modification evaluations [Don03] (section 4.5 subsection "Activity and chemical composition modifications in an ADS target"). Testing INCL4 within MCNPX has recently started.

(d) A new transport code MC4 above 20 MeV

In case of the HERMES high-energy transport code [Clo88], the spallation regime was traditionally covered by HETC which can also be found within L AHET [Pra89], CALOR [Gab77] and other systems in different derivates and implementations. The implemented models (namely the Bertini's INC [Ber62], the Dresner's EVAP [Dre62] and the RAL fission model [Atc80]) have frequently been changed and exist in many significantly different versions. Furthermore HETC is written in a mixture of FORTRAN IV and Fortran 77 implying problems concerning portability and reliability. MC4 is intended to overcome the drawbacks of HETC using a modular structure where up to date models can easily be plugged in, providing the necessary transport algorithms, analysis algorithms, and a user interface.

Program features and structure

MC4 is integrated into the HERMES System. This means, it uses the same geometry modules than HERMES, it can read source particles from HERMES submission files, and writes particles to submission files whenever they cannot be treated in MC4 and on user demand. These particles are then treated in the other HERMES packages. The program structure of MC4 itself is modular as shown in Fig. 3.49.

Any input to MC4 is processed by the command interpreter CMD which serves as the standard user interface. A sequence of commands determine the models to be used throughout a run, read the model options, define the geometry and material setup of the problem and describe the analysis to be performed. CMD provides user variables for scalars and vectors, arithmetical operations, and simple loop structures and branches. The data collected with

CMD is handed over to the modules performing the particle transport Monte Carlo at start of run time for consistency checking.

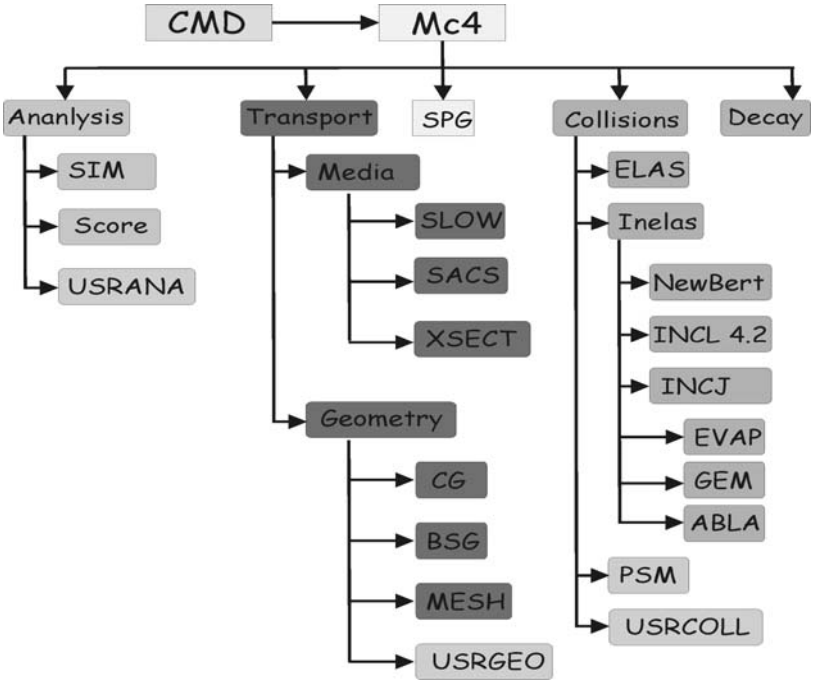

Figure 3.49 : *Scheme of performance of the transport module MC4 for high energy applications.*

The main module of MC4 controls the histories of particles from source to death. It invokes the modules for source particle generation, particle transport, collisions, and decay through general interface routines. The physics models are linked below these interfaces. The main module provides the primary and secondary particle stacks and methods to store and retrieve particles. It arranges particle histories in batches for the analysis of fluctuations of observed response.

The different modules

- *Source Particle Generator (SPG)*

The source particle generator produces source particles in a special Cartesian coordinate system. In this system the z-axis is used as reference direction (beam direction), x denotes the horizontal and y the vertical dimension of the source (the beam profile). There are two input commands to define the transformation between the source coordinate system (SCS) and the geometry coordinate system. For the source points a uniform distribution in a cube (or a plane rectangle), a Gaussian distribution on an elliptical footprint, and a parabolic distribution on an elliptical footprint are used. In addition to read in a beam profile in two dimensions i.e. for measured beam profiles is possible. Different distributions of source points can be shaped using a source region defined in the geometry. For source particle flight directions an isotropic distribution optionally cut at a maximum angle, and a read-in tabulated distribution function of cos (θ) is implemented. Kinetic energy spectrum and the momentum spectrum can be chosen by the user. Predefined spectra as a uniform distribution of kinetic energy in a given interval, a Gaussian distribution of kinetic energy, a Maxwell spectrum with a given temperature, an evaporation spectrum with a given mean energy, a uniform momentum

distribution, a Gaussian distribution of the momentum, and user-tabulated distribution functions are also provided. The time distribution of source particle can be specified as uniform, Gaussian, and by a tabulated spectrum.

SPG has access to the collision kernels of MC4. The user can specify a target for INC to simulate thin (atomic) target experiments or he can specify a target particle and a final state for PSM.

- *The TRANSPORT Module*
The TRANSPORT module consists of the MEDIA sub module which handles the media dependant data structures (i.e. X-section, charged particle slow down tables, etc.) and the matching transport algorithms (i.e. small angle coulomb scattering SACS, slow down schemes) and of a set of GEOMETRY packages. In the combinatorial geometry package (CG) regions are defined by intersections and unions of predefined bodies. The user has to take care that the regions cover all space and do not overlap. We enhanced CG (already in HERMES) by adding more body definitions, introducing a 3 layer hierarchy in the region definition, and by the use of the CMD interpreter. With the enhancements we support the design of flexible geometry setups needed for geometry parameter studies. The GEOTEST tool, also integrated into MC4 allows debugging geometries and producing graphs of plane cuts through the geometry. In the bisection geometry package (BSG) [Clo93] space is divided into two parts by means of surfaces of 1^{st} and 2^{nd} order. Each part can be divided in the same way, building a tree like hierarchy. The leaves in the tree define the regions. This basic principle makes it impossible to leave undefined space or to overlap regions. In place of a region one can also mount another geometry hierarchy. Such sub-geometries use their own coordinate system and can be relocated by transformation operations. The input of BSG uses a description language which is compiled in a separate task. The utility program EXD can be used to visualize, test, and edit BSG geometries. The MESH generator can be used to generate regular geometry structures (x,y,z), (r,φ,θ), or (r,φ,z) arbitrarily located and oriented in geometry coordinate space for independent resolution of space in the analysis packages. At last there is a set interface routines to user written geometry modules.

The charged particle slowdown algorithm (SLOW) is based on SPAR [Arm73] written by T. W. Armstrong and K.C. Chandler. SPAR uses the theory of Bethe and Bloch to describe the electronic stopping power with shell and density corrections, and Barkas' formula to include the charge screening effect for low beta particles. Additionally SPAR applies nuclear stopping power based on Lindhard's theory. We modified the stopping power function for high beta including the influence of the limited energy transfer onto an unbound electron. From the stopping power function we construct range tables in the energy range from 100 keV to 100 GeV in 1000 logarithmic steps, stopping time and the variance of the range. In MC4 two methods for slowing down are implemented. When inverse range-table lookup is used like in HETC, only Gaussian straggling can be applied. This method is very fast and could be used under most circumstances. For structures, where this method is not applicable like thin layers, where the fluctuation is influenced by the number of ionization or for high energies where the fluctuation comes from the generation of gamma-rays, or for energies where no data is tabulated, one can use local integration. Local integration is an adaptive numerical integration method using a step-length procedure which limits the error of integration to a specified maximum. Along with the local integration method, Landau distributed energy straggling can be applied.

Small angle Coulomb scattering (SACS) is optionally taken into account using Moliere's multiple collision theory [Par96]. The theory gives distribution functions for the deflection angle and displacement of a particle penetrating a given layer of matter. The thickness of that

layer can be translated into a transportation step in the MC4. MC4 only uses the deflection angle at the end of the step, because displacement and deflection are correlated and the displacement can be simulated by increasing the number steps. Optionally deflection can be applied after a given step-length, an automatically calculated step-length representing a given relative energy loss, or on geometrical boundaries only (useful in mesh structures).

- *Collision Kernels*

Collision kernels are linked into MC4 through a common interface routine, called at collision sites. Another interface routine inside the MC4 main module is called at 'start of run' to collect the kernel parameters as provided by user commands and to initialize the collision kernels. This routine also checks the consistency of user input and extracts model dependent data like the geometric cross-section which influence other modules like the transport module.

Collision kernels implemented are:

- INC programs:
  - NewBert [Clo96]: a reprogrammed version of Bertini's INC code, extended to higher energies.
  - INCL 4.2 [Cug97a]: This is currently the INC code with the best predictive power, valid up to Δ- resonance.
  - INCJ 1.0 [Woh03]: An INC code from the Thesis of M.Wohlmuther.
- Evaporation codes:
  - EVAP: Dresner's evaporation code enhanced with the Jülich level density handling and combined with the fission model of the Rutherford Appleton Lab. The code was furnished and some minor errors have been removed
  - GEM [Fur01]: The generalized evaporation module takes intermediate mass fragments into account and uses state of art parameter sets.
  - ABLA [Sch91]: The ABLA code also uses refined parameter sets and a new fission model taken into account the dynamical nature of fission.

- *The Analysis Tools*

At last MC4 provides 2 standard analysis tools:

- SIM: This module implements HERMES style detectors (tallies) for particle yields, currents, and fluxes, for energy deposition and residual nuclei distributions.
- CSS: The central score stack method provides a toolbox to extract physical observables from particle histories, convert them into derived physical properties and technical detector responses, and interface this data to reconstruction algorithms. The CSS technique mainly addresses user written special analysis programs which may be linked into MC4 through the wide API or may work externally through different file interface standards.

4. Implications of HINDAS results for ADS design. Activity and chemical composition modification in an ADS target.

4.1. Introduction

In an Accelerator-Driven System (or a spallation neutron source) spallation target, a large variety of isotopes is produced by spallation reactions in addition to those created by activation by the low energy neutron flux. A lot of them are radioactive and are a source of concern for radioprotection. Long-lived isotopes are also produced, which will be responsible for the long-term radiotoxicity of the target after operation. In addition, the chemical modifications due to the growth of impurities could lead to corrosion problems on the structure materials in contact with the liquid metal.

Up to recently, little confidence could be granted to the predictions of spallation residue production by high-energy models. Thanks to both the experimental data collected within HINDAS, described in section 3.2.3, and the improvement of the physics models, discussed in section 3.2.4, it is now possible to have a better confidence in the simulations and assess the quality of the prediction power of the codes. As shown in the preceding section (see Fig. 3.48), the high-energy models used in standard high-energy transport code, in fact the Bertini-Dresner [Ber63, Dre62] combination, does not correctly predict in particular the isotopic distributions and the fission fragment production measured in [Wla00, Enq01]. On the other hand, the INCL4 /ABLA model has been shown to give a satisfying agreement with the isotopic distributions of spallation residues in the region of fission and heavy evaporation products. With these models being implemented into the LAHET3 code system [Pra01], it is now possible to calculate quantities like the activity due to the spallation residues or chemical impurity production for real spallation targets with an improved confidence and compare with results of standard codes, as those obtained for instance by Shubin et al. [Shu95b].

4.2. Activation of the ADS target

4.2.1. Calculation method

Calculations have been made for a 10 cm radius, 1 m long Pb-Bi target, supposed to have been irradiated by a 1 GeV, 1 mA proton beam during one year. Spallation residue production due to the primary interactions and secondary neutron (down to 20 MeV) and proton (down to stopping) induced reactions has been estimated using the LAHET3 high-energy transport code. Two different options for the models that generate the elementary cross-sections were studied: either the (standard) Bertini-Dresner or the new INCL4-ABLA combination of intranuclear cascade-deexcitation models. The evolution of the nuclides concentrations as a function of time has been calculated with the ORIHET3 [Atc02] decay code. The neutrons below 20 MeV were transported by MCNP4C. To evaluate the activation due to the resulting neutron flux, the DARWIN [Tzi00] code (with 33 energy groups) was used. We assumed a constant target composition, as it was checked that the activation of the spallation products should be negligible. Since in an ADS or a spallation source the target will also be subject to an external neutron flux from the sub-critical core or the moderator/reflector, a calculation has also been performed with a target surrounded by D_2O, in order to estimate this contribution.

4.2.2. Calculations of activity

It has been shown in [Don02] that the main contribution comes from the spallation products and is almost two orders of magnitude larger than the one due to activation by the low energy neutron flux up to one hundred years. Even in the case of a target surrounded by D_2O, leading to a total neutron flux of $3x10^{14}$ $n.cm^{-2}.s^{-1}$, the spallation products always dominate the activity except between one month and one year when the activation of ^{209}Bi, leading to ^{210}Bi and then ^{210}Po which have respective half lives of 5 and 138 days, is of the same order of magnitude.

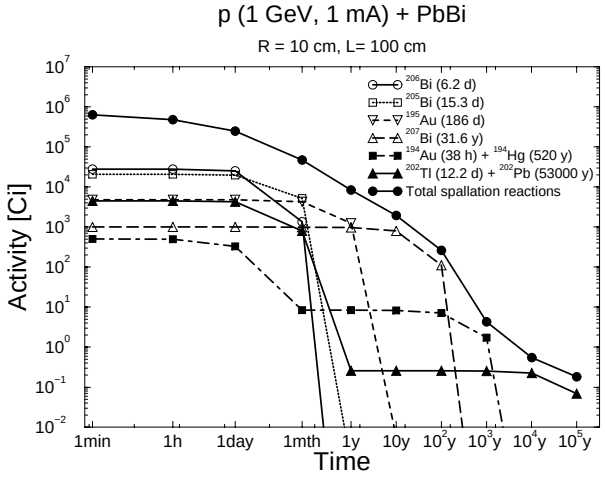

Figure 4.1 : *Activity (in Curies) of a Pb-Bi target as a function of time, after one year of irradiation, due to the spallation products (solid line), activation by the neutron flux below 20 MeV in the case of a bare target (dotted line) or in the case of a target surrounded by D_2O (dashed-dotted line).*

As far as the spallation products are concerned, a large number of isotopes is actually contributing to the total activity. During the irradiation phase, the total activity almost saturates at $5x10^5$ Ci after about one month. At this time and up to one day after irradiation, the main contributors to the activity are ^{206}Bi and ^{205}Bi for both the Bertini-Dresner and INCL4-ABLA calculations. For the decay stage, shown in Fig. 4.1 in the case of the INCL4-ABLA calculations, it can be seen that the contribution of these two nuclides is less than 10% of the total activity. This means that a large number of different isotopes contribute almost equivalently to the total activity. A similar behavior is observed up to almost a month of decay, in fact because most of these nuclides have rather short periods ($T_{1/2}$ < 30 d). For longer decay times the activity is due to a few long-lived nuclides only. For example, after 10 years of decay the nuclide ^{207}Bi represents 60% of the activity, and after 10^4 years the dominant nuclide, representing 50% of the activity, is ^{202}Tl, populated by the beta-decay of the long-lived ^{202}Pb. It can be noticed that only heavy residues close to the target elements contribute significantly. The activity due to the fission products is always less than 10-15% of the total.

When Bertini-Dresner is used instead of INCL4-ABLA, the results are globally the same although the relative contributions of individual isotopes may be different. In Fig. 4.2, we show the ratio between the activity calculated with INCL4-ABLA and the one with Bertini-Dresner as a function of the decay time.

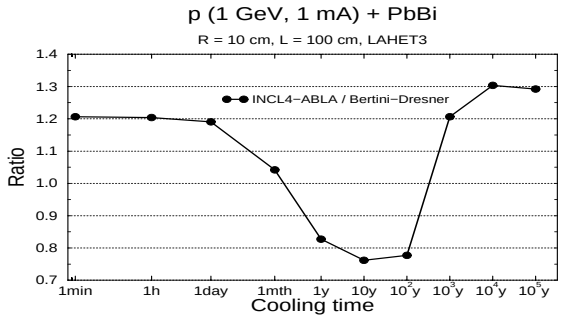

Figure 4.2 : *Ratio of the activity due to the spallation products calculated using the INCL4-ABLA and the Bertini-Dresner models, for a Pb-Bi target, as a function of time after one year of irradiation.*

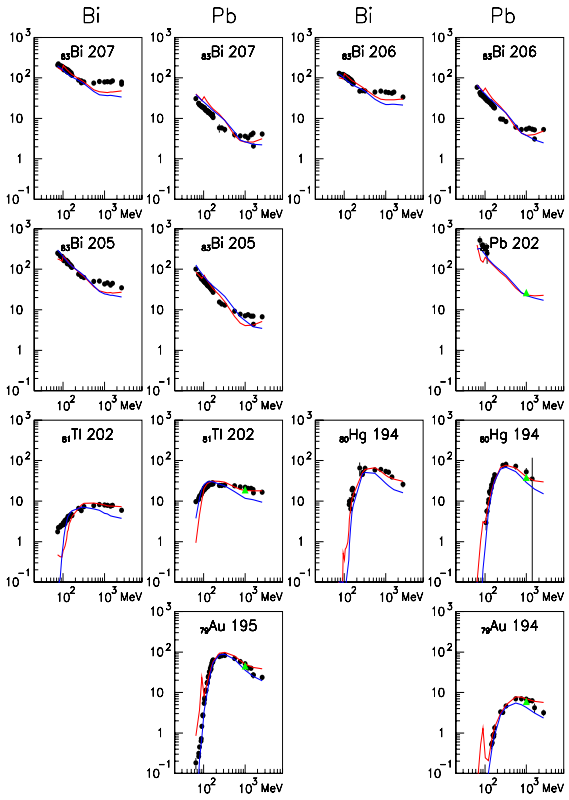

Figure 4.3 : *Comparison of INCL4-ABLA and Bertini-Dresner predictions with the production cross-sections (mb) of a few isotopes (which are the main contributors to the activity in a thick Pb-Bi target) measured in p+Pb or p+Bi by γ-spectroscopy [13] as a function of the incident energy.*

It can be seen that maximum differences are of the order of ±30%. This is not surprising since actually the models give similar results for residues very close to the target elements (see Fig. 4.3), with slight differences on the isotopic distributions, the larger discrepancies appearing for lighter isotopes. However, what is new is that we can now rely more confidently on these predictions because we know that the INCL4-ABLA does predict correctly the production of the involved isotopes. As already said, the model agrees totally with the isotopic production at 1 GeV. However, in a such thick target, the primary proton induces on average one high-energy and two secondary lower energy interactions, so it is also important to predict correctly the energy dependence of the production cross-sections. This is the case, down at

least to a few tens of MeV, as it can be seen in Fig. 4.3 where the models are compared to the elementary production cross-sections of the isotopes found to be the main contributors. The data are the ones presented in section 3.2.3 (subsection "Escitation function of residual nuclide production by proton-induced reactions"), measured by γ-spectrometry [Glo01, Mic03]. The discrepancies between the model and the data being at most 30-40%, a similar uncertainty can be assessed for the predicted activity.

4.2.3. Production of Impurities

As already stated, in a liquid metal target, chemical impurities produced by spallation reactions, can lead to corrosion problems on the container of the target or on the window if in contact with the metal. We have therefore calculated the concentrations of the different elements generated after one year of irradiation for a Pb and a Pb-Bi target. The results obtained with INCL4-ABLA (dotted curve) and Bertini-Dresner (dashed-dotted curve) are shown in Fig. 4.4. The ratio between the two calculations (solid line) is also shown. Here the discrepancy between the two models can reach a factor 3 in the region of fission fragments and up to 30 for the very light evaporation residues.

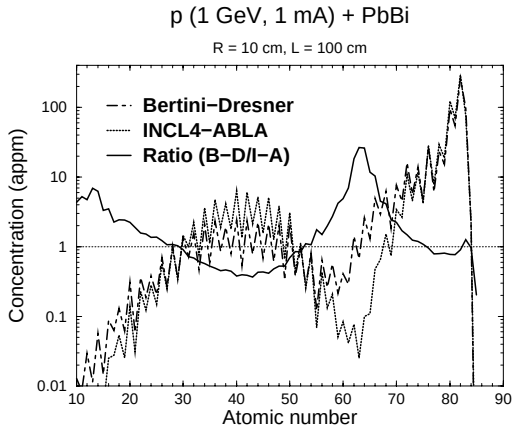

Figure 4.4 : *Concentration in appm of the different chemical impurities produced by spallation in a Pb-Bi target after one year of irradiation, calculated with LAHET3 using the INCL4-ABLA (dotted curve) or the Bertini-Dresner (dashed-dotted curve) model and ratio between the two calculations (solid line).*

Actually, this reflects exactly the differences in the elementary production of the fission fragments at 1 GeV as these fragments are produced only in relatively high-energy reactions. Since it has been established that INCL4-ABLA reproduces much better the fission region, as it can be seen in Fig. 3.46, this calculation is obviously an improvement compared to the standard codes. For the light evaporation residues that arise in very low concentrations, the situation is not as good since none of the models correctly predicts the elementary cross-sections but this gives an idea of the uncertainty on their production.
Some of the fission products are volatile gases, of which some isotopes are radioactive and can be a concern for radioprotection in case of a containment failure. It is therefore important to investigate more precisely these elements. Table 4.1 gives the results from the two models, for the expected concentrations of krypton, iodine and xenon isotopes and the total for each element. The element concentrations foreseen by the two models differ by a factor 2 maximum as found in Fig. 4.4 for these elements. However, for isotopic concentrations the discrepancies can reach a factor 4, due to the fact that the isotopic distributions are different in the two models. Here again, we can stress that with INCL4-ABLA we have a more reliable prediction but also that when using Bertini-Dresner the error on the prediction is certainly not larger than a factor 4 to 5.

Table 4.1 : *Comparison of INCL4-ABLA and Bertini-Dresner predictions for volatile gas production and ratio between the two calculations.*

Isotope	half life	PbBi		
		Concentration (appm)		Ratio I-A/B-D
		Bert-Dres	Incl4-Abla	
81 Kr	2.3E+05 y	2,4E-01	4,0E-01	1,67
85 Kr	10,8 y	8,1E-02	2,8E-01	3,46
Kr		**2,3E+00**	**4,7E+00**	**2,04**
124 I	4,1 d	9,6E-04	1,2E-03	1,25
125 I	59,4 d	3,1E-02	3,4E-02	1,10
126 I	13,1 d	2,4E-03	2,9E-03	1,21
129 I	1.7E+07 y	6,2E-02	4,3E-02	0,69
131 I	8,0 d	9,1E-04	2,8E-04	0,31
I		**2,8E-01**	**2,5E-01**	**0,89**
127 Xe	36,4 d	1,5E-02	1,6E-02	1,07
129m Xe	8,9 d	3,8E-03	3,1E-03	0,82
131m Xe	11,9 d	5,6E-04	6,0E-04	1,071
133 Xe	5,2 d	6,9E-04	2,1E-04	0,30
133m Xe	2,2 d	1,9E-05	2,9E-05	1,526
135 Xe	9,1 d	2,0E-05	5,0E-06	0,25
Xe		**8,2E-01**	**7,7E-01**	**0,94**

4.3. Gas-production and DPAs induced in an ADS window

A detailed report on this subject and the implications on applications has been delivered in the D14 within the WP4 of the HINDAS project in September 2002. Within that deliverable, estimates on the life time of structural materials have been performed.

4.3.1 Radiation Damage Parameters

- *Gas Production*

Hydrogen and its isotopes are soluble in many metals. The effect of hydrogen in metals is well documented in literature from nuclear technology. More important than hydrogen production is the formation of helium. Helium atoms are insoluble in most, if not all, metals. The helium atoms tend to migrate and form large bubbles that at least embrittle the irradiated metal. The helium embrittlement of metals has been extensively studied. A detailed review can be found in [Ull91].

- *Radiation Effects on Materials*

The other type of radiation damage to materials stems from the displacement of lattice atoms resulting from the collision of the projectile particle upon the target atom or from the recoil energy that the atom receives upon emission of a nuclear particle. In Fig. 4.5 the number of displacements produced (per ion) is shown as an example for ions of various types and initial energies stopping in aluminium. The radiation induced degradation properties appears to be similar to those of reactor neutron irradiation. The exposure for materials - beam windows and targets - in ADS or spallation sources - however are of a severity in terms of neutron and proton fluxes and energies that has no parallel in previous experience. Estimations and

calculations of damage energy and total displacements are performed by using the theory of Lindhard et al. and the semi-empirical formula of Robinson (see [Dor72, Kon92]).

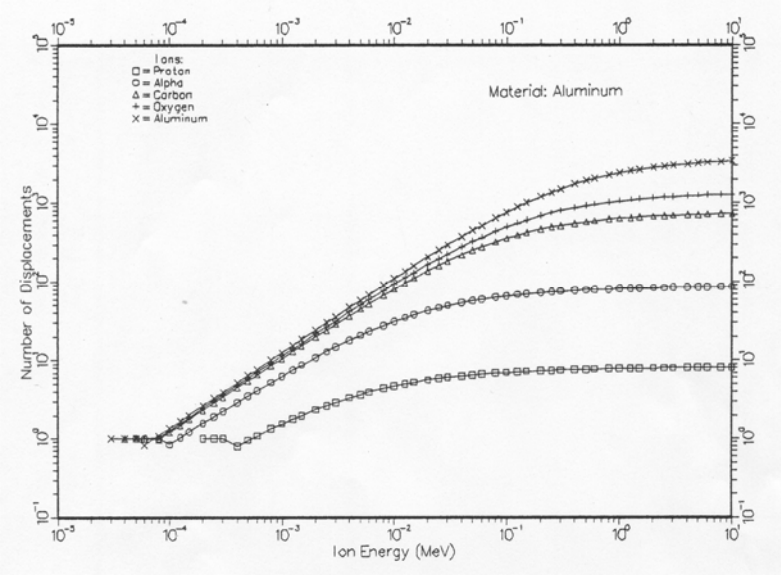

Figure 4.5 : *Number of atomic displacements produced (per ion) for ions of various types and initial energies stopping in aluminium*

Helium Production Cross Section

In particular the H- and He-production cross sections are of great importance for estimations of damages of target- and structure-materials of the planned spallation source since the lifetime of window and target materials is directly associated to those cross sections. Exactly these H- and He- measurements show large discrepancies not only between experiment and theory, but already among different models as demonstrated in Fig. 4.6. The large spread in experimental cross sections found in literature was already mentioned in section 3.2.2 for He-production cross sections following proton-induced reactions on Fe.

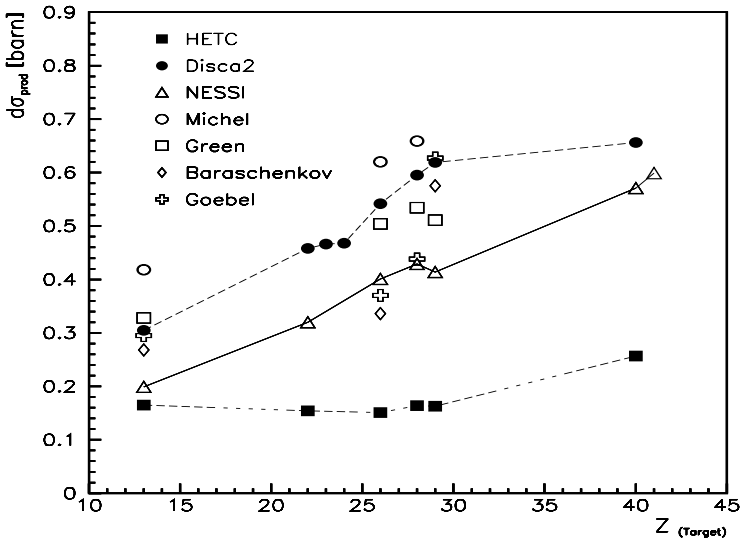

Figure 4.6 : *He-production cross sections (measured and simulated) as a function of various target materials for 0.8 GeV proton induced reactions. Data are taken from [Bar92, Enk99, Goe64, Gre88, Hil01, Kon92, Mic95].*

The calculated He cross section with Disca2 are taken from [Kon92]. Partly, these discrepancies within the models are understood: On the one hand the energy originally transferred to the nucleus during the intra nuclear cascade is differently re-distributed in various exit channels [Gol00] and on the other hand strongly different Coulomb barriers lead to differing production cross sections of charged particles [Enk99, Her00].

In the NESSI experiment [Enk99] at COSY hydrogen and helium production cross sections were measured over a wide range of target materials and incident proton-beam energies and compared with standard INC/evaporation codes. For low atomic mass targets (Z<30) the agreement of all the model predictions to the experimental values is quite good, whereas for masses above Z>30 only the INCL-code could predict the measured cross sections. Details are given in Ref. [Hil01]. Explicitly data are given for p+Fe and p+Ta in Fig. 4.7 as a function of incident proton energy.

The helium production cross sections from the NESSI experiment are about a factor of 2 smaller for p+Fe and show particular different energy dependence than the data of Michel et at. [Mic95]. The predictions of the INCL-model are for both targets (Fe and Ta) in good agreement. As stated earlier an agreement between data and calculations – INCL2 model- could be found also for all other targets for the H- and He-production cross sections. A compilation of available data on H- and He-cross sections in the energy regime up to 2.5 GeV is compiled in Tables 2 – 7 of the deliverable D14 contribution.

In summary the experimental data from NESSI represent strong constrains on the comparison with state of the art model calculations and provide an important benchmark for obtaining key parameters on gas production for ADS and spallation sources.

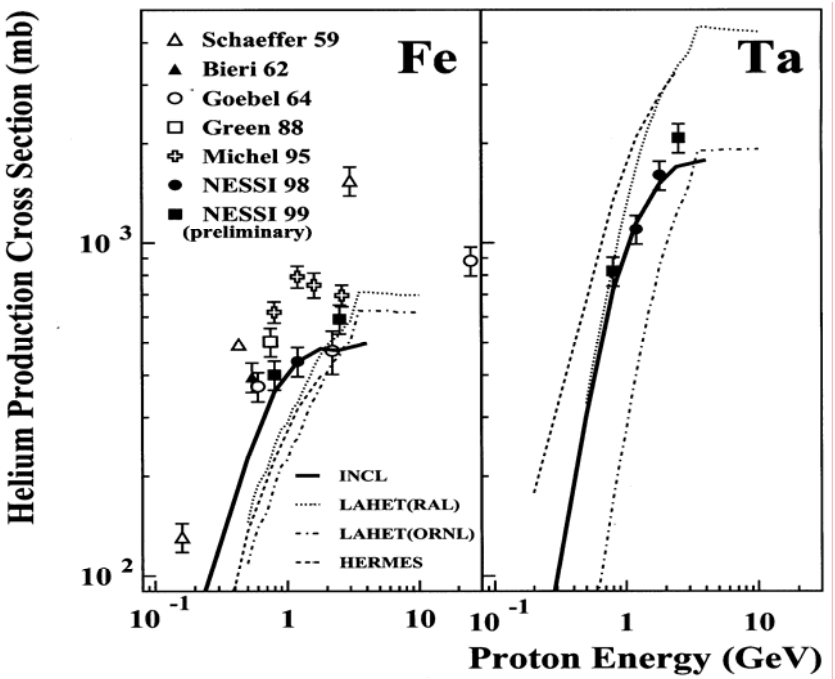

Figure 4.7 : *Compilation of experimental He-production cross sections for p+Fe and p+Ta and comparison with different INC/Evaporation models. INCL means INCL2 coupled to GEMINI evaporation code.*

4.3.2. Investigation of Radiation damage He/dpa Ratio

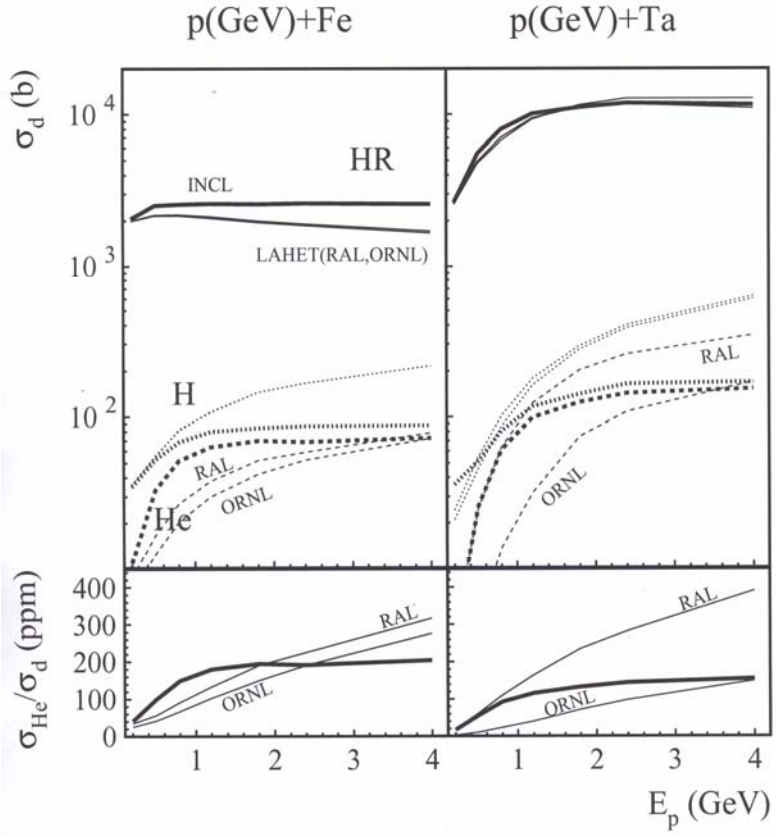

Figure 4.8 : *Comparison for Fe and Ta targets (2mm thick) -upper part- of damage cross sections σ_d of hydrogen, helium and HR (heavy residuals); lower part - comparison of He/dpa-ratios with different INCE models*

To investigate the He/dpa ratio in Fe and Ta the INCL model and for the so-called displacement cross sections to evaluate the dpa´s the Bertini-EVAP models (LAHET / HERMES) can be used to calculate recoil energy spectra via the Lindhard formalism [Dor72] taking into account the effective threshold displacement energies 40 eV for Fe and 88 eV for Ta. The dpa´s are resulting from an event-wise evaluation with the TRIM-code [Bie80] and the SID-code [Fil89].

The results are shown in Fig. 4.8 as function of incident proton energy for 2 mm thick Fe and Ta target material. The upper two panels of Fig. 4.8 show the damage cross-section σ_d in barns. The damage by hydrogen is larger as for helium because in the INCL calculations the hydrogen yield is 5-7 larger as the helium yield. The damage cross section is, however, completely dominated by the heavy residuals (HR´s). The damage cross sections are almost constant above 1,5-2 GeV incident proton energy (≈2.8 x 10^3 b for Fe and 12 x 10^3 b for Ta). As pointed out above radiation induced damage by spallation reactions is characterized by a large He/dpa ratio compared to fission and fusion devices. The ratio of helium production to displacements per atom is given by He/dpa = σ_{He}/σ_d in the lower part of Fig. 4.8. The ratio increases with proton energy up to about 1-1.5 GeV and is essentially constant for Fe about 200 x 10^{-6} and 140 x 10^{-6} for Ta. Damage cross section calculations for Fe are very similar both calculated with LAHET-TRIM or HETC-SID [Fil96]. For a time integrated proton flux of $\phi(t)$ = 1.9 x 10^{22} p/cm^2 - about one year of operation of ESS - one yields about 55 and 230 displacements per atom (dpa = σ_d x $\phi(t)$ for Fe and Ta.

4.3.3. Life Time Estimations

A more detailed study also including H, He and dpa´s from neutrons was made for a more realistic target system - the ESS target-window system [Fil96]. The influence of the H- and He concentration and damage on lifetime for targets or target windows can only be estimated on empirical results from irradiation experience of target of existing spallation sources. For this purpose we use lifetime and irradiation data of the LANL-LAMPF irradiation experiment on a proton beam window of stainless steel (Inconel 718) [Wec92]. This window is usually changed after a dose of about 10^{22} protons/cm2 at 0.8 GeV incident protons. The dose of 10^{22} protons/cm^2 is obtained in about one year irradiation time. The window is then still functional and not damaged. For a 5 MW proton beam of ESS (maximum proton beam intensity ≈4.7 x 10^{14} protons x cm^{-2} x s^{-1}) a comparable dose of 10^{22} protons is obtained in about 250 days assuming a proton energy of 0.8 GeV. Using the measured He production cross section at incident proton energy of 0.8 GeV from NESSI (Fig. 4.4) σ_{He} = 400 mb this results in an acceptable He concentration of about C_{He} = 4005 appm.

Table 4.2. : *Maximum He production and displacements using production cross sections DISCA2 evaluations (see Fig. 4.6) for an ESS like target-window interface of 5 MW proton beam power and 1.3 GeV incident proton beam energy.*

	He production [appm/day]	**displacements [appm/day]**	**He/dpa ratio**
target window (1)	**32 (18 (2))**	**0.3**	**107**
target container (1)	**0.5**	**0.06**	**5**

(1) material HT9, **(2)** contribution only by 1.3 GeV protons using NESSI production cross sections of He in Fe

At incident proton energy at 1.3 GeV we assume from the measurements σ_{He}≈450 mb and a comparable lifetime of about 220 days concerning damage by He production inside a proton beam window.
Using a detailed calculational model with a realistic geometry to determine also the contribution by neutrons produced in the target the following damage rates for the ESS like target window and container - both at stainless steel HT9 - are obtained (Table 4.2). Table 4.2 shows a much higher helium production due to the additional contributions by neutrons. Using the NESSI data the production by protons gives a value of about 18 appm/day. If we assume again lifetime and service time of the LANL-LAMPF window one may estimate a lifetime, which maybe in the order of about 100 days for a stainless steel window of a ESS like spallation source with an incident proton energy of 1.3 GeV, 5 MW beam power and a maximum proton fluence of about 4.7 x 10^{14} protons x cm^{-2} x s^{-1} on the target proton beam window.

4.3.4. Conclusions

The damage cross sections calculated with the standard HETC and the INCL were shown to be very similar despite considerable differences in other observables. The He/dpa ratios, however, differs considerably in absolute numbers as well as in energy dependence (see Fig. 4.6). There are no data for He/dpa ratios induced from high energy neutrons. A disagreement exists between different experiments on He production. More systematic measurements on different target masses and incident beam energies will be needed.

5. Assessment of Results and Conclusions

The HINDAS-project focused on high- and intermediate-energy data that are specific to an ADS, in particular on the energy region between 20 and 2000 MeV. It has been restricted on a few key elements: Fe as a structural material, Pb as representative element for the spallation target and U as representative of the actinide elements.

An European-wide collaboration of experimentalist and theoreticians merged their complementary expertise to meet basic nuclear data requests for transmutation. Various European experimental facilities were at the disposal of the project: TSL Uppsala, KVI Groningen and UCL Louvain-la-Neuve for intermediate energies up to 200 MeV, and GSI Darmstadt and FZJ Julich for energies above 200 MeV. Since both the experimental facilities as the nuclear models are changing in the energy region around 200 MeV, the project has been divided in 2 main parts: experiments and theory at intermediate energies between 20 MeV and 200 MeV and at high energies between 200 MeV and 2 GeV.

5.1. The Intermediate Energy program - from 20 MeV to 200 MeV – has provided a large set of new nuclear data, which have been compared to existing or new theoretical models and codes. The experiments have been focused on neutron, proton and light charged particles production and on residues production induced by proton and neutron beams. The obtained data have been directly used by the theoretical model developers and nuclear data evaluators.

The most important achievements concerning **theoretical models and nuclear data libraries** are the following:

- New ENDF-6 formatted nuclear data libraries from the unresolved resonance range up to 200 MeV were produced for Fe, Pb and U isotopes, for both incident neutrons and protons. Promising results are obtained with the first integral tests. Inclusion in the JEFF-3.1 data library and further application in ADS analyses is foreseen.
- A new nuclear model code, TALYS, was developed for energies from the unresolved resonance range up to 200 MeV. The code describes basically all HINDAS-experiments between 20 and 200 MeV, ranging from elastic scattering distributions, double-differential spectra, residual production cross sections to fission yields. TALYS was used to create the nuclear data libraries for Fe and Pb.
- A new global optical model for neutrons and protons up to 200 MeV was developed. Also new coupled-channels optical model and fission model (including a triple humped fission barrier penetration model) were developed for U-238 to enable data evaluation for all energies up to 200 MeV.
- Prompt neutron multiplicity models:
  - from Madland-Nix-Vladuca-Tudora and extended by Morillon up to 40 MeV,
  - from Duarte up to 200 MeV in the frame of his INC model (code BRIC).
- Promising results are obtained with the fully microscopic DYWAN model for the prediction of double-differential spectra.
- The predictive power of the TUL model for preequilibrium reactions has been demonstrated for double-differential cross sections at low excitation energies and small angles for charge-exchange reactions at intermediate energies. Thus this model might in the future be included in the TALYS code.
- The developed theoretical and computational techniques are all applicable for energies *below* 20 MeV. In particular the TALYS code, which was partly developed outside the HINDAS project, can be used for future nuclear data evaluations from the unresolved resonance range up to 200 MeV.

Numerous new **experimental results** have been obtained with renewed or new original experimental methods at proton and neutron energies between 20 MeV and 200 MeV.

The study of light charged particle production (p, d, t, ^{3}He and ^{4}He) induced by proton beams has been performed between 20 and 65 MeV at UCL-Louvain-la-Neuve, at 100 MeV at TSL-Uppsala and at 135 MeV at KVI-Gronigen. The experiments involving quasi-monoenergetic neutron beams were performed at the two first facilities.

- The (p,xlcp) reactions have been performed at 65 and at 135 MeV on Fe, Pb and U. On the other hand, the (p,xlcp multiplicities) and angle-differentiated cross sections of light-charged particles have been measured for the first time at 190 MeV for the 3 targets. For those last measurements, a large hemispheric plastic ball detector has been developed and used fot the backward angles and a small-angle large-acceptance detector (SALAD) at the forward angles.
- The (n,xlcp) reactions have been studied between 30 and 65 MeV and at 100 MeV. Complete angular distributions between 20° and 160° have produced a large amount of new Double Differential Cross Sections (DDXS) $d^2\sigma/d\Omega dE$ has been obtained as well as $d\sigma/d\Omega$, $d\sigma/dE$ and total production cross sections in an energy region were almost no neutron-induced reactions had been previously measured. Comparison of ^{nat}Fe and ^{nat}Pb targets to isotopically pure targets like ^{59}Co and ^{209}Bi have not shown measurable effects in these experiments.
- Comparisons of the data with existing nuclear codes and especially with the new TALYS code have produced important informations on the preequilibrium part of the reaction mechanism and overall rather good fits to the data.

The study of neutron production induced by proton and neutron beams has produced the following new results:

- The (p,xn) reaction on Pb and U at 62.9 MeV provide an interesting comparison with the (n,xp) and the (p,xp) reaction at the same energy. Comparison with TALYS show a large improvement compared to the Los Alamos GNASH code.
- The elastic (n,n) scattering on Fe and Pb has beeeen measured at 100 MeV at TSL. Excellent fits to the data have been obtained with the global optical model included in TALYS.
- The study of (n,xn) reactions at this energy are much more difficult to perform. Two detectors assemblies, sensitive respectively to the lower part (10 to 50 MeV) and to he higher part (40 – 100 MeV) of the energy spectrum have been constructed and successfully tested. The experiments will be performed in the near future.

The production of residual nuclides has been studied by irradiation with proton beams between 20 and 70 MeV and with neutron beams between 20 and 200 MeV on a large set of elements, including Fe, Pb and U. Besides classical off-line γ-spectrometric methods, accelerator-mass spectrometry (AMS) has been used for the determination of long-lived radionuclides. The following conclusions may be drawn :

- Cross sections for the production of long-lived radionuclides, such as those obtained on iron and lead within the HINDAS project, are essential with respect to estimating the long term and waste deposition problems of accelerator driven systems.
- For uranium, new and comprehensive data for the production of residual nuclides by proton-induced reactions were measured for energies from 21 MeV to 69 MeV. Further measurements at higher energies are needed.
- For neutron-induced reactions on iron, lead and uranium, a first comprehensive set of excitation functions for the production of residual radionuclides was measured, exhibiting major differences between neutron- and proton-induced production of residuals. In residual

nuclide production, the neutron- and the proton-induced reactions have to be carefully distinguished. The assumption of equal cross sections does not hold.
- Finally, the experimental data base for fission cross sections on elements relevant for neutron metrology as well as accelerator driven technologies was extended to 200 MeV.

5.2. The high-energy program of the HINDAS project – from 200 MeV to 2 GeV - has permitted the collection of a large amount of new and high-quality experimental data covering all the most important reaction channels (neutron, light charged particles and residue production) in three regions of the periodic table around iron, lead and uranium for proton incident energies above 800 MeV. All the collected data have been compared to well-known nuclear physics models, in particular those widely used in high-energy transport codes. The following conclusions could be drawn:

- As regards neutron production, there now exists a complete and coherent set of experimental data on double-differential cross-sections and multiplicities on both thin and thick targets that has been used to assess the quality of the predictions of different high-energy transport codes. It can now be stated that total neutron production in an ADS target can be predicted with a precision of 10-15%, which is also the precision of the experiments. General trends of energy, angular or geometry dependence are also well understood.
- Light charged particle (hydrogen and helium) measurements, for which very few data were available before HINDAS, have been performed at different energies on different targets. While data from different measurement techniques agree for lead targets, not understood discrepancies remains for iron. Comparisons with codes have revealed severe deficiencies in most of the currently used models, in particular for helium predictions.
- The production of some intermediate mass residual nuclei important for radioprotection, such as ^{7}Be or ^{10}Be, has been measured on a wide energy range and found underpredicted by orders of magnitude by the nuclear models, likely because of a production mechanism not yet well understood.
- For residue production, HINDAS has brought a considerable enhancement of available data thanks both to the reverse kinematics technique, which has lead to the measurements of thousands of identified isotopes and to excitation functions obtained in direct kinematics experiments, which allow testing the energy dependence of the production. The comparison of the predictions of available codes with the measured isotopic distributions has pointed out wrong behaviours of the nuclear models concerning the competition between neutron, charged particle emission and fission.

Meanwhile, an important effort has been devoted to the testing and improving of theoretical models in view of including the best possible physics. This has been possible because the quality of the HINDAS experimental data have often lead to a better understanding of the reaction mechanism and of the reasons for deficiencies in the previous models.

- A new version of the intra-nuclear cascade from Liège, INCL4, has been developed in which the introduction of a realistic nuclear surface diffuseness, better Pauli blocking, angular momentum treatment, among other improvements, have resulted in much better predictions of total reaction cross-sections and peripheral reactions.
- For the de-excitation stage of the reaction, the ABLA model has proved to give a much better reproduction of isotopic distributions and fission yields than other well known models.
- The INCL4-ABLA combination has been compared to the whole set of available experimental data obtained during the HINDAS project but also to earlier experimental results. An overall good agreement has been found out that, it must be stressed, with the

same set of parameters in the models, whatever the system studied, the observable compared or the bombarding energy.
- This INCL4-ABLA combination has been implemented into high-energy transport codes widely used for ADS design, as LAHET3, MCNPX and HERMES/MC4 and are now available to the whole community.
- The MC4 new high energy transport code, which is written in a modern language and includes the possibility to use different models and analysis tools, has been developed for the HERMES code system.

Concerning the impact of the work done during the HINDAS project for what concerns the ADS design, several studies have been conducted:
- Simulations of thick Pb and Pb-Bi targets have been performed with the LAHET3 code which have shown that total activity are predicted with a precision of about 30% independently of the choice of models while factors up to 3 of discrepancies can expected for volatile fission fragment emission when using standard model rather than ours.
- Neutron leakage energy spectra from thick targets, which are important for shielding, are rather well predicted by INCL4-ABLA.
- Helium production and damage cross-section in ADS window have been estimated: while DPA calculated with the standard models and INCL are rather similar, Helium production varies considerably.

At the end of the HINDAS project, it can be said that the situation concerning high-energy data and models has been largely improved. However, the work performed within HINDAS was limited in the energy range (most experimental results above 800 MeV) and in the studied targets (Fe, Pb and U). Also, a few remaining discrepancies between experimental data and lacks have been pointed out and there are still not well understood (from a physical point of view) deficiencies of the models. If we want that the high-energy transport codes could be able to predict any quantity related to the spallation target and environment, this calls for a pursuing of the work in the future. Among the most important points to be addressed are:
- The large disagreement existing on helium production in iron targets, which may have important consequence for the window life time
- The production of intermediate mass fragments, for which we need more experimental data and a mechanism to produce them in the models
- The understanding of the under prediction of the light evaporation residues by the models, which could be due either to a too low excitation energy at the end of the cascade or to deficiencies of the evaporation model. For this we need more constraining experiments, in which several observables can be measured simultaneously. During HINDAS, the feasibility of two such experiments, SPALADIN and PISA, has been studied and are now under preparation at GSI and COSY respectively.
- The energy dependence of residue isotropic distributions, which has not been studied in HINDAS, and could help solving the two preceding points.
- Measurements on one element intermediate between lead and iron, since different behaviours in the comparisons with the models have been observed and are not presently understood. Niobium, which is also employed in the superconducting cavities, could be an example.
- Measurements on lighter elements, such as aluminium present in some structure materials, would also be necessary, since the models may be for this system out of their range of validity and new approaches have to be considered.

At the end of the HINDAS project, the obtained results have been presented in 31 deliverables, which have been produced in time. Those results are already being used in other FP5 projects such as MUSE and PDS-XADS, and more applications of HINDAS data are expected in the near future.

Results of the HINDAS project have been made available to the public at various conferences.
Mentioned here are the Nuclear Data Conference for Science and Technology in Tsukuba (2001), the Accelerator-Driven Transmutation Technology and Applications conferences in Reno (2001) and San Diego (2002) and the Workshop on Nuclear Data for Transmutation in Darmstadt (2003), which was largely devoted to HINDAS. Synthesis of those results are published in the refereed most important journals.

6. Acknowledgements

We acknowledge the European Community who has relied on us and who has given the necessary financial support for the accomplishment of this project. We are especially very grateful to our scientific manager, Ved Bhatnagar, who always accepted to inform us and who helped us in the administrative tasks of this project.

At the end of the project, we would also like to thanks all collaborators who did of HINDAS a fruitful project full of new experimental data, set-ups, theoretical calculations … To carry out this project, the knowledge and skills of many people have been required and it is impossible to mention everybody here.

We would like to thank the different collleagues who organized the 6-month meeting at the University of Santiago de Compostela, at TSL-Uppsala, at KVI-Groningen, at PSI-Villigen and ETH-Zürich, at COSY-Jülich and especially at GSI-Darmstadt for the Final meeting and the TRAMU conference, organized in a masterly way by Dr.K.-H.Schmidt and Mrs. Alexandra Kelic.

We also wish to thank the different accelerator staffs of the TSL, KVI, UCL, PSI, COSY and GSI facilities who delivered us excellent beams for our experiments.

Finally, a special tribute has to be paid to Dr.Isabelle Slypen for her unvaluable help and deep involvement in the scientific and administrative support of the coordinator and the different partners of the project.

7. References

[Ada03] J. Adam et al., Investigation of cross sections for the formation of residual nuclei in reactions induced by 660 MeV protons interacting with natural uranium targets, Proceedings TRAMU: Workshop on Nuclear Data for Transmutation of Nuclear Waste, GSI Darmstadt (Germany), September 1 - 5, 2003, in preparation.
[Akk85] J.M. Akkermans and H. Gruppelaar, Phys. Lett. 157B (1985) 95
[Ala75] J.P. Alard et al., Il nuovo cimento, Vol. 30a, n°2 (1975)
[Ali95] S.T.Ali et al., Rev. Math. Phys 7 (1995) 1013
[Alm75] E. Almen-Ramstroem, AE-report AE-503 (1975)
[Ana83] N. Anantaraman, H. Toki, G.F. Bertsch, Nucl. Phys. A 398 (1983) 269
[Arm77] T. W. Armstrong and K. C. Chandler, HETC Monte-Carlo Nucleon-Meson Transport Code, Report CCC-178, ORNL(1977) and Nucl. Sci. Eng. 49 (1972) 110

[Arm93] T. W. Armstrong, K. C. Chandler, SpaR – Stopping Powers and Ranges, ORNL-RSIC CCC-228 (1973)
[Ash58] A. Ashmore, D.S. Mather, S.K. Sen, Proc. Phys. Soc. A 71 (1958) 552
[Atc80] F.Atchinson, Report Juel-Conf-34, Kernforschungsanlage Jülich GmbH (1980)
[Atc94] F.Atchison, Intermediate Energy Nuclear Data: Models and Codes, Proc. of a Specialists' Meeting, OECD/NEA, Issy-le-Moulineaux, France, May 30 - June 1 (1994) 199
[Atc02] F.Atchison and H. Schaal, private communication (2002)
[Bab02] M. Baba et al, J. Nucl. Sci. Technol. Suppl. 2 (2002) 204
[Bad01] A. Baden et al., Nucl. Instr. and Meth. 203 (1982) 189
[Bai77] D.E. Bainum, R.W. Finlay, J. Rapaport, J.D. Carlson, and W.G. Love, Phys. Rev. C16 (1977) 1377
[Bal86] R. Balian et al., Phys. Rep. 1 (1986) 131
[Bar03] R.Barna et al. Nucl. Instr. Meth. Phys. Res. A (2003) in press
[Bar92] V. S. Barashenkov, F.D. Toneev, Atomizat, Moscow (1992) (in Russian)
[Bar93] B.C. Barashenkov, Cross sections of interactions of particles and nuclei, JINR Dubna 1993
[Bas68] R. Bass and R. Wechsung, report EANDC(E)-89 (1968) 58
[Ben97] S. Benck, I. Slypen, V. Corcalciuc and J.-P. Meulders, Nucl. Phys. A 615 (1997) 220
[Ben98] S.Benck, I. Slypen, J.-P. Meulders and V. Corcalciuc, Eur. Phys. J. A 3 (1998) 149
[Ben98b] S. Benck, I. Slypen, J.-P. Meulders and V. Corcalciuc, Eur. Phys. J. A 3 (1998) 159
[Ben98c] S. Benck, I. Slypen, J.-P. Meulders, V. Corcalciuc and M. Chadwick, Phys. Rev. C 58 (1998) 1558
[Ben98d] J.Benlliure et al, Nucl. Phys. A 628 (1998) 458
[Ben99a] S.Benck, I. Slypen, J.-P. Meulders and V. Corcalciuc, Atomic Data and Nuclear Data Tables 72 (1999) 1
[Ben99b] J.Benlliure et al., Nucl. Phys. A 660 (1999) 87
[Ben01] J.Benlliure et al., Nucl. Phys. A 638 (2001) 513
[Ben02] J.Benlliure, J. Pereira-Conca, K.-H. Schmidt, Nucl. Instrum. Methods A 478 (2002) 493
[Ber03] M. Bernas *et al.*, Nucl. Phys. A 725 (2003) 213
[Ber03] O. Bersillon, Bruyeres-le-Chatel, private communication.
[Ber63] H. W. Bertini et al., Phys. Rev. 131 (1963) 1801
[Ber73] F.E. Bertrand and R.W. Peelle Phys. Rev. *C* 8 (1973) 1045
F.E. Bertrand and R.W. Peelle *Oak Ridge Report* ORNL-4799 (1973)
[Ber96] O. Bersillon, "2nd Int. Conf. on Accelerator Driven Transmutation Technologies", Kalmar, Sweden, June 3-7, 520, (1996).
[Ber03] M. Bernas et al., Nucl. Phys. A 725 (2003) 213
[Bha86] K.-H. Bhatt, P. Grangé and B. Hiller, Phys. Rev. C 33 51986) 954
[Bie62] R.H.Bieri et al., Helvetia Phy.Acta 35 (1962) 553
[Bie80] J. P. Biersack and L.G. Haggmark, Nucl. Instr. and Meth. 174 (1980) 257
[Bla52] J.M. Blatt and L.C. Biedenharn, Rev. Mod. Phys. 52 (1952) 725
[Bla92] M. Blann, in Workshop on Computation and Analysis of Nuclear Data Relevant to Nuclear Energy and Safety, edited by M.K. Mehta and J.J. Schmidt, Feb. 10 - March 13 1992, Trieste, Italy, (1993), p. 622.
[Bla94] M. Blann, H. Gruppelaar, P. Nagel and J. Rodens, International Code Comparison for Intermediate Energy Nuclear Data, OECD/NEA (1994)
[Bli03] V. Blidaenu, Ph D thesis , Caen, France (2003)
[Blo03] J. Blomgren, Uppsala Accelerator News, n°21 (2003)
[Blo82] J. Blons, thesis, Orsay (France) 1982
[Blo89] J. Blons et al., NPA 502 (1989) 121c
[Boh55] A. Bohr, in Conference on Peaceful Uses of Atomic Energy, Genève, 151 (1955)
[Bon95] J. P. Bondorf, A. S. Botvina, A. S. Iljinov, I. N. Ishustin, K. Sneppen, Phys. Rep. 257 (1995) 133
[Bor97] F.Borne et al., Nucl. Instrum. Methods Phys. Res. A385 (1997) 339
[Bou02] A.Boudard et al., Phys. Rev. C66 (2002) 044615
[Bou03a] A.Boudard, contribution to the TRAMU conference, Darmstadt, Germany, Sept. 1-5, 2003, to be published.
[Bou03b] A.Boudard et al., The Liège intranuclear cascade code INCL4.1 and the K.-H. Schmidt code KHSv3p, 2003, HINDAS Report

[Bra50] A. Bratenahl et al, Phys. Rev. 77 (1950) 597
[Bra84] F.P. Brady et al, Nucl. Instr. Meth. A 228 (1984) 89
[Bri97] J.F. Briesmeister, MCNP - A Monte Carlo n-particle transport code, Los Alamos National Laboratory Report, LA-12625-M (1997).
[Bri97] J.F. Briesmeister, MCNP - A Monte Carlo n-particle transport code, Los Alamos National
[Bro90] U. Brosa, S. Grossmann, and A. Müller, Phys. Rep. 4 (1990) 197
[Car91] R.F. Carlton, R.R. Winters, J.A. Harvey, N.W. Hill, C.H. Johnson, and J. Schiedmayer, Bull. Amer. Phys. Soc. 36 (1991) 1349
[Car97] A.D. Carlson et al., Update to Nuclear Data Standards for Nuclear Measurements, Summary Report of a Consultants' Meeting held in Vienna, Austria, 2 to 6 December 1996, International Atomic Energy Agency Report INDC(NDS)-368
[Cas01] E. Casarejos, PhD thesis, 2001, University of Santiago de Compostela, Spain
[Cha43] S. Chandrasekhar, Rev. Mod. Phys. 15 (1943) 1
[Cha88] R.J. Charity et al., Nucl. Phys. A 483 (1988) 391
[Cha98] M.B. Chadwick et al., Nucl. Sci. Eng. 131 (1999) 293
[Cha99] M. Chadwick et al., Acta Physica Slovaca 49 (1999) 365
[Che97] P. Chesny et al., GSI Scientific Rep. 1996, GSI 97-1 (1997) 190
[Clo88] P.Cloth et al., HERMES, Report Jülich 2203, ISSN 0366-0885, (1988)
[Clo93] P.Cloth, D, Filges, G. Sterzenbach, Proceedings of MC93 Int. Conf. on Monte Carlo Simulation in High Energy and Nuclear Physics, Tallahassee, Florida USA 1993.
[Clo96] P.Cloth, et al., For the ZEUS Collaboration, Jül 3200, Feb.1996, ISSN 0944-2952 p 128
[Coh63] S.Cohen, W. J. Swiatecki, Ann. Phys. 22 (1963) 406
[Coh74] S.Cohen, F. Plasil, and W.J. Swiatecki, Ann. of Phys. 82 (1974) 557
[Con90] H.Conde et al., Nucl. Instr. Meth. Phys. Res. A 292 (1990) 121
[Cos00] R. Coszach et al., Phys. Rev. C61 (2001) 054601
[Cug87] J.Cugnon, Nucl. Phys. A462 (1987) 751
[Cug96] J.Cugnon, DL'Hôte, J. Vandermeulen, Nucl. Instr. and Meth. in Phys. Res. B 111 (1996) 215
[Cug97a] J. Cugnon, C. Volant and S. Vuillier, Nucl. Phys. A620 (1997) 475
[Cug97b] J. Cugnon et al., Phys. Rev. C56 (1997) 2431
[Cug01] J. Cugnon et al., Nucl. Phys. A620 (1997) 475
[Cug02] J. Cugnon and P. Henrotte, Eur. Phys. J. A 16 (2003) 393
[Cun47] B.B. Cunningham et al.., Phys. Rev. 72 (1947) 739
[Cha88] R.J.Charity et al., Nucl. Phys. A483 (1988) 371
[Dan00] S. Dangtip et al., Nucl. Instr. Meth. Phys. Res. A 452 (2000) 484
[Dau92] I. Daubechies, Ten lectures on Wavelets, Ams providence (1992)
[Dav63] J.H. Davies et al., Canad. J. Phys. 41 (1963) 762
[Dav03] J.-C. David et al., contribution to the TRAMU conference, Darmstadt, Germany, Sept. 1-5, 2003, to be published.
[DeV81] R.P.DeVito, S.M.Austin, W. Sterrenburg, U.E.P. Berg, Phys. Rev. Lett. 47 (1981) 628
[DeV83] R.P.DeVito, S.M.Austin, U.E.P. Berg, R. De Leo, W.A. Sterrenburg, Phys. Rev. C 28 (1983) 2530
[Dic77] J.K. Dickens, Nucl. Sci. Eng. 63 (1977) 101
[Dol76] T.J. Dolan, Fusion Research, Volume III-Technology, Pergamon Press (1976)
[Don02] L. Donadille et al., J. of Nucl. Science and Techn., Suppl. 2, (August 2002) 1194
[Don03] L. Donadille et al., Contribution to Int. Conf. AccApp'03, San Diego, USA, June 2003
[Dor72] D. G. Doran, Nucl. Sci. Eng. 49 (1972) 130
[Dre62] L. Dresner, Oak Ridge report ORNL-TM-196 (1962)
[Dua04] H. Duarte and O. Bersillon, unpublished
[Dua99] H. Duarte, in Proceedings of the 3rd International Conference on ADTTA, Praha, Czech Republic (1999)
[Duf00] C. Dufauquez, I. Slypen, S. Benck, J.-P. Meulders and V. Corcalciuc, Nucl. Phys. A 671 (2000) 20
[Dui01] M.C. Duijvestijn, A.J Koning, and F.-J. Hambsch, Phys. Rev. C64 (2001) 014607
[Dui99] M.C. Duijvestijn et al., Phys. Rev. C59 (1999) 776
[Dun01] C. Dunford, ENDF Utility Codes Release 6.12 (2001)
[Eis96] V.P. Eismont et al., Phys. Rev. C 53 (1996) 2911

[Emp01] M. Herman, in Workshop on Nuclear Reaction Data and Nuclear Reactors: Physics, Design and Safety, edited by N. Paver, M. Herman and A. Gandini, March 13 - April 14 2000, Trieste Italy, (2001), p. 137.
[ENDF] Cross Section Evaluation Working Group (Data Formats and Procedures for Evaluated Nuclear Data Files ENDF-6 Working) (2001)
[Enk99] M. Enke et al., Nucl Phys. A.657 (1999) 317
[Enq99] T. Enqvist et al., Nucl. Phys. A 658 (1999) 47
[Enq01] T.Enqvist et al., Nucl. Phys. A. 686 (2001) 481
[Enq02] T.Enqvist et al., Nucl. Phys. A. 703 (2002) 435
[Fes80] H. Feshbach, A. Kerman, S. Koonin, 1980
[Fil89] D. Filges et al., ECFA Study Week on Instr. Techn. for High-Luminosity Hadron Colliders, Report CERN 89-10, ECFA 89-124, Vol. 1,2, (Nov. 1989) 165
[Fil95] D. Filges, P. Nagel and R.D. Neef, OECD thick target benchmark, Report NSC/DOC (95) 2 (1995)
[Fil96] D. Filges et al., Report ESS 96-45-T, 1996
[Fil01] D. Filges et al., Eur. Phys. J. A11 (2001)467
[Fin84] R.W. Finlay et al., Phys. Rev. C30 (1984) 796
[Fin93] R.W. Finlay et al., Phys. Rev. C47 (1993) 237
[Fos71] D.G. Foster Jr. and D.W. Glasgow, Phys. Rev. C3 (1971) 576
[Fou02] Y. Foucher, Ph D thesis , Nantes, France (2002)
[Fow62] J.L. Fowler and E.C. Campbell, Phys. Rev. 127 (1962) 2192
[Fre80] J. Frehaut, A. Bertin, R. Bois, and J. Jary, in Symposium on neutron cross sections from 10-50 MeV, Upton, USA, May 12-14 1980
[Fri63] E.M. Friedlander et al., Phys. Rev. 129 (1963) 1809
[Fur01] S. Furihata et al., The GEM Code – A Simulation program for the Evaporation and theFission Process of an Excited Nucleus, JAERI-Data/Code 2001-015, 2001
[Gab77] T.A. Gabriel et al., CALOR: a Monte Carlo program package for the design and analysis of calorimeter systems, Report ORNL/TM-5619, Oak Ridge 1977
[Gal94] J. Galin, U.Jahnke, Nucl.Part.Phys. 20 (1994) 1105
[Gar84] D.G. Gardner, in Neutron Radiative Capture, OECD/NEA Series on Neutron Physics and Nuclear Data in Science and Technology, eds. A. Michaudon et al. (1984) 62
[Gei92] H. Geissel et al. 1992, Nucl. Instrum. Methods B 70 (1992) 286
[Gil65] A. Gilbert and A.G.W. Cameron, Can. J. Phys. 43 (1965) 1446
[Gin83] J. E. Gindler, L. E. Glendenin, D. J. Henderson, and J. W. Meadows, Phys. Rev. C 27 (1983) 2058
[Gla02] W.Glasser et al., Nucl. Science Technology, Supplement 2 (2002) 373
[Glo01] M.Gloris et al., Nucl. Instr. Meth. Phys. Res. A 463 (2001) 593
[Goe64] K.Goebel et al.,Report CERN 64-12 (1964)
[Gol74] A.S.Goldhaber, Statistical models of fragmentation processes, Phys. Lett. B 53 (1974) 306-308.
[Gol96] F.Goldenbaum et al., Phys. Rev. Lett. 77 (1996) 1230
[Gol00] F.Goldenbaum et al., Proc. of the Int. Conf. on Advanced Monte Carlo for Radation Phys., Lisbon, Portugal, 23-26 October (2000)
[Gra83] P. Grangé, L. Jun-Qing, and H.A. Weidenmüller, Phys. Rev. C 27 (1983) 2063
[Gre88] S.L.Green et al., J.Nucl.Mat.115-157 (1988) 1350
[Gru86] H. Gruppelaar, P. Nagel ans P.E. Hodgson, Riv. Nuovo Cimento 9, No. 7 (1986) 1
[Gue01] A. Guertin, Ph D thesis , Nantes, France (2001)
[Har58] R.S. Harding, Phys. Rev. 111 (1958) 1164
[Hau52] W. Hauser and H. Feshbach, Phys. Rev. 87 (1952) 366
[Hau00] J. A. Hauger and EOS collaboration, Phys. Rev. C 62 (2000) 024616
[Hen03] J.S. Hendricks et al., MCNPX, Version 2.5.d, Los Alamos National Laboratory Report LA-UR 03 5916 (2003)
[Her00] C.M.Herbach et al., Proc. of the SARE-5meeting, OECD, Paris, July 2000
[Her01] C.M. Herbach et al., FZJ Jülich annual report (2001)
[Her03] C.M. Herbachet al, Nucl. Instrum. Methods A508 (2003) 315
[Hil53] D.L. Hill and J.A. Wheeler, Phys. Rev. 89 (1953) 1102
[Hil98] D.Hilscher et al., Nucl. Inst. and Meth. A414 (1998) 100

[Hil01] D.Hilscher et al., J. Nucl. Mat. 296 (2001) 83
[Hil03] S. Hilaire et al., , Ann. Phys. 306 (2003) 209
[Hjo94] E.L. Hjort et al., Phys. Rev. C 50 (1994) 275
[Hjo96] E.L. Hjort et al., Phys. Rev. C 53 (1996) 237
[Hor86] D.J. Horen, C.H. Johnson, J.L. Fowler, A.D. MacKellar, and B. Castel, Phys. Rev. C34 (1986) 429
[Hor92] D. Horn et al., Nucl Instrum. Methods Phys. Res. Sect. A 321 (1992) 273
[HPRL] High Priority Request List, www.nea.fr/html/science/projects/nucleardata.html.
[Hug97] H.G.Hughes et al., MCNPX – The LAHET/MCNPX Code Merger, X-Division Research Note XTM-RN(U)97-012, LA-UR-97-4891, Los Alamos National Laboratory, 1997
[Iba00] M. Ibaraki et al.,J. Nucl. Sci. Technol., Suppl. 1 (2000) 683
[Ign75] A.V. Ignatyuk, M. G. Itkis, V. N. Okolovich, G. N. Smirkin, A. S. Tishin, Yad. Fiz. 21 (1975) 1185, (Sov. J. Nucl. Phys. 21 (1975) 612
[Ign77] A.V.Ignatyuk, M. G. Itkis, V. N. Okolovich, G. R. Ruskina, G. N. Smirenkin, A. S. Tishin, Yad. Fiz. 25 (1977) 25 (Sov. J. Nucl. Phys. 25 (1977) 13)
[Ign79] A.V.Ignatyuk, K. K. Istekov, G. N. Smirenkin, Yad. Fiz. 29 (1979) 875 (Sov. J. Nucl. Phys. 29 (1979) 450).
[Itk85] M.G. Itkis, V.N. Okolovich, A.Ya. Rusanov, and G.N. Smirenkin, Sov. J. Nucl. Phys. 41 (1985) 544
[Itk88] M.G. Itkis et al., Sov.J.Nucl.Phys. 47(1988) 4
[Jah03] U. Jahnke et al., Nucl. Instrum. Methods A508 (2003) 295
[JEFF] Nuclear Energy Agency (*The JEF2.2 Nuclear Data Library*) (2000)
[Jon98] M. de Jong et al., Nucl. Phys. A 628 (1998) 479
[Jou98] B. Jouault, F. Sebille and V. de la Mota, Nucl. Phys. A628 (1998) 119
[Jun96] A.R. Junghans *et al.,* Nucl. Instrum. Methods A 370 (1996) 312
[Jun98] A. R. Junghans et al., Nucl. Phys. A629 (1998) 635
[Jur02] B. Jurado, K.-H. Schmidt, K.-H. Behr, Nucl. Instrum. Methods A 483 (2002) 630
[Jur03] B. Jurado, K.-H. Schmidt, J. Benlliure, Phys. Lett. B 533 (2003) 186
[Kal01] C. Kalbach, PRECO-2000: Exciton model pre-equilibrium code with direct reactions, Duke University 2001, www.nndc.bnl.gov/nndcscr/model-codes/preco-2000/
[Kal01] N. Kalantar-Nayestanaki et al., Nucl. Instr. and Meth. A444 (2000) 591
[Kal88] C. Kalbach, Phys. Rev. C37 (1988) 2350
[Ker02] M. Kerveno et al., Phys. Rev. C66 (2002) 014601
[Kim99] E.J. Kim et al., J. Nucl. Sci. Techn., 36 (1999) 29
[Kla69] R. Klapisch, Ann. Rev. Nucl. Science 19 (1969) 33
[Klu02] J. Klug et al., Nucl. Instr. Meth. Phys. Res. A489 (2002) 282
[Klu03a] J. Klug et al., Phys. Rev. C 67 (2003) 031601(R)
[Klu03b] J. Klug et al., accepted for publication in Phys. Rev. C.
[Kol03] D. Kollár, Ph.D. thesis, Comenius University, Bratislava (2003)
[Kon92a] A.Y.Konobenev et al., Data library for radiation damage , Carl Hanser Verlag München 1992, Kernt Technik 57, No.3 (1992)
[Kon92b] AYU. Konobeyev, YU. A. Korovin, J. of Nucl. Mat. 195 (1992) 286
[Kon92c] A. YU. Konobeyev et al., J. of Nucl. Mat. 186 (1992) 117
[Kon98] A.J. Koning, J.-P. Delaroche and O. Bersillon, Nucl. Instr. and Methods A414 (1998) 49
[Kon03] A.J. Koning and J.P. Delaroche, Nucl. Phys. A713 (2003) 231
[Kon03] A.J. Koning, S. Hilaire, M. Duijvestijn and J.P. Delaroche, Proceedings of the 2002 Frederic Joliot/Otto Hahn summer school in reactor physics: Modern reactor physics and the modelling of complex systems, Aug. 21-30, 2002, Cadarache, France.
[Kon03b] A.J.Koning and J.P. Delaroche, 2003, Local and global nucleon optical models
[Kon04] A.J.Koning and M. Duijvestijn, to be published (2004)
[Kon04] A.J.Koning, S. Hilaire and M.C. Duijvestijn, unpublished (2004)
[Kon04b] A.J.Koning and M.C. Duijvestijn, to be published (2004)
[Kop90] . Kopecky and M. Uhl, Phys. Rev. C42 (1990) 1941
[Kra40] H.A. Kramers, Physika VII 4 (1940) 284
[Kun01] P.D. Kunz, University of Colorado, (1983) unpublished;
B. Mukherjee and M.N. Harakeh, KVI report (2003)
[Lan89] Accelerator Production of Tritium, LANL Report La-UR 90-3651, October 25 (1989)

[Lar89] N.M.Larson, Users' Guide to Sammy, Oak Ridge National Lab. report,ORNL/TM-9179/R1 (1989)
[Lec03] F.R. Lecolley, in Workshop on Nuclear Data for the Transmutation of Nuclear Waste, 2003, GSI-Darmstadt, Germany (2003)
[Led99] X. Ledoux et al., Phys. Rev. Lett. 82 (1999) 4412
[Len92] H. Lenske, H.H. Wolter, Nucl. Phys. A 538 (1992) 483c
[Ler02] S. Leray et al., Phys. Rev. C65 (2002) 044621
[Let00] A. Letourneau, Nucl. Instr. and Meth. in Phys. Res. B170 (2000) 299
[Let02] A. Letourneau et al., Nucl. Phys. A 712 (2002) 113
[Ley00] I. Leya at al., Meteoritics & Planetary Science 35 (2000) 287
[Lis91] P.W. Lisowski et al., Procceedings of a Specialists‘ Meeting on Neutron Cross Section Standards for the Energy Region above 20 MeV, Uppsala, Sweden, 1991, OECD/NEA Report NEANDC-305 ‘U‘, p. 177
[Lop04] M.J. Lopez et al., to be published
[Mac00] R.E. Macfarlane, NJOY99 - Code system for producing pointwise and multigroup neutron and photon cross sections from ENDF/B Data, RSIC PSR-480 (2000)
[Mad88] D.G. Madland, in Proceedings of a Specialists' Meeting on Preequilibrium Reactions, Semmering, Austria, February 10-12 1988 (OECD, Paris 1988) 103
[Mar97] M. Matzke, Proc.3rd ASTM-Euratom Symposium on Reactor Dosimetry, Ispra, 1.-5.10.1979 (1979) 721
[Mei99] S. Meigo et al., Nucl. Instrum. Methods Phys. Res. A431 (1999) 521
[Mén98] S. Ménard, PhD Thesis, Université d'Orsay (1998)
[Meu00] J.-P. Meulders et al., “Physical aspects of Lead as a neutron producing target for accelerator transmutation devices”, Concerted Action Contract FI4I-CT98-0017, Final report (2000)
[Mia02] M.M.H. Miah et al., Nucl. Science Technology, Supplement 2 (2002) 369
[Mic73] A. Michaudon, Advances in Nuclear Physics, Vol. 6, Chapter 1, p. 136. Edited by M. Baranger and E.Vogt, 1973
[Mic95] R. Michel et al., Nucl. Instr. Meth. B103 (1995) 183
[Mic97a] R. Michel et al., Nucl. Instr. Meth. Phys. Res. B129 (1997) 153
[Mic97b] R. Michel, P. Nagel, 1997, International Codes and Model Intercomparison for Intermediate Energy Activation Yields, NSC/DOC(97)-1, NEA/OECD, Paris.
[Mic02] R. Michel et al., Nucl. Science Technology, Supplement 2 (2002) 242
[Mic03] R. Michel, private communication (2003)
[Mol80] P.A. Moldauer, Nucl. Phys. A344 (1980) 185
[Möl95] P. Möller, J. R. Nix, W. D. Myers, W. J. Swiatecki, At. Data Nucl. Data Tables 59 (1995) 185
[Mor89] D. Morrissey, Systematics of momentum distributions from reactions with relativistic ions, Phys. Rev. C 39 (1989) 460
[Mot01] V.de la Mota and F. Sébille, Eur. Phys. J. A12 (2001) 479
[Mug81] S.F.Mughabghab, M. Divadeenam, and. N.E. Holden, Neutron Cross Sections, Vol. I, Neutron Resonance Parameters and Thermal Cross Sections (Academic Press, 1981).
[Muk01] B.Mukherjee et al., KVI annual report (2002) 32
[Muk02] B.Mukherjee et al., Phys. Rev. C (2003) communicated
[Nel98] R.Nelson, private communication
[Neu98] S.Neumann et al., Conf. Proc. Vol. 59, Nuclear Data for Science and Technology“, G. Reffo, A. Ventura and C. Grandi (Eds.), Società Italana di Fisica, Bologna (1998) 379
[Neu99] S.Neumann, Aktivierungsexperimente mit Neutronen mittlerer Energien und die Produktion kosmogener Nuklide in Meteoriten, Ph. D. thesis, Universität Hannover (1999)
[Nic02] N. Nica et al., J. Phys. G: Nucl. Part. Phys. 28 (2002) 2823
[Nis88] H. Nishioka, H.A.Weidenmüller, S. Yoshida, Ann. Phys. 183 (1988) 166
[Nol00] R. Nolte, private communication (data obtained within the HINDAS collaboration)
[Nün01] K. Nünighoff, Report JÜL-3916, October 2001
[Oko74] V.N. Okolovich, O.A. Zhukova, M.G. Itkis, S.I. Mulgin, IYFK (1974) 112
[Per71] D. G. Perry, A. W. Fairhall, Phys. Rev. C 4 (1971) 977
[Per77] F.G. Perey, Least-squares dosimetry unfolding: The program STAY’SL, Rep. ORNL-TM-6062., revised by L.R. Greenwood (1977)

[Per03] J. Pereira, PhD thesis, 2003, University of Santiago de Compostela, Spain
[Pie97] L. Pienkowski et al., Phys. Rev. C56 (1997) 1909
[Plo92] A.J.M. Plompen et al., Proceedings of the International conference on nuclear data for science and technology, Oct. 7-12 2001, Tsukuba, Japan, Journal of Nuclear Science and Technology, Supplement 2, August 2002, 192
[Pra88] R.E.Prael, M.Bozoian, Report Los Alamos National Laboratory LA-UR-88-3238, 1988
[Pra89] R. Prael and H. Lichtenstein, User guide to LCS: The LAHET Code System, Los Alamos Rep. UR-89-3014 (1989)
[Pra97] R.E. Prael and M.B. Chadwick, Los Alamos preprints LA-UR-97-1744, 1997
[Pra01] R. Prael, private communication (2001)
[Pro99] A.V. Prokofiev et al., Nucl. Sci. Eng. 131 (1999) 78
[Pro02] A.V. Prokofiev et al., Nucl. Science Technology, Supplement 2 (2002) 112
[Rae03a] E. Raeymackers et al., Phys. Rev. C 68 (2003) 024604-1
[Rae03b] E. Raeymackers et al., Nucl. Phys. A 726 (2003) 210
[Rah01] J. Rahm et al, Phys. Rev. C 63 (2001)
[Ram04] E.Ramstroem, H. Lenske, and H.H. Wolter, in Workshop on Nuclear Data for the Transmutation of Nuclear Waste, 2003, GSI-Darmstadt, Germany (2003)
[Ray94] J. Raynal, code ECIS95; Note CEA-N-2772 (1994)
[Ray94] J. Raynal, Notes on ECIS94, CEA Saclay Report No. CEA-N-2772, 1994
[Rej01] F. Rejmund et al., Nucl. Phys. A 638 (2001) 540
[Ric92] W.A. Richter et al, Phys. Rev. C 46 (1992) 1030
[Ric94] W.A. Richter et al, Phys. Rev. C 49 (1994) 1001
[Ric96] W.A. Richter et al, Phys. Rev. C 54 (1996) 1756
[Ric03] M. V. Ricciardi, PhD thesis, 2003, University of Santiago de Compostela, Spain
[Rip98] Handbook for calculations of nuclear reaction data Reference Input Parameter Library, IAEA-TECDOC-1034 (1998)
[Ris89] H. Risiken, 'The Fokker-Planck Equation', Springer -Verlag, Berlin Heidelberg, 1989, ISBN 0-387-50498-2.
[Rom96] P. Romain et al., in Proceedings of the NEA Specialists'Meeting on the Nucleon-Nucleus Optical Model up to 200 MeV, Bruyères-le-Châtel (1996)
[Ros83] G. Rossi, Z. Phys. 82 (1983) 151
[Roy00] G. Royer and C. Bonilla, private communication.
[Sak80] H. Sakai et al., Nucl. Phys. A 344 (1980) 41
[Sal60] G.L. Salmon, Nucl. Phys. 21 (1960) 15
[Sau83] H. Sauvageon, S. Regnier, G.N. Simonoff, Z. Phys. A 314 (1983) 181
[Sch59] O.A.Schaeffer et al., Phys.Rev. 113 (1959) 674
[Sch82] K.-H.Schmidt, H. Delagrange, J. P. Dufour, N. Carjan, A. Fleury, Z. Phys. A 308 (1982) 215
[Sch87] K.-H.Schmidt et al., Nucl. Instrum. Methods A 260 (1987) 287
[Sch91] K.-H.Schmidt et al., Nucl. Phys. A 531 (1991) 709
[Sch92] U.J.Schrewe et al., in: S.M. Qaim (ed.): Nuclear Data for Science and Technology, Springer Verlag, Berlin (1992) 669
[Sch97] D. Schmidt, W. Mannhart, and B.R.L. Siebert, in Proceedings of the International Conference on Nuclear Data for Science and Technology, Trieste, Italy, edited by G. Reffo (1997) 407
[Sch99] H. Schuhmacher et al., Nucl. Instrum. Methods Phys. Res. A 421 (1999) 284
[Sch00] K.-H. Schmidt et al., Nucl. Phys. A 665 (2000) 221
[Sch02] K.-H. Schmidt, M. V. Ricciardi, A. Botvina, T. Enqvist, Nucl. Phys. A 710 (2002) 157
[Seg82] R.E. Segel et al, Phys. Rev. C26 (1982)
[Shi73] O.E. Shigaev, V.S. Bychenkov, M.F. Lomanov, A.I. Obukhov, N.A. Perfilov, G.G. Shimchuk, R.M. Jakovlev, RI-17 (1973)
[Shu95a] Yu.N. Shubin et al., Cross-section data library MENDL-2 to study activation and transmutation of materials irradiated by nucleons of intermediate energies, IAEA INDC(CCP)-385, Vienna, Austria (1995)
[Shu95b] Yu.N. Shubin et al., Proc. Int. Conf. Evaluation of Emerging Nuclear Fuel Cycle System, GLOBAL 1995, Sept. 11-14 (1995)
[Sie86] A.J. Sierk, Phys. Rev. C33 (1986) 2039

[Sim93] S.P. Simakov et al. , Yadernye Konstanty 4 (1993) 93
[Sly00a] I. Slypen, S. Benck, J.-P. Meulders and V. Corcalciuc, Nucl. Phys. A 671 (2000) 3
[Sly00b] I. Slypen, S. Benck, J.-P. Meulders and V. Corcalciuc, Atomic Data and Nuclear Data Tables 76 (2000) 26
[Sly03] I. Slypen et al., J. Physics G.: Nucl. Part. Phys. 30 (2004) 45
[Sly94] I. Slypen, V. Corcalciuc and J.-P.Meulders, Nucl. Phys. B 88 (1994) 275
[Smi95] A.N. Smirnov et al., Rad. Meas. 25 (1995) 151
[Ste98] G. Sterzenbach et al., "2nd Int. Topical meeting on nuclear Application of Accelerator Technology, AccApp98", ISBN 0-89448-633-0, Sep. 20-23, Getlinburg (1998)
[Str87] Ch. Straede, C. Budtz-Jørgensen, H. -H. Knitter, Nucl. Phys. A 462 (1987) 85
[Sub83] T. Subramanian et al, Phys. Rev. C 28 (1983) 521
[Sub86] T. Subramanian et al., Phys. Rev. C 34 (1986) 1580
[Tai03] J. Taieb et al., Nucl. Phys. A 724 (2003) 413
[Tam65] T. Tamura, Reviews of Modern Physics, Vol. 37, No. 4 (1965)
[Tam82] T. Tamura, T. Udagawa, H. Lenske, Phys. Rev. C 26 (1982) 379
[Til95] I.Tilquin et al, Nucl. Instr. Meth. Phys. Res. A 365 (1995) 446
[Tow63] .H. Towle and W.B. Gilboy, Nucl. Phys. 44 (1963) 256
[Tra72] B.L. Tracy et al., Phys. Rev. 5, No. 1 (1972) 222
[Tzi00] T. Tzilanitzara et al., J. of Nucl. Sc. And Tech., Suppl. 1 (2000) 845
[Uhl76] M. Uhl and B. Strohmaier, Computer code for particle induced activation cross sections and related quantities, IRK report No. 76/0, Vienna (1976).
[Var99] C. Varignon, PhD Thesis, Université de Caen (1999)
[Vla01] G. Vladuca and A. Tudora, Annals of Nuclear Energy 28 (2001) 1653
[Vla03] G.Vladuca, A.Tudora, F. -J. Hambsch, S. Oberstedt, I. Ruskov, Nucl. Phys. A 720 (2003) 274
[Von94] H. Vonach et al., Phys. Rev. C50 (1994) 1952
[Wei37] V. F. Weisskopf, Phys. Rev. 52 (1937) 295
[Wla00] W. Wlazlo et al., Phys. Rev. Lett. 84 (2000) 5736
[Woh03] M. Wohlmuther, PhD Thesis. January 2003, TU-Graz (not published)
[Wol56] R. Wolfgang et al., Phys. Rev. 103 (1956) 394
[Wu79] J.R. WU et al, Phys. Rev. C19 (1979) 370
[Yar79] Y.Yariv and Z. Fraenkel, Phys.Rev. C20 (1979) 2227
[Yar81] Y.Yariv and Z. Fraenkel, Phys.Rev. C24 (1981) 448
[Yok96] A.Yokoyama, Z. Phys. A356 (1996) 55
[You92] P. Young, E. Arthur, M. Chadwick, 1992, Los Alamos National Laboratory Report No. LA-12343-MS ; GNASH-FKK version gn9cp0, PSR-0125, program received from NEA Data Bank (1999)
[You96] P.G. Young et al., "Comprehensive nuclear model calculations / Introduction to the theory and use of the GNASH code", Workshop on Nuclear reaction data and nuclear reactors, Trieste (1996)
[Zyl56] C.P. van Zyl, R.G.P. Voss, R. Wilson, Phil. Mag. 1 (1956) 1003.